The Spatially-Resolved Stellar Populations of Nearby Early-type Galaxies

PADRAIG DAVID EDMUND ALTON

The Spatially-Resolved Stellar Populations of Nearby Early-type Galaxies

Padraig D. Alton.

We report our investigation into the stellar populations of early-type galaxies (ETGs) in the local universe. Massive ETGs are thought to form in a manner very different to our own Milky Way, with their cores formed via a swiftly-quenched rapid starburst $\gtrsim 10\,\mathrm{Gyr}$ ago and their outskirts assembled later through cumulative mergers with predominantly less-massive systems. This formation history is encoded in the properties of their stellar populations.

Various evidence indicates that in the cores of massive ETGs, the stellar initial mass function differs from that of the Milky Way, with an increased fraction of dwarf stars formed. This effect, along with signatures in the chemical abundance properties of these stars, has been linked to ETG assembly histories. We use a combination of infrared and optical spatially-resolved spectroscopy of a sample of eight nearby massive ETGs ($\sigma_{\mathrm{average}} \sim 230\,\mathrm{kms}^{-1}$) to measure empirical gradients in the strengths of spectroscopic absorption features, some of which are not hitherto well-explored. Using state-of-the-art stellar population models and robust methods for statistical inference, we link these to the underlying properties of the stars in these galaxies.

We measure strong gradients in spectroscopic features linked to Na I (at 0.82 μm, 1.14 μm, and 2.21 μm) as well as the Ca II 0.86 μm triplet. We measure weak/no gradient in several features that trace the IMF, such as the FeH 0.99 μm Wing-Ford band. We use models to interpret these measurements, inferring e.g. an [Fe/H] gradient of –0.16±0.05 per dex in fractional radius and an average [Na/Fe] gradient of –0.35±0.09. We find a large but radially-constant enhancement to [Mg/Fe] of ∼0.4 and a much lower [Ca/Fe] enhancement of ~ 0.1. Finally, we find no significant IMF gradient either on average or even in individual galaxies where such gradients have been previously reported.

The Spatially-Resolved Stellar Populations of Nearby Early-type Galaxies

Padraig D. Alton

A Thesis presented for the degree of
Doctor of Philosophy

Centre for Extragalactic Astronomy
Department of Physics, University of Durham

June 2017

Contents

List of Tables

List of Figures

List of Abbreviations

ETG Early-Type Galaxy

IMF (stellar) Initial Mass Function

MCMC Markov-Chain Monte-Carlo

SPINDRIFT Stellar Population Inference Driven by Index Fitting Techniques

KMOS K-band Multi-Object Spectrograph

FIRE Folded-port Infrared Echellette

WiFeS Wide-Field Spectrograph

KINETyS KMOS Infrared Nearby Early-Types Survey

Declaration

The work presented in Chapters 3 and 4 has been previously published as part of Alton et al. (2017).

Statement of Copyright

Acknowledgements

On a cold night in early spring, under skies unusually free of clouds for temperate North-West England, I first looked up. It was twenty years ago, I'd been allowed to stay up late, and the Great Comet of 1997 was approaching perihelion. Over the next months the comet faded, returning to the far reaches of the solar system, but a new-found obsession with space and everything in it did not.

Inevitably, there's a long list of people to thank for getting me to where I am (i.e. writing a corny lede for an almost-finished astrophysics thesis) – starting (Oscars-style) with my family. In particular, my extremely-tolerant parents, who seemed happy enough to supply endless books about the universe and to allow me to drag them around science museums for many hours. More importantly, they have supported and encouraged me in the pursuit of my academic goals throughout. Likewise, things might have gone very differently without many years of shared enthusiasm (and friendly rivalry) with Joe Lea. I was also extremely fortunate to have several excellent teachers, but I'll single out Mrs. Fisher in particular for teaching me that in physics, an integral in the hand is worth two flaky hypotheses in the bush.

I am also indebted to a plethora of people at Cambridge: to the gang of Peterhouse NatScis, my comrades – and especially my astrophysical co-conspirator Ellis Owen – without whom it would have been a lonelier degree; to various supervisors (very forgiving of my imperfections as a student) and lecturers; and to all those members of staff without whom a college community would collapse.

Focusing on the path that led me into research, thanks are due to Br. Guy Consolmagno for providing me with my first real experience, and to Dr. Digby Symons for taking me on for a summer project, despite not being an engineering student (and thereby ensuring that my publication history will be forever eclectic). My MSci supervisor, Dr. Bethan

James, provided singular guidance and encouragement, as well as the project that first led me into the realm of extragalactic astrophysics (and thence to Durham).

With a move to Durham comes a whole other list of people to say thank you to: Helen and Tim, for putting up with me; Andrew, with whom I've covered many miles; Saavi, James, and others with whom I've shared good conversations and good times; Ben and Ruari for office camaraderie, coding advice, and good-humoured political debate. Thanks also to all the rowers of St. Aidan's College whom I've coached, for reminding me what putting yourself on the line for others looks like – and to the various people who make that most excellent college a welcoming home for all. In particular, thanks to (Dr!) Matthieu Schaller for helping me get my bearings from day one, keeping my presidency of the S.C.R. afloat, and for being the bridge between college and the physics department ... as well as an excellent pub-quiz team-mate.

However, above all else I am indebted to my supervisors, Dr. John Lucey and Dr. Russell Smith. To John, for making this project possible, for the extra level of scientific rigour you helped me to bring to my work, and for your invaluable depth of knowledge (apparently regarding every single galaxy, telescope, or paper in existence) that enabled me to see the wood, despite all the trees. To Russell, for pouring vast amounts of time and effort into advice and encouragement over the last four years, providing an always-open door, and somehow contriving to spin every single set-back into something positive! It's sometimes said that the most important thing required to complete a PhD is to first find the right supervisor, and it's clear to me that in coming to Durham I very much fell on my feet. It has been a genuine privilege to work with both of you.

Dedication

To Rebecca Tsao, who inspires me to excellence and with whom life is brighter – thank you for supporting me throughout.

✦

As in all things, A. M. D. G.

Chapter 1

Introduction

1.1 A tale of two galaxies

Luminous galaxies in the nearby universe can be broadly classified, using their observable properties, as belonging to two distinct groups. One group comprises galaxies that are actively forming stars, often contain large amounts of molecular gas, typically display spiral arms, and have blue photometric colours. In contrast to these are galaxies which are no longer forming stars, host old stellar populations, and have redder photometric colours. Such galaxies often have an elliptical morphology. This latter group are often referred to as 'early-type' or 'red-sequence galaxies'. The first of these terms was used historically to emphasise the dichotomy in complexity of appearance between these fairly featureless objects and the other class of galaxy ('late-type'/'blue cloud' galaxies), which often display complex morphological features. In reality early-type galaxies are *not* the progenitors of late-type galaxies (Baldry, 2008). The second term refers to their photometric properties, which follow a tight relationship between the magnitude and colour of the galaxy, with brighter (more massive) galaxies being redder. Sometimes the term 'elliptical galaxies' is misleadingly used for the entire class. This, however, is imprecise since some quiescent (that is, non-star-forming) galaxies are not elliptical, e.g. lenticular/S0 galaxies and passive spiral galaxies.

1.2 The formation of early-type galaxies

Discussions of how early-type galaxies (ETGs) are formed have historically focussed on two alternative scenarios. In the monolithic collapse theory (Eggen et al., 1962), galaxies start life as an overdense region in the early universe that undergoes gravitational collapse and is eventually stabilised by rotational and collisionless pressure support. In the hierarchical assembly paradigm (White & Rees, 1978), massive galaxies are instead assembled via minor and major mergers of smaller systems formed at early times. This picture is in better agreement with cosmological simulations and with observations of high-redshift galaxies, i.e. galaxies viewed at an earlier epoch. These distant galaxies are considerably more compact than their local counterparts (van Dokkum et al., 2008), indicating that the counterparts have undergone additional mergers to grow in size.

The most massive ETGs are now thought to be assembled in two stages, a hybrid of the two scenarios just presented. First, a dense core of stars grows rapidly via dissipative accretion of gas and/or via gas-rich galaxy mergers. At the bottom of the growing galaxy's gravitational potential well the gas quickly becomes chemically enriched by many supernovae. Star formation is swiftly quenched, most likely through a combination of AGN and stellar feedback, ending this phase. Observations indicate that the dense, quiescent core then accumulates a larger envelope of stars via a series of minor 'dry' (gas-poor) galaxy mergers, leading to significant size growth between the end of star formation (at redshift $z \approx 2$) and the present day (see Bezanson et al., 2009, Hopkins et al., 2009, Hopkins et al., 2010). Hydrodynamic galaxy formation simulations appear to support this model (Oser et al., 2010, Oser et al., 2012, Hilz et al., 2013).

The ETG population can be further subdivided into fast and slow rotators, a classification scheme based on angular momentum (Emsellem et al., 2007). Broadly speaking, in slow rotators equilibrium against collapse is maintained principally by collisionless pressure, while in fast rotators there is a significant level of rotational support. It is believed that the two classes may have different formation histories; in particular, there is evidence that slow rotators are significantly more likely to have undergone major ($\sim$ equal mass) mergers (see Bois et al., 2010, Khochfar et al., 2011, and Naab et al., 2014). These events are quite disruptive and so could strongly affect the kinematics of the evolved galaxy.

1.3 The stellar populations of early-type galaxies

The stellar populations hosted by ETGs bear the marks of their rapid assembly and quenching. ETGs have red photometric colours, a consequence of their quiescent nature. Massive stars on the main sequence have hotter surface temperatures and therefore bluer colours than low-mass stars, but are also shorter-lived. Without ongoing star formation to replenish the massive star content of the ETG, the ETG quickly becomes dominated by less massive, more evolved, cooler stars.

ETGs are typically metal enriched and strongly 'α-enhanced', meaning that the ratio of the abundance of α-capture elements (O, Ne, Mg, Si, S, Ar, Ca, Ti) relative to the abundance of Fe is significantly higher than in the solar neighbourhood. This feature results from short star formation timescales: the long time delay between the first Type II and the first Type Ia supernova following a burst of star formation conspires with their different nucleosynthetic yields to produce this effect.

In detail, Type II supernovae result from the core-collapse of massive stars ($\gtrsim 8\,\mathrm{M}_{\odot}$) that have expended their supply of fuel for nuclear fusion. This process proceeds very rapidly for the most massive, short-lived stars (lifetimes range from under a Myr to a few tens of Myr) and creates α elements in great abundance, as well as Fe-peak elements. Stellar material is then scattered throughout the interstellar medium by the supernova and can be reincorporated into a new generation of stars. By contrast, Type Ia supernovae originate in binary systems and arise from longer-lived, lower mass progenitor stars, which leave behind a white dwarf stellar remnant after evolving off the main sequence. In these cases stellar evolution takes hundreds of Myr or even several Gyr. There are multiple theoretical channels by which Type Ia supernovae may be caused, but all involve dynamical evolution of the binary system and lead to the degenerate white dwarf star approaching/exceeding the Chandrasekhar limit, causing a thermonuclear runaway. Every Type Ia supernova that occurs therefore only takes place after sufficient time has passed for the progenitor star to evolve off the main sequence *and* for the binary system to evolve dynamically. Combined, these processes can take many Gyrs (Worthey et al., 1992, Maoz et al., 2012). Type Ia supernovae primarily create Fe-peak elements, yet only if star formation is still ongoing after this delay can the enriched material be reincorporated into

new stars; otherwise Fe-peak enrichment lags behind α enrichment.

The level of α-enhancement is observed to be correlated with galaxy velocity dispersion (Thomas et al., 2005, Greene et al., 2015). We can therefore infer that the most massive galaxies also had the fastest, most violent initial starburst phases.

The formation of individual stars is governed by complex physics which we have only begun to understand relatively recently (for a review, see McKee & Ostriker, 2007). The gravitational collapse of molecular clouds is interrupted by turbulent fragmentation, creating many protostellar cores which continue to accrete material for some time. Particular populations of stars form at different times from gas under different conditions (e.g. pressure, density); the gas may be composed of a varying mix of chemical elements, which affect the gas cooling rate and ionisation balance. Despite this complexity, we observe that throughout our own galaxy each population of stars starts out with a very similar distribution of masses, as noted in Kroupa (2001) and Chabrier (2003). In other words, the spatially-averaged *outcome* of the star formation process has been observed to be remarkably uniform. For a review, see Bastian et al. (2010).

This is perhaps an unintuitive result. What it amounts to is a statement as follows: regardless of the initial conditions, everywhere in the Milky Way where stars are being formed, stars of a given mass form at a fixed rate relative to stars of other masses. As a result, we may speak of a stellar 'initial mass function' – a distribution of masses that characterises any freshly-formed population of stars.

1.4 The stellar initial mass function

The stellar initial mass function, or IMF, was first constrained in the Milky Way by Salpeter (1955). In that work, direct counts of stars in the Milky Way were used to determine the distribution of stellar luminosities and – via models for stellar evolution – thence to fit a functional form to the inferred distribution of stellar masses of bright stars (1 $M_\odot$ or higher). The distribution was found to obey a power law:

$$\frac{dN}{dM} \propto M^{-2.35}$$

Here N is the number density of (newly-formed) stars and M is stellar mass. This

'classical' IMF is usually referred to as the Salpeter power law. It is also sometimes expressed with respect to logarithmic stellar mass, which is related to the first expression by a factor of M:

$$\frac{dN}{dlnM} \propto M^{-1.35}$$

Throughout this work the first of these conventions will be followed unless otherwise stated.

The IMF of low mass stars remained perforce unconstrained for some time due to the difficulty of directly observing dim sub-solar mass stars. Clearly, however, the power law form cannot extend to arbitrarily low stellar masses, else we would conclude that there should be an arbitrarily large number of arbitrarily small stars. A cut-off must therefore be applied, limiting the mass range over which the IMF applies. Such a cut-off does have physical motivation: the turbulent fragmentation of molecular clouds cannot create arbitrarily small protostellar cores, since the opacity of fragments below a certain size is too high for them to efficiently radiate away the gravitational energy liberated as they collapse (Hoyle, 1953, Rees, 1976). Miller & Scalo (1979) suggested that in fact the IMF 'flattens' for stars below $1M_{\odot}$; more detailed studies at the turn of the millennium measured this behaviour in detail, with Kroupa (2001) describing the IMF as a segmented power law and Chabrier (2003) proposing a lognormal distribution for low mass stars. The two descriptions are similar in practice.

Fig. 1.1 shows these various functional forms. The cumulative mass distributions are also shown (the IMFs have been normalised such that the total initial mass is equal in each case).

Variations in the IMF

It is not at all clear, *a priori*, why the IMF should be so consistent across different Milky Way stellar populations. Notwithstanding a handful of claimed detections of IMF variations (see, for example, Luhman et al., 2003 and Marks et al., 2012), the IMF appears to be robust against rather large changes in star formation conditions – star formation timescales, gas composition and physical conditions – between the Milky Way disc field,

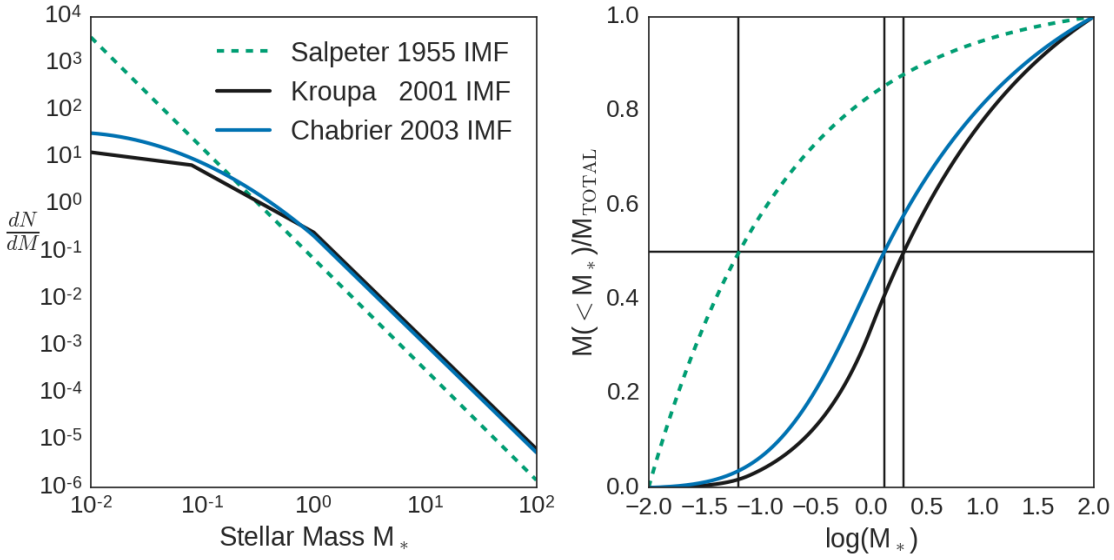

Figure 1.1: *Left panel:* Milky Way IMF descriptions for stellar populations of equal total initial stellar mass. The Salpeter power law holds for stars above $1\mathrm{M}_\odot$ but at lower masses provides a poor description of the Milky Way stellar populations, producing an excess of low-mass stars compared to the other, more accurate descriptions.

Right panel: cumulative mass functions for each of these IMFs, integrated between cut-offs at 0.01 and $100\,\mathrm{M}_\odot$. For the Salpeter power law extrapolated down to this limit, most of the stellar mass immediately after a burst of star formation is contained in dwarf stars with $M < 0.1M_\odot$: in practice this is not true in the Milky Way, where the Kroupa and Chabrier IMFs provide a better description. $50^{\rm th}$ percentiles are shown by black lines.

starburst clusters, globular clusters, and the galactic centre (e.g. see Chabrier, 2003, Bastian et al., 2010).

Why ought the complex physics of star formation be resilient against changes in gas composition, total star formation rate, local environment etc? It may be that star-formation really is isolated from the surrounding conditions, but even so there are strong theoretical arguments *against* a completely universal IMF. For example, Population III stars are formed early in the life of the universe out of pristine gas. As-yet unobserved, they are not expected to form according to the local IMF, instead having high masses (and therefore short lifetimes) due to the inability of metal-free gas to cool efficiently via emission (see Bromm & Larson, 2004 and citations therein) – star-forming gas may be somewhat isolated from surrounding conditions, but its own composition cannot be ignored. Perhaps it is simply the case that gas conditions are too uniform across the Milky Way for differences in the outcome of the star formation process to be apparent? In that case, we ought to look at other galaxies where conditions may be substantially different. It is possible that the IMF in these is, in fact, *not* the same as in the Milky Way.

This is a crucial question. Whatever the truth is, it will have important implications for our understanding of the star formation process. Moreover, there are other practical reasons for considering this issue, as will now be detailed.

Two stellar populations with initial stellar masses distributed respectively according to a Salpeter power law and a Milky Way-like IMF (e.g. Kroupa or Chabrier) will have very different cumulative mass distributions; this was shown in Fig. 1.1. However, these populations will nonetheless have quite similar cumulative *luminosity* functions, as shown in Fig. 1.2 (right panel). This is because the most massive surviving stars ($\sim 1\,\mathrm{M}_\odot$) contribute almost all ($> 90\%$) of the light. Fig. 1.2 is for a 10 Gyr old stellar population. After this length of time, stars with $\mathrm{M}_* \gtrsim 1\,\mathrm{M}_\odot$ have left the main sequence, becoming very much more luminous in the process (more massive stars than this will have already ended their lives in supernovae explosions). As a result, two equally bright stellar populations formed according to these different IMFs would have very different total mass. The population formed according to a Salpeter IMF would have a large excess of dwarf stars over the Milky Way-like population – in other words, it would be 'bottom-heavy'.

In summary, the functional form of the IMF has a direct effect on the mass-to-light

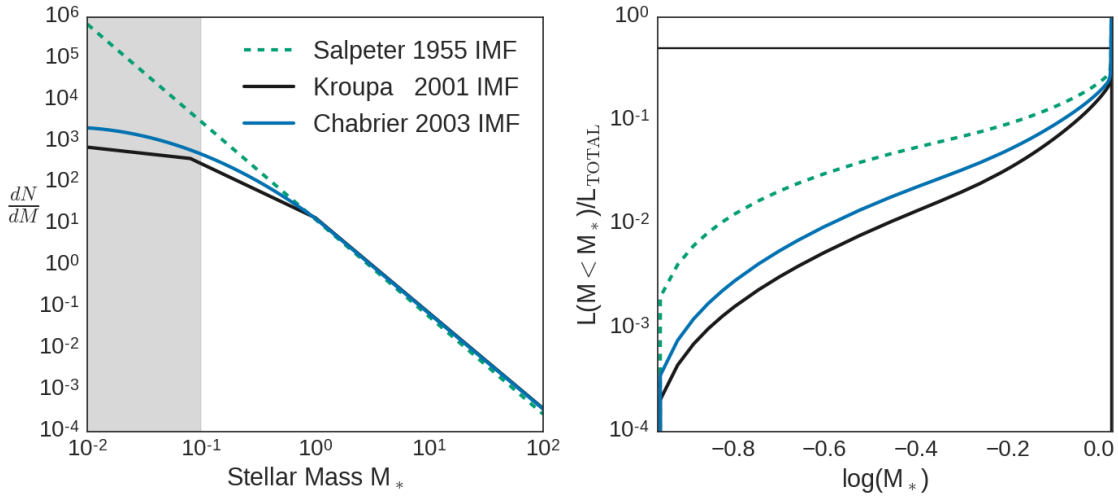

Figure 1.2: *Left panel:* Similar to the corresponding panel in Fig. 1.1, but with each IMF normalised by J-band luminosity after $t = 10$ Gyr (this time using a lower mass cut-off of 0.1 $M_\odot$, indicated by the grey band). The J-band luminosities were calculated using the BaSTI isochrones (Pietrinferni et al., 2004).

Right panel: cumulative J-band luminosity functions for 10 Gyr old stellar populations with lower mass cut-off of 0.1 $M_\odot$. A log axis has been used since the overwhelming majority of the light in each case comes from giant stars that have left the main sequence: black lines have been used to show the $50^{\rm th}$ percentile contribution to the light.

ratio (M/L) of a galaxy, since the total mass locked up in dim dwarf stars can be varied almost independently of the total luminosity, which is mostly due to giant stars. The effect is not small: in the example just given of a 10 Gyr old population the bottom-heavy stellar population would have M/L $\sim$1.6 times higher than the Milky Way-like population. Thus, if the IMF were to vary, this would greatly affect the calculation of the total stellar mass contained within a galaxy derived from its emitted light (see also Maraston, 1998). This would have an adverse effect on attempts to investigate the evolution of galaxies.

Also of interest for studies of galaxy evolution are the effects of variations of the high-mass IMF. As was shown in Fig. 1.2, evolved stellar populations of equal luminosity have very similar numbers of $\sim$1 $M_\odot$ stars, with low mass stars not contributing much to the light ($<$10% of the total) and higher mass stars no longer extant. As a result, from an observational point of view the high and low mass IMF (above and below $M_* = 1\,M_\odot$ respectively) are decoupled. Variations in the IMF functional form above $1M_\odot$ do however have some important effects. High mass stars will leave behind dim, massive, compact remnants (white dwarfs, neutron stars, and black holes) which permanently lock up mass. If the high mass IMF slope were to markedly differ from Salpeter in a stellar population, this would change the supernova rate in, and the chemical evolution of, the galaxy hosting the stars (see e.g. Lacey et al., 2016). Likewise, this would affect calculations of star formation rates.

1.5 The IMF in unresolved stellar populations

The stellar populations of all but the most local galaxies are unresolvable. This means that a direct census of individual stars cannot be made in most cases and we must resort to other measures if we are to constrain the IMF in galaxies other than our own.

One approach is to utilise methods which measure the M/L ratio in a galaxy (since this depends on the IMF). Spatially resolved stellar dynamics (e.g. see Cappellari et al., 2012) can be used to infer the gravitational potential profile of a galaxy, while cases in which a galaxy is lensing a background source can also provide useful constraints on the galaxy mass (Auger et al., 2010). In either case, the measurement is of the total mass, including dark matter as well as compact stellar remnants and dwarf stars. Given well-

motivated assumptions about the dark matter profile, these methods *can* be used to extract information about stellar M/L ratio and hence the IMF, subject to the degeneracy between the high mass and low mass IMF described above.

Specific constraints on the high mass IMF can be obtained in various ways. First, high mass stars are responsible for the chemical enrichment of a population over time. In any given population, therefore, the level of chemical enrichment can in principle provide a constraint on the steepness of the IMF (see e.g. Thomas, 1999, Weidner et al., 2013). It has been argued from both a theoretical (Larson, 2005, Krumholz et al., 2010 – but see Hopkins, 2013) and observational (Gunawardhana et al., 2011) perspective that rapid star formation leads to a top-heavy IMF (i.e. an excess of massive stars). Perhaps related to this, observations of the ratio of ultraviolet and Hα line emission in star forming galaxies have consistently found a correlation with inferred star formation rate (Meurer et al., 2009, Lee et al., 2009, Hunter et al., 2010). Hα is a nebular emission line: it traces gas which is being ionised by the most massive, short-lived stars. Meanwhile, direct measurements of UV emission trace stars from a somewhat broader mass range. In galaxies with low star formation rates, the ratio of these two star formation tracers (Hα/FUV) is depressed, suggesting a relative deficit of the most massive stars (a top-light IMF). Taken together, therefore, there is evidence for a positive correlation between star formation rate and the relative production rate of the most massive stars. However, such a scenario would lead to an enhancement in the number of compact remnants in evolved systems formed in rapid starbursts, something which observations appear to be inconsistent with (Peacock et al., 2014, Coulter et al., 2017).

Spectroscopic probes of evolved extragalactic stellar populations can be used to specifically probe the low-mass IMF. The integrated light from other galaxies is the sum of the light from all of a galaxy's stars. Absorption features at particular wavelengths encode information from every star that contributes to the light. In particular, certain absorption features in stellar spectra are sensitive to the surface gravity of the star (Conroy & van Dokkum, 2012a). This means that the strength of those features has a dependence on whether the star is a giant or a dwarf *irrespective* of any other difference in conditions (e.g. temperature, chemical composition, age). The strength of such features in a galaxy spectrum therefore provides information about the relative amount of light at that

wavelength emitted by dwarf stars and giant stars, which means that information about the low-mass IMF – upon which this ratio of luminosities depends – can in principle be recovered from these systems.

This task is not without its challenges. The velocity dispersion of extragalactic stellar populations in massive galaxies is typically a few hundred kms^{-1}, which means that narrow absorption features related to a wide range of chemical elements and molecules in stellar atmospheres are significantly broadened in the integrated light and interfere with each other. Only the strongest features remain clearly distinguishable in the galaxy spectrum, and the strength of these features will depend on a great number of variables besides the abundance of the principal chemical species from which the feature arises and the IMF. Other chemical species may affect the feature strength directly e.g. by changing the ionisation balance in a stellar atmosphere, or simply by affecting the strength of other absorption lines included in the velocity-blended feature. As a result of this, the effect of IMF variations on any given spectral feature is always degenerate with other effects, which must be disentangled.

By considering a variety of spectral features in galactic absorption spectra covering a wide spectral range, it is in principle possible to constrain various characteristics of the stellar population, including its IMF, the age of the population, and the relative abundances of a variety of chemical elements. Simultaneous consideration of many different absorption lines is required to break the degeneracies inherent to this technique.

Absorption line spectroscopy has been widely used as a probe of extragalactic stellar populations for many years, proving especially useful for constraining stellar populations ages and mean metallicities (Spinrad & Taylor, 1971, Tinsley, 1972, Faber, 1973, Worthey et al., 1994). Such techniques have also been used with high quality spectroscopic data to examine chemical abundance patterns in detail (i.e. the ratios of specific elemental abundances), e.g. Thomas et al. (2003a), Cenarro et al. (2003). Latterly, absorption line strengths have been used in conjunction with spatially resolved (integral field) spectroscopy to create 2D maps of stellar population properties, providing crucial information for understanding galaxy assembly histories (Kuntschner et al., 2010, McDermid et al., 2015, Goddard et al., 2017).

In this thesis we are particularly interested in the use of these techniques to constrain

the IMF in the manner described above. We now discuss some salient recent results.

1.6 Recent results in early-type galaxies

ETGs represent radically different star-forming environments to those found in the local universe. The rapid assembly and swift quenching of their stellar populations differs markedly from the more prosaic star formation that occurs in the Milky Way thin disc and occurs under quite different physical conditions, with higher densities, gas pressures, and temperatures and enhanced turbulence; these conditions may lead to a different IMF (e.g. Hopkins, 2013, Chabrier et al., 2014). They are therefore excellent laboratories for testing for different IMFs *a priori*. Moreover, unlike e.g. population III stars (the as-yet unobserved first generation of stars formed), the stellar populations of ETGs account for a significant fraction of the stellar mass in the local universe (e.g. see Baldry et al., 2004). If the IMF is unchanged both in these galaxies and throughout all local star-forming environments then that would strongly suggest that the IMF is *de facto* universal. On the other hand, if the IMF *is* different in these galaxies then there are important implications for e.g. calculations of the total stellar mass in these galaxies, inferred supernova and chemical enrichment rates – and hence also for our understanding of galaxy evolution on cosmological scales.

Spectroscopic techniques for measuring the IMF have a long history (e.g. see Carter et al., 1986) and have recently been employed with some success by Conroy & van Dokkum (2012b) – hereafter CvD12b, Smith et al. (2012), Spiniello et al. (2012), La Barbera et al. (2013), Martín-Navarro et al. (2015), McConnell et al. (2016), Zieleniewski et al. (2015), and others. A consensus has been building behind the hypothesis that in ETGs the IMF has a relationship with galaxy mass, with the most massive ETGs found to be significantly richer in dwarf stars ($M_* < 0.5\,M_\odot$) than their less massive counterparts – i.e. they exhibit a bottom-heavy IMF. Thus, these massive galaxies are expected to have elevated stellar mass-to-light ratios.

These results have been bolstered by the actual detection of trends in the *total* M/L ratios of massive galaxies. For example, Auger et al. (2010) and Cappellari et al. (2012) use measurements of gravitational lensing and stellar dynamics respectively, while Thomas

et al. (2011c) uses both methods in tandem, to independently constrain the stellar mass in these systems (with the precise mass subject to an assumed dark-matter profile), finding enhanced M/L ratios in massive ETGs which follow a trend consistent with the spectroscopic results. Such enhancements also depend on the high-mass IMF via the fraction of compact stellar remnants, which spectroscopic methods are not sensitive to, but there is some evidence against variations in the high-mass IMF (Peacock et al., 2014, Coulter et al., 2017). On the other hand, Smith (2014) showed that while the *average* mass vs. M/L trends derived for ETGs via spectroscopic and mass-measurement methods are in agreement, the measurements for individual galaxies are often not. This could be due either to unresolved systematic errors in one or both methods, or else reflect real variations in the M/L ratio of individual galaxies decoupled from variations in the low-mass IMF (e.g. variations in the remnant fraction or dark matter contribution). Related to this, Smith et al. (2015b) presents lensing observations of three high mass ETGs, which are found to have M/L consistent with a Milky Way-like (*not* bottom heavy) stellar population – despite having spectra typical of massive ETGs. These three systems are of particular interest since the lens configuration in each case is such that only the innermost region of each galaxy is probed. In these innermost regions the contribution to the mass from dark matter is minimal (of order $\sim$10%), so if the stellar remnant fraction does not vary, a Milky Way-like IMF is implied. Taken at face value, this means that these particular galaxies lie off-trend – though there is significant scatter in the trend and so this small sample may simply be unrepresentative. Indeed, Spiniello et al. (2015a) propose that the IMF may correlate more strongly with galaxy stellar density than with total galaxy mass and suggest that if this trend is more fundamental the tension may be lessened.

The two-phase model of ETG formation suggests that the violent, rapid assembly of the central stellar population is followed by gradual accumulation of quiescent systems of lower mass. The conditions under which stars are formed in the starburst phase are very different to those encountered in the Milky Way thin disc, which might provide a natural explanation for IMF variation (Chabrier et al., 2014). If this scenario is broadly correct then, assuming that the low-mass accreted systems formed their stars via a Milky Way-like IMF, the IMF may only deviate from that form in the cores of ETGs. This would lead to radial gradients in the fractional dwarf star content of these galaxies. Spectroscopic

constraints on the IMF typically utilise spectra taken from the bright cores of ETGs. In contrast, the M/L methods typically probe the wider mass distribution. Because of this difference in scale, radial IMF gradients may provide a partial explanation for the observed mismatch between the measured M/L (from dynamics or lensing) and that inferred from a spectroscopically-derived IMF.

Other stellar population properties apart from the IMF are also expected to vary within galaxies assembled via the two-phase mechanism, and these too may cause radial variations in the spectra of ETGs. Although the stellar populations in massive ETG cores are thought to be assembled at a faster rate than those in the outskirts, a radial trend in α-enhancement is *not* seen. For example, the MASSIVE survey (Greene et al., 2015) of high mass ETGs replicated the well-known positive correlation between α-enhancement and galaxy velocity dispersion, yet did not find a radial trend in this quantity. This is in agreement with earlier work by e.g. Mehlert et al., 2003, but contrasts with the study conducted by Coccato et al., 2010 of NGC 4889. In that work a flat trend in α-enhancement with radius was also found, but with a hint of a sharp break at high radius not seen in the MASSIVE data. This flat profile may appear curious, since the argument underpinning the two-phase formation paradigm is that the outskirts of massive, high velocity dispersion ETGs are built up via minor mergers with lower mass systems. Naively, these merging systems ought to be analogous to surviving low-mass ETGs (which are not α-enhanced in their cores). However, ETGs also exhibit an overall metallicity gradient, with high metallicity stellar populations in the core and low metallicity populations further out. Low metallicity stars have a much higher ratio of α-elements to Fe-peak elements than solar metallicity stars even in the Milky Way (see Milone et al., 2011): they are formed from gas which has been enriched by far fewer cycles of star formation, so a high star formation rate is not required to form these stars over a short timescale. In other words, these stars were not formed under the special star-forming conditions that have been linked to IMF variations.

Observations of radial variations in spectroscopic features have a long history (see for example Cohen, 1979, in which they were used to constrain the overall metallicity gradients of ETGs), but their use in specific attempts to constrain the dwarf star content of ETGs dates back to Carter et al. (1986) – in which it was concluded that ETG cores

might be slightly enriched in dwarf stars relative to their outskirts.

The growing body of evidence for IMF variation in massive galaxies has given new impetus to such studies. Martín-Navarro et al. (2015) present evidence from optical spectra (measurements of a variety of Mg, TiO, Na, and Ca absorption features) of three galaxies that supports a radially varying IMF in the most massive ETGs ($\sigma \sim 300\,\mathrm{kms}^{-1}$).

McConnell et al. (2016) present data from two ETGs ($\sigma = 220\,\mathrm{kms}^{-1}$ and $250\,\mathrm{kms}^{-1}$), measuring the strengths of a variety of optical and infrared absorption features, including TiO, CN, Ca, Mg, Na, and Fe features, Hβ, and also the Wing-Ford FeH molecular band, which is extremely gravity-sensitive (Wing & Ford, 1969). They argue that the radial variation in these strengths is best accounted for by elemental abundance gradients, rather than requiring a varying IMF. However, they do this without quantitative fitting of models to their data and rely primarily on the lack of strong radial variation of the Wing-Ford band.

In contrast La Barbera et al. (2016) use a model-based approach, measuring a number of optical (TiO) features and the Wing-Ford band for a single extremely massive ($\sigma = 320\,\mathrm{kms}^{-1}$) ETG. They find that the optical features are best fit with a radially varying IMF. However, like McConnell et al. they do not measure significant radial variation of the Wing-Ford band and invoke a more complex (broken power law) IMF functional form to account for this.

In neither work did the authors find the Wing-Ford band was strong in the cores of their target galaxies (compared to spectra from stellar populations formed with a Milky Way-like IMFs), whereas in some previous work, e.g. van Dokkum & Conroy (2010), this has been found in ETGs.

The overall picture has remained ambiguous, with van Dokkum et al. (2016) finding evidence for strong radial IMF variations in some members of a sample of six galaxies. By contrast, Vaughan et al. (2016) (two galaxies) and Zieleniewski et al. (2017) (three galaxies) do not find clear evidence for variations.

1.7 A way forward

Most of the studies mentioned have relied primarily on optical spectra of ETGs, with some venturing into the infrared (IR). The near-IR is a promising wavelength range for spectroscopic studies of the IMF since it contains a variety of strong absorption features, both gravity-sensitive and otherwise. The near-IR is dominated by the light from stars with cool surface temperatures, i.e. dwarf stars and post-main-sequence giants – the very stars we are most interested in. The development of empirical spectral libraries that cover near-IR wavelengths, e.g. Rayner et al. (2009) have recently opened up these features for study by allowing models for the stellar population spectra to be constructed (this will be discussed in detail in the next chapter).

The near-IR remains a challenging wavelength regime to operate in, with strong atmospheric absorption features and a plethora of narrow OH sky-emission lines to be reckoned with – a particular problem given the high signal-to-noise ratio required to robustly measure the subtle effects of the IMF on spectral features. To date, these issues have greatly restricted the use of infrared spectroscopy in studies of stellar populations. However, advances in instrumentation have made such studies increasingly feasible. In particular, the advent of integral field and multi-object spectroscopy covering the infrared regime is particularly promising in the context of the specific problem of measuring spatial variations in the IMF. The ambiguous picture presented in the previous section can only be resolved by studies incorporating spatially resolved measurements of a wide range of optical and IR spectral features and by covering a larger sample of ETGs than has previously been possible. Our approach to these challenges and the results thereby obtained comprise the rest of this work.

1.8 Outline

This Thesis is structured as follows:

Chapter 2: We discuss the various procedures that have been used to model the spectra of unresolved stellar populations and introduce our particular implementation of these procedures; we present a comprehensive list of the spectral features discussed

in this work and the results of tests of our procedures. Finally, we discuss and test biases that might arise from our model assumptions.

Chapter 3: We present measurements of various spectral features from the KMOS Infrared Nearby Early-Type Survey (KINETyS), a study of radial variations in the stellar populations of a sample of eight nearby luminous ETGs. Measurements are made of gradients in feature strengths, demonstrating substantial radial variation of the stellar populations of the sample.

Chapter 4: We use the procedures discussed in Chapter 2 to model the feature measurements presented in Chapter 3, discuss our results and present our conclusions regarding the implication of our measurements for radial IMF variations and chemical abundance gradients.

Chapter 5: We present additional K-band measurements complementary to those presented in Chapter 3 and use these along with a more sophisticated model treatment to further constrain the stellar population properties of the KINETyS sample.

Chapter 6: In this concluding chapter we remark on the implications of this work for theories of galaxy mass-assembly and discuss the potential for future advances.

Chapter 2

Stellar demographics with SPINDRIFT

Preamble

As described in the Introduction, the integrated light of galaxies contains a great deal of information about the stellar populations they host. This information can in principle be recovered by comparing galaxy spectra with appropriate models. In the following chapter we discuss the principles behind the creation of such models and how statistical inference of the model parameters can be accomplished, also introducing the code and methods used in subsequent chapters.

In Section 2.1 we describe how a single stellar population model can be created and how these can be compared with data. Section 2.2 summarises the specific models and key spectral features used in our analysis. In Section 2.3 we describe our procedures for conducting a statistical comparison between models and data. In Section 2.4 we describe some key features of our model. In Section 2.5 we present some tests of the modelling procedures. Finally, in Section 2.6 we explore the possibility of biases arising from the fundamental assumptions of the modelling procedure.

This chapter includes material originally published in Alton et al. (2017) as well as significant extensions to that work.

2.1 SSP models

A simple (or single-burst) stellar population (SSP) model is created by assuming a coeval population of stars formed in a rapid burst with a common chemical abundance distribution, drawn from the same stellar initial mass function (IMF). Given these assumptions, we can then consider what this population will look like after time t has elapsed (assuming no additional stars form) using model stellar evolutionary tracks/isochrones. Empirical spectra for Milky Way stars with given effective surface temperatures, metallicities, and surface gravitational strengths (or alternatively synthetic theoretical stellar spectra) can then be used to represent the light from each individual star in the model. The luminosity-weighted sum of these spectra then provides a model for how the integrated spectrum of the stellar population would appear. Throughout this work the term 'SSP model' will refer to these model spectra.

SSP models have long been a useful tool for inferring the properties of unresolved stellar populations, going back at least as far as Crampin & Hoyle (1961) and developed by e.g. Tinsley (1968), Worthey (1994), Maraston (1998), Trager et al. (2000), Bruzual & Charlot (2003), and Schiavon (2007). Models created with certain sets of 'ingredients' can be matched with actual data from unresolved stellar populations, allowing the underlying properties of such populations to be inferred.

Before discussing the procedures used to fit SSP models to data, it is worth reflecting on the validity of the assumptions made during the construction of the models. First, the assumptions of coevality and single chemical abundance are connected and are not generally true in the strictest sense. The stellar populations of massive elliptical galaxies are thought to be assembled extremely rapidly, as described in the previous chapter. Yet since the gas which the galaxy accretes is initially close-to-pristine (i.e. of low metallicity), multiple generations of massive stars must form during the starburst in order to reach the high metallicity typical of nearby large galaxies. Hence there must also exist a spread of chemical abundances among the lower mass stars, all of which survive until the present day. Secondly, if the IMF is *not* universal, then (depending on the physical driver of IMF variations) some of these stars may have been drawn from a different IMF to others: the IMF may evolve over time. Indeed, if it is true that in some cases the IMF continuously

evolves (as suggested in e.g. Vazdekis et al., 1996 and Ferreras et al., 2015) then the very idea of an 'initial mass function' is not well defined; we may, however, revert to a more fundamental view of the IMF as the relative star formation rate as a function of mass (e.g. as originally outlined in Salpeter, 1955). In that case, however, it is better to refer to the 'Creation function' $C(m, t)$ (Chabrier, 2003), which defines the number of stars formed with masses in the interval $m + dm$ between times t and $t + dt$. These limitations must be borne in mind when attempting to fit the data with a single-burst stellar population model representing the *average* properties of the composite population. Potential biases related to the composite nature of real stellar populations will be discussed later in this chapter.

There are two general approaches to model fitting in this context. The first is to compute flux as a function of wavelength across some wavelength range (i.e. create a model spectrum) and to find the combination of parameters that best reproduces the real spectrum. The alternative is to measure the equivalent widths (i.e. absorption strengths) of certain spectral indices – narrow features in the spectrum that are particularly sensitive to the model parameters. The latter approach greatly simplifies the analysis by reducing a large dataset (a spectrum) to a small one (the equivalent widths of a set of absorption indices) which can be chosen to maximise sensitivity to parameters of particular interest. This is a trade-off between utility and the information loss entailed by the procedure.

One advantage to the use of absorption indices is that measurements thereof can be used to demonstrate significant differences between the stellar populations probed by different observations, independent of any model and accompanying assumptions. However, simple interpretations of changes in measured index strengths can be misleading due to the degeneracies between SSP model parameters (e.g. a particular spectral feature might be strengthened either by increasing the abundance of a particular element or by changing the IMF). Breaking these degeneracies requires the use of a comprehensive set of spectral index measurements and a multi-parameter model fit to all of these simultaneously.

2.2 Spectral features

In this work we make use of various updated versions of the models presented in Conroy & van Dokkum (2012a) (CvD12a). These models are hereafter referred to collectively

as 'the CvD models'. These models can be used to predict the (rest-frame) integrated flux of an unresolved stellar population over the 0.35–2.50 μm range. They are based on empirical spectral libraries, but with synthetic spectra used to calculate the spectral response to changes in elemental abundance ratios (similar to the method outlined in Thomas et al., 2003b). This means the CvD models can be used to fit variations in the abundance of specific elements.

In CvD12a a variety of spectral indices are presented, some of which we make use of in this work. Additionally, we also make use of certain other indices defined elsewhere. All index definitions are given in Table 2.1.

Taken together, these indices have sensitivity to stellar population age, overall metallicity, and the IMF, as well as the specific abundance of several key elements such as the α-elements Mg and Ca, Fe, C, and Na. We treat several of these indices as 'composite indices', summing the equivalent widths of several distinct features with strengths which have similar dependencies on the underlying stellar population parameters in order to create a single measurement with higher signal-to-noise. Components of composite indices are marked in Table 2.1 with letters a, b, c. This is done for the Ca II Triplet, the K I 1.17 μm doublet, the Ca I 1.98 μm doublet and the first two lines of the CO molecular bandhead at 2.30 μm.

2.3 Parameter estimation technique

Given some data and a model (intended to represent the data) with a number of free parameters, finding the most probable values for the parameters θ entails finding the maximum of the posterior probability distribution $p(\theta|d,\sigma)$ (that is, the probability of the parameter values θ being the true values, given some data d and statistical uncertainties σ).

In our case, d would be a vector of measured equivalent widths with corresponding uncertainties σ, while θ would be a list of parameter values that act as inputs to a model for the data, m. The (log-)likelihood function can then be written

$$\ln p(d|\theta,\sigma) = -\frac{1}{2}\sum_i \left(\frac{d_i - m_i(\theta)}{\sigma_i}\right)^2$$

Given a prior probability distribution, $p(\theta)$, the posterior probability function $p(\theta|d,\sigma)$

Table 2.1: List of absorption index names and definitions (vacuum wavelength definitions, given in Å)

Index name	blue continuum	Feature band	red continuum
C_2 (0.47 μm)	4612.8–4631.6	4635.3–4721.6	4744.1–4757.8
Hβ	4827.875–4847.875	4847.875–4876.625	4876.625–4891.625
Fe 5015	4946.5–4977.75	4977.75–5054.0	5054.0–5065.25
Mg*b*	5142.625–5161.375	5160.125–5192.625	5191.375–5206.375
Fe I (0.52 μm)	5234.7–5249.7	5247.2–5287.6	5287.2–5319.7
Fe I (0.53 μm)	5306.1–5317.4	5313.6–5353.6	5354.9–5364.9
Na I (0.59 μm)	5862.2–5877.2	5878.5–5911.0	5923.7–5949.7
Na I (0.82 μm)	8177.0–8205.0	8170.0–8177.0	8205.0–8215.0
Ca II (0.86 μm a)	8474.0–8484.0	8484.0–8513.0	8563.0–8577.0
Ca II (0.86 μm b)	8474.0–8484.0	8522.0–8562.0	8563.0–8577.0
Ca II (0.86 μm c)	8619.0–8642.0	8642.0–8682.0	8700.0–8725.0
Mg I (0.88 μm)	8777.4–8789.4	8801.9–8816.9	8847.4–8857.4
FeH (0.99 μm)	9855.0–9880.0	9905.0–9935.0	9940.0–9970.0
Ca I (1.03 μm)	10300–10320	10337–10360	10365–10390
Na I (1.14 μm)	11340–11370	11372–11415	11417–11447
K I (1.17 μm a)	11667–11680	11680–11705	11710–11750
K I (1.17 μm b)	11710–11750	11765–11793	11793–11810
K I (1.25 μm)	12460–12495	12505–12545	12555–12590
Al I (1.31 μm)	13090–13113	13115–13165	13165–13175
Ca I (1.98 μm a)	19740–19765	19770–19795	19800–19840
Ca I (1.98 μm b)	19800–19840	19845–19880	19885–19895
Na I (2.21 μm)	22035–22045	22047–22105	22107–22120
Ca I (2.26 μm)	22500–22575	22580–22700	22705–22780
CO (2.30 μm a)	22860–22910	22932–22982	23020–23070
CO (2.30 μm b)	23150–23200	23220–23270	23300–23350

can be evaluated. Most straightforwardly, we could use a set of 'top-hat' constraints for $p(\theta)$ which are flat (i.e. uninformative) within some plausible range before cutting off sharply. The method allows us to efficiently find the choice of model parameters θ required to maximize the posterior probability function and determine how well constrained this solution is.

In this work, model parameter estimation is accomplished using a bespoke code (fully described in Section 2.5) that utilises the `emcee` routine (Foreman-Mackey et al., 2013). This is a `python` implementation of an affine-invariant Markov-Chain Monte Carlo (MCMC) ensemble sampler (see Goodman & Weare, 2010) used to characterise the posterior probability distribution for a chosen model, given data and statistical uncertainties.

The algorithm works as follows: first, an initial distribution of a large number of 'walkers', each of which occupies a specific point in parameter space, is generated. At each walker's location, the posterior probability is evaluated. The walkers may then move to a new point in the parameter space according to a probabilistic rule: each walker is randomly paired with another and then displaced along the vector that joins their positions, whereupon the posterior probability is evaluated at the new position. The move is always accepted if the new position corresponds to more probable parameters, while if the new position is not more probable the move has a finite probability of not being accepted. In that case the walker will remain in its previous location. The lower the evaluated posterior probability at the proposed position, the lower the chance of the move being accepted; specifically, the acceptance probability is proportional to the ratio of the posterior probabilities at the two positions. This procedure is repeated for each walker in the ensemble and then repeats.

After a certain number of steps the ensemble of walkers will reach an equilibrium distribution, with most walkers located at (or near) the peak of the posterior probability distribution and the density of walkers declining with the probability. All the walkers would *prefer* to be at the peak of the distribution, but in each step walkers near the peak probability have a finite chance of being moved away from it – a chance that is proportional to the posterior probability at the new location. The density distribution of the walkers after equilibrium is achieved can therefore be identified with the posterior probability distribution.

After running many iterations of this procedure, a conservative number of initial steps (the 'burn-in' phase) are discarded in order to remove combinations of parameters that were not drawn from the equilibrium distribution (typically 50-100 are sufficient in our case). Each remaining walker position in parameter space is then a valid sample drawn from the posterior probability distribution.

2.4 Key model parameters

Using an MCMC method for the particular problem of stellar population modelling requires a number of choices to be made other than what probabilistic prior to use, namely which spectral features to include in the fits and which stellar population parameters to fit for (or more generally, which model to use).

Given the procedures used to create SSP models we can immediately identify that the chosen model parameters must encapsulate the stellar population age, the IMF from which the population was drawn, and the chemical abundance pattern of the gas that the stars were formed from. The first of these can be dealt with straightforwardly by using stellar population age (or the logarithm of the age) as a variable model parameter, but the other two require a more involved discussion.

Parameterising the IMF in SSP models

In the case of the IMF a number of choices are available. One option is to choose a parametrization of the IMF (e.g. a broken power law) and vary the parameters (e.g. the gradients of the power law slopes) which specify the IMF. These choices may be more or less flexible. However, the key point in all cases is that variation of these parameters changes the relative contribution to the integrated light (in a given wavelength band) from dwarf stars and giant stars. Some stellar spectral features are 'gravity sensitive', meaning they have different strengths in dwarf and giant stars with the same effective temperature (blackbody spectral shape) and chemical composition. This is due to the variation of the detailed atmospheric physics under changes in stellar surface gravity. The strength of such features in the integrated light depends on the relative contribution to the total light of the dwarfs and the giants. This is principally determined by the IMF and the age of the

stellar population.

In subsequent chapters we parameterise the IMF using the fractional contribution of dwarf stars to the integrated light, $\mathrm{f_{dwarf}}$:

$$f_{\mathrm{dwarf}} = \frac{1}{\mathrm{L_{tot}}} \int_{0.1\,\mathrm{M_\odot}}^{\mathrm{M_{dwarf}}} \mathrm{L(M;\,t_{pop})\,N(M)\,dM}$$

where M refers to the initial stellar mass, $\mathrm{t_{pop}}$ is the population age, and L is the present-day luminosity of a star in some chosen bandpass. $\mathrm{M_{dwarf}}$ defines what the maximum mass of a dwarf star is deemed to be and we take $0.1\,\mathrm{M_\odot}$ to be the low-mass cutoff for the IMF. The attraction of using such a quantity to parameterise the IMF is that it relates more directly to the observable spectroscopic changes being used to measure the IMF than, for example, the fraction of the stellar *mass* contained in dwarf stars, or the mass-to-light ratio of the stellar population, or the power law slope(s) of the IMF.

In practice, to calculate $\mathrm{f_{dwarf}}$ for a given IMF we use the J-band stellar luminosity predicted using the BaSTI isochrones (Pietrinferni et al., 2004), i.e. $\mathrm{L(M;\,t_{pop})}$, for populations with various ages and solar metallicity.

In Tables 2.2 and 2.3 we show $\mathrm{f_{dwarf}}$ for several IMFs and choices of $\mathrm{M_{dwarf}}$. IMFs described with a single power-law can be compared with Vazdekis-type IMFs (in which the power law breaks at $0.6\,\mathrm{M_\odot}$ and is shallower at low mass – see Vazdekis et al., 1996) and the Chabrier (Milky-Way) IMF. In Figure 2.1 we show the linearity of the index strengths in the CvD models with respect to $\mathrm{f_{dwarf}}$. Index strengths for the Chabrier IMF and three power-law IMFs (X = 2.3, 3.0, and 3.5) are shown. Particular attention should be paid to those indices with strong variation with respect to the IMF. In these indices the detailed shape of the IMF seems to be a second-order effect (demonstrated by the typically small deviation of the models generated with a Chabrier IMF from the linear relation given by the models generated using three single-slope power law IMFs) and the model index strengths follow an approximately linear relation.

In general, the relative response of a particular spectral index to changes in the IMF will have some dependence on the IMF functional form. However, for the cases already shown we will demonstrate that this is a subtle effect – at least for a reasonably high definition of $\mathrm{M_{dwarf}}$ (throughout this work we use $\mathrm{M_{dwarf}} = 0.5\mathrm{M_\odot}$). In Fig. 2.2 we show the predictions of a subset of the CvD models in which both $\mathrm{f_{dwarf}}$ and the IMF shape

Table 2.2: $f_{\rm dwarf}$ is the fraction of the continuum J-band luminosity provided by stars with masses below $M_{\rm dwarf}$. This table gives $f_{\rm dwarf}$ values for a variety of IMFs and definitions of $M_{\rm dwarf}$. Note that Vazdekis-type IMFs are usually quoted in logarithmic units, a formalism we use in this table for Γ_b, the slope above $0.6M_\odot$. Γ_b+1 gives X, so in this formalism $\Gamma_b = 1.3$ corresponds to the Salpeter slope at high mass. Computed at t = 13.5 Gyr.

$M_{\rm dwarf}$	Chabrier	X=2.3	X=3.0	X=3.5	Vazdekis (Γ_b = 1.3)	(Γ_b = 3.1)
$0.5M_\odot$	4.3%	8.4%	19.0%	32.6%	3.6%	7.2%
$0.4M_\odot$	3.0%	6.6%	16.3%	29.4%	2.2%	4.5%
$0.3M_\odot$	1.8%	4.7%	12.9%	24.7%	1.2%	2.4%
$0.2M_\odot$	0.7%	2.4%	7.9%	16.7%	0.4%	0.9%

Table 2.3: This table gives $f_{\rm dwarf}$ values for a variety of IMFs and definitions of $M_{\rm dwarf}$. Computed at t = 10.0 Gyr.

$M_{\rm dwarf}$	Chabrier	X=2.3	X=3.0	X=3.5	Vazdekis (Γ_b = 1.3)	(Γ_b = 3.1)
$0.5M_\odot$	3.3%	6.6%	16.1%	29.1%	2.8%	6.4%
$0.4M_\odot$	2.3%	5.2%	13.8%	26.2%	1.7%	4.0%
$0.3M_\odot$	1.4%	3.7%	10.9%	22.1%	0.9%	2.1%
$0.2M_\odot$	0.5%	1.9%	6.7%	14.9%	0.3%	0.8%

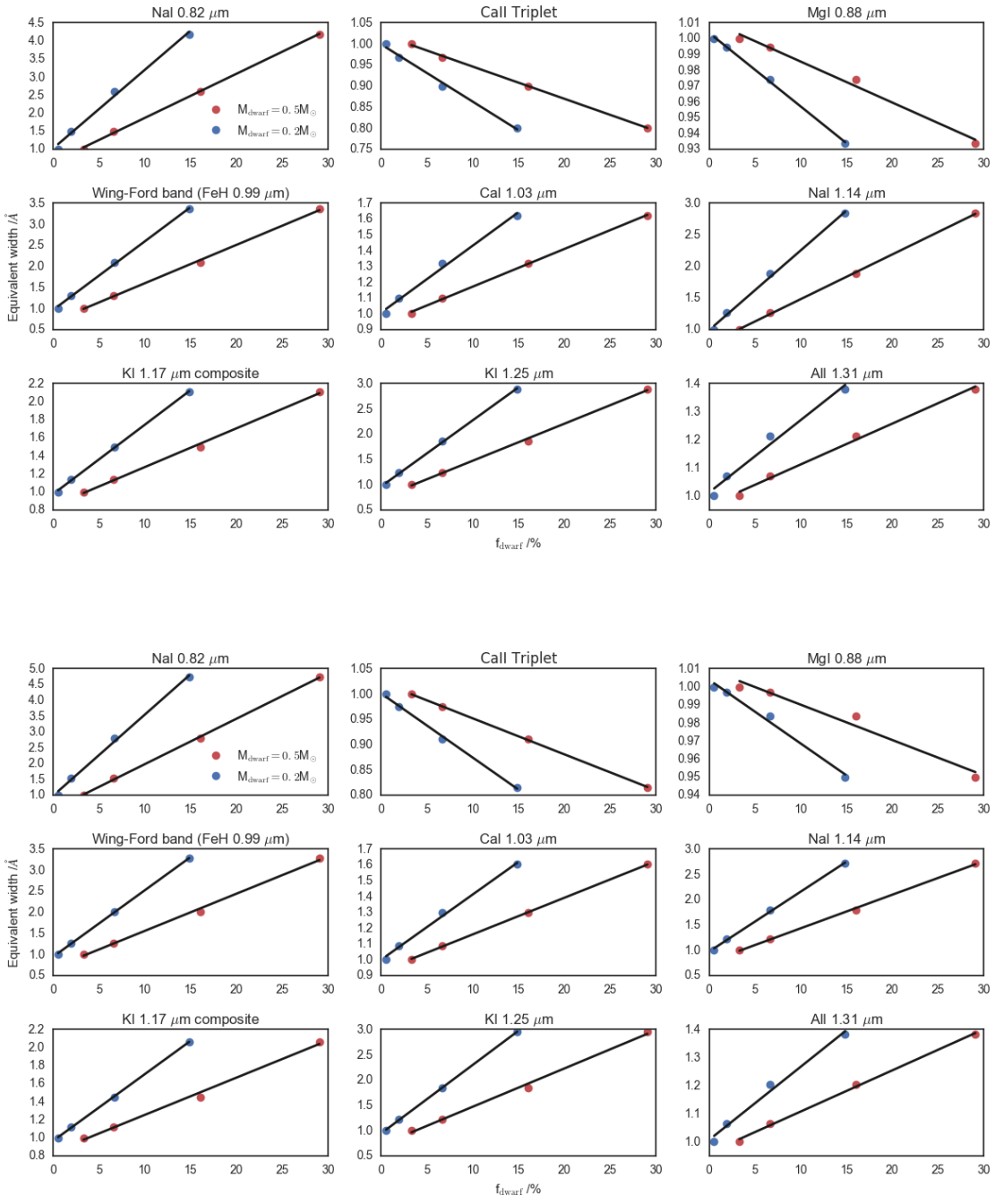

Figure 2.1: This plot displays the linear variation of a variety of spectral indices with f_{dwarf}, for two different definitions of M_{dwarf}, computed at t = 13.5 Gyr (top panel) and t = 10.0 Gyr (bottom panel). Fractional variations in index strengths are shown.

vary, thereby making clear the accuracy of a single-parameter approach for the given indices. In these models the IMF is parameterised with independent power-law slopes X1 and X2, covering stellar mass ranges 0.08–0.5 $M_\odot$ and 0.5–1.0 $M_\odot$ respectively. The predictions of this model for X1, X2 $\in$ [0.5, 3.5] are shown in Fig. 2.2 as the vertices of a grid. A linear relationship between $f_{\rm dwarf}$ and index strength, computed via the diagonals of this grid (i.e. X1 = X2, the single power law case) is also shown, making clear the limitations of this approach. In general the grids fold up tightly around the linear relation (e.g. Na I 0.82 μm, Na I 1.14 μm, Ca II Triplet): the parameters X1 and X2 have some degeneracy. Nevertheless, shape-dependent deviations clearly do matter in some cases (e.g. FeH 0.99 μm and Hβ strength can both vary by $\lesssim$10% at fixed $f_{\rm dwarf}$). It is also noteworthy that for bottom-light IMFs (lower fraction of dwarf stars than the Milky Way case, which can be approximated as X1 = 1.3, X2 = 2.3) the linear relation tends not to be a good model.

In different wavelength regimes, different stars dominate the total luminosity. One way to extract more information about the detailed shape of the IMF may be to consider spectral indices over a long wavelength range. In Fig. 2.3 a similar set of relationships to those depicted in Fig. 2.2 are shown for four K-band ($\sim$ 2 μm) spectral features; all of these have significant sensitivity to the IMF and all apart from Na I 2.21 μm have a fairly strong dependence on the IMF shape.

In this work we make use of two different approaches to modelling the IMF. On the one hand, when the data provide limited information about the IMF shape we treat the IMF as a single power-law and use the linear relationship between the index strengths and $f_{\rm dwarf}$ directly in the fit. On the other hand, where appropriate we use a flexible IMF model with variable slopes X1 and X2. In this case $f_{\rm dwarf}$ is calculated afterwards and provided for comparison.

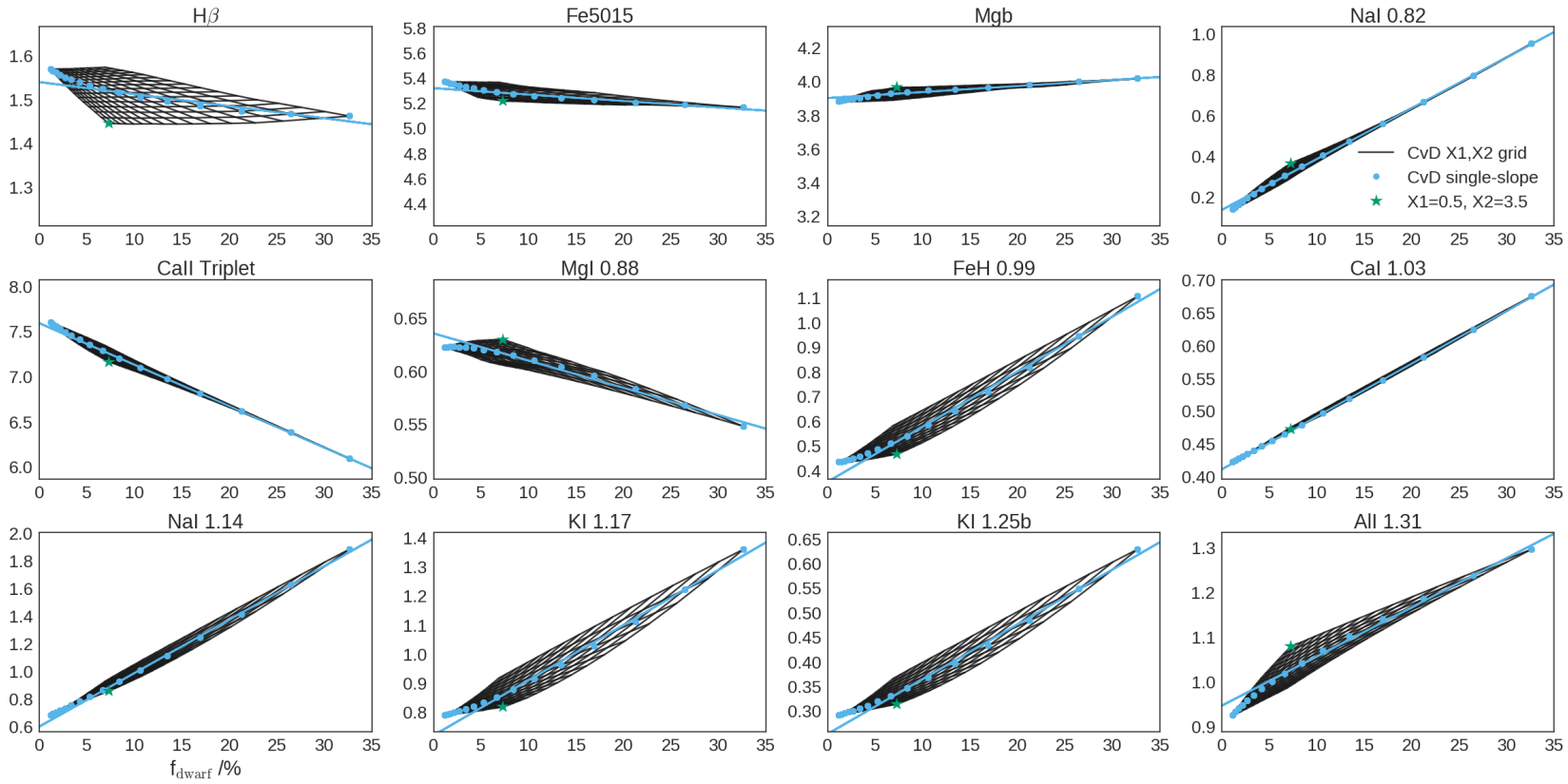

Figure 2.2: A set of spectral indices, computed for a flexible two-part power-law IMF (described in the text) with slope X1 below 0.5 $M_\odot$ and X2 above. Units are index equivalent width in Å. The black grid shows the predictions of the model assuming various combinations of values for X1 and X2 between 0.5 and 3.5. The blue points mark the diagonals of the grid (X1 = X2, the single power-law case) and the blue line is a linear fit to these points for f_{dwarf} >5%. In each panel the most convex IMF is marked with a green star.

Parameterising chemical abundance variations

The simplest approach to parameterisation of chemical abundance variations is to assume that all the elements vary in lockstep, i.e. introduce a single 'metallicity' parameter (usually denoted Z). Often this is expressed as a relative logarithmic abundance [Z/H]=log(Z/H) – log($Z/H|_{\odot}$). In these units [Z/H] $= 0$ means the solar abundance pattern holds (the fraction of heavier elements relative to hydrogen is the same as in the Sun), while e.g. [Z/H] $= +0.3$ means the fraction is twice as high.

However, this simple approach is far from sufficient since the relative abundance of elements created via different nucleosynthetic pathways is *not* consistent across all stellar populations. As described in Chapter 1, the stellar populations of early-type galaxies are typically overabundant in α-capture elements (O, Ne, Mg, Si, S, Ar, Ca, Ti) in comparison to Fe-peak elements (elements with similar atomic masses to Fe). This issue can be addressed by decomposing metallicity into two parameters, [Fe/H] and [α/Fe], if it is assumed that the α elements all vary together (and likewise the Fe-peak elements). However, this has not proven to be a good assumption in all cases, e.g. there is an extensive body of work showing Ca is underabundant with respect to the other α elements (see Saglia et al., 2002, Cenarro et al., 2003, and Thomas et al., 2003a). One can instead introduce a set of parameters for individual elements representing abundance deviations on top of an overall metallicity parameter, [Z/H]. These are usually presented as [X/Fe] for element 'X', which necessitates calculation of [Fe/H].

An alternative approach is to treat variations in the abundance of individual elements relative to hydrogen separately, including model parameters for each element to which the models are sensitive (at least in the wavelength range covered by the data/in the set of spectral indices measured). The limitation of this approach is that the cumulative effects on the spectrum of many unconstrained elements may lead to a measurable effect on the model. In addition, this choice implicitly assumes that the model parameters are all independent. In fact, the stellar isochrones in general change in response to variations in total metallicity: $L(M_{\rm init}; t_{\rm age})$ is also a function of the chemical abundances. This and other factors must therefore be accounted for, e.g. with additional model parameters.

In this work we make use of both approaches, the latter in Chapter 4 and the former in Chapters 6 and 7.

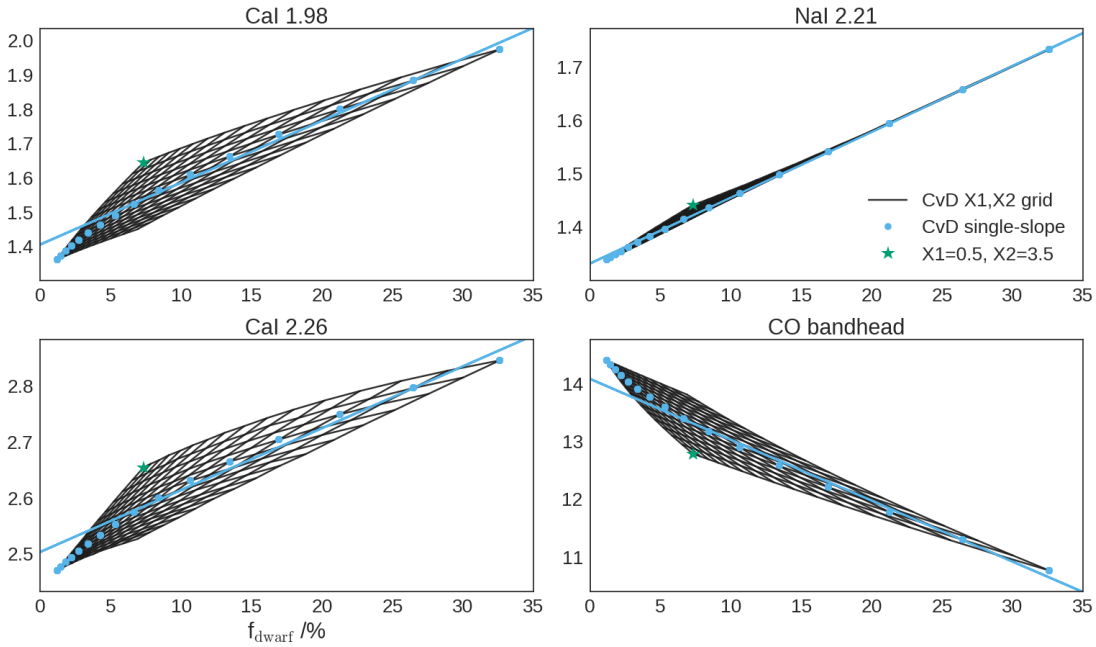

Figure 2.3: Four K-band spectral indices, computed for a flexible two-part power-law IMF (described in the text). Units are index equivalent widths in Å. In this case some indices have non-negligible dependence on the detailed IMF shape: the one-to-one relationship between f_{dwarf} and feature strength given by the blue line only holds strongly for Na I 2.21 μm. In each panel the most convex IMF is marked with a green star.

2.5 The model fitting procedure (SPINDRIFT)

In the preceding sections we have outlined the various components of our model fitting procedure. We implemented the full procedure in `python`, which works as follows:

First, the CvD spectral models – which are evaluated for various combinations of parameters – are broadened to a reference velocity dispersion (throughout this work we use 230 kms^{-1}) and the equivalent widths of the spectral features summarised in Table 2.1 are measured. We thus obtain a grid of index measurements corresponding to different values of the underlying stellar population parameters.

We constructed a predictive model for the full set of index strengths, which can be used to evaluate the expected index strengths given a set of stellar population parameter values. In order to create this model, the model index grid was interpolated using a set of splines. This has the advantage of allowing the grid to be smoothly interpolated, avoiding discontinuities in the model. An example of this method is shown in Fig. 2.4. More sophisticated versions of the model used later in this work drop the assumption that the responses of an index to changes in different stellar population parameters are not coupled and use multivariate spline interpolation to properly handle coupled responses.

Using this model, we can generate the strengths of different spectral features for any given point in the SSP model parameter space. This means that the MCMC procedure outlined in Section 2.3 can be used in conjunction with a set of actual index measurements (and statistical uncertainties) to evaluate the posterior probability distribution over the parameter space and hence to find the most probable set of parameter values and their associated uncertainties.

Our implementation, SPINDRIFT.py (Stellar Population INference DRiven by Index Fitting Techniques), allows flexible choices to be made concerning which particular set of indices to use, which parameters to include in the fit, and the range of the prior 'box' – as well as, of course, the number of walkers to deploy, the number of MCMC steps to be taken, and the length of the burn-in phase. Typically a few hundred walkers take around 1000 steps each, perhaps 50-100 of which are discarded. In such a case the posterior probability distribution may take as long as an hour to evaluate, a limit imposed by the speed at which model spectral feature strengths can be generated.

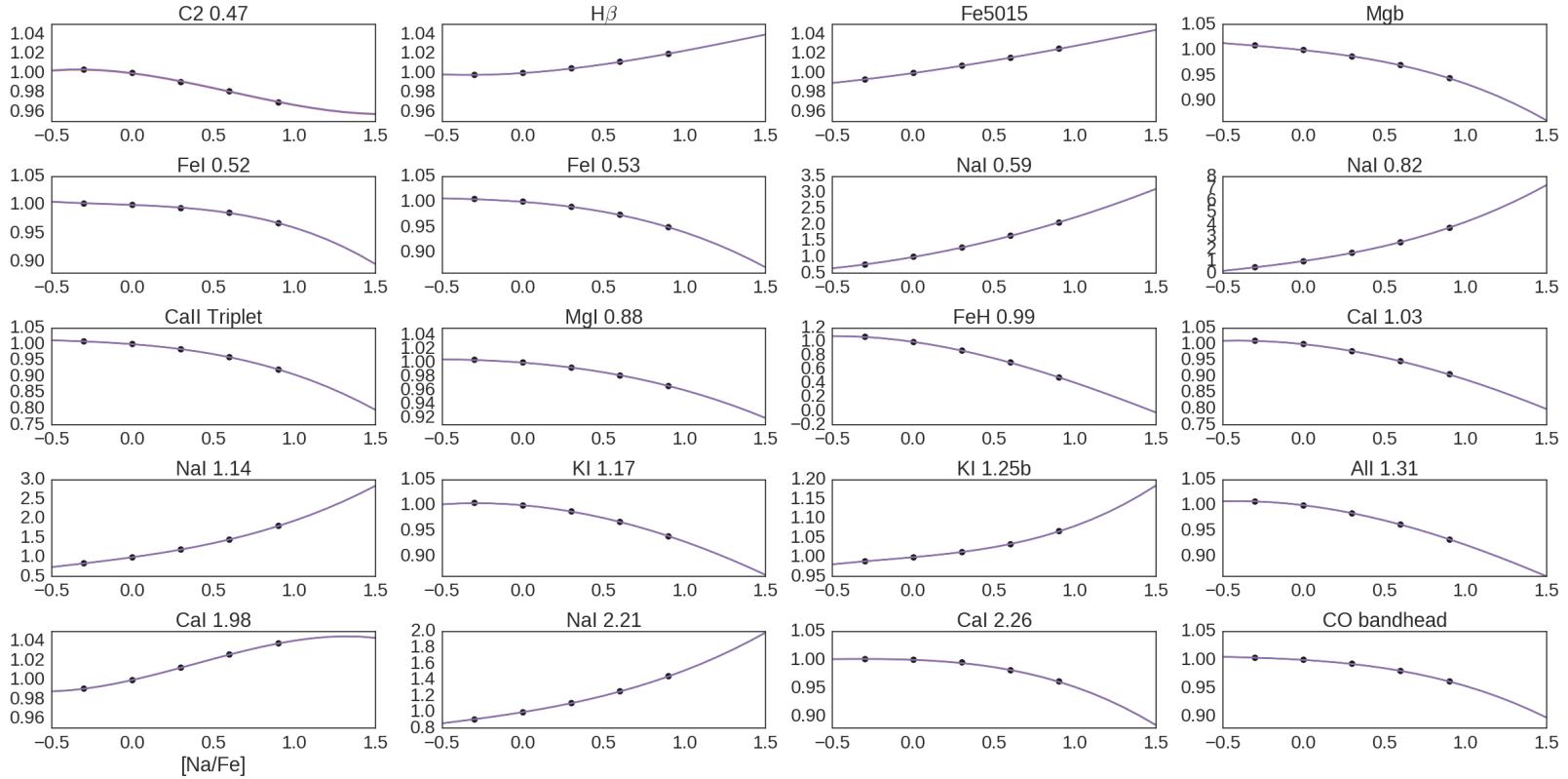

Figure 2.4: An example of our model implementation. The model index strengths have been computed for a 13.5 Gyr old stellar population with a Milky Way-like IMF and solar chemical abundance, for five different values of [Na/Fe]. For clarity, here these model index strengths have been normalised by the [Na/Fe] = 0 case and plotted against [Na/Fe] (black points) – note the disparate scales for different indices. The interpolated model is also shown (solid line), showing that the model grid is accurately reproduced and smoothly interpolated across for the indices defined in Table 2.1.

To calculate headline results, SPINDRIFT applies kernel density estimation to the marginalised parameter distributions in order to infer the parameter values with maximum probability. Asymmetric errors are then calculated for each parameter by splitting the marginalised distributions around the peak value.

2.6 Tests of the model fitting procedure

In this section we demonstrate use of the SPINDRIFT code using a simulated data set. First we create a model which returns a set of spectral index equivalent widths given a set of parameter values. The chosen model parameters in the version of the code used for this example are $\log_{10}(t_{\rm age})$, $\mathrm{f}_{\rm dwarf}$, and the relative logarithmic abundances [X/H]. These parameters have the advantage that variations in the strength of most spectral indices are approximately linear with respect to variations in these parameters (although our model does not treat these variations as precisely linear in all cases, e.g. see Fig. 2.4). The responses of the indices to abundance variations are assumed to be decoupled from all other parameters (that is, here we assume that changing the abundance of one element does not affect the response of the model to changes in another parameter), but the IMF and age are treated simultaneously. Since this version of the model does not fit directly for [Z/H], we also include an additional 'nuisance' parameter, $\Delta\mathrm{T}_{\rm eff}$, which is used to account for metallicity-dependent changes to the isochrones used to create the CvD models (i.e. a shift in the stellar effective temperatures).

The predictive model used in the MCMC procedure can also be used to simulate data. For this example we generated the strengths of eight spectral indices with a seven parameter model (parameter values are given in Table 2.4). Normally distributed random errors were then applied to each generated measurement with magnitude 5% of the equivalent widths (an idealised case with rather low errors).

In this test, where we have included all the important parameters in the model, we can reconstruct the underlying parameter values with appropriate asymmetric statistical uncertainties. Results are given in Table 2.4. In this case a relatively short MCMC run was sufficient – 100 walkers and 800 steps after a generous 200 step burn-in phase (more than was necessary to reach equilibrium). The [K/H] parameter is an example of a parameter

Table 2.4: The parameters used to simulate the data, alongside the values estimated after 5% errors were applied to the simulated equivalent widths (the same errors were applied with opposite sign to create simulations a and b). The recovered parameters and uncertainties are clearly consistent with the true values. Note that these are the parameters directly invoked by the model, but in future chapters it will sometimes be useful to reorganise these, e.g. using them to compute the value of [α/Fe].

Parameter name	True Values	Estimated Values (a)	Estimated Values (b)
$[\alpha/\mathrm{H}]$	0.40	$0.38^{+0.06}_{-0.06}$	$0.40^{+0.04}_{-0.06}$
$\mathrm{f_{dwarf}}$	8.0%	$9.7^{+2.1}_{-2.7}$%	$6.8^{+1.6}_{-2.1}$%
$[\mathrm{Na/H}]$	0.50	$0.47^{+0.06}_{-0.05}$	$0.52^{+0.04}_{-0.03}$
$[\mathrm{Ca}/\alpha]$	–0.10	$-0.16^{+0.09}_{-0.07}$	$-0.05^{+0.07}_{-0.08}$
$[\mathrm{Fe/H}]$	0.05	$0.03^{+0.07}_{-0.06}$	$0.07^{+0.06}_{-0.05}$
$[\mathrm{K/H}]$	0.15	$-1.16^{+0.10}_{-1.55}$	$1.09^{+1.55}_{-0.14}$
$\Delta\mathrm{T_{eff}}$	–55 K	-31^{+36}_{-35} K	-67^{+30}_{-35} K

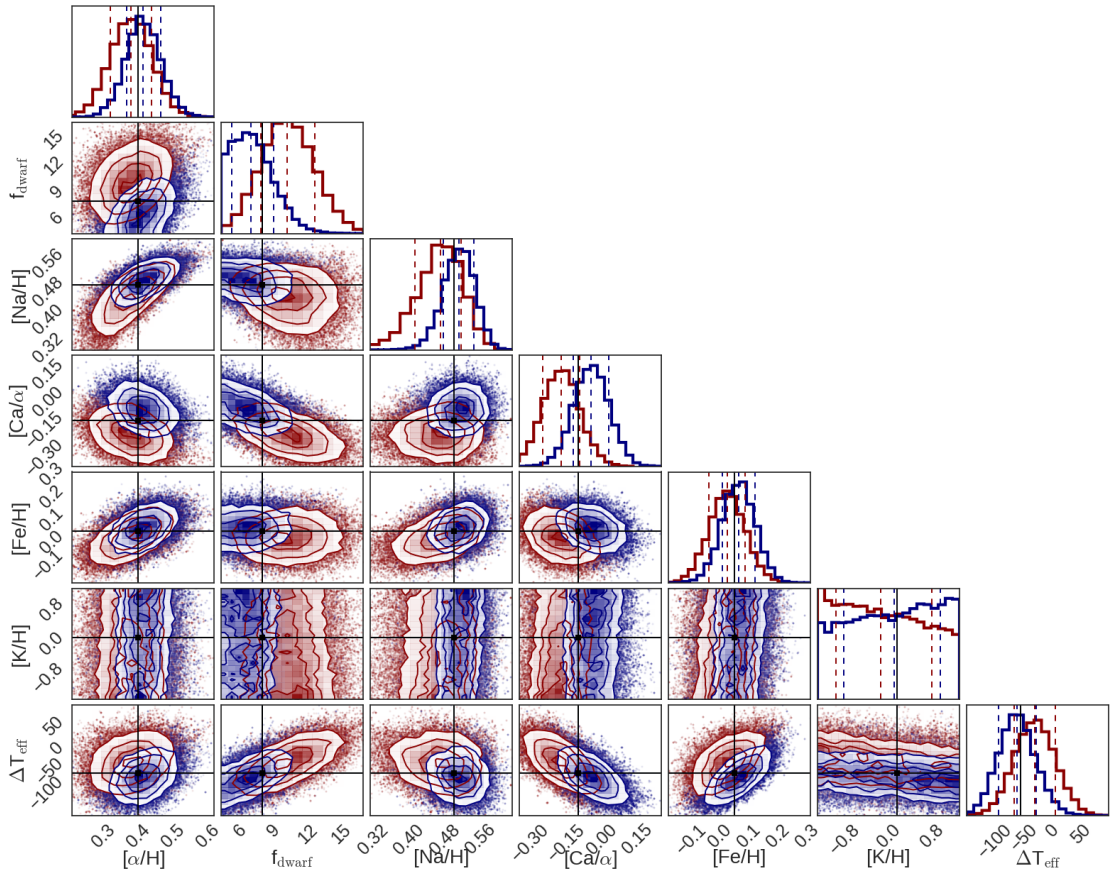

Figure 2.5: Two sets of marginalised 2-parameter (covariance) and 1-parameter posterior probability distributions estimated using an MCMC procedure (100 walkers, 800 steps). The true parameter values used to generate the simulated data are given in Table 2.4 and here are indicated by the black lines. The same set of random errors (of magnitude 5% of the index equivalent widths) were applied to the simulated data, but with the signs flipped, which shifts the inferred probability distributions (shown in red/blue) away from the true parameters in opposite senses. Contours delineate $\frac{1}{2}\sigma$ intervals, dashed lines show the $16^{\rm th}$, $50^{\rm th}$, and $84^{\rm th}$ percentiles of the 1-parameter distributions. This (and similar plots in later chapters) were created using the `corner` module (Foreman-Mackey, 2016).

that could not be well constrained via the simulated data. This demonstrates the comparative insensitivity of the set of features to this parameter. As a result, the most probable parameter values reported for [K/H] are very near the edges of the prior box, while the asymmetric uncertainties are consistent with the true value of [K/H] on one side and take account of the edge of the box on the other. Despite the use of a wide range of spectral features to break parameter degeneracies, there remains a small amount of covariance between some of the parameters used in this example, e.g. [α/H] and [Na/H].

2.7 Composite population biases

Real stellar populations are not truly composed of stars with a single age and composition (and may not even be drawn from the same IMF). A real stellar population must consist of an ensemble of stars with a distribution of properties arising from a realistic star-formation history. Moreover, the property distribution will be highly covariant, with the oldest stars being of low metallicity and the youngest stars being highly enriched (even if the distribution of ages is narrow due to a rapid starburst assembling the mass). This situation can be complicated by the question of IMF variations. It is not clear *a priori* whether a bottom-heavy IMF ought to be assumed to apply to all stars formed in ETGs during the initial starburst (just as in the Milky Way a single IMF is found throughout) or if in fact the IMF evolves, becoming progressively more bottom-heavy. This is discussed by Weidner et al. (2013), who argue that rapid chemical enrichment is simply not possible if, in the earliest section of the stellar population to be assembled, most of the mass is incorporated into dwarf stars. They therefore suggest that the IMF evolves from being top-heavy (initially boosting the supernova rate and thus chemical enrichment) to bottom-heavy (to match the inferred contribution of dwarf stars to the integrated light).

In some cases it is possible for composite population biases to arise. These are related to, but distinct from, biases caused by *multiple* (discrete) populations. For example, the modelling procedure used in CvD12b includes a parameter designed to capture the contribution of a subdominant population of stars formed at relatively late times. Here we restrict our discussion to consideration of a composite population formed in a single extended-yet-short burst of star formation at early times.

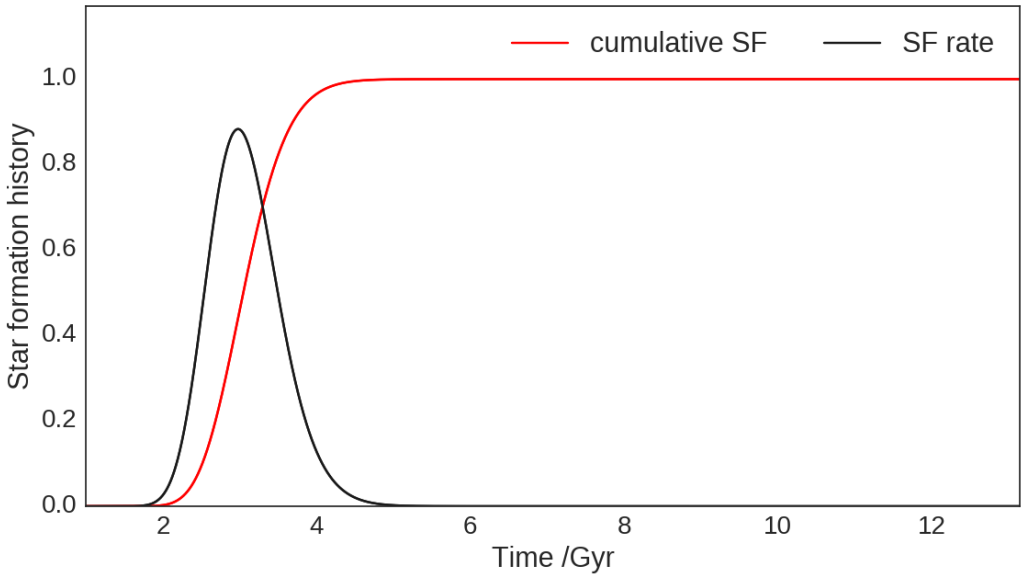

Figure 2.6: Model star formation history, normalised so that total mass = 1. The model is intended to represent a short burst of star formation at early times followed by quenching.

To quantify these biases we first consider a very simple model with a constant Milky Way-like IMF and a narrow log-normal star formation history which peaks around 3 Gyr (more than 95% of the stellar mass is assembled between 2 and 4 Gyr). This model history is shown in Fig. 2.6. Chemical enrichment is assumed to roughly track cumulative mass in a linear fashion, e.g. $Z/Z_{\odot}$ runs from 0.01 to 2.5 as cumulative mass runs from zero to M(t=13.5 Gyr).

This star formation history qualitatively stands in for a short, but not instantaneous, burst of star formation. A more sophisticated model might incorporate some form of IMF variation, but this would make it harder to predict the appropriate chemical enrichment rate. In any case, a simple, conservative model should be sufficient to examine the order of magnitude of composite population biases.

Fig 2.7 shows the outcome of this test scenario in terms of the integrated light. A large number of component stellar populations are drawn from the star formation history and assigned chemical properties appropriate to the time at which they formed (chemical enrichment is presumed to simply track the fraction of the final mass assembled at any time). For each component, formation times are converted to ages at t = 13.5 Gyr and a model SSP spectrum is created. These are summed together to create a composite

population spectrum. These can be compared with the underlying distribution of spectra. Composite population bias arises from the fact that the average (median) spectrum is distinct from the observed (mean) spectrum.

The predicted equivalent widths of this model spectrum can be measured, allowing us to quantify the effect of this bias on various spectral features and also the MCMC inference of the underlying parameters (a procedure that assumes a single stellar population, rather than a composite one).

Composite population bias can be quite significant on the level of individual features. In some cases the equivalent widths are strengthened or weakened by more than 10%. This effect is particularly noticeable at optical wavelengths, since in this regime metal-line blanketing significantly reduces the luminosity of the youngest, most chemically enriched component populations; these populations usually have the strongest intrinsic line strengths, but are comparatively dim. By contrast, in the K-band the youngest component populations (with ages $\lesssim 10\,\mathrm{Gyr}$) are comparatively bright. They have had slightly less time to evolve and therefore contain a greater number of bright, massive stars ($\mathrm{M}_* \gtrsim 1\mathrm{M}_\odot$), which in older populations have already expended their fuel. The effect of the bias may therefore be mitigated by considering a large number of features across a wide wavelength range.

A test MCMC run was conducted on the equivalent width measurements from the simulated observed spectra with random statistical uncertainties of 5% (comparable to the average bias) assumed. A comparison between the underlying property distribution and the posterior probability distribution is made in Fig. 2.8. This makes clear that, at least in the example case presented, some bias may remain in the parameter estimates (in the sense that these do not necessarily represent either the median or mode of the underlying parameter distribution). While a single example case with a simple enrichment model cannot be generalised, this ought to be borne in mind when interpreting the analysis presented in later chapters (e.g. here [Mg/Fe] is clearly underestimated). Fortunately, however, this bias does not seem to strongly affect the inference of the IMF in this test.

More generally, a focus on differential measurements of parameters may prove to be a more robust approach, i.e. we may be able to better quantify the differences between two stellar populations than the absolute values of the parameters themselves.

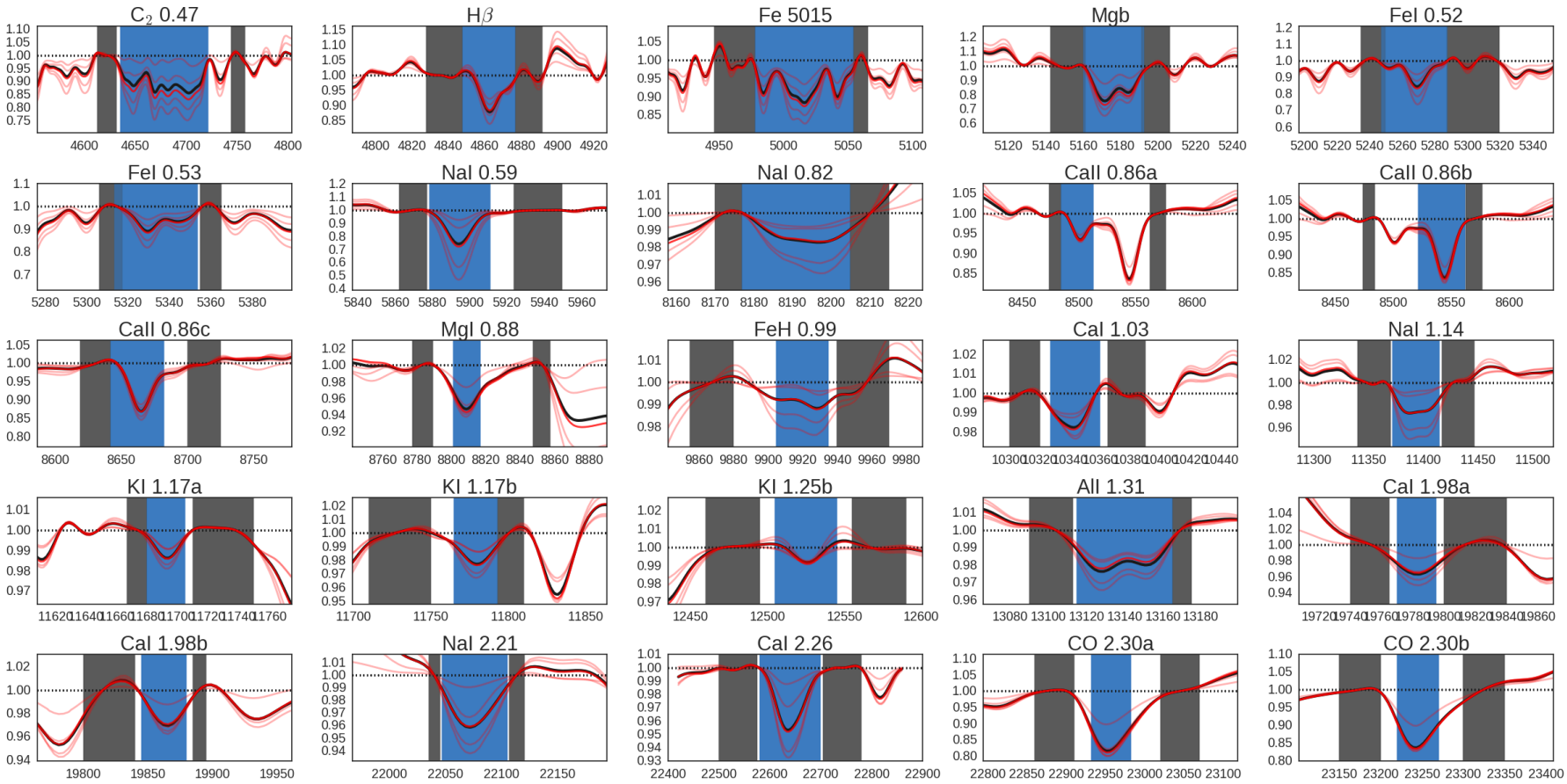

Figure 2.7: Normalised spectra around the regions of various features of interest. Black line: the mean (i.e. observed) spectrum. Red lines: percentile contours from the full distribution of spectra at 2.5%, 16%, 50%, 84%, and 97.5%. The 50% (median) contour is the spectrum drawn with the median properties of the composite population and is distinct from the observed spectrum. Wavelengths in Å.

Summary

In this chapter we have summarised how a model for the integrated light of an unresolved stellar population (an SSP model) can be created. We have introduced the particular set of SSP models (the CvD models) used throughout this work and presented a variety of spectral features that these models indicate can be used to differentiate between stellar populations with different properties.

In light of this, we have described how a model for a particular unresolved stellar population might be parameterised in terms of population age, chemical composition, and the IMF from which it was drawn. We have introduced our code for model parameter estimation, SPINDRIFT, which uses a Monte-Carlo Markov-Chain procedure for statistical inference of stellar population parameters from measurements of spectral indices.

Using a simulated set of spectral index equivalent widths with added noise, we have demonstrated our ability to recover the stellar population parameters of interest. Furthermore, we have explored the assumptions underlying our technique, such as the approximation that the stellar population forms in a single instantaneous burst.

In the next chapter we present spatially-resolved measurements of various spectral indices for a sample of eight nearby ETGs and describe the procedures by which these were obtained.

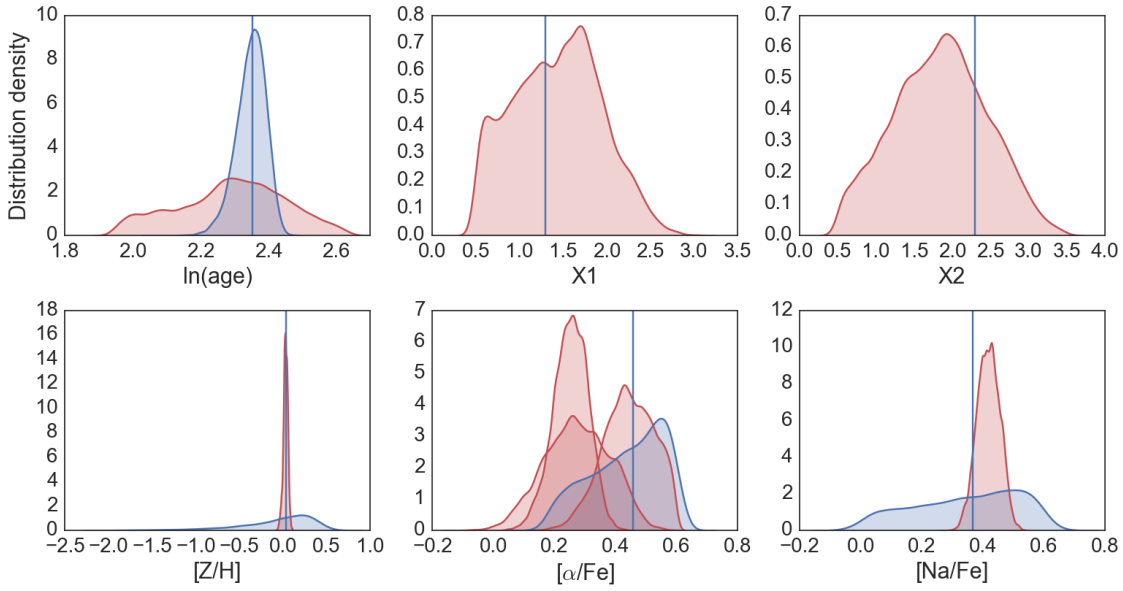

Figure 2.8: Blue: KDE representation of the distribution of parameters in the composite population (a fixed value for the IMF slopes X1 and X2), with the vertical line showing the median. Red: KDE representation of the posterior probability distribution for the parameters. Note that for [α/Fe] three distributions are shown; these represent [Mg/Fe], [Ti/Fe], and [O/Fe].

Chapter 3

KINETyS: data

Preamble

In this chapter we introduce the KMOS Infrared Nearby Early-Type Survey (KINETyS). This is an investigation of radial stellar population gradients in ETGs by means of IR spectroscopy of a variety of spectral features. The principal aim is to constrain IMF trends.

As outlined in Section 1.6, evidence for IMF variations in massive galaxies has driven demand for studies of this kind. The evidence for radial IMF trends remains ambiguous and has primarily been supplied by optical spectroscopy, with fewer studies incorporating infrared data. Moreover, only a handful of galaxies have been studied, which makes it hard to draw general conclusions about galaxy formation. This problem is exacerbated by differences in the methods and data used by different studies.

For KINETyS, we initially studied eight ETGs, alleviating some of the issues with studying individual galaxies (e.g. by allowing the sample variance to be constrained). We studied a variety of gravity-sensitive features, including some which were previously unexplored. We used single stellar population models to fit these measurements. This allowed us to draw quantitative conclusions about variation of the IMF and chemical abundances patterns with radius.

The chapter is organised as follows: in Section 3.1, we first describe our sample of ETGs and the observing strategy used. We next describe our methods for reducing the data to obtain measurements of spectral features. In Section 3.2 we provide a full set

of data tables. In Section 3.3 we present the galaxy-galaxy variations in the strengths of various absorption features that we measure and discuss the way in which these may be interpreted. We defer a model-based analysis of our data, using the SPINDRIFT code introduced in the previous chapter, to Chapter 4.

3.1 Data

3.1.1 Observations:

The eight nearby ($z < 0.01$) ETGs observed span $\sim$150–300 kms^{-1} in velocity dispersion, with most having $\sigma \sim 250\,\mathrm{kms}^{-1}$. Seven of our sample were in the original sample of CvD12b and have a reported average central M/L of ~ 1.6 times that expected for a Milky-Way-like IMF (we hereafter quote all M/L values according to this convention), consistent with a modestly bottom-heavy IMF (e.g. a Salpeter IMF, a power law with slope X = 2.3). The most extreme reported M/L is ~ 2, consistent with a very bottom-heavy IMF (e.g. a steeper power law IMF with slope X = 3). Full details of the sample properties are given in Table 3.1. The data were gathered using the K-band Multi-Object Spectrograph (KMOS) on the VLT (Sharples et al., 2013), primarily between 1^{st} April and 17^{th} July 2014 (Run ID: 093.B-0693(A)), with additional data for NGC 1407 and NGC 3379 obtained on 27^{th} January 2015 (Run ID: 094.B-0061(C)).

KMOS uses 24 pick-off arms, each equipped with an integral field unit (IFU), to take spatially resolved spectra from different targets in the field of view. Each arm yields a 14×14 pixel region covering a $2.8''\times2.8''$ field. For these observations we deployed the pick-off arms in a sparse mosaic covering one galaxy at a time, with a single arm on the galaxy's core and the others arranged along lines of isophotal flux with major axes corresponding approximately to $\frac{1}{3}\mathrm{R_{eff}}$, $\frac{2}{3}\mathrm{R_{eff}}$, and $\mathrm{R_{eff}}$ (ellipticities are given in Table 3.1). A larger number of arms were deployed to the outer regions in order to mitigate the lower surface brightness. An example of this strategy is shown in Fig. 3.1 (left panel). The arms were allocated for observations in cross-beam switch mode, so that in each pointing of an AB pair around half were on-source. In most cases an arm was allocated to the galaxy core in both pointings.

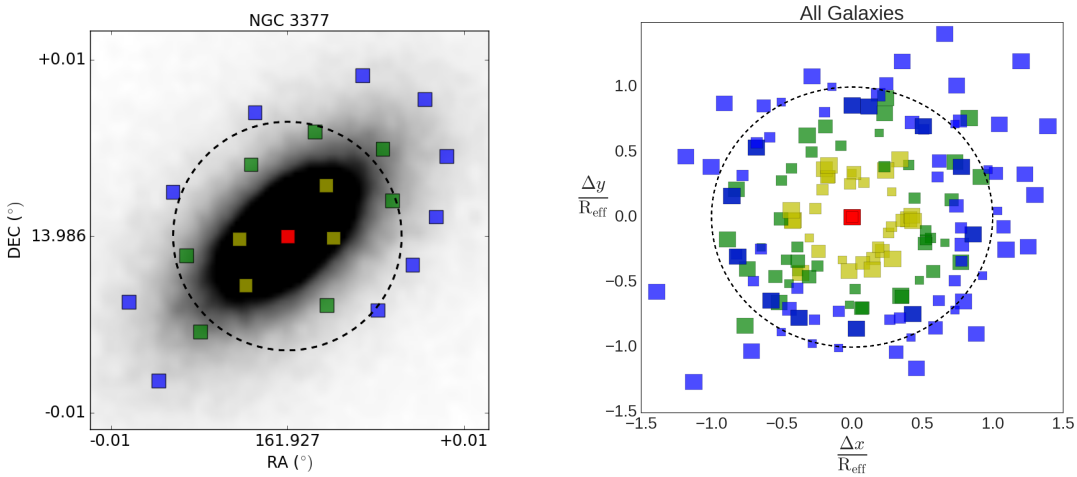

Figure 3.1: *Left panel:* The KINETyS observing strategy for an example galaxy. KMOS fields of view (2.8″ x 2.8″) are shown to scale, colour coded by the isophote they are sampling. Dashed line indicates the J-band effective radius. *Right Panel:* IFU fields for the ensemble of all galaxies scaled relative to the J-band circular effective radius. Colour scheme as in left panel.

Observations were made using the IZ (0.78–1.08 μm) grating and, for six of the eight galaxies, the YJ (1.03–1.34 μm). Note that KMOS spectra are calibrated to vacuum wavelengths, which will be quoted throughout this work. These bands have resolving power R = 3400 and R = 3600 respectively. For each target we took 3×450s exposures in each pointing, resulting in a total integration time of 2700s on-source. The FWHM seeing ranged from 0.8″ to 1.8″, with an average of 1.25″. The signal-to-noise ratio ranges from ∼100–270 (IZ band) and ∼150–370 (YJ band) per ∼ 0.35Å pixel in case of the data for the innermost region of each galaxy; this falls to ∼ 5–40 in both bands at the effective radius, so those data are useful only when combined across the sample.

3.1.2 Data reduction

We reduced the data as follows. Initially, the data were reduced using a slightly modified version of the standard ESO data reduction pipeline, with the flat-fielding, wavelength calibration, and illumination correction steps intact, but neither the (standard-star based) telluric correction nor the sky subtraction step applied. The output data cubes were then

Table 3.1: List of sample galaxies with observation details and key properties listed. Effective radii and total (J-band) magnitudes within the effective radius were extracted from 2MASS J-band images and used to calculated the mean surface brightness. Recession velocities were derived using pPXF (see Section 2.3) and $\sigma(\mathrm{R_{eff}}/8)$ values and fast/slow rotator status were taken from the ATLAS 3D survey (except for NGC 1407 for which a value was derived from our pPXF fits). Relative M/L taken from CvD12b.

Name	Bands	Seeing /arcsec	$\mathrm{R_{eff}}$ /arcsec	cz $/\mathrm{kms}^{-1}$	$\sigma(\mathrm{R_{eff}}/8)$ $/\mathrm{kms}^{-1}$	surface brightness /mag$_J$ arcsec^{-2}	relative M/L (Milky Way = 1)	ellipticity	Notes
NGC 0524	IZ,YJ	1.3, —	23.3	2400	243	17.8	1.09	0.00	Fast rotator
NGC 1407	IZ	1.4, 1.0	36.2	1950	301	17.4	—	0.00	Slow rotator
NGC 3377	IZ,YJ	1.8, —	23.3	690	146	17.0	1.16	0.40	Fast rotator
NGC 3379	IZ	1.2, 0.8	28.5	900	213	16.5	1.60	0.00	Fast rotator
NGC 4486	IZ,YJ	1.1, 1.3	44.5	1290	314	16.9	1.90	0.00	Slow rotator
NGC 4552	IZ,YJ	1.1, 1.6	24.1	390	262	16.6	2.04	0.00	Slow rotator
NGC 4621	IZ,YJ	1.3, 1.6	27.7	480	224	16.8	1.96	0.33	Fast rotator
NGC 5813	IZ,YJ	1.3, 1.2	33.7	1920	226	17.9	1.37	0.25	Slow rotator

processed to produce 1D spectra, in most cases by summing the pixel fluxes at each wavelength (i.e. using each IFU as a 'light-bucket'). In the case of the IFUs covering the galaxy core, the IFU was first subdivided into pixels within $0.7''$ of the centre and pixels further away, producing two spectra with roughly equal S/N. Since the seeing was in almost all cases better than $1.4''$, the spreading of flux between the two spectra will not significantly affect our conclusions. Following this, a telluric correction and sky-subtraction were applied. The spectra were not flux-calibrated, this being unnecessary for absorption index measurements.

Removal of sky emission lines was accomplished using ESO's SKYCORR tool (v1.0.0); see Noll et al. (2014). These lines are strong in the near infrared and vary rapidly (on shorter timescales than the length of an observation) making good sky subtraction challenging. SKYCORR addresses this problem by rescaling physically related 'families' of lines in the sky observations (in all cases taken from the same arm as the source observation but in the corresponding off-source pointing, which was pre-processed in the same way) to achieve a better match with those in the source observations prior to subtraction (see also Davies, 2007 for details). Example output for this procedure is shown in Fig. 3.2. We found performance was best in high S/N spectra when a first-order model for the source spectrum was first subtracted; this was accomplished by fitting a model spectrum to a conventionally sky-subtracted spectrum. Following the application of SKYCORR this first-order model was then added back to the spectrum. In addition, modelling and correcting for systematic variation of the sky line strengths between observations necessarily introduces additional statistical uncertainty, due to uncertainties in the parameters of the emission model. We characterised this additional uncertainty by comparing the scatter of fluxes around the mean in line regions post-subtraction with the corresponding average formal statistical uncertainty; the quadratic difference was then reincorporated into the formal uncertainty.

Atmospheric absorption was corrected using ESO's MOLECFIT tool (v.1.0.2); see Smette et al. (2015), Kausch et al. (2015). There are several wavelength ranges within our observations where this absorption is particularly strong and therefore difficult to deal with. MOLECFIT creates a best-fit atmospheric absorption profile for several key molecular absorbers, specifically O_2 and H_2O, which is then used to correct the spectrum.

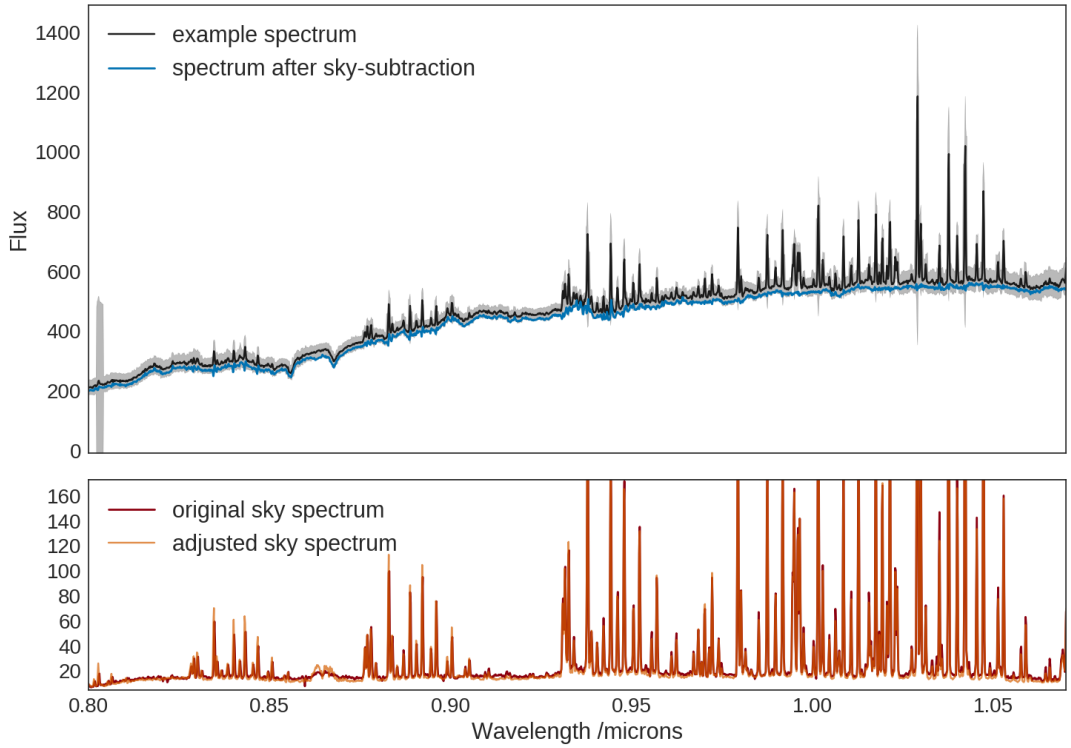

Figure 3.2: Operation of SKYCORR in the IZ band. The top panel shows a high S/N example spectrum before and after subtraction (grey band shows estimated confidence region for the flux in this exposure). The bottom shows a close-up of the adjusted sky spectrum, overlaid on the original.

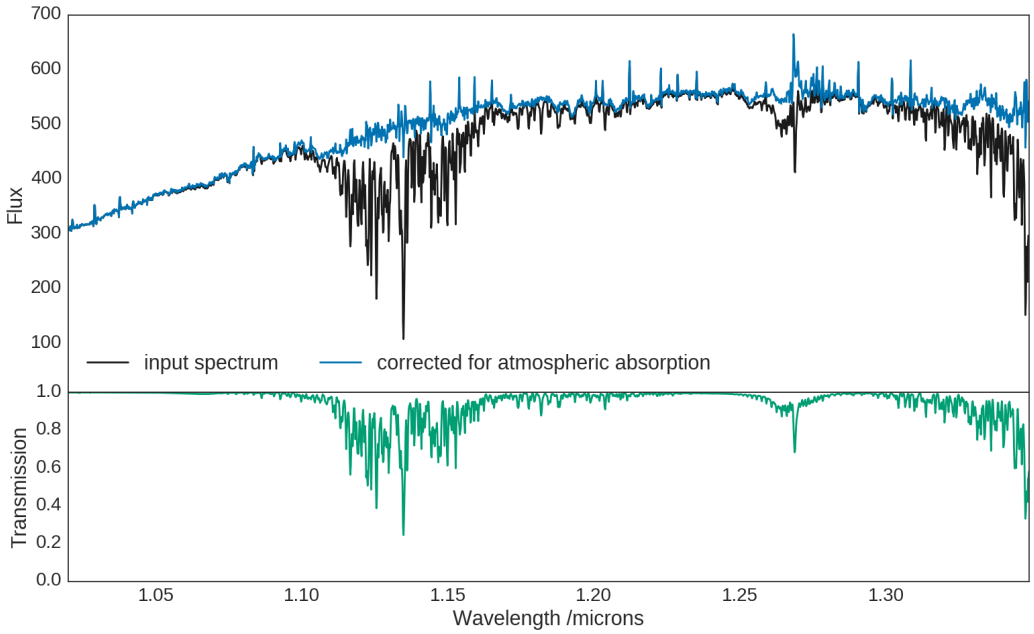

Figure 3.3: Operation of MOLECFIT in the YJ band. The top panel shows a (roughly sky-subtracted) high S/N example spectrum before and after correction for atmospheric absorption. The bottom panel shows the best-fit atmospheric transmission model which was divided out to make the correction. Sky subtraction was then re-run with the input exposures corrected in the same way.

For each exposure the central spectrum for each galaxy (i.e. the highest S/N spectrum) was used in the fitting process and the resulting correction was then applied to the spectra taken from the other KMOS arms (depicted in Fig. 3.3). In the IZ band corrections were fit to the range 8010–10856Å and 10210–13505Å in the YJ band.

MOLECFIT does not introduce systematics for the majority of the absorption lines we measure since it only adjusts the spectrum in specific spectral regions. A comparison with a standard star spectrum in the spectral regions around affected features indicates differences in the applied correction of up to a few percent in any given pixel.

We found that in different arms aimed at the same source, relative throughput could vary significantly (10% or more) by wavelength on scales of a few hundred pixels, in a way not corrected for by the standard pipeline. This effect, which appears to be stable over time, is most likely due to variations in the multi-layer filter coatings KMOS uses

(Sharples, private communication). Using the flat lamp exposures, we were able to characterise and correct for this (multiplicative) effect by fitting a spline through the brightness profile of each arm.

Additionally, a small additive effect (significant only in the low surface brightness arms) was found on similar wavelength scales, specific to individual exposures (and thus not dealt with by sky-subtraction). This is possibly due to scattered light in the instrument: the effect was present at the unilluminated edges of the detector, allowing us to characterise and subtract the variations from all arms (again, by fitting splines). The effect was not constant along the wavelength axis but appeared roughly constant across the spatial axis of the detector.

Accounting for these systematic errors ultimately leads to small corrections (less than the formal statistical uncertainty) to our measurements of spectral features (described in Section 2.3), with a few exceptions where the corrections are comparable in magnitude to the formal uncertainty. Uncertainty in the application of these corrections therefore does not significantly increase the uncertainty of the measurements.

3.1.3 Velocity dispersions and absorption line index measurements

After applying these procedures, spectra from multiple arms pointed at the same radial region were combined to produce a single spectrum for each physical region of each galaxy. Spectra from arms assigned to particular regions were initially summed together. Individual spectra were then divided through by this roughly combined spectrum and a sixth-order polynomial was fit to the result. Dividing each individual spectrum by the corresponding polynomial then maps each one to a common (average) continuum shape, following which they can be median-stacked in order to reduce the sensitivity of the combined spectrum to outlying pixel fluxes.

Using the penalised pixel-fitting (pPXF) tool (Cappellari & Emsellem, 2004) we determined redshifts and velocity dispersions for these spectra (we used an approximately consistent *rest-frame* wavelength fitting range of 8300–8800Å and 9600-10350Å, extending this to 10900Å for those galaxies with YJ band data). For this process we used a set of template spectra based on updated versions of the models of CvD12a (hereafter "the CvD models") which included variations in stellar population age (3.0 to 13.5 Gyr), [α/H]

Table 3.2: List of absorption index names and definitions (vacuum wavelength definitions, given in Å); originally from CvD12a.

Index name	blue continuum	Feature band	red continuum
Na I (0.82 μm)	8177.0–8205.0	8170.0–8177.0	8205.0–8215.0
Ca II (0.86 μm a)	8474.0–8484.0	8484.0–8513.0	8563.0–8577.0
Ca II (0.86 μm b)	8474.0–8484.0	8522.0–8562.0	8563.0–8577.0
Ca II (0.86 μm c)	8619.0–8642.0	8642.0–8682.0	8700.0–8725.0
Mg I (0.88 μm)	8777.4–8789.4	8801.9–8816.9	8847.4–8857.4
FeH (0.99 μm)	9855.0–9880.0	9905.0–9935.0	9940.0–9970.0
Ca I (1.03 μm)	10300–10320	10337–10360	10365–10390
Na I (1.14 μm)	11340–11370	11372–11415	11417–11447
K I (1.17 μm a)	11667–11680	11680–11705	11710–11750
K I (1.17 μm b)	11710–11750	11765–11793	11793–11810
K I (1.25 μm)	12460–12495	12505–12545	12555–12590
Al I (1.31 μm)	13090–13113	13115–13165	13165–13175

(0.0 to +0.4), and the IMF (Milky-Way-like to extremely bottom-heavy).

We characterised the spectra using a series of Lick-like absorption line indices, following the pseudo-continuum and feature band definitions given in CvD12a (reproduced in Table 3.2). The chosen features were selected for their strength, their IMF-sensitive nature, and their origins in a variety of different chemical species.

Using the derived velocity dispersions and redshifts we created a suite of appropriately broadened and shifted model spectra. These were generated from the updated version of the CvD models described in Conroy et al. (2014) and included a range of chemical abundances, population ages, and possible IMFs. In Fig. 3.4 we show three model spectra covering the same wavelength range as the data. These include a fiducial model corresponding to a single stellar population with an age of 13.5 Gyr and solar chemical abundance pattern, formed according to a Milky-Way-like IMF. The other two models are variations, firstly with a large enhancement of sodium ([Na/H] = +0.9) and secondly with a bottom-heavy IMF (parameterised as a power law with a slope of X = 3, in comparison to X = 2.35 for a Salpeter IMF). The definitions of the indices we measure are also

depicted.

Velocity broadening will change the measured equivalent width of a line due to flux being spread out of the feature definition, so it was necessary to correct the measured equivalent widths to a common velocity dispersion ($230\,\mathrm{kms}^{-1}$, representative of our sample, was chosen). We measured each index in a variety of model spectra broadened to $230\,\mathrm{kms}^{-1}$, then compared these measurements to those taken from model spectra at the observed velocity dispersion. Each feature has a different intrinsic strength in each model, so these comparisons together gave us the relationship between the strength of an index at the observed velocity dispersion and its strength at $230\,\mathrm{kms}^{-1}$.

We thus obtained, for each galaxy in our sample and for several locations within each galaxy, a set of measurements of absorption line strengths – strengths which are dependent on the properties of the stellar population observed. We also derived the uncertainties on these measurements by creating a set of Monte-Carlo realisations of our spectra from the statistical uncertainties on each pixel's flux. All the measurements are reported in Section 3.2.

We did not correct for the relative rotational velocity of spectra from arms pointed at the same radial region during the combination procedure described at the beginning of this section. Given the use of multiple arms – and because the intrinsic velocity dispersion of spectra from each arm is relatively large compared to the velocity shifts between them – the resultant velocity distribution underlying the combined spectrum is indistinguishable from a Gaussian distribution in almost all cases (and therefore accurately characterised by pPXF). We tested the effect of non-Gaussianity on the most extreme case, the inner ring of four arms on NGC 3377, but found that for synthetic spectra (with realistic noise added) broadened using a realistic kernel and the best-matching Gaussian kernel, changes to the absorption line index measurements were still well within the 1-σ measurement uncertainties even in this extreme case. The realistic kernel we used was estimated using velocities and velocity dispersions from the ATLAS^{3D} survey (Emsellem et al., 2004, Cappellari et al., 2011). Unfortunately velocity maps are not available out to the effective radius for all galaxies in our sample and S/N is not high enough to fit kinematics to spectra from individual arms. This prevents us from removing relative rotational velocities prior to combination, as would otherwise be optimal.

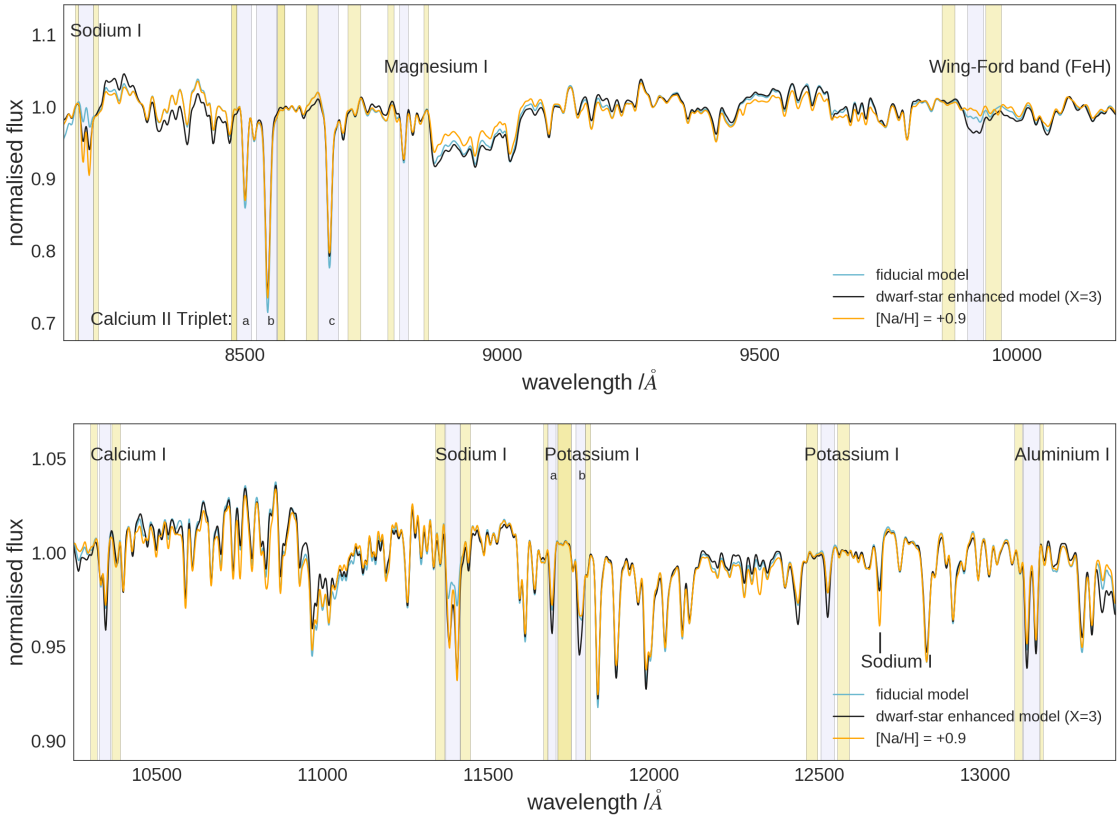

Figure 3.4: Three models of NIR spectra are illustrated: the solar abundance, Milky-Way-like IMF fiducial model (cyan); a model with [Na/H] = +0.9 (orange), and a model with a dwarf-enriched stellar population formed according to an X = 3 IMF (black). The models are broadened to 230 kms^{-1} We include absorption index definitions for a number of absorption lines whose strength is measurably dependent on the chosen model. The equivalent width of a feature is calculated in the purple highlighted wavelength range, relative to a local (pseudo-)continuum defined in the pale side-bands and interpolated across the feature (N.B. a spline has been fit through these pseudo-continua and divided out to enable a clearer comparison of feature strengths in different models. Outside the feature definitions these models are therefore not normalised).

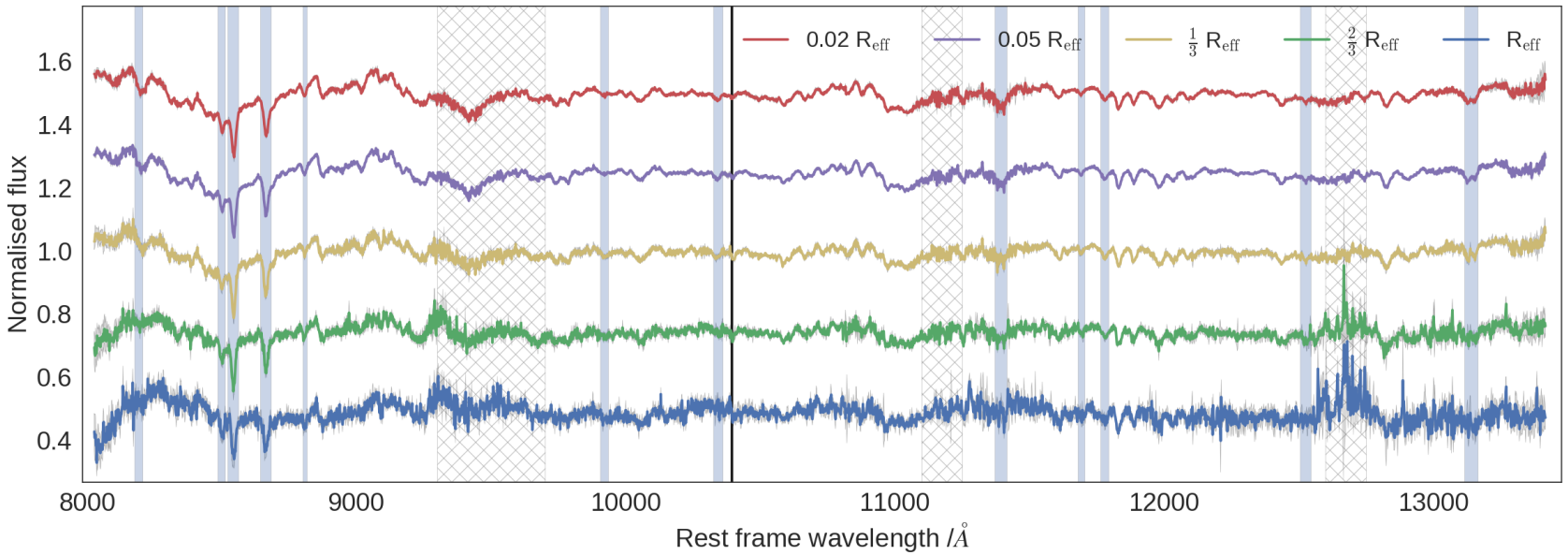

Figure 3.5: The data, median-stacked at fixed R/R_{eff}, indicating the recovery of the signal in the absorption line spectra even in the outlying regions of the galaxy (feature measurement bands indicated). The colour scheme is as in Fig. 1. The hatched regions indicate particularly strong telluric absorption, visible as an increased level of noise in these regions. The dividing line between the IZ and YJ bands is also shown.

3.1.4 Correction for AGN emission

Before interpreting the measured index equivalent widths, we assessed the impact of contamination of our absorption features by active galactic nuclei (AGN). Four of our sample are known to contain low-ionisation nuclear emission regions (LINERs): NGC 3379, NGC 4486, NGC 4552, and NGC 5813 (see for example Ho et al., 1997). In particular, strong nuclear emission lines were observed in the core spectrum of NGC 4486 when the region within a $0.7''$ radius was isolated. To assess how widespread this contamination might be, we created maps of the strengths of two emission lines: the [S III] λ 9533 + Pa-ϵ composite line, and various other lines known to be strong in many AGN – see Landt et al. (2008). For this purpose, the data from the central IFU in each galaxy was re-reduced, using a straightforward subtraction of the datacubes in each pair of exposures (justifiable due to the high signal-to-noise of these cubes) and applying the telluric correction derived in the full reduction pipeline. The three exposures were then combined, taking offsets in the targeting into account. This method preserved the full spatial information carried in the datacubes.

It is clear from Fig. 3.6 (in which we show the strongest emission line signature we identified) that only in NGC 4486 is AGN line emission detectable, and even then it is only significant in the very centre. Although most of our absorption features in this spectrum are not compromised by AGN emission lines, continuum AGN emission could contaminate all the absorption features in that spectrum (an additional continuum component will reduce the equivalent width measurement for each index).

We estimate the level of AGN continuum contamination as follows: In Prieto et al. (2016), Hubble observations of the central parsecs of M87 are used to measure the AGN flux at wavelengths of ~ 1 μm. This is quoted as $\sim 10^{-3}$ Jy, or magnitude 15.5. Meanwhile, the 2MASS large galaxies atlas (Jarrett et al., 2003), quotes the core surface brightness (within $2''$ of the centre) as 14.7 mag arcsec^{-2}.

From this, we calculate the total flux expected within the R$< 0.7''$ region, which will contain almost all the AGN flux, assuming a de Vaucouleurs brightness profile. We obtain a magnitude of 13.4 for the extraction region, which we compare with the AGN magnitude of 15.5 to estimate an AGN contribution of $\sim 15\%$ to the total continuum level.

This estimate allowed us to make a rough correction to the equivalent widths mea-

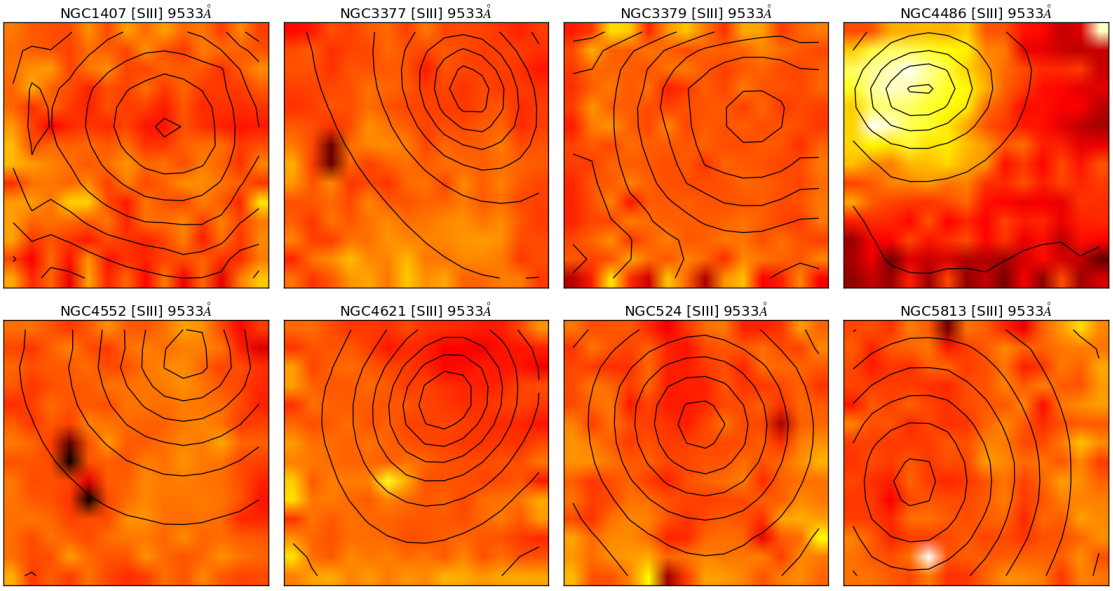

Figure 3.6: Maps of the strength of [S III] (λ 9533) emission in a central $2.8'' \times 2.8''$ IFU arm for each galaxy (normalised by the continuum emission level). Pixel coordinates. Black contours indicate continuum emission derived by collapsing the datacube along the wavelength axis.

sured for absorption lines in NGC 4486's central spectrum. The small number of feature measurements contaminated by line emission (the Wing-Ford band, Ca I at 1.03 μm, and K I at 1.25 μm – contaminated by [C I] λ 9853, [S II] λ 10323, and [Fe II] λ 12570 respectively) in this spectrum were not included in the analysis.

3.2 Tables of data values

This section contains the full set of measured equivalent widths for all spectra, derived according to the procedures just described. For definitions of the spectral indices used, we refer the reader to Table 3.2.

The tables also contain velocity dispersion derived using pPXF, which have been corrected for instrumental broadening. The tables additionally contain average S/N (per spectral bin) for the observations in the IZ and, where applicable, YJ bands.

Table 3.3: Equivalent widths and corresponding statistical uncertainties measured from NGC 0524, given for each radial extraction region and adjusted to a common velocity dispersion of 230 kms^{-1}. R1 and R2 correspond to the two extraction regions in the central IFU ($< 0.7''$, $> 0.7''$) while R3, R4, and R5 correspond to the rings of IFUs arranged at $\sim 1/3\,\mathrm{R_{eff}}$, $\sim 2/3\,\mathrm{R_{eff}}$, and $\sim\mathrm{R_{eff}}$ (N.B. for this galaxy only two rings of IFUs were used). Uncertainties were derived by creating many Monte-Carlo realisations of the spectra. Also shown: best-fit velocity dispersion used to correct the measurements, average continuum signal-to-noise ratio in the IZ and YJ band observations.

NGC 0524	R1	R2	R3	R4	R5
Na I 0.82 μm	0.47 ± 0.14	0.17 ± 0.08	–0.04 ± 0.42	0.63 ± 0.66	—
Ca II Triplet	7.60 ± 0.25	6.95 ± 0.19	6.57 ± 0.49	6.65 ± 1.11	—
Mg I 0.88 μm	0.59 ± 0.05	0.49 ± 0.03	0.16 ± 0.10	0.72 ± 0.26	—
Wing-Ford band	0.40 ± 0.04	0.29 ± 0.03	0.60 ± 0.10	0.37 ± 0.22	—
Ca I 1.03 μm	0.25 ± 0.06	0.45 ± 0.04	0.41 ± 0.15	0.52 ± 0.95	—
Na I 1.14 μm	1.08 ± 0.07	0.97 ± 0.06	0.8 ± 0.12	1.03 ± 0.44	—
K I 1.17 μma+b	0.81 ± 0.05	0.78 ± 0.03	0.65 ± 0.09	0.75 ± 0.32	—
K I 1.25 μm	0.35 ± 0.07	0.30 ± 0.06	0.43 ± 0.10	0.73 ± 0.31	—
Al I 1.31 μm	1.42 ± 0.09	1.16 ± 0.05	1.42 ± 0.14	1.81 ± 0.64	—
σ_{pPXF} /kms^{-1}	261.0 ± 3.9	217.0 ± 2.2	198.0 ± 8.6	198.0 ± 17.3	—
S/N (IZ)	170	254	68	30	—
S/N (YJ)	301	450	126	41	—

Table 3.4: Equivalent widths and corresponding statistical uncertainties measured from NGC 1407, given for each radial extraction region and adjusted to a common velocity dispersion of 230 kms^{-1}. R1 and R2 correspond to the two extraction regions in the central IFU ($< 0.7''$, $> 0.7''$) while R3, R4, and R5 correspond to the rings of IFUs arranged at $\sim 1/3\,\mathrm{R_{eff}}$, $\sim 2/3\,\mathrm{R_{eff}}$, and $\sim\mathrm{R_{eff}}$. Uncertainties were derived by creating many Monte-Carlo realisations of the spectra. Also shown: best-fit velocity dispersion used to correct the measurements, average continuum signal-to-noise ratio in the IZ and YJ band observations.

NGC 1407	R1	R2	R3	R4	R5
Na I 0.82 µm	0.46 ± 0.23	0.69 ± 0.10	-0.79 ± 0.22	-2.25 ± 1.00	-4.58 ± 3.30
Ca II Triplet	8.08 ± 0.37	7.17 ± 0.29	6.34 ± 0.34	8.51 ± 0.73	7.51 ± 5.10
Mg I 0.88 µm	0.60 ± 0.12	0.63 ± 0.05	0.60 ± 0.07	0.45 ± 0.17	0.42 ± 0.77
Wing-Ford band	0.02 ± 0.09	0.16 ± 0.06	0.40 ± 0.11	0.27 ± 0.23	0.76 ± 1.31
Ca I 1.03 µm	—	—	—	—	—
Na I 1.14 µm	—	—	—	—	—
K I 1.17 µma+b	—	—	—	—	—
K I 1.25 µm	—	—	—	—	—
Al I 1.31 µm	—	—	—	—	—
σ_{pPXF} /kms^{-1}	313.0 ± 6.6	323.0 ± 6.1	234.0 ± 7.9	268.0 ± 22.6	123.0 ± 41.4
S/N (IZ)	99	168	84	36	6
S/N (YJ)	0	0	0	0	0

Table 3.5: Equivalent widths and corresponding statistical uncertainties measured from NGC 3377, given for each radial extraction region and adjusted to a common velocity dispersion of 230 kms^{-1}. R1 and R2 correspond to the two extraction regions in the central IFU ($< 0.7''$, $> 0.7''$) while R3, R4, and R5 correspond to the rings of IFUs arranged at $\sim 1/3\,\mathrm{R_{eff}}$, $\sim 2/3\,\mathrm{R_{eff}}$, and $\sim\mathrm{R_{eff}}$. Uncertainties were derived by creating many Monte-Carlo realisations of the spectra. Also shown: best-fit velocity dispersion used to correct the measurements, average continuum signal-to-noise ratio in the IZ and YJ band observations.

NGC 3377	R1	R2	R3	R4	R5
Na I 0.82 µm	0.29 ± 0.07	0.34 ± 0.05	0.07 ± 0.39	–0.13 ± 0.78	–0.66 ± 1.00
Ca II Triplet	5.94 ± 0.18	7.12 ± 0.11	6.31 ± 0.63	2.71 ± 1.71	2.00 ± 2.16
Mg I 0.88 µm	0.44 ± 0.04	0.49 ± 0.02	0.38 ± 0.11	0.24 ± 0.17	0.09 ± 0.42
Wing-Ford band	0.25 ± 0.04	0.21 ± 0.04	0.06 ± 0.18	–0.72 ± 0.27	–0.11 ± 0.74
Ca I 1.03 µm	0.27 ± 0.08	–0.22 ± 0.07	–0.14 ± 0.25	–1.24 ± 0.64	–2.06 ± 1.06
Na I 1.14 µm	1.54 ± 0.09	1.04 ± 0.09	0.41 ± 1.42	1.35 ± 1.93	0.41 ± 2.06
K I 1.17 µma+b	0.75 ± 0.05	0.82 ± 0.05	0.37 ± 0.51	1.21 ± 0.78	0.88 ± 0.88
K I 1.25 µm	0.13 ± 0.07	0.22 ± 0.07	0.25 ± 0.34	1.65 ± 0.74	1.28 ± 1.58
Al I 1.31 µm	1.07 ± 0.08	1.27 ± 0.08	0.46 ± 1.1	–1.09 ± 1.78	–1.14 ± 3.09
σ_{pPXF} /kms^{-1}	142.0 ± 1.1	104.0 ± 1.4	149.0 ± 8.2	99.0 ± 15.5	94.0 ± 4.0
S/N (IZ)	211	243	52	29	11
S/N (YJ)	191	236	27	12	11

Table 3.6: Equivalent widths and corresponding statistical uncertainties measured from NGC 3379, given for each radial extraction region and adjusted to a common velocity dispersion of 230 kms^{-1}. R1 and R2 correspond to the two extraction regions in the central IFU ($< 0.7''$, $> 0.7''$) while R3, R4, and R5 correspond to the rings of IFUs arranged at $\sim 1/3\,\mathrm{R_{eff}}$, $\sim 2/3\,\mathrm{R_{eff}}$, and $\sim\mathrm{R_{eff}}$. Uncertainties were derived by creating many Monte-Carlo realisations of the spectra. Also shown: best-fit velocity dispersion used to correct the measurements, average continuum signal-to-noise ratio in the IZ and YJ band observations.

NGC 3379	R1	R2	R3	R4	R5
Na I 0.82 µm	0.26 ± 0.06	0.26 ± 0.03	1.02 ± 0.30	0.77 ± 0.28	-0.24 ± 4.51
Ca II Triplet	6.65 ± 0.15	6.35 ± 0.15	6.90 ± 0.30	5.30 ± 0.41	7.54 ± 5.97
Mg I 0.88 µm	0.58 ± 0.07	0.49 ± 0.04	0.48 ± 0.06	0.31 ± 0.08	0.53 ± 0.84
Wing-Ford band	0.10 ± 0.05	0.12 ± 0.04	0.11 ± 0.07	0.83 ± 0.15	-0.08 ± 1.6
Ca I 1.03 µm	—	—	—	—	—
Na I 1.14 µm	—	—	—	—	—
K I 1.17 µma+b	—	—	—	—	—
K I 1.25 µm	—	—	—	—	—
Al I 1.31 µm	—	—	—	—	—
σ_{pPXF} /kms^{-1}	226.0 ± 1.5	205.0 ± 1.4	160.0 ± 3.1	108.0 ± 6.3	97.0 ± 90.3
S/N (IZ)	238	394	120	62	5
S/N (YJ)	0	0	0	0	0

Table 3.7: Equivalent widths and corresponding statistical uncertainties measured from NGC 4486, given for each radial extraction region and adjusted to a common velocity dispersion of 230 kms^{-1}. R1 and R2 correspond to the two extraction regions in the central IFU ($< 0.7''$, $> 0.7''$) while R3, R4, and R5 correspond to the rings of IFUs arranged at $\sim 1/3\,\mathrm{R_{eff}}$, $\sim 2/3\,\mathrm{R_{eff}}$, and $\sim\mathrm{R_{eff}}$. Uncertainties were derived by creating many Monte-Carlo realisations of the spectra. Also shown: best-fit velocity dispersion used to correct the measurements, average continuum signal-to-noise ratio in the IZ and YJ band observations.

NGC 4486	R1	R2	R3	R4	R5
Na I 0.82 µm	0.47 ± 0.45	1.34 ± 0.19	1.28 ± 0.30	–0.02 ± 0.61	–0.87 ± 1.93
Ca II Triplet	8.29 ± 0.62	5.93 ± 0.23	5.78 ± 0.46	5.67 ± 0.66	3.45 ± 2.21
Mg I 0.88 µm	0.47 ± 0.05	0.60 ± 0.05	0.59 ± 0.09	0.29 ± 0.16	0.40 ± 0.91
Wing-Ford band	—	—	0.24 ± 0.14	0.74 ± 0.25	0.65 ± 2.31
Ca I 1.03 µm	—	—	0.08 ± 0.17	0.02 ± 0.31	–0.27 ± 2.71
Na I 1.14 µm	2.65 ± 0.26	2.16 ± 0.12	1.83 ± 0.20	1.69 ± 0.82	–1.05 ± 1.94
K I 1.17 µma+b	0.87 ± 0.19	0.78 ± 0.08	1.16 ± 0.10	0.39 ± 0.31	1.31 ± 0.72
K I 1.25 µm	—	—	–0.28 ± 0.12	0.72 ± 0.26	0.18 ± 0.55
Al I 1.31 µm	1.25 ± 0.23	1.16 ± 0.07	1.30 ± 0.12	0.45 ± 0.34	–0.84 ± 0.99
σ_{pPXF} /kms^{-1}	400.0 ± 11.8	341.0 ± 2.9	293.0 ± 4.7	257.0 ± 11.2	300.0 ± 22.7
S/N (IZ)	108	165	81	45	11
S/N (YJ)	164	299	144	50	23

Table 3.8: Equivalent widths and corresponding statistical uncertainties measured from NGC 4552, given for each radial extraction region and adjusted to a common velocity dispersion of 230 kms^{-1}. R1 and R2 correspond to the two extraction regions in the central IFU ($< 0.7''$, $> 0.7''$) while R3, R4, and R5 correspond to the rings of IFUs arranged at $\sim 1/3\,\mathrm{R_{eff}}$, $\sim 2/3\,\mathrm{R_{eff}}$, and $\sim\mathrm{R_{eff}}$. Uncertainties were derived by creating many Monte-Carlo realisations of the spectra. Also shown: best-fit velocity dispersion used to correct the measurements, average continuum signal-to-noise ratio in the IZ and YJ band observations.

NGC 4552	R1	R2	R3	R4	R5
Na I 0.82 µm	1.03 ± 0.13	0.75 ± 0.06	0.46 ± 0.23	0.19 ± 1.00	1.45 ± 0.69
Ca II Triplet	6.41 ± 0.22	6.29 ± 0.16	6.48 ± 0.57	4.40 ± 1.53	6.08 ± 1.50
Mg I 0.88 µm	0.72 ± 0.06	0.48 ± 0.04	0.36 ± 0.10	0.19 ± 0.21	0.29 ± 0.24
Wing-Ford band	0.22 ± 0.07	0.21 ± 0.05	0.16 ± 0.11	–0.34 ± 0.31	0.92 ± 0.66
Ca I 1.03 µm	0.28 ± 0.09	0.22 ± 0.05	0.34 ± 0.13	0.49 ± 0.33	0.27 ± 0.74
Na I 1.14 µm	2.24 ± 0.08	1.95 ± 0.06	1.79 ± 0.20	1.33 ± 0.98	1.83 ± 0.74
K I 1.17 µma+b	0.77 ± 0.07	0.82 ± 0.06	0.53 ± 0.18	0.18 ± 1.32	0.71 ± 0.63
K I 1.25 µm	0.33 ± 0.06	0.22 ± 0.05	0.06 ± 0.13	–0.35 ± 0.85	0.04 ± 0.56
Al I 1.31 µm	1.52 ± 0.08	1.49 ± 0.06	0.48 ± 0.36	–0.49 ± 3.08	–1.95 ± 1.22
σ_{pPXF} /kms^{-1}	256.0 ± 1.6	234.0 ± 1.2	178.0 ± 4.2	160.0 ± 9.1	124.0 ± 10.5
S/N (IZ)	154	244	75	28	18
S/N (YJ)	226	343	70	11	18

Table 3.9: Equivalent widths and corresponding statistical uncertainties measured from NGC 4621, given for each radial extraction region and adjusted to a common velocity dispersion of 230 kms^{-1}. R1 and R2 correspond to the two extraction regions in the central IFU ($< 0.7''$, $> 0.7''$) while R3, R4, and R5 correspond to the rings of IFUs arranged at $\sim 1/3\,\mathrm{R_{eff}}$, $\sim 2/3\,\mathrm{R_{eff}}$, and $\sim\mathrm{R_{eff}}$. Uncertainties were derived by creating many Monte-Carlo realisations of the spectra. Also shown: best-fit velocity dispersion used to correct the measurements, average continuum signal-to-noise ratio in the IZ and YJ band observations.

NGC 4621	R1	R2	R3	R4	R5
Na I 0.82 µm	1.18 ± 0.10	0.70 ± 0.05	0.36 ± 0.20	0.09 ± 0.36	–0.74 ± 0.37
Ca II Triplet	7.26 ± 0.21	7.03 ± 0.14	6.04 ± 0.42	7.08 ± 0.68	3.87 ± 0.73
Mg I 0.88 µm	0.70 ± 0.06	0.62 ± 0.04	0.59 ± 0.10	0.44 ± 0.15	0.72 ± 0.21
Wing-Ford band	0.23 ± 0.04	0.21 ± 0.03	0.37 ± 0.10	0.39 ± 0.19	–0.12 ± 0.29
Ca I 1.03 µm	0.56 ± 0.05	0.56 ± 0.04	0.68 ± 0.14	0.44 ± 0.20	–0.15 ± 0.33
Na I 1.14 µm	1.69 ± 0.04	1.50 ± 0.04	1.03 ± 0.16	0.70 ± 0.20	2.12 ± 0.39
K I 1.17 µma+b	0.98 ± 0.06	0.90 ± 0.04	0.97 ± 0.14	0.88 ± 0.25	1.71 ± 0.55
K I 1.25 µm	0.07 ± 0.06	0.05 ± 0.06	–0.06 ± 0.15	0.12 ± 0.35	1.12 ± 0.59
Al I 1.31 µm	1.71 ± 0.07	1.59 ± 0.05	1.38 ± 0.16	0.79 ± 0.27	–1.21 ± 0.93
σ_{pPXF} /kms^{-1}	270.0 ± 1.3	228.0 ± 1.3	207.0 ± 3.3	192.0 ± 7.7	217.0 ± 17.9
S/N (IZ)	223	286	93	52	40
S/N (YJ)	343	480	141	75	32

Table 3.10: Equivalent widths and corresponding statistical uncertainties measured from NGC 5813, given for each radial extraction region and adjusted to a common velocity dispersion of 230 kms^{-1}. R1 and R2 correspond to the two extraction regions in the central IFU ($< 0.7''$, $> 0.7''$) while R3, R4, and R5 correspond to the rings of IFUs arranged at $\sim 1/3\,\mathrm{R_{eff}}$, $\sim 2/3\,\mathrm{R_{eff}}$, and $\sim\mathrm{R_{eff}}$. Uncertainties were derived by creating many Monte-Carlo realisations of the spectra. Also shown: best-fit velocity dispersion used to correct the measurements, average continuum signal-to-noise ratio in the IZ and YJ band observations.

NGC 5813	R1	R2	R3	R4	R5
Na I 0.82 µm	0.15 ± 0.14	0.33 ± 0.09	–0.49 ± 0.88	–0.59 ± 0.83	–0.43 ± 1.53
Ca II Triplet	6.64 ± 0.27	7.10 ± 0.20	5.62 ± 1.13	8.20 ± 1.51	6.15 ± 4.64
Mg I 0.88 µm	0.49 ± 0.06	0.44 ± 0.05	0.42 ± 0.18	0.73 ± 0.22	0.54 ± 0.66
Wing-Ford band	0.18 ± 0.08	0.36 ± 0.06	0.29 ± 0.25	1.04 ± 0.38	0.75 ± 1.42
Ca I 1.03 µm	0.41 ± 0.09	0.48 ± 0.07	0.43 ± 1.24	–0.63 ± 0.58	0.93 ± 1.50
Na I 1.14 µm	1.25 ± 0.09	1.29 ± 0.07	1.35 ± 0.89	–0.07 ± 0.43	–1.63 ± 1.25
K I 1.17 µma+b	0.73 ± 0.07	0.64 ± 0.05	0.50 ± 0.48	0.61 ± 0.25	0.93 ± 0.60
K I 1.25 µm	–0.12 ± 0.09	–0.02 ± 0.07	–0.02 ± 0.57	–0.43 ± 0.4	–0.88 ± 0.86
Al I 1.31 µm	0.56 ± 0.08	0.63 ± 0.06	0.71 ± 1.32	–0.23 ± 0.49	–0.86 ± 1.56
σ_{pPXF} /kms^{-1}	249.0 ± 2.8	221.0 ± 2.8	219.0 ± 14.9	119.0 ± 1.9	133.0 ± 30.2
S/N (IZ)	135	182	31	19	7
S/N (YJ)	230	294	20	35	14

3.3 Radial variations in the measured index strengths

As described in Chapter 1, some measured absorption features are sensitive to the IMF. However, the effect of dwarf enrichment of the stellar population on any given feature is always degenerate with other effects (e.g. chemical abundances). This not only follows from the individual dependence of particular atomic/molecular transitions on multiple parameters, but also from blending with neighbouring features (due to velocity broadening).

In Fig. 3.5 we show spectra from each of the radial extraction regions, median-stacked over the eight galaxies (after normalising the continua) in order to suppress noise. The features that were highlighted in Fig. 3.4 are readily apparent.

We created these stacked spectra in the following way: first, we took the spectra from the innermost extraction region (the central $0.7''$ of the subdivided central IFU) for each galaxy, shifted them into the rest-frame and binned them onto a common wavelength grid. We then divided out their relative continuum variation (by first fitting a 6^{th} order polynomial to the ratio of each spectrum with the mean spectrum and dividing through by this polynomial) and then evaluated the median flux at each wavelength. Errors were then created by bootstrap resampling of the input spectra, since galaxy-galaxy variations are larger than the statistical uncertainty on any given spectrum. We followed a similar procedure for the other spectra, but in each case divided the spectra by that taken from the innermost extraction region prior to stacking (i.e. we stacked the variations in the spectra). These 'variation-stacks' were then multiplied by the previously-calculated central stacked-spectrum. This procedure is intended to maximise the radial variation signal by dividing out any constant offset in the strength of spectral features between different galaxies in the stack.

The main goal of this work is to constrain the radial variation of the stellar populations within a sample of several large, nearby ETGs. This is accomplished by measuring the radial variation of a variety of spectral features between the stacked spectra just described. In Chapter 4 we will use stellar population models to explain the observed variations, but for now focus on our empirical findings. We measure indices for these stacked spectra in precisely the same way as for the individual spectra, including the correction of all measurements to a common velocity dispersion and the inference of errors through multiple

Monte-Carlo realisations of the data. These measurements are recorded in Table 3.11, along with the best fit velocity dispersion at each radius for both wavebands. A brief outline of these features and their nature follows.

Our wavelength range contains two sodium absorption features, Na I 0.82 μm and Na I 1.14 μm. Both are primarily sensitive to the IMF and to the abundance of sodium (Conroy & van Dokkum, 2012a).

The 0.82 μm feature has made a significant contribution to measurements of bottom-heavy IMFs, dating back to Spinrad & Taylor (1971). The 1.14 μm sodium feature is relatively unexplored. Smith et al. (2015a) reported that in ETGs it is often much stronger than would be expected from the fiducial SSP model. In the CvD models the 1.14 μm feature has particularly high sensitivity to the IMF in comparison with its sensitivity to sodium abundance.

The Ca II 0.86 μm Triplet is the strongest absorption feature we measure. The feature is weakened in models with bottom-heavy IMFs and/or enhanced [Na/H] and is of course sensitive to [Ca/H]. Calcium is formally an α element, but its abundance does not always track [α/H] in α-enhanced stellar populations (e.g. Thomas et al., 2003a).

We measure a second Ca feature, a weak line at 1.03 μm. Unlike the other features mentioned so far, it is insensitive to the sodium abundance – see Smith et al., 2012. This feature is complementary to the Ca II Triplet in the sense that variation in the IMF slope will alter their strengths in opposite ways (the triplet is weakened in the CvD models in the bottom-heavy case, while the Ca I feature gets stronger). In contrast both are strengthened if [Ca/H] is enhanced. Thus, taken in concert, the two features in principle provide a powerful constraint on IMF variations.

The Wing-Ford band is a molecular absorption band at 0.99 μm associated with the FeH molecule. It is particularly sensitive to the IMF, being present in cool dwarf stars but not giants (Nordh et al., 1977) and also weakens as [Na/H] increases.

We have measured the K I 1.17 μm composite feature and the K I 1.25 μm line, neither of which have previously been studied in detail. Both are primarily sensitive to the IMF and to [K/H], while the K I 1.25 μm line is dramatically weakened as [α/H] increases (due to changes in the local continuum behaviour).

We measure the Al I 1.31 μm doublet, which is sensitive to the IMF but is not well

Table 3.11: Equivalent widths and corresponding statistical uncertainties measured from the stacked spectra, given for each radial extraction region and adjusted to common velocity dispersion of 230 kms^{-1}. Definitions as in Table 3.3. Uncertainties were derived from and reflect the scatter among the input spectra used to create the stacks, since this exceeds the formal statistical uncertainties in some cases. Also given: average extraction radius of spectra comprising each stack and velocity dispersions of the stacks (corrected for instrumental broadening).

Index	R1	R2	R3	R4	R5
Na I 0.82 μm	0.38± 0.20	0.38± 0.09	0.08± 0.19	0.16± 0.22	–0.5± 0.43
Ca II Triplet	6.62± 0.25	6.38± 0.19	6.23± 0.25	5.91± 0.50	5.33± 0.69
Mg I 0.88 μm	0.51± 0.05	0.50± 0.03	0.39± 0.06	0.40± 0.10	0.51± 0.14
Wing-Ford band	0.21± 0.05	0.24± 0.03	0.32± 0.06	0.30± 0.18	0.29± 0.24
Ca I 1.03 μm	0.31± 0.03	0.36± 0.03	0.47± 0.08	0.25± 0.07	0.32± 0.22
Na I 1.14 μm	1.56± 0.24	1.32± 0.09	1.05± 0.14	0.98± 0.25	1.18± 0.78
K I 1.17 μma+b	0.75± 0.07	0.73± 0.04	0.62± 0.10	0.67± 0.11	1.07± 0.20
K I 1.25 μm	0.08± 0.15	0.05± 0.08	0.06± 0.14	0.23± 0.28	0.34± 0.86
Al I 1.31 μm	1.26± 0.23	1.24± 0.09	1.15± 0.13	0.83± 0.34	0.41± 0.69
Extraction radius R/R_{eff}	0.02	0.05	0.33	0.67	1.00
σ_{IZ} /kms^{-1}	219 ± 19	217 ± 6	192 ± 12	175 ± 13	146 ± 30
σ_{YJ} /kms^{-1}	235 ± 20	197 ± 8	167 ± 7	172 ± 18	180 ± 15

explored. Because the CvD models do not explictly account for variations in [Al/H] at the time of writing, we do not attempt to draw quantitative conclusions from this feature, but include our measurements for completeness.

Taken together, these features have significant sensitivity to the abundance of α-elements (in particular Mg and Ca), Fe, Na, Ca, K, and the IMF.

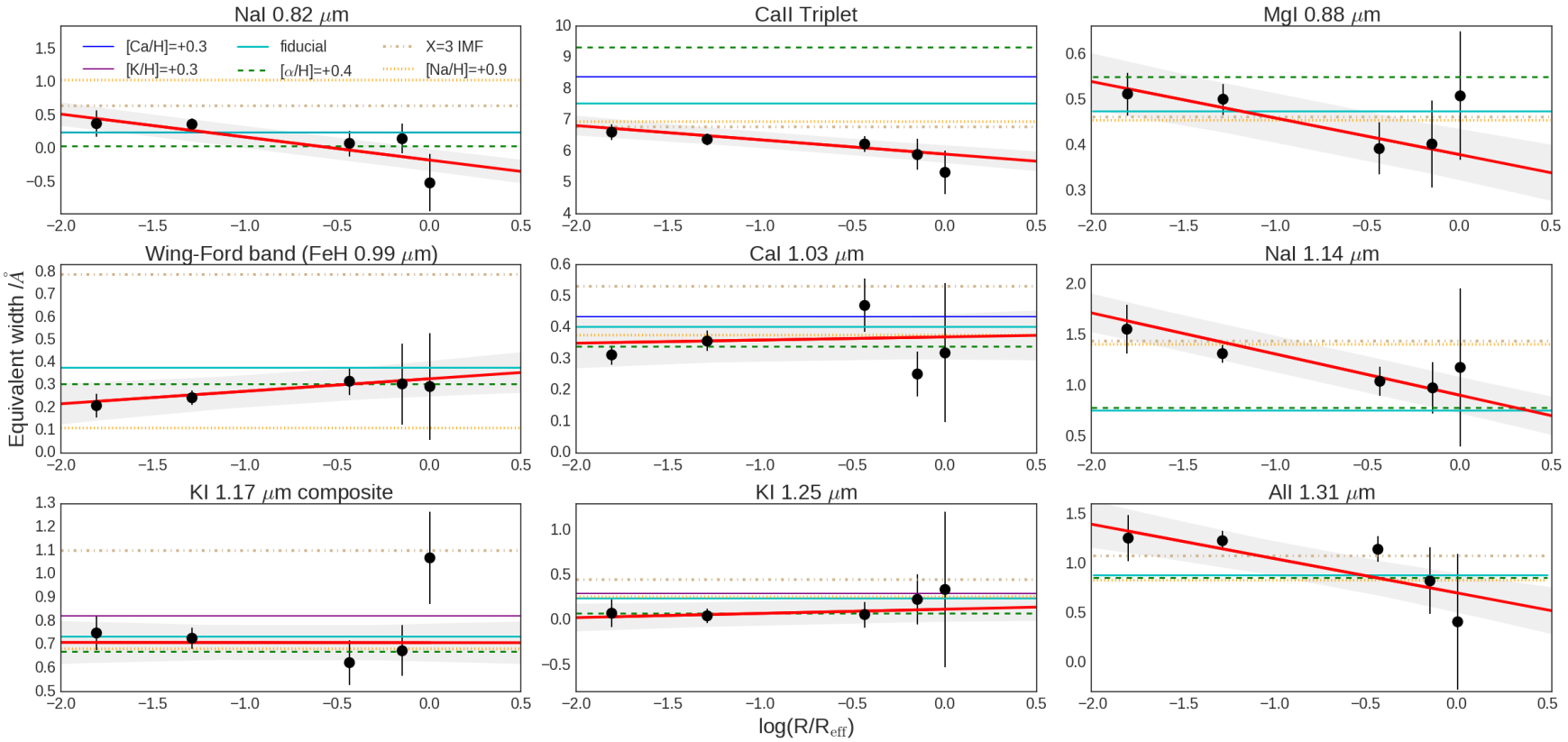

Figure 3.7: The index trends with log(R/R$_{\rm eff}$). The index measurements for each radial extraction region (corrected to 230 kms^{-1} in all cases) are shown in black with errors. The best fit trends are in red with the calculated 1σ uncertainty region shown (grey shaded). The SSP model predictions are denoted by horizontal lines (Cyan: fiducial model; Green: [α/H]=+0.4; Tan: X=3 IMF; Orange: [Na/H]=+0.9; Dark blue: [Ca/H]=+0.3 (but note that Ca is also an α-element so scales with [α/H] too); Purple: [K/H]=+0.3)

Table 3.12: Measured absorption indices and their best-fit radial gradients. The most significant trends are highlighted in bold.

Index Name	best-fit gradient /Å per dex in $\log(R/R_{eff})$
Na I 0.82 μm	**–0.34 ± 0.05**
Ca II Triplet	**–0.45 ± 0.14**
Mg I 0.88 μm	**–0.08 ± 0.02**
Wing-Ford band	+0.06 ± 0.04
Ca I 1.03 μm	+0.01 ± 0.03
Na I 1.14 μm	**–0.40 ± 0.05**
K I 1.17 μm a+b	–0.00 ± 0.04
K I 1.25 μm	+0.05 ± 0.06
Al I 1.31 μm	–0.34 ± 0.12

We now consider the variation of spectral features between the stacked spectra created by the procedure outlined earlier in this section. By stacking in the rest frame we gain by suppressing systematic effects and are able to quantify any radial gradients by using the full range of spectra available to us, at the cost of 'washing out' information about the individual galaxies. We therefore treat the stacked spectra as being representative of an average massive ETG at a given fraction of the effective radius.

We first look at line strength trends with $\log(R/R_{eff})$ for the stacked spectra. It is not clear *a priori* whether parametrizing the radial coordinate linearly or logarithmically is more 'natural', but we note that the logarithmic description gives more leverage over the fit to the high S/N data from the central IFU. The trends are shown in Fig. 3.7, in which the measurements from the stacked spectra are displayed along with the best fitting trend line. The error bars were created by bootstrap resampling as detailed above, so indicate the spread of measurements across the sample of galaxies from which the stacks were created. Also shown (as horizontal lines) are the predictions of the CvD models for comparison. In this section we report these empirical correlations, setting aside explicit model fitting until the next chapter.

In Table 3.12 we provide the best-fitting linear trends of index strength with $\log(R/R_{eff})$.

These were measured through a maximum-likelihood procedure in which we accounted for the statistical uncertainty estimated for each measurement as well as the possibility of intrinsic scatter around the linear relation. We highlight trends with particular statistical significance ($> 3\sigma$) in bold in the table. We measure negative radial trends in the Ca II Triplet and the Na I 1.14 μm line (i.e. these lines are significantly weaker at the effective radius than they are in the core). More marginal trends are observed in some other indices, but we note in particular that our measurements of the IMF-sensitive Wing-Ford band are consistent with no radial trend.

The uncertainties listed in Table 3.12 account for the uncertainties on each pixel in the stacked spectra and the (small) uncertainties introduced by the velocity dispersion correction to the stacked spectra, as well as accounting for the uncertainty in the best-fit gradient due to the scattering of the points around a straight-line relationship.

The measurements and the best-fit trends with $\log(R/R_{\rm eff})$ are presented together in Fig. 3.7, along with the predictions of some reference stellar population models.

Summary

In conclusion, it is clear that several of the measured spectral features derived from our sample vary in strength with radius when averaged over the sample. This demonstrates that the stellar populations in these galaxies (again, averaged over the sample) are systematically different in the cores of the galaxies from those at the effective radius.

In the next chapter we will quantify these differences by employing the stellar population fitting methods outlined in Chapter 2. We will analyse our data using our model parameter fitting code in two complementary ways. First, we will use the measurements from the stacked spectra in conjunction with the models to infer the average radial behaviour of the stellar populations in our sample of massive ETGs. Secondly, for a subset of our sample of galaxies, we will fit the strength of the measured absorption features in the three inner radial bins where the S/N is sufficiently high. We aim to use these two approaches in tandem to characterise the average and individual stellar populations of these galaxies. By this means we aim to infer how the properties of their stellar populations vary with radius on average and also how much variance there is in these radial trends.

Chapter 4

KINETyS: Stellar population gradients

Preamble

In Chapter 3 we presented empirical spectroscopic measurements for the KINETyS sample of eight nearby massive ETGs. We quantified the strengths of a variety of spectral features and reported the average radial variation of these features in our sample galaxies. In this chapter we build on this work, presenting stellar population modelling of the data presented in the previous chapter using a version of the SPINDRIFT code introduced in Chapter 2.

In Section 4.1 we describe our modelling decisions and assumptions. In Section 4.2 we present the results of modelling the data. In Section 4.3 we discuss the interpretation of these results and we present our conclusions in Section 4.4.

4.1 Model fitting to the measured index strengths

The general procedure we have used for fitting SSP models to the data – a Markov-Chain Monte-Carlo (MCMC) method – has been described in Chapter 2, along with our specific implementation of this method, the SPINDRIFT code. In this section we outline our modelling choices specific to the analysis in this chapter, namely the probablistic prior we use, the spectral features included in the fitting procedure and which stellar population parameters we include in the fit.

In order to break the degeneracies between different stellar population parameters

Table 4.1: Model parameters and upper and lower cutoffs for the imposed priors.

Model Parameter	Minimum value	Maximum value
$[\alpha/\mathrm{H}]$	–0.4	0.7
$[\mathrm{Fe/H}]$	–0.5	0.4
$\mathrm{f_{dwarf}}$	4.3%	30.0%
$[\mathrm{Na/H}]$	–1.3	1.3
$[\mathrm{Ca}/\alpha]$	–0.9	0.2
$[\mathrm{K/H}]$	–1.3	1.3

more effectively, we make use of some archival optical line strength maps for the Mgb, Hβ, and Fe 5015 indices in addition to the infrared spectroscopic data presented in Chapter 3. These line strength maps were made available by McDermid et al. (2015) as part of the ATLAS^{3D} survey (which includes all of our sample, except NGC 1407). The optical features collectively act as powerful constraints on [α/H], [Fe/H], and stellar population age, all of which are key parameters in the CvD models. Using the 2D line-strength maps allows us to carefully choose appropriate radial extraction regions to match our own data.

In addition to the optical measurements derived for individual galaxies, we estimated complementary measurements for the stacked spectra. For the central radial extraction region we used the median optical measurement, inflating the measurement uncertainty to the uncertainty of the next most central radial bin to compensate for any aperture mismatch. In the other radial extraction regions we measured the ratio of the line strengths with the central line strengths and applied the median *ratio* with the central estimate to create estimates for the other radii (in an analogous way to our procedure for creating the stacked infrared spectra).

Our model is parameterised principally by [α/H], [Fe/H], [Na/H], [Ca/H], [K/H], and $\mathrm{f_{dwarf}}$ (a parameter that expresses variations in the low-mass end of the IMF, as described in Section 2.4). Given that Ca is already accounted for in [α/H], fitting for [Ca/H] in fact reduces to fitting for [Ca/α]. The priors imposed on these parameters are uniform (uninformative) within some plausible range, outside which they cut off sharply. Details are given in Table 4.1.

Each MCMC run in the analysis consisted of 100 ‘walkers’ exploring the posterior

probability distribution over 5000 steps. The first 200 of these steps were discarded in order to remove the 'burn-in' stage, during which the walkers move into the equilibrium distribution.

4.2 Results of the analysis

We now present the results of our analysis both for the stacked spectra described in Section 3.3 and five individual galaxies (NGC 0524, NGC 3377, NGC 4552, NGC 4621, and NGC 5813). These individual galaxies have a full set of (non-AGN contaminated) optical, IZ, and YJ data.

In Figure 4.1 we display some example output from our method, indicating the parameter covariances derived from our method for three stacked spectra (innermost three extraction radii).

Our results are shown in Figure 4.2. We are able to demonstrate the existence of chemical abundance gradients as expected and, moreover, show that these gradients are rather uniform between galaxies, even though those galaxies have disparate central chemical abundance patterns. The stacked spectra appear to represent this behaviour well: the parameters inferred appear to be close to the average in the inner three radial bins and the gradients in the stack appear similar to those in individual galaxies. We infer a strong metallicity gradient with [α/H] falling by $\sim$0.2 per decade in R/R$_{\rm eff}$. [α/Fe] appears to be constant with radius ($\sim +0.35$) and Ca appears to track Fe rather than the other α-elements, with [Ca/α] roughly constant at –0.35. Meanwhile, [Na/H] exhibits an extremely strong radial gradient, the steepness of which is remarkably consistent between galaxies.

By contrast, the radial behaviour of the IMF which we infer appears to be complex. From the stacked spectra, we infer an IMF which is moderately bottom heavy (corresponding to a Salpeter IMF) and roughly constant with radius. The individual galaxies however exhibit a wide variety of radial IMF trends; some we infer to host extremely bottom-heavy IMFs while others are more consistent with Salpeter in the core. In some galaxies there is evidence of radial variation, but this is by no means true in all cases.

Our full results for individual galaxies are given in Tables 4.2, 4.3, and 4.4. Results

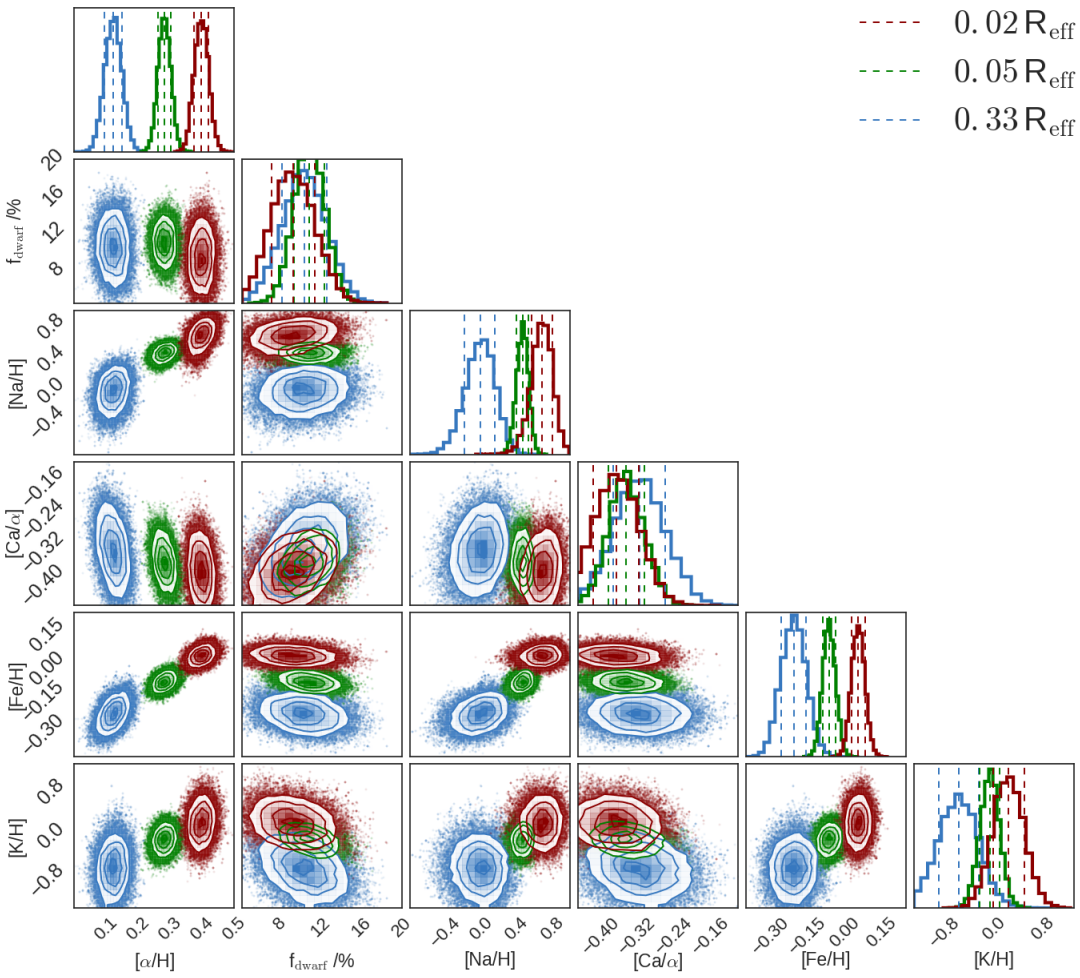

Figure 4.1: MCMC output for the stacked spectra at three different radii (the two outermost stacks have been omitted for clarity). The 1D distributions are plotted along the diagonal, with the vertical dashed lines showing the 16^{th}, 50^{th}, and 84^{th} percentiles. The 2D (covariance) distributions are also plotted, with contours at $\frac{1}{2}\sigma$ intervals. The radial changes in chemical abundance are clearly visible and well constrained in most cases. The [Ca/α] ratio appears to be constant and nor do we see a radial gradient in the IMF (parameterised by f_{dwarf}).

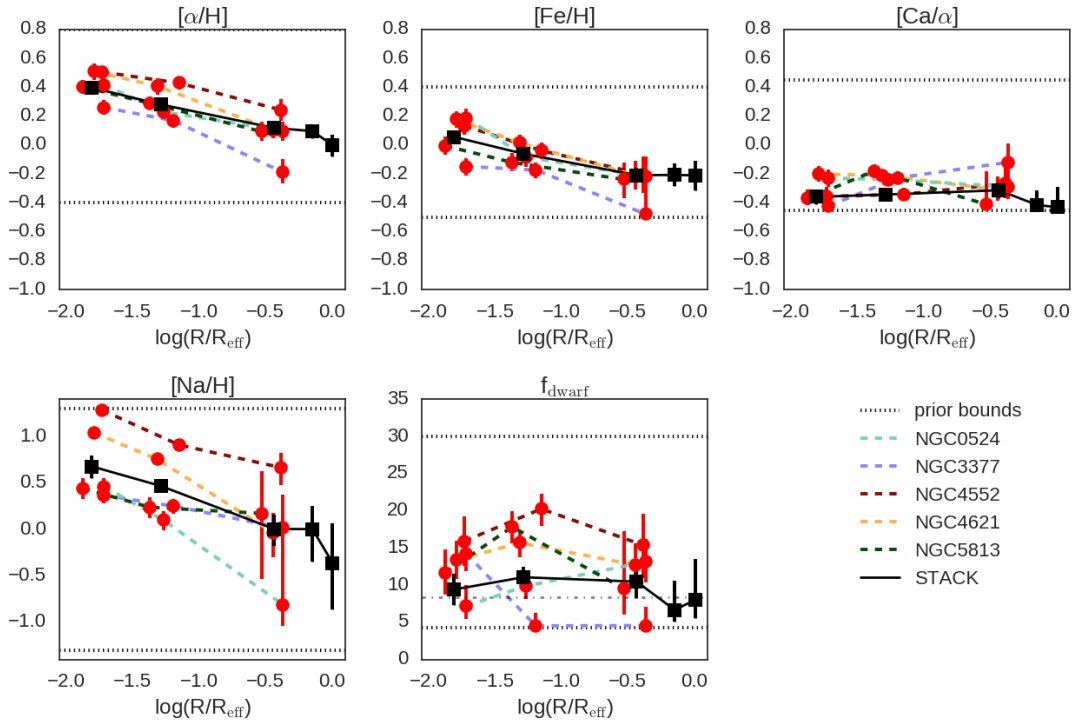

Figure 4.2: Results of parameter estimation for five galaxies (red points) with IZ and YJ band data and ATLAS^{3D} optical data at three different radial extraction regions (in which S/N is sufficient for parameter estimation). Also shown are the results derived from the stacked spectra (black squares) at five different radii. The log-radial chemical abundance gradients appear rather uniform, while there is some diversity for f_{dwarf}. The dotted horizontal lines indicate the prior constraints on the model parameters, while the dash-dotted line on the f_{dwarf} panel displays the particular case, for reference, of a constant IMF with the Salpeter slope.

Table 4.2: Model parameters and best fit values ($R < 0.02\,R_{eff}$), and reduced χ^2 of each fit.

Galaxy	$[\alpha/H]$	$[Fe/H]$	f_{dwarf}	$[Na/H]$	$[Ca/\alpha]$	red. χ^2
NGC 0524	$0.42^{+0.05}_{-0.05}$	$0.19^{+0.06}_{-0.07}$	$7.2^{+2.9}_{-1.8}$	$0.46^{+0.09}_{-0.11}$	$-0.23^{+0.06}_{-0.06}$	3.22
NGC 3377	$0.26^{+0.05}_{-0.05}$	$-0.15^{+0.06}_{-0.06}$	$14.2^{+2.4}_{-2.3}$	$0.37^{+0.09}_{-0.09}$	$-0.42^{+0.05}_{-0.02}$	6.21
NGC 4552	$0.50^{+0.04}_{-0.05}$	$0.13^{+0.05}_{-0.06}$	$15.9^{+3.3}_{-3.4}$	$1.28^{+0.01}_{-0.07}$	$-0.36^{+0.07}_{-0.05}$	8.03
NGC 4621	$0.51^{+0.06}_{-0.06}$	$0.18^{+0.06}_{-0.06}$	$13.4^{+2.6}_{-2.6}$	$1.04^{+0.04}_{-0.05}$	$-0.20^{+0.06}_{-0.05}$	9.34
NGC 5813	$0.40^{+0.05}_{-0.05}$	$-0.01^{+0.06}_{-0.06}$	$11.7^{+3.2}_{-2.9}$	$0.44^{+0.10}_{-0.11}$	$-0.37^{+0.05}_{-0.05}$	3.82

Table 4.3: Model parameters and best fit values (R = 0.02–0.05 R_{eff}), and reduced χ^2 of each fit.

Galaxy	$[\alpha/H]$	$[Fe/H]$	f_{dwarf}	$[Na/H]$	$[Ca/\alpha]$	red. χ^2
NGC 0524	$0.23^{+0.04}_{-0.04}$	$-0.08^{+0.06}_{-0.07}$	$9.9^{+1.7}_{-1.7}$	$0.10^{+0.09}_{-0.11}$	$-0.24^{+0.05}_{-0.04}$	2.93
NGC 3377	$0.17^{+0.06}_{-0.05}$	$-0.17^{+0.05}_{-0.06}$	$4.5^{+1.7}_{-0.2}$	$0.25^{+0.08}_{-0.09}$	$-0.23^{+0.05}_{-0.05}$	16.30
NGC 4552	$0.43^{+0.04}_{-0.04}$	$-0.04^{+0.06}_{-0.06}$	$20.3^{+2.1}_{-2.3}$	$0.91^{+0.05}_{-0.05}$	$-0.34^{+0.04}_{-0.04}$	8.54
NGC 4621	$0.41^{+0.05}_{-0.06}$	$0.01^{+0.05}_{-0.06}$	$15.7^{+1.7}_{-1.9}$	$0.75^{+0.04}_{-0.06}$	$-0.21^{+0.04}_{-0.05}$	11.2
NGC 5813	$0.29^{+0.05}_{-0.04}$	$-0.12^{+0.06}_{-0.06}$	$17.8^{+2.1}_{-2.2}$	$0.24^{+0.11}_{-0.11}$	$-0.18^{+0.04}_{-0.05}$	1.29

for the stacked spectra are given in Table 4.5. For the stacked spectra, we also derive the best-fitting parameter gradients, e.g. $\Delta[\alpha/H]/\Delta\log(R/R_{eff})$; these are also given in Table 4.5.

Figure 4.3 shows the level of agreement between the best fit model and the feature strengths derived from the stacked spectra. We also show the predictions of the model for the data which were not used to directly constrain the fit (Hβ and the Al I 1.31 µm doublet). Figure 4.4 is related, showing the outcome of the modelling process projected onto index-index space (i.e. the distributions of index strengths corresponding to the distributions of parameter values) alongside the data for the three innermost stacked spectra. We now discuss a few salient features included in these plots.

Table 4.4: Model parameters and best fit values (R = $\frac{1}{3}$ R_{eff}), and reduced χ^2 of each fit.

Galaxy	$[\alpha/H]$	$[Fe/H]$	f_{dwarf}	$[Na/H]$	$[Ca/\alpha]$	red. χ^2
NGC 0524	$0.10^{+0.06}_{-0.07}$	$-0.22^{+0.14}_{-0.12}$	$13.1^{+3.0}_{-2.8}$	$-0.81^{+0.34}_{-0.23}$	$-0.29^{+0.11}_{-0.09}$	3.98
NGC 3377	$-0.19^{+0.09}_{-0.08}$	$-0.48^{+0.14}_{-0.02}$	$4.6^{+2.5}_{-0.2}$	$0.01^{+0.36}_{-0.49}$	$-0.12^{+0.13}_{-0.15}$	1.18
NGC 4552	$0.24^{+0.07}_{-0.07}$	$-0.20^{+0.12}_{-0.13}$	$15.4^{+4.3}_{-4.4}$	$0.66^{+0.16}_{-0.19}$	$-0.27^{+0.12}_{-0.10}$	1.31
NGC 4621	$0.1^{+0.06}_{-0.06}$	$-0.21^{+0.1}_{-0.1}$	$12.7^{+3.0}_{-3.0}$	$-0.04^{+0.21}_{-0.27}$	$-0.31^{+0.09}_{-0.08}$	3.36
NGC 5813	$0.09^{+0.07}_{-0.06}$	$-0.24^{+0.12}_{-0.13}$	$9.5^{+7.7}_{-3.4}$	$0.17^{+0.45}_{-0.71}$	$-0.41^{+0.23}_{-0.03}$	0.32

Table 4.5: Model parameters and best fit values for stacked spectra at five radii. Gradients are calculated per decade in log(R/R_{eff}).

	$[\alpha/H]$	$[Fe/H]$	f_{dwarf}	$[Na/H]$	$[Ca/\alpha]$	red. χ^2
$< 0.02\,R_{eff}$	$0.40^{+0.02}_{-0.02}$	$0.06^{+0.03}_{-0.03}$	$9.4^{+2.1}_{-2.1}$	$0.68^{+0.12}_{-0.12}$	$-0.36^{+0.05}_{-0.05}$	0.84
0.02–0.05 R_{eff}	$0.28^{+0.02}_{-0.02}$	$-0.06^{+0.03}_{-0.03}$	$11.1^{+1.5}_{-1.5}$	$0.47^{+0.07}_{-0.07}$	$-0.34^{+0.04}_{-0.04}$	2.00
$\frac{1}{3}$ R_{eff}	$0.12^{+0.03}_{-0.03}$	$-0.21^{+0.05}_{-0.05}$	$10.5^{+2.1}_{-2.2}$	$0.00^{+0.15}_{-0.18}$	$-0.31^{+0.06}_{-0.06}$	1.54
$\frac{2}{3}$ R_{eff}	$0.10^{+0.05}_{-0.05}$	$-0.21^{+0.08}_{-0.08}$	$6.7^{+3.9}_{-1.6}$	$0.00^{+0.24}_{-0.35}$	$-0.41^{+0.10}_{-0.02}$	0.35
R_{eff}	$0.00^{+0.07}_{-0.08}$	$-0.21^{+0.10}_{-0.10}$	$8.0^{+5.6}_{-2.5}$	$-0.36^{+0.43}_{-0.5}$	$-0.43^{+0.14}_{-0.01}$	0.91
gradients	-0.20 ± 0.01	-0.17 ± 0.02	-0.6 ± 0.8	-0.48 ± 0.07	0.00 ± 0.04	

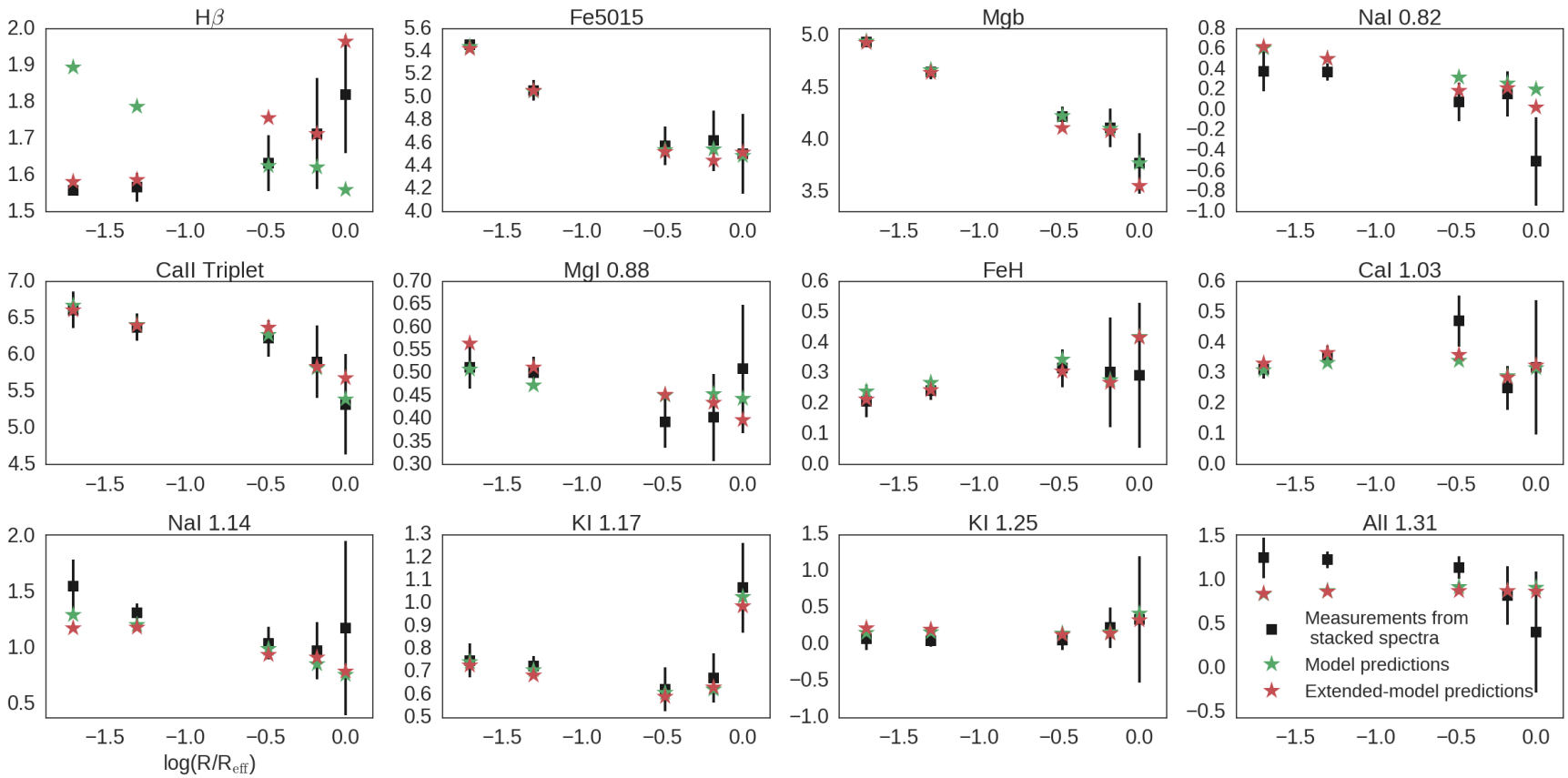

Figure 4.3: The results from the fitting procedure applied to the stacked spectra, projected onto the data (black points: equivalent width measurements from the stacked spectra, corrected to 230 kms^{-1}. A green star has been used for the model predictions, while the red stars are the predictions from a different version of the model with additional parameters log(Age) and [C/H]. These allow Hβ to be adequately fit but do not substantially improve the fit to the other lines. The Al I 1.31µm feature was not included in the fit but can be compared with the predictions of the models.

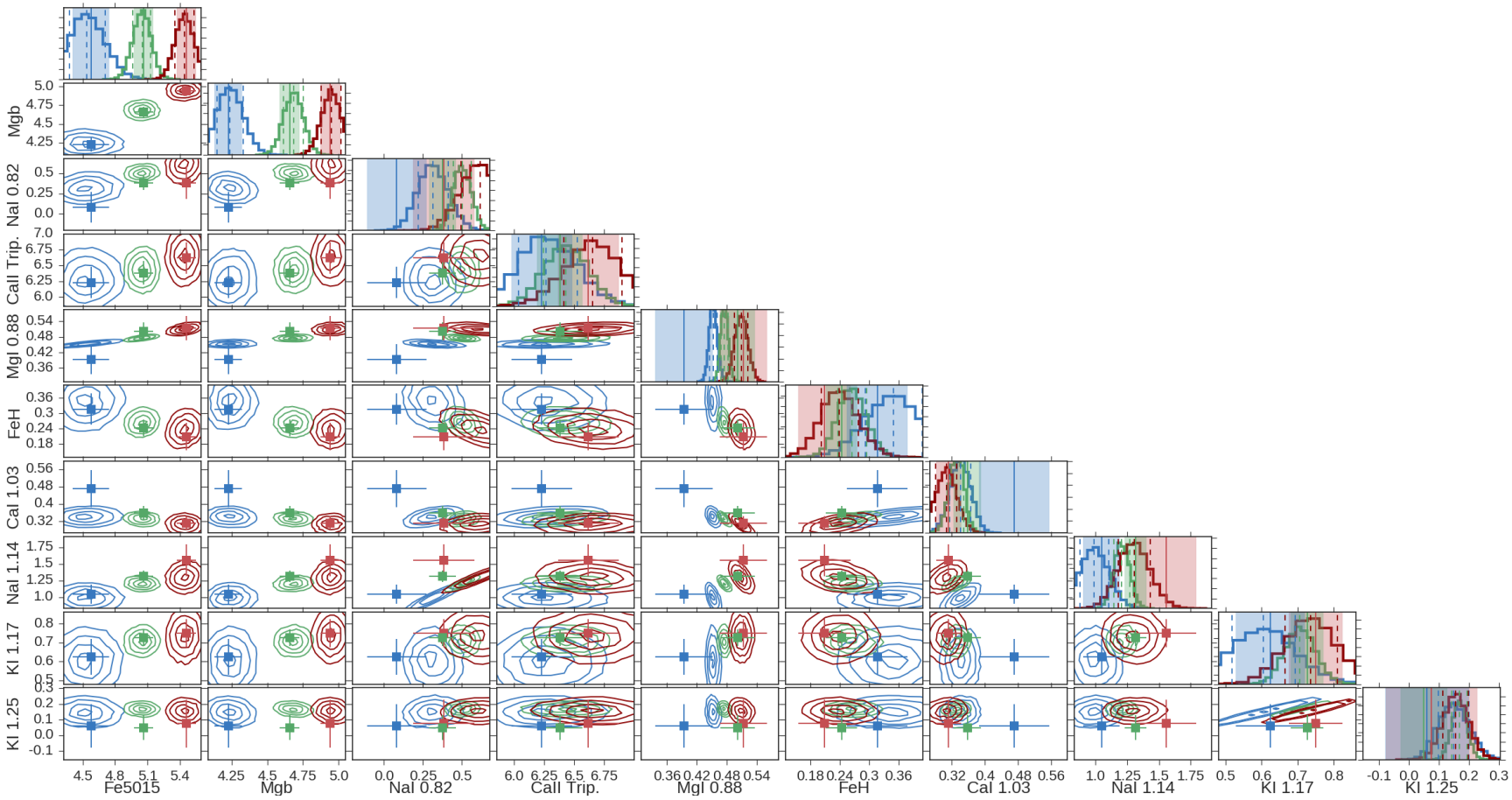

Figure 4.4: An alternative comparison of the best-fit model predictions and the measurements from the stacked data. The colour-scheme is as in Figure 4.1; contours/histograms indicate the distribution of line strengths corresponding to the MCMC parameter sampling distribution while points indicate the data for the three highest S/N stacks.

Hβ and stellar population age

In our model prescription we have mostly ignored the effects of stellar population age. NIR features have little sensitivity to this: in the SSP models the strengths of most of the absorption features we measure change by a negligible amount for populations with ages between 7 Gyr and 13.5 Gyr. Nevertheless, the inferred IMF does have a dependence on stellar population age, as detailed in Chapter 2 (dwarf stars contribute less to the total light in a younger population, since slightly higher mass stars will remain on the main sequence). The optical line strengths we use to constrain [α/H] and [Fe/H] are also sensitive to age.

However, the optical line strength maps reveal that the stellar populations in our sample are – as expected for massive ETGs – uniformly extremely old ($\sim$ 13.5 Gyr) in their cores. In most of these, the Hβ line is weaker than can be readily accounted for within the CvD model grid using the parameters discussed so far. This discrepancy can be reconciled (at the 1σ level) by a fairly large enhancement to [C/H], an additional parameter to which our other indices are insensitive. Such an enhancement may not be unexpected, e.g. see Johansson et al. (2012), in which galaxies comparable to our sample typically exhibited [C/Fe] = 0.1–0.4, but note that in that work the models used predict Hβ to be insensitive to [C/H] (Thomas et al., 2011a). This method of reconciling the discrepancy means that while Hβ can be adequately recovered by the models, doing so requires us to fit for two additional parameters; the consequence is that, without additional constraints on [C/H], stellar age is not well constrained. The results of this test are given in Table 4.6, which shows that marginalising over these two additional parameters affects our results by less than the statistical uncertainties. The predictions of this model with extra freedom are shown in Fig. 4.3 alongside those of the standard model.

Sodium lines

A consideration of the fits to the Na I features makes clear that the best-fit value of [Na/H] is a compromise between the two, with the solution predicting stronger Na I 0.82μm than is observed and weaker Na I 1.14μm. However, the line strength *gradient* appears to be consistent with the gradient in the model predictions in both cases, indicating that there

Table 4.6: Model parameters and best fit values for stacked spectra at five radii, after marginalising over log(Age) and [C/H]. Gradients are calculated per decade in log(R/$R_{\rm eff}$).

	$[\alpha/{\rm H}]$	$[{\rm Fe/H}]$	$f_{\rm dwarf}$	$[{\rm Na/H}]$	$[{\rm Ca}/\alpha]$	red. χ^2
$< 0.02\,R_{\rm eff}$	$0.39^{+0.03}_{-0.03}$	$0.14^{+0.03}_{-0.05}$	$8.1^{+2.4}_{-1.9}$	$0.64^{+0.13}_{-0.12}$	$-0.40^{+0.06}_{-0.03}$	2.30
0.02–$0.05\,R_{\rm eff}$	$0.30^{+0.02}_{-0.03}$	$0.03^{+0.03}_{-0.04}$	$11.8^{+2.5}_{-1.6}$	$0.51^{+0.05}_{-0.08}$	$-0.34^{+0.04}_{-0.04}$	3.31
$\frac{1}{3}\,R_{\rm eff}$	$0.16^{+0.03}_{-0.04}$	$-0.13^{+0.05}_{-0.08}$	$11.0^{+4.0}_{-2.5}$	$0.07^{+0.14}_{-0.20}$	$-0.31^{+0.06}_{-0.06}$	2.63
$\frac{2}{3}\,R_{\rm eff}$	$0.11^{+0.06}_{-0.05}$	$-0.23^{+0.11}_{-0.08}$	$7.0^{+4.9}_{-1.8}$	$0.04^{+0.23}_{-0.34}$	$-0.41^{+0.10}_{-0.03}$	0.29
$R_{\rm eff}$	$0.03^{+0.08}_{-0.07}$	$-0.18^{+0.1}_{-0.13}$	$7.8^{+7.8}_{-2.3}$	$-0.26^{+0.42}_{-0.51}$	$-0.39^{+0.12}_{-0.04}$	1.57
gradients	-0.18 ± 0.01	-0.20 ± 0.03	0.3 ± 1.5	-0.43 ± 0.06	0.01 ± 0.02	

may be a systematic offset in the strength of one or both lines in the models (consistent with the findings of Smith et al., 2015a) or in the data. This is shown more clearly in the panel of Fig. 4.4 depicting the joint distribution of model predictions for the two indices, where there is a clear offset from the data.

We find that removal of the Na I 0.82μm line weakens the inferred [Na/H] gradient slightly (-0.46 ± 0.07), but by less than the 1σ uncertainty. However, the inferred absolute value of [Na/H] is stronger by 0.14 for the central spectrum. Removing the Na I 1.14μm line also weakens the inferred [Na/H] gradient slightly (-0.49 ± 0.07); again, by less than the 1σ uncertainty. The inferred absolute value of [Na/H] weakens by 0.09 for the central spectrum.

Wing-Ford band

The rather flat radial behaviour of the Wing-Ford band's strength, alongside its weak absolute strength relative to the fiducial CvD model throughout our sample, adds considerable weight to our results. It is hard to reproduce this behaviour if there are strong IMF variations, given other constraints on [Na/H] (the effect of which on the Wing-Ford band is discussed in Section 4.3). Nevertheless, removing it from the fit does not qualitatively change the outcome of the analysis: we still recover a radially flat $f_{\rm dwarf}$ with $f_{\rm dwarf} = 9.9^{+2.5}_{-2.1}\%$ in the innermost stack. The [Na/H] gradient steepens slightly (-0.57 ± 0.11), but

by less than the 1σ uncertainty, while the inferred absolute value of [Na/H] decreases by 0.12 for the central spectrum.

Potassium lines

In practice, because an enhancement of [α/H] ensures that the K I 1.25μm line becomes extremely weak in the CvD models, we find that including it in our analysis has no substantive effect. This is unfortunate, since the combination of two K I features ought to have allowed us to constrain [K/H] while providing additional constraints on the IMF. In reality, [K/H] is effectively constrained only by K I 1.17μm in the high S/N spectra – and even then, only loosely; e.g. in the stacked spectra from the two innermost regions we fit [K/H] = $-0.12^{+0.25}_{-0.25}$ and $-0.07^{+0.16}_{-0.16}$ Given the uncertainties and because no additional information about the IMF is carried, we cannot conclude much of interest about the behaviour of [K/H] and do not present it in our headline results.

We find that removing the K features and the [K/H] parameter from the fit has a negligible effect on the other parameters.

Al I 1.31μm

The CvD models do not currently incorporate an [Al/H] parameter, so as discussed in Section 3.3 we chose not to try and fit this line. However, while the data at the effective radius are consistent with the predictions of our best-fit model, those in the core are in significant tension. At face value this indicates enhanced [Al/H] in the core regions of our sample.

4.2.1 Other model parameters

Including other parameters in the model than those already discussed does not produce a significantly better fit to the data. However, it is important to consider the possible effects of certain 'nuisance parameters', which, when marginalised over, may alter the preferred values and uncertainties of the parameters of interest. For this reason we re-analysed our data with two additional parameters included in the model.

The revised CvD models include an 'effective temperature' ($T_{\rm eff}$) parameter which

encapsulates a shift in the (solar metallicity) isochrones they use. Such shifts can occur given changes in total metallicity, or simply due to uncertainty in the fundamental calibration of the stellar models. For example, Spiniello et al. (2015b) found marginal evidence that in ETGs comparable to our sample the isochrones were shifted to lower effective temperature (–50±30 K).

It is important to consider whether α-element abundances which are not directly constrained from the data track Mg abundance (as expected). The CvD models allow for simultaneous variation of O, Ne, and S abundances to test this scenario, so we can include in our model a variable [O,Ne,S/α] parameter.

These parameters are, as expected, not well constrained by the data. In the stacked spectra we find little evidence for a gradient in $T_{\rm eff}$ (preferred gradient 19±64K) and find $T_{\rm eff}$ = $+58^{+62}_{-51}$K in the central stack. For [O,Ne,S/α] we find $0.32^{+0.23}_{-0.32}$ in the central stack and a gradient of –0.33±0.05. This result is driven by the weakness of the K I 1.25μm line, the only feature with measurable sensitivity to the [O,Ne,S/α] parameter. The extremely high value inferred is likely non-physical, but does not affect the other spectral features.

Marginalising over these two additional parameters alters the preferred values of the parameters of interest at a fairly minor level, the details of which are contained in Table 4.7. In summary: the inferred values for [α/H] and [Fe/H] are not significantly changed; the inferred gradients for [Na/H] and [Ca/α] are also not significantly changed, however the absolute values for these parameters are reduced by ~ 0.1 and ~ 0.05 respectively; we infer a slightly negative $f_{\rm dwarf}$ gradient of –2.6±1.1%. These changes are driven by the $T_{\rm eff}$ parameter, with [O,Ne,S/α] variations proving inconsequential. A positive $T_{\rm eff}$ weakens the Wing-Ford band slightly, allowing the model freedom to return a combination of lower [Na/H] enhancements and higher $f_{\rm dwarf}$.

4.3 Discussion

We have measured average line strength gradients for a stacked sample of eight ETGs. We have investigated nine infrared spectral features, most notably finding a strong radial gradient in the strength of the Na I 1.14μm doublet and no significant gradient in the

Table 4.7: Model parameters and best fit values for stacked spectra at five radii, after marginalising over T_{eff} and [O,Ne,S/α]. Gradients are calculated per decade in log(R/R_{eff}).

	$[\alpha/H]$	[Fe/H]	f_{dwarf}	[Na/H]	$[Ca/\alpha]$	red. χ^2
$< 0.02\,R_{eff}$	$0.41^{+0.03}_{-0.03}$	$0.04^{+0.03}_{-0.03}$	$11.9^{+4.3}_{-3.6}$	$0.65^{+0.12}_{-0.18}$	$-0.40^{+0.07}_{-0.03}$	1.49
0.02–0.05 R_{eff}	$0.30^{+0.02}_{-0.02}$	$-0.06^{+0.03}_{-0.03}$	$14.7^{+3.6}_{-3.7}$	$0.37^{+0.10}_{-0.11}$	$-0.37^{+0.05}_{-0.04}$	3.24
$\frac{1}{3}\,R_{eff}$	$0.14^{+0.04}_{-0.04}$	$-0.22^{+0.05}_{-0.05}$	$12.1^{+5.3}_{-4.5}$	$-0.09^{+0.24}_{-0.26}$	$-0.36^{+0.08}_{-0.06}$	3.07
$\frac{2}{3}\,R_{eff}$	$0.09^{+0.05}_{-0.06}$	$-0.22^{+0.08}_{-0.08}$	$6.8^{+5.5}_{-1.7}$	$0.03^{+0.24}_{-0.39}$	$-0.43^{+0.12}_{-0.01}$	0.37
R_{eff}	$0.01^{+0.08}_{-0.08}$	$-0.24^{+0.11}_{-0.1}$	$7.7^{+7.7}_{-2.3}$	$-0.39^{+0.45}_{-0.5}$	$-0.43^{+0.14}_{-0.01}$	1.63
gradients	-0.20 ± 0.01	-0.17 ± 0.02	-2.9 ± 1.1	-0.46 ± 0.08	0.00 ± 0.03	

strength of the Wing-Ford molecular band. At an empirical level this is in agreement with the line strength gradients in the samples measured by McConnell et al. (2016) and La Barbera et al. (2016). McConnell et al. argue, through qualitative reference to the CvD models, that the observed gradients are best explained by a large [Na/H] enhancement in the core, rather than by a bottom-heavy IMF concentrated in the core. Our quantitative analysis of the line strengths in the context of the CvD models is in agreement with this, finding evidence for at most only modest radial IMF variation (Chabrier at the effective radius, Salpeter in the innermost region) on average. However, we find that the IMFs of these galaxies are in general bottom-heavy and find evidence for radial IMF variations in some *individual* galaxies.

By contrast, La Barbera et al. (2016) find that their measurements are best accounted for by an IMF gradient, but only if the IMF strongly deviates from a single power law functional form. This is motivated by the measured absence of a radial gradient in the strength of the Wing-Ford band (which we also find) in concert with their measurements of gradients for two TiO indices. A broken power law can reproduce this since these TiO features and the Wing-Ford band are strongest in stars with different ranges of stellar masses ($\lesssim 0.3\,M_\odot$ for the Wing-Ford band, $\sim 0.6\,M_\odot$ for the TiO features). We note that, unlike TiO, the Na I 1.14μm feature and the Wing-Ford band are both selectively sensitive to stars of similar masses (Rayner et al., 2009), so large deviations from a single power

law for the IMF functional form are not a good explanation for our results. Rather, the relative weakness of the Wing-Ford band in the central regions of our sample, despite the enhanced [Fe/H], can best be explained by the high sodium enrichment there (a possibility not accounted for in the method of La Barbera et al.), since Na is an electron donor and promotes the dissociation of the FeH molecule.

The index gradients we measure are also qualitatively similar to those measured in M31 by Zieleniewski et al. (2015). Whilst the authors do not explicitly calculate gradients, they find the Wing-Ford band does not vary in strength significantly with radius in M31. Meanwhile, a steep Na I 0.82μm gradient is measured within the central $\sim 40''$(corresponding to $< 0.1\,R_{\rm eff}$ in our sample). The authors show that a consideration of these two features with respect to the CvD12a model grid favours no deviation from a Milky-Way-like IMF throughout the galaxy, with an enhancement of +0.7 in [Na/H] in the core relative to the disc. In CvD12b a spectral fit indicated an only moderately bottom-heavy IMF in the bulge of M31, which was in fact consistent with the results of Zieleniewski et al. The gradients we measure in ETGs are hence at least qualitatively similar to those measured in a galaxy not thought to host a stellar population formed according to a notably bottom-heavy IMF.

A number of other works have recently been published on the subject of radial IMF gradients in addition to those already mentioned. van Dokkum et al. (2016) find evidence for strong radial IMF variations in some members of a sample of six galaxies. By contrast, Vaughan et al. (2016) (two galaxies) and Zieleniewski et al. (2017) (three galaxies) do not find clear evidence for variations.

Regardless of the variation of the IMF, our results indicate a radial variation in sodium abundance ([Na/H]). The absolute strength of the Na I 1.14μm feature is very high in the central extraction region and in tension with the absolute strength of the 0.82μm feature. This is similar to the result reported in Smith et al. (2015a) in which this feature was found to be stronger than expected given other constraints on stellar populations. Additionally, as shown in the same work there is a weak sodium line at 1.27μm, which becomes visible only in model spectra with very high [Na/H] and which is rather insensitive to the IMF (in contrast to the 0.82μm and 1.14μm lines). This feature is clearly visible in our stacked galaxy core spectra. For this line we define an absorption index with blue continuum

12655–12665Å, red continuum 12705–12715Å, and feature band 12675-12690Å. Under this definition the fiducial SSP model predicts an equivalent width of 0.14Å, while an extremely sodium enhanced model ([Na/H] = +0.9) instead predicts 0.27Å. By contrast, even for an X = 3 power law IMF the line's strength is only 0.17Å. Notably, we measure an equivalent width of 0.33± 0.08Å in the innermost stacked spectrum. The line is however in a region of particularly strong atmospheric absorption, which becomes prohibitive in the outer rings. Though we do not, therefore, include this feature in our quantitative analysis, it appears to support extreme sodium abundances of [Na/H] $>$ +0.9 in the core and is consistent with the [Na/H] we infer from other lines.

The Al I 1.31 μm line has not been studied in ETGs before. Like Na I 1.14 μm it is dramatically stronger than in the models in the cores of our sample of galaxies and cannot be matched even by SSP models with very bottom-heavy IMFs. We note that the galaxies with strong Al I 1.31 μm features in their core spectra are generally the ones with strong Na I 1.14 μm features too. Interestingly, sodium and aluminium have closely related formation channels (see Lecureur et al., 2007, and references therein). These elements are unusual in having strongly metallicity-dependent Type II SNe yields (Kobayashi et al., 2006). The Al I 1.31 μm and Na I 1.14 μm features are both sensitive to IMF (in the same sense), but probe slightly different stellar mass ranges (Rayner et al., 2009; Conroy & van Dokkum, 2012a): a steeper low-mass slope has a larger effect on the sodium feature's strength than it does on the aluminium feature, which is chiefly sensitive to 0.4–0.7 $M_{\odot}$ stars. The extreme strength of the Al I 1.31 μm feature therefore may be interpreted as further anecdotal support for the hypothesis that chemical abundance effects are the dominant cause of the measured radial variation in absorption feature strengths in ETGs.

Radial gradients in the relative contribution of dwarf stars to the integrated light of ETGs are motivated by a combination of observations and theory, as discussed in the Introduction. Spectroscopy of the cores of ETGs has indicated that the IMF is bottom-heavy in the most massive systems and Milky-Way-like in less massive galaxies; this is supported by measurements of the M/L ratio for these systems via dynamics and lensing. In our work we replicate these results using a set of infrared spectral indices, some of which are not heretofore well-studied in ETGs. Yet our current understanding of the formation of the most massive ETGs is that their outer regions are assembled by accretion

of lower mass galaxies through minor mergers, which is required to explain their evolution in size for $z < 2$ (e.g. Bezanson et al., 2009, Hopkins et al., 2009, Hopkins et al., 2010) and supported by simulations (e.g. Oser et al., 2010, Oser et al., 2012, Hilz et al., 2013). These merging systems presumably contain stars which formed according to a Milky-Way-like IMF, and they are expected to be deposited at around the effective radius, so this type of growth should lead to a radial gradient in the population dwarf fraction (note, however, that it is believed that ETGs that are slow rotators – there are several in our sample – are more likely to have undergone recent major mergers; see Bois et al., 2010, Khochfar et al., 2011, and Naab et al., 2014. These events are much more disruptive. We do not, however, see a clear dichotomy between fast and slow rotators in our results).

Our work suggests that radial IMF variations in ETGs are on the whole rather gentle, even in those galaxies for which we infer very bottom-heavy central IMFs. In the case of those individual galaxies in our sample for which we are able to make robust estimates of the IMF, most are at least marginally consistent with a non-radially varying IMF. The average behaviour (as probed via the stacked spectra) of our entire sample tracks this, being consistent with a modestly bottom-heavy IMF with a slope slightly steeper than Salpeter at all radii. Within the 'inside-out' paradigm of galaxy formation, this would suggest that minor mergers deposit stellar mass largely beyond the effective radius. This possibility has some observational support, with Coccato et al. (2010) arguing that spectroscopy of the very massive galaxy NGC 4889 ($\sigma \sim 300\,\mathrm{kms}^{-1}$) indicates the deposition of accreted mass at $\gtrsim 1.2\,R_{\mathrm{eff}}$. Meanwhile simulations present an ambiguous picture, with Rodriguez-Gomez et al. (2016) finding that the fractional radius at which accreted stars are deposited varies quite strongly with total stellar mass (being typically less than R_{eff} for the most massive ellipticals, however). The strong average line strength gradients we observe for our sample indicate that the stellar populations at R_{eff} are chemically distinct from those in the core, but do not necessarily show that they formed entirely *ex situ*: such gradients are also a consequence of monolithic collapse (see e.g. Kobayashi, 2004). A shallow IMF gradient could indicate the following: first, that the IMF is uniform within the progenitor systems that form the cores of present day ETGs (being bottom-heavy throughout) and secondly, that minor systems accreted onto this core deposit little mass inside the effective radius. Thus, our results may clarify the details of this growth channel by constraining

the radius at which most of the accreted mass is deposited.

Summary

In this chapter we have studied the spatially-resolved infrared spectra of eight nearby ETGs, extracting information about the radial variation in the strength of a variety of absorption features between 0.8 and 1.35μm, including some which have not been previously studied. These were chosen for their sensitivity to both the IMF and a variety of chemical abundances. By interpreting the strength of these features with reference to the CvD stellar population models, via our SPINDRIFT code for stellar population parameter inference, we have probed the radial variation of the stellar populations of our sample of galaxies. Our main conclusions are as follows:

1. In stacked spectra derived from our sample we measure significant negative gradients in the strengths of several IMF-sensitive features, namely the Na I 0.82 and 1.14μm features (–0.34±0.05Å and –0.40±0.05Å per decade in R/R_{eff}, respectively), the Ca II Triplet (–0.45±0.14Å), the Mg I 0.88μm line (–0.08±0.02Å) and Al I 1.31μm doublet (–0.34±0.12Å). We measure a marginal positive gradient for the Wing-Ford band (+0.06±0.04Å), while the Ca I 1.03μm line, K I 1.17μm composite feature, and the K I 1.25μm line are also consistent with no radial variation. The only IMF-sensitive features in which strong radial absorption strength gradients are found are those for which enhancing the stellar population dwarf-fraction is degenerate with enhancing the abundance of sodium or aluminium (which are formed by related nucleosynthetic mechanisms).

2. We interpret these results in terms of variations in both the dwarf star content and element abundances using state-of-the-art stellar population models and Markov-Chain Monte Carlo parameter estimation. The absorption index gradients we measure can be primarily explained by radial variations in the chemical abundance pattern of the stellar population. We infer from the stacked spectra an average sodium abundance (i.e. [Na/H]) gradient of –0.53±0.07 per decade in radius (alternatively expressed as a [Na/Fe] gradient of –0.35), leading to an enhancement

of [Na/H] $\gtrsim$ +0.7 in the core. This may be connected to the metallicity-dependent yield of sodium in Type II SNe. We infer an average gradient in the fractional contribution of dwarf stars to the luminosity, $f_{\rm dwarf}$, of –0.7$\pm$0.7% (the difference in $f_{\rm dwarf}$ between Chabrier and Salpeter is $\sim 4\%$).

3. The chemical abundance gradients for individual galaxies in our ETG sample (those with the highest quality, most comprehensive data) appear comparable to those derived from the stacked spectra. These gradients appear to be fairly uniform across the sample, even though the chemical abundances themselves vary substantially within the sample at fixed radius.

4. Our results suggest that on average the IMF in our sample galaxies is bottom-heavy out to a significant fraction of the effective radius, with little evidence for a strong gradient. There may however be significant variation in radial IMF trends between galaxies. Our results may suggest that minor mergers deposit stars largely beyond the effective radius of the present-day systems.

In the next chapter, we will present additional K-band observations of our sample. This band contains a variety of strong, gravity-sensitive absorption features associated with a variety of elements. These features are largely unexplored in recent work and, in combination with a more sophisticated model, will help us further constrain the stellar population parameters of ETGs.

Chapter 5

Investigating K-band spectral features

Preamble

In this chapter we present an extension to the KINETyS project, using measurements of several strong spectral features in the K-band to expand on the work already presented in Chapters 3 and 4. In addition to this we include infrared measurements from the central regions of a wider sample of nearby massive ETGs spanning a comparable range of wavelengths and including K-band spectroscopy.

The K-band light is dominated by the dwarf and giant stars with the coolest surface temperatures, which leads to significant IMF sensitivity in some spectroscopic features. As we demonstrated in Section 2.4, the different contribution to the K-band light of stars in particular mass ranges means that a combination of these features with those at bluer wavelengths is sensitive to the IMF shape. Regarding the other stellar population properties contained in the models, K-band features provide additional constraints on the abundance of Ca and Na, both of which have unusual abundances in massive ETGs (Ca because it is underabundant with respect to the other α-elements and Na because it is superabundant by a large factor). Finally, measurements of the strong CO bandhead at 2.30 μm allow us to break the degeneracy between stellar population age and carbon abundance described in Chapter 4.

In Section 5.1 we present the new data for the KINETyS galaxy sample and the new sample of galaxies which were observed using the Magellan-FIRE instrument. We outline the reduction procedures used in each case. In Section 5.2 we discuss how these data were

Table 5.1: Table of K-band KINETyS observations.

Name	Seeing /arcsec	observation time /s
NGC 1407	0.68–0.75	1440
NGC 3377	0.88–1.16	2880
NGC 3379	0.95–1.24	2880
NGC 4486	0.99–1.34	2880
NGC 4552	0.89–1.07	2880
NGC 4621	1.02–1.22	1440
NGC 5813	1.13–1.57	2880

processed for analysis, presenting our measurements of a variety of spectral features in Section 5.3. In Section 5.4 we give an empirical analysis of these measurements, and compare these with the predictions of the models used in Chapter 4. We defer a model-based analysis of these data to Chapter 6.

5.1 Data

5.1.1 K-band data from VLT KMOS

Observations:

Seven of the eight nearby ETGs introduced in Chapter 3 were re-observed in the K-band (1.93–2.50 μm) using the same 'sparse mosaic' observing strategy as previously described. The data were obtained between 20$^{\rm th}$ February and 8$^{\rm th}$ of August 2016 (run ID: 097.B-0882(A), PI: Alton). In the K-band, KMOS has resolving power R = 4200. For most targets we took 6×480s exposures on each pointing, resulting in a total on-source integration time of 2880s (for NGC 1407 and NGC 4621 it was only possible to take half as many exposures, for a total of 1440s on-source). The signal-to-noise ratio ranges from >200 per pixel for the innermost region of the galaxies, falling to ~ 10 at the effective radius (so those data are only useful when combined across the sample). The observations are summarised in Table 5.1.

Data reduction:

The KMOS data were reduced mostly as in Chapter 3, using a slightly modified version of the ESO standard pipeline. However, we modified the atmospheric absorption correction procedure with the MOLECFIT (v1.0.2) tool. To achieve optimal performance we separately fit the atmosphere in two wavelength ranges, 19587–21075Å and 21075–23964Å, modelling H_2O, CH_4, and CO_2 absorption. The first of these ranges contains strong, broad absorption by CO_2 which makes it difficult to fit a polynomial continuum through this range. Splitting the fit into two (largely independent) segments prevents this issue from affecting the redder part of the spectrum where most of the stellar features of interest are.

We improve our methods from Chapter 3 by characterising the variability of the atmospheric correction in each observing run, i.e. over six exposures (at each wavelength we estimate the 68% scatter between the set of six applied corrections). This likely represents an overestimate of the error (since, in reality, we expect that the atmospheric absorption profile will vary between observations, rather than differences being entirely due to observational uncertainties/scatter). Nevertheless we propagate it to later reduction steps.

As before, spectra from the same radial extraction region were, for each galaxy, combined to create a single 1D spectrum for each physical region of the galaxy probed. This was accomplished by first dividing out continuum variations, then median-stacking the spectra.

5.1.2 Magellan-FIRE data

Observations:

An additional sample of 12 early-type galaxies, eight of which were drawn from the sample of Conroy & van Dokkum (2012b) were investigated for this work using data obtained using the FIRE (Folded-port Infrared Echellette) instrument on the Magellan-Baade telescope. These data consisted of infrared spectra (0.82–2.51 μm wavelength range, spectral resolution R = 4800 ($\sim 63\,\mathrm{kms}^{-1}$), with 3×450s exposures per galaxy. The data were taken in echelle mode. Slit length was 7″, with the slit centered on the middle of the galaxy. The observations we made between 31$^{\mathrm{st}}$ March and 2$^{\mathrm{nd}}$ April 2012.

Table 5.2: List of sample galaxies and key properties. Spectra were extracted from the central 1.25″of the galaxy, so $R_{extract}$ is given here as a fraction of R_{eff}.

Name	Exposure Times	Seeing	Effective Radius	$R_{extract}$ /R_{eff}	cz /kms^{-1}	$\sigma(R_{eff}/8)$ /kms^{-1}
NGC 3608	2×450s	0.6–1.0″	29.6″	0.042	1259	193
NGC 4261	3×450s	0.6–1.0″	44.8″	0.028	2188	294
NGC 4262	3×450s	0.5″	11.6″	0.107	1349	195
NGC 4374	3×450s	0.6″	61.2″	0.020	989	288
NGC 4382	3×450s	0.5″	82.8″	0.015	749	184
NGC 4459	3×450s	0.5″	43.1″	0.029	1199	179
NGC 4472	3×450s	0.8–1.4″	104.5″	0.012	1019	288
NGC 4546	2×450s	1.0″	33.0″	0.038	1049	221
NGC 4649	3×450s	1.0–1.5″	76.6″	0.016	1109	314
NGC 4660	2×450s	0.5″	12.9″	0.097	1079	218
NGC 5838	2×450s	0.6″	23.7″	0.053	1379	276
NGC 5845	3×450s	0.5–0.6″	5.1″	0.245	1529	270

Details of the sample are given in Table 5.2. Effective radii are taken from Cappellari et al. (2013a). Velocity dispersions (within $R_{eff}/8$) are taken from Cappellari et al. (2013b).

Data reduction:

The FIRE data were reduced using the standard pipeline, FIREHOSE, with two modifications.

First, because nearby targets are being observed and the echelle slit is short, the targets fill the aperture. Thus sky subtraction requires the use of a corresponding off-source pointing. However, the bright OH sky emission lines which are plentiful in the wavelength range of these observations vary in strength between exposures. In order to mitigate this issue, we used a linear combination of pairs of sky exposures instead of individual sky

exposures. The combined raw 2D sky frame was optimised by subtracting it from the corresponding 2D source frame and minimising the residuals. The modified sky frame was then passed to FIREHOSE, which accounts for additional issues such as instrument flexure.

Secondly, the standard pipeline uses a correction for atmospheric absorption based on the work of Vacca et al. (2003), in which the observed spectrum of a standard star is modified by modelling and dividing out the intrinsic strong H absorption lines in order to create an atmospheric absorption spectrum free of underlying stellar absorption features. In practice however this modelling process is challenging; there may be unaccounted-for weak absorption in metal lines and, moreover, strong H lines are not reliably corrected for to the required precision. For these data an alternative procedure was used which operated on a similar principle to MOLECFIT.

After reducing the spectra to 1D the data were analysed using the same procedures as the KMOS spectra, as described in the next section.

5.2 Velocity dispersions and index measurements

Using the penalised pixel-fitting (pPXF) tool (Cappellari & Emsellem, 2004) we measured redshifts and velocity dispersions for the FIRE data using the strong Ca II Triplet absorption feature and surrounding spectral region (8300–9000Å in rest-frame, vacuum wavelengths). For this purpose and throughout this and following chapters we used an updated version of the set of models used in Chapter 4: hereafter references to "the CvD models" refer to this updated version (based on the updated IRTF library of Villaume et al., 2017 and described in full in van Dokkum et al., 2017). In Fig. 5.1 we show a few of these models corresponding to the K-band spectra of different stellar populations. For the KMOS data we made use of the redshifts and velocity dispersions derived in Chapter 3 (N.B. for spectra with such high intrinsic velocity dispersion the difference in instrumental broadening between bands has a negligible effect).

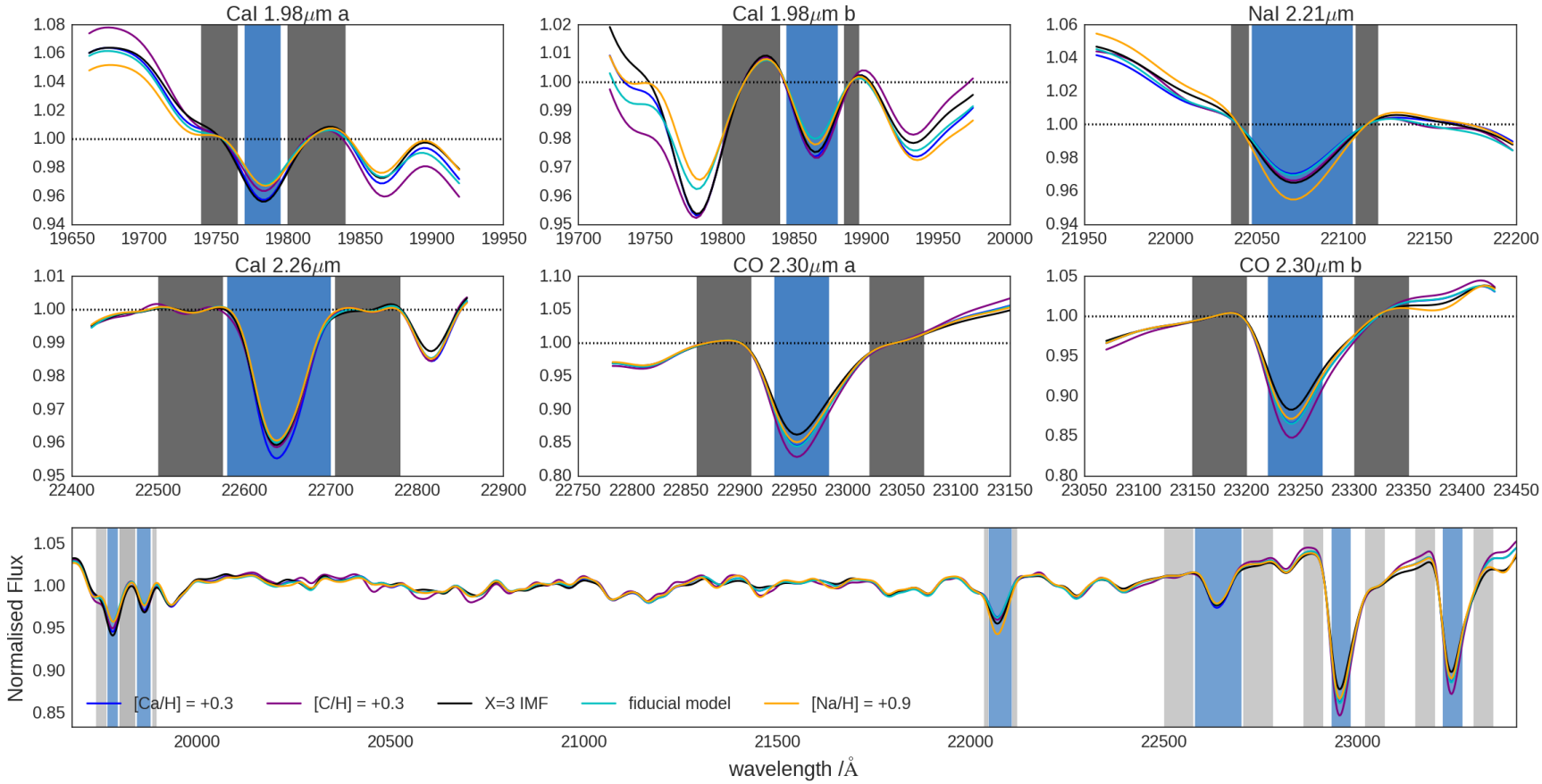

Figure 5.1: A subset of the models used in this work, indicating the effect of particularly important parameters. *Lower panel:* full models for the K-band with measured feature bands indicated in blue and associated pseudo-continuum bands in grey. *Upper panels:* close-up view of each measured feature, with the models normalised with respect to the feature pseudo-continua.

For each spectrum we measured the equivalent widths of a set of spectral indices. Table 5.3 describes all spectral features considered in this work. This set of indices includes three optical features, for which we use archival ATLAS^{3D} measurements presented in McDermid et al. (2015) – these are essential for providing good constraints on [Fe/H] and strengthen constraints on other properties. In addition, we make use of the index measurements presented in Chapter 3 and measure the same indices for the FIRE spectra (with the exception of Na I 0.82 μm, which lies beyond the FIRE wavelength range). We also measure a number of features in the K-band from both KMOS and FIRE spectra.

For each feature we used the flux uncertainties to create a set of Monte-Carlo realisations of our spectra from which the uncertainties of these index measurements could be inferred. The measured velocity dispersions were used to correct all index measurements to 230 kms^{-1}; the uncertainty on these corrections was also propagated.

5.2.1 Stacked spectra

As in earlier chapters we chose to make use of stacked spectra in our analysis. This has a number of advantages, the most important being that stacking spectra with slightly different redshifts in the source rest-frame suppresses any systematics introduced in the observed rest-frame (e.g. due to poor subtraction of sky emission lines or sub-par telluric corrections). Additionally, stacked spectra can be used to constrain the average behaviour of the sample (and, in turn, this can be used to identify unusual objects that deviate from this average).

For the FIRE data and the centrally extracted KMOS spectra, the stacking procedure was as follows: we shifted the input spectra into the rest-frame and binned them onto a common wavelength grid. We characterised the relative continuum variation by dividing each spectrum by the mean spectrum and fitting a 6^{th} order polynomial to the ratio of the two. This relative continuum variation was then divided out and the median flux at each wavelength was evaluated. Errors were created by bootstrap resampling of the input spectra (since the scatter between galaxies is larger than the statistical uncertainty on any given spectrum). Using this procedure we created three stacks: one for the seven KMOS galaxies, and a low (σ <230 kms^{-1}) and high (σ >230 kms^{-1}) velocity dispersion stack for the FIRE data. The inputs for each of the FIRE stacks comprised six galaxies.

Table 5.3: List of absorption index names and definitions (vacuum wavelength definitions, given in Å); originally from CvD12a.

Index Name	Blue continuum	Feature Definition	Red continuum	Notes
Hβ	4827.9–4847.9	4847.9–4876.6	4876.6–4891.6	ATLAS^{3D} data
Fe 5015Å	4946.5–4977.8	4977.8–5054.0	5054.0–5065.3	
Mg*b*	5142.6–5161.4	5160.1–5192.6	5191.4–5206.4	
Na I (0.82 μm)	8170.0–8177.0	8177.0–8205.0	8205.0–8215.0	KMOS only
Ca II (0.86 μm a)	8484.0–8513.0	8474.0–8484.0	8563.0–8577.0	FIRE+KMOS
Ca II (0.86 μm b)	8522.0–8562.0	8474.0–8484.0	8563.0–8577.0	
Ca II (0.86 μm c)	8642.0–8682.0	8619.0–8642.0	8700.0–8725.0	
Mg I (0.88 μm)	8801.9–8816.9	8777.4–8789.4	8847.4–8857.4	
FeH (0.99 μm)	9905.0–9935.0	9855.0–9880.0	9940.0–9970.0	
Ca I (1.03 μm)	10337–10360	10300–10320	10365–10390	
Na I (1.14 μm)	11372–11415	11340–11370	11417–11447	
K I (1.17 μm a)	11680–11705	11667–11680	11710–11750	
K I (1.17 μm b)	11765–11793	11710–11750	11793–11810	
K I (1.25 μm)	12505–12545	12460–12495	12555–12590	
Al I (1.31 μm)	13115–13165	13090–13113	13165–13175	
Ca I (1.98 μm a)	19740–19765	19770–19795	19800–19840	new KMOS data
Ca I (1.98 μm b)	19800–19840	19845–19880	19885–19895	for this chapter
Na I (2.21 μm)	22035–22045	22047–22105	22107–22120	
Ca I (2.26 μm)	22500–22575	22580–22700	22705–22780	
CO (2.30 μm a)	22860–22910	22932–22982	23020–23070	
CO (2.30 μm b)	23150–23200	23220–23270	23300–23350	

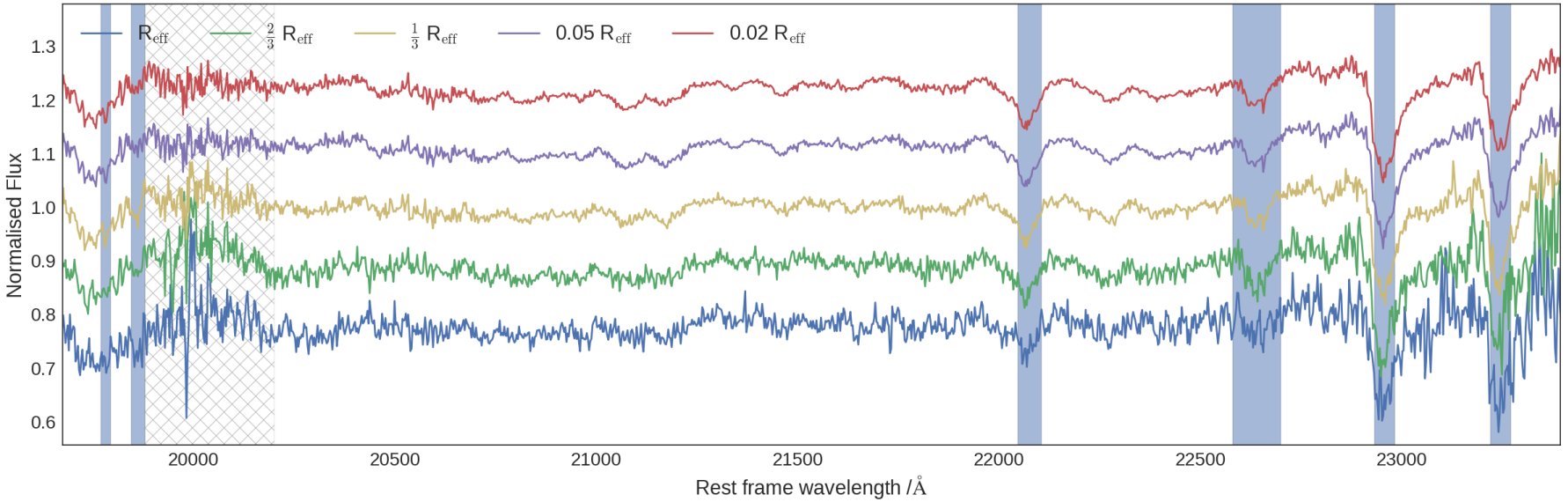

Figure 5.2: K-band spectra from KMOS, median-stacked at fixed fraction of the effective radius. Even in the outlying regions of the galaxy the signal of the strong absorption features are recovered via this method. The hatched region shows a region of particularly strong telluric absorption (atmospheric transmission $\lesssim 50\%$)

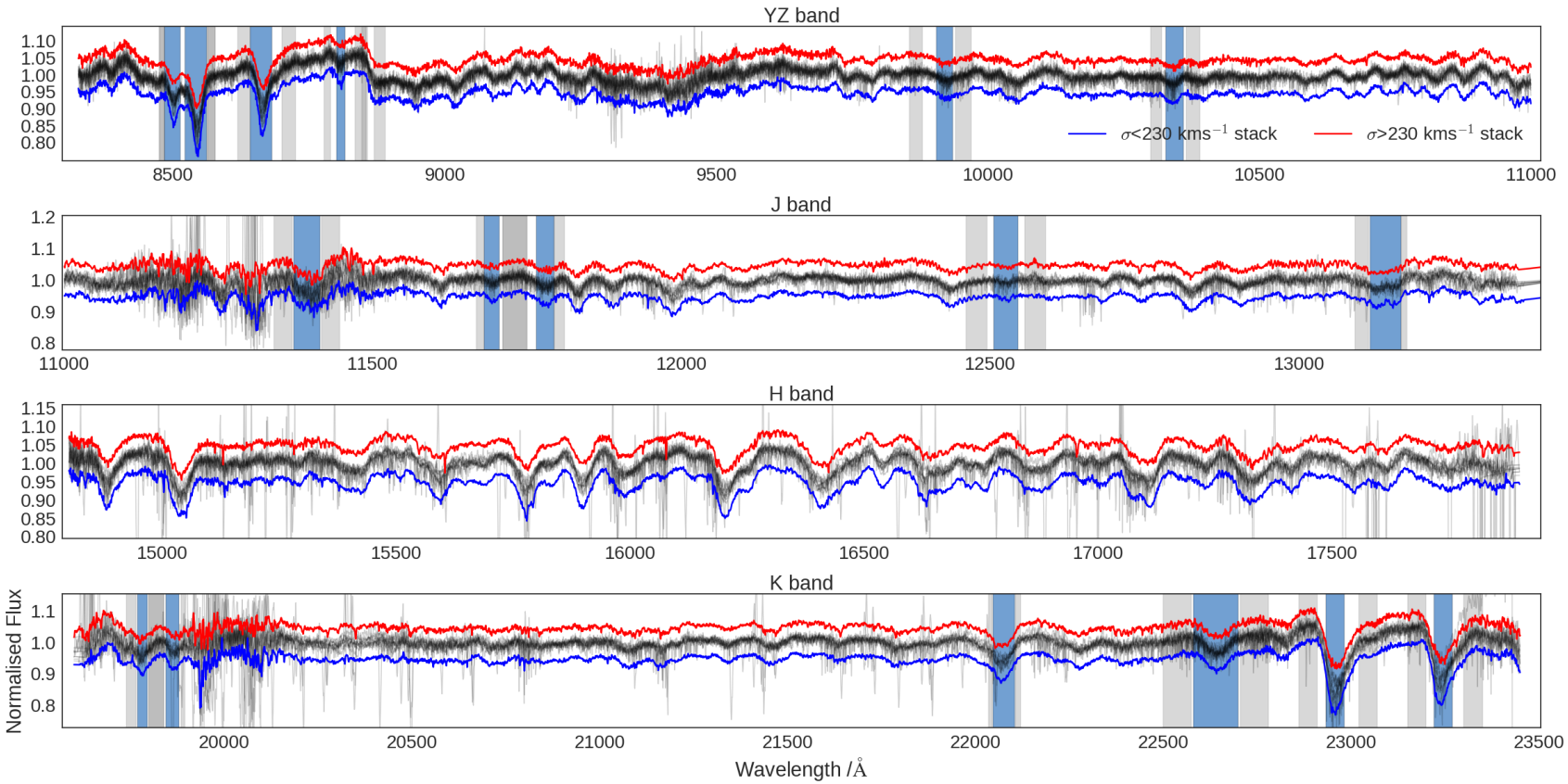

Figure 5.3: Data from the FIRE instrument, split into four bands and continuum normalised. The two stacks are shown (high velocity dispersion in red, low velocity dispersion in blue) offset from the individual galaxy spectra (grey). The scatter in the set of individual spectra increases in telluric absorption bands and where sky emission has been subtracted. Also shown: feature measurement bands in blue and feature pseudo-continuum bands in grey.

For the other KMOS spectra the same procedure as in Chapter 3 was followed: the spectra were divided by the centrally-extracted spectrum prior to stacking, so that we stacked the *radial variations* of the spectra. We then multiplied these 'variation stacks' by the stacked spectrum already derived from the central extraction region. This procedure maximises the radial variation signal: any constant offset in the strength of spectral features between different galaxies in the stack is divided out.

The KMOS K-band spectra are shown in Fig. 5.2, while the FIRE stacked spectra are shown in Fig. 5.3.

5.3 Absorption feature tables

The full set of measurements for both sets of data and the stacked spectra are presented in this section. These measurements are corrected to 230 kms^{-1}. The actual velocity dispersions of the stacked spectra are measured as above, using pPXF: for the FIRE stacked spectra the same wavelength range as for the individual spectra was used (8300–9000Å), while for the K-band stacked spectra we calculated velocity dispersions using the spectral region around the CO bandhead (21200–23400Å) instead. These velocity dispersion measurements are also given in the data tables.

5.3.1 Measurements of absorption indices from FIRE spectra

The feature equivalent widths measured for the FIRE galaxies are presented in two tables, Tables 5.4 and 5.5. The measurements from the stacked spectra are given in Table 5.6.

5.3.2 Measurements of K-band absorption indices from KMOS spectra

The measured equivalent widths for the KMOS data are presented galaxy-by-galaxy in Tables 5.7 to 5.13. The data from the stacked spectra are given in Table 5.14.

Table 5.4: A list of index measurements (in Å) for the first half of the FIRE sample, corrected to 230 kms^{-1}. Features badly contaminated by sky emission/telluric correction residuals have been removed.

	N3608	N4261	N4262	N4374	N4382	N4459
CaII Triplet	7.36±0.15	8.46±0.16	7.00±0.08	7.46±0.11	7.84±0.09	8.37±0.07
MgI 0.88	0.30±0.03	0.54±0.06	0.23±0.02	0.50±0.02	0.35±0.01	0.40±0.01
FeH 0.99	0.53±0.04	0.21±0.04	0.56±0.02	0.63±0.03	0.43±0.03	0.58±0.02
CaI 1.03	0.38±0.05	0.59±0.05	0.41±0.03	0.56±0.05	0.53±0.03	0.55±0.03
NaI 1.14	1.69±0.09	1.29±0.10	1.97±0.04	1.53±0.06	0.86±0.05	1.78±0.04
KI 1.17	1.01±0.06	1.26±0.09	1.03±0.03	0.99±0.07	0.70±0.03	1.02±0.03
KI 1.25b	0.05±0.04	0.53±0.06	0.06±0.02	0.20±0.04	–0.04±0.03	0.12±0.03
AlI 1.31	1.05±0.07	1.36±0.10	1.24±0.05	0.95±0.07	1.25±0.04	1.14±0.04
CaI 1.98	1.60±0.06	—	1.46±0.05	1.54±0.11	0.70±0.03	1.34±0.03
NaI 2.21	1.85±0.10	3.60±0.19	1.78±0.06	3.86±0.11	1.12±0.05	1.80±0.07
CaI 2.26	2.58±0.22	3.74±0.16	3.30±0.11	3.06±0.13	2.85±0.11	3.18±0.09
CO 2.30 µm a	8.64±0.12	7.87±0.10	7.88±0.06	7.86±0.08	6.64±0.05	8.37±0.03
CO 2.30 µm b	6.65±0.10	6.73±0.17	6.67±0.05	7.51±0.08	6.17±0.05	7.12±0.04
$\sigma_{\mathrm{spectrum}}$ /kms^{-1}	203 ± 23	363 ± 25	209 ± 14	354 ± 19	130 ± 7	171 ± 7
S/N (95% range)	40—220	50—260	90—360	70—340	80—350	100—390

Table 5.5: A list of index measurements (in Å) for the second half of the FIRE sample, corrected to 230 kms^{-1}.

	N4472	N4546	N4649	N4660	N5838	N5845
CaII Triplet	8.16±0.14	7.87±0.09	8.31±0.19	7.58±0.07	8.50±0.12	7.68±0.08
MgI 0.88	0.42±0.03	0.48±0.02	0.42±0.01	0.35±0.02	0.47±0.02	0.23±0.02
FeH 0.99	0.66±0.03	0.46±0.03	0.45±0.04	0.49±0.02	0.60±0.03	0.55±0.02
CaI 1.03	0.36±0.06	0.43±0.03	0.32±0.07	0.54±0.03	0.52±0.03	0.29±0.03
NaI 1.14	2.25±0.07	1.74±0.04	2.19±0.08	1.54±0.03	2.79±0.05	2.14±0.04
KI 1.17	0.92±0.07	1.12±0.04	1.57±0.12	0.90±0.03	1.73±0.06	1.10±0.04
KI 1.25b	–0.12±0.04	0.43±0.04	0.05±0.05	0.08±0.02	0.27±0.04	0.20±0.02
AlI 1.31	0.59±0.09	1.30±0.05	1.14±0.09	0.70±0.04	1.53±0.07	0.82±0.05
CaI 1.98	1.52±0.12	1.13±0.05	1.92±0.24	1.19±0.03	4.07±0.14	1.36±0.05
NaI 2.21	5.04±0.13	1.95±0.09	3.61±0.27	2.12±0.07	4.20±0.10	1.95±0.09
CaI 2.26	3.63±0.17	3.20±0.10	2.87±0.21	3.18±0.09	3.29±0.12	3.15±0.10
CO 2.30 µm a	8.26±0.09	8.21±0.05	9.51±0.12	8.06±0.04	9.60±0.06	8.14±0.05
CO 2.30 µm b	7.13±0.10	7.15±0.06	7.84±0.11	6.97±0.04	8.00±0.06	6.64±0.06
$\sigma_{\mathrm{spectrum}}$ /kms^{-1}	336 ± 26	227 ± 12	425 ± 22	208 ± 12	355 ± 22	241 ± 15
S/N (95% range)	50—300	90—330	50—290	110—400	80—360	90—350

5.3.3 Systematic differences between datasets

While the KMOS and FIRE samples do not overlap, the target galaxies are nevertheless similar and the central aperture sizes are comparable. The instruments themselves are rather different, so a comparison between the datasets is useful for quantifying instrumental systematic effects on the data in order to determine whether these have any effect on the inference from the data.

In Fig. 5.4 we make this comparison, showing the full FIRE dataset and also the KMOS central spectra which are extracted from a comparable aperture. We also show how the strength of each line varies with radius via the KMOS stacked data and with velocity dispersion via the FIRE stacks.

It is clear that in some cases there are some sizeable and significant systematic differences between the datasets. The optical data are all taken from ATLAS 3D and it is clear that for those lines the sample means agree well, suggesting that the two samples observed with KMOS and FIRE are comparable. There are some uncorrected systematic differences between the two datasets, including for some particularly important spectral features such as the Ca II Triplet and the Wing-Ford (FeH) band. In Figs. 5.5 and 5.6 we examine the data in more detail in order to uncover any issues. We believe that the differences are due in part to the procedure by which adjacent echelle orders are combined in the FIRE data: for bluer wavelengths the orders are extremely short, so this is challenging to do. In Fig. 5.6 we examine this issue more closely. It seems likely that it affects the FIRE measurements of the Ca II triplet, Mg I 0.88 μm line and Wing-Ford band.

In the case of these indices, a comparison with recent literature is instructive. Of course, there is some galaxy-galaxy scatter (and differences in velocity dispersion), but it can be seen from Fig. 5.6 that in these indices the offset is larger than the scatter. In the case of the Ca II triplet, McConnell et al. (2016), Vaughan et al. (2016), and Zieleniewski et al. (2017) all measure consistent central values of 6.6–7.5Å, very much consistent with our KMOS sample and less so with the FIRE data. A large scatter in Mg I 0.88 μm is observed (0.2–0.6Å), which appears more consistent with the FIRE data (two KMOS galaxies exhibit stronger Mg I 0.88 μm than the upper limit of this broad range). Finally, these three studies, together with La Barbera et al. (2016) find a range of values for the Wing-Ford (FeH) band from 0.4–0.6Å, whereas our KMOS data lie primarily between

Table 5.6: A list of index measurements (in Å) for the stacked spectra created from the FIRE sample, corrected to 230 kms^{-1}. N.B. 'noise' in S/N calculation represents scatter between input spectra, not the formal flux uncertainty (which is much lower). This S/N distribution is strongly skewed (e.g. 95% range of 12 galaxy stack is 60—760).

	12 galaxy stack	low σ stack	high σ stack
CaII Triplet	7.34±0.08	7.59±0.09	7.95±0.12
MgI 0.88	0.34±0.02	0.35±0.03	0.41±0.04
FeH	0.47±0.02	0.46±0.02	0.48±0.03
CaI 1.03	0.37±0.03	0.42±0.04	0.40±0.05
NaI 1.14	1.78±0.10	1.50±0.11	2.12±0.13
KI 1.17	0.97±0.04	0.98±0.05	1.17±0.08
KI 1.25	0.13±0.03	0.10±0.04	0.16±0.04
AlI 1.31	1.05±0.06	1.14±0.06	0.99±0.07
CaI 1.98	1.35±0.06	1.30±0.05	2.05±0.21
NaI 2.21	2.21±0.06	1.85±0.06	3.19±0.15
CaI 2.26	2.98±0.06	2.99±0.07	3.03±0.10
CO 2.30 μm a	7.44±0.05	7.66±0.06	7.96±0.13
CO 2.30 μm b	6.54±0.06	6.80±0.05	7.07±0.10
σ_{stack} /kms^{-1}	231±13	217±9	329±22
S/N (68% range)	110—400	100—500	80—360

Table 5.7: A list of index measurements (in Å) for the KMOS sample K-band observations of NGC 1407, corrected to 230 kms^{-1}. R1 and R2 correspond to the two extraction regions in the central IFU ($< 0.7''$, $> 0.7''$) while R3, R4, and R5 correspond to the rings of IFUs arranged at $\sim 1/3\,\mathrm{R_{eff}}$, $\sim 2/3\,\mathrm{R_{eff}}$, and $\sim\mathrm{R_{eff}}$.

NGC1407	R1	R2	R3	R4	R5
Ca I 1.98 μm	0.61±4.15	2.53±5.05	–6.46±9.09	–21.67±28.53	29.21±69.27
Na I 2.21 μm	2.75±0.32	2.85±0.98	1.65±0.49	2.39±1.65	–3.21±2.74
Ca I 2.26 μm	3.17±0.65	3.10±1.14	3.67±2.49	1.84±7.82	3.25±5.98
CO 2.30 μm a	6.65±0.49	6.82±0.52	6.95±1.88	9.63±9.40	4.91±4.61
CO 2.30 μm b	4.36±1.36	8.02±1.44	8.03±5.69	23.71±45.27	6.31±12.01
average S/N	71	24	33	14	12

Table 5.8: A list of index measurements (in Å) for the KMOS sample K-band observations of NGC 3377, corrected to 230 kms^{-1}. R1 and R2 correspond to the two extraction regions in the central IFU ($< 0.7''$, $> 0.7''$) while R3, R4, and R5 correspond to the rings of IFUs arranged at $\sim 1/3\,\mathrm{R_{eff}}$, $\sim 2/3\,\mathrm{R_{eff}}$, and $\sim\mathrm{R_{eff}}$.

NGC3377	R1	R2	R3	R4	R5
Ca I 1.98 μm	1.13±0.15	0.80±0.20	0.90±0.35	1.42±0.77	0.55±1.11
Na I 2.21 μm	1.73±0.11	1.34±0.22	1.00±0.45	1.89±0.88	3.20±1.39
Ca I 2.26 μm	3.60±0.32	2.41±0.48	3.18±1.65	8.02±2.32	2.37±4.13
CO 2.30 μm a	8.33±0.18	7.96±0.21	5.52±1.73	6.23±2.75	2.67±5.15
CO 2.30 μm b	6.94±0.20	6.58±0.22	5.58±2.17	376.21±335.59	1.32±5.59
average S/N	71	24	33	14	12

Table 5.9: A list of index measurements (in Å) for the KMOS sample K-band observations of NGC 3379, corrected to 230 kms^{-1}. R1 and R2 correspond to the two extraction regions in the central IFU ($< 0.7''$, $> 0.7''$) while R3, R4, and R5 correspond to the rings of IFUs arranged at $\sim 1/3\,\mathrm{R_{eff}}$, $\sim 2/3\,\mathrm{R_{eff}}$, and $\sim\mathrm{R_{eff}}$.

NGC3379	R1	R2	R3	R4	R5
Ca I 1.98 µm	1.37±0.22	1.31±0.84	0.96±0.10	0.70±0.15	0.81±0.23
Na I 2.21 µm	2.26±0.18	2.01±0.93	1.67±0.20	1.39±0.44	1.39±0.78
Ca I 2.26 µm	3.60±0.29	3.61±0.77	3.80±0.46	3.26±1.04	2.71±1.83
CO 2.30 µm a	8.73±0.10	8.38±0.20	7.29±0.41	7.07±1.04	8.40±1.54
CO 2.30 µm b	6.24±0.15	5.91±0.27	5.29±0.58	4.79±1.66	5.47±2.69
average S/N	71	24	33	14	12

Table 5.10: A list of index measurements (in Å) for the KMOS sample K-band observations of NGC 4486, corrected to 230 kms^{-1}. R1 and R2 correspond to the two extraction regions in the central IFU ($< 0.7''$, $> 0.7''$) while R3, R4, and R5 correspond to the rings of IFUs arranged at $\sim 1/3\,\mathrm{R_{eff}}$, $\sim 2/3\,\mathrm{R_{eff}}$, and $\sim\mathrm{R_{eff}}$.

NGC4486	R1	R2	R3	R4	R5
Ca I 1.98 µm	2.17±2.97	1.74±0.22	2.09±0.27	1.23±0.40	1.48±0.88
Na I 2.21 µm	1.83±1.33	1.85±0.19	2.48±0.32	1.16±0.66	1.46±0.98
Ca I 2.26 µm	2.10±0.79	3.93±0.44	3.97±1.01	2.79±1.91	2.32±3.34
CO 2.30 µm a	5.20±0.42	7.47±0.30	9.16±0.90	8.40±1.77	8.54±3.20
CO 2.30 µm b	4.42±0.43	5.82±0.37	7.53±1.11	5.01±2.06	7.50±3.44
average S/N	71	24	33	14	12

Table 5.11: A list of index measurements (in Å) for the KMOS sample K-band observations of NGC 4552, corrected to 230 kms^{-1}. R1 and R2 correspond to the two extraction regions in the central IFU ($< 0.7''$, $> 0.7''$) while R3, R4, and R5 correspond to the rings of IFUs arranged at $\sim 1/3\,\mathrm{R_{eff}}$, $\sim 2/3\,\mathrm{R_{eff}}$, and $\sim\mathrm{R_{eff}}$.

NGC4552	R1	R2	R3	R4	R5
Ca I 1.98 µm	2.96±0.27	3.01±0.29	1.79±0.28	0.23±0.64	0.59±0.70
Na I 2.21 µm	2.29±0.21	2.15±0.25	1.22±0.37	1.72±0.85	1.93±1.03
Ca I 2.26 µm	3.44±0.27	3.26±0.26	2.34±0.98	3.31±2.01	3.59±2.63
CO 2.30 µm a	8.39±0.33	8.14±0.31	6.61±0.85	6.58±1.77	8.15±2.50
CO 2.30 µm b	6.55±0.16	6.71±0.15	5.78±0.94	7.16±2.12	6.11±2.96
average S/N	71	24	33	14	12

Table 5.12: A list of index measurements (in Å) for the KMOS sample K-band observations of NGC 4621, corrected to 230 kms^{-1}. R1 and R2 correspond to the two extraction regions in the central IFU ($< 0.7''$, $> 0.7''$) while R3, R4, and R5 correspond to the rings of IFUs arranged at $\sim 1/3\,\mathrm{R_{eff}}$, $\sim 2/3\,\mathrm{R_{eff}}$, and $\sim\mathrm{R_{eff}}$.

NGC4621	R1	R2	R3	R4	R5
Ca I 1.98 µm	0.16±0.23	0.44±0.52	0.09±0.22	0.54±0.40	1.34±0.48
Na I 2.21 µm	3.31±0.28	2.73±0.53	2.18±0.52	0.66±1.06	1.77±1.67
Ca I 2.26 µm	2.69±0.26	2.15±0.59	1.83±1.32	1.62±2.56	2.66±4.87
CO 2.30 µm a	8.57±0.41	8.35±0.47	7.62±1.30	8.26±3.05	105.53±33.77
CO 2.30 µm b	7.64±0.24	7.06±0.35	6.70±1.81	6.34±4.95	7.12±73.43
average S/N	71	24	33	14	12

Table 5.13: A list of index measurements (in Å) for the KMOS sample K-band observations of NGC 5813, corrected to 230 kms^{-1}. R1 and R2 correspond to the two extraction regions in the central IFU ($< 0.7''$, $> 0.7''$) while R3, R4, and R5 correspond to the rings of IFUs arranged at $\sim 1/3\,\mathrm{R_{eff}}$, $\sim 2/3\,\mathrm{R_{eff}}$, and $\sim\mathrm{R_{eff}}$.

NGC5813	R1	R2	R3	R4	R5
Ca I 1.98 μm	1.86±0.65	2.27±0.78	3.86±3.59	5.98±4.70	1.29±12.11
Na I 2.21 μm	1.94±0.27	1.97±0.65	1.71±1.32	1.05±1.98	2.98±4.11
Ca I 2.26 μm	3.40±0.41	3.35±0.72	1.19±3.34	3.67±5.30	3.60±8.98
CO 2.30 μm a	6.84±0.39	7.02±0.46	7.64±2.94	8.43±5.21	0.40±10.77
CO 2.30 μm b	6.41±1.31	6.18±1.34	4.58±10.22	7.50±14.47	15.56±36.31
average S/N	71	24	33	14	12

Table 5.14: A list of index measurements (in Å) for the stacked spectra from the KMOS sample K-band observations, corrected to 230 kms^{-1}. N.B. 'noise' in S/N calculation represents scatter between input spectra, not the formal flux uncertainty (which is much lower). This S/N distribution is strongly skewed (e.g. 95% range of central stack is 20—1780). R1 and R2 correspond to the two extraction regions in the central IFU ($< 0.7''$, $> 0.7''$) while R3, R4, and R5 correspond to the rings of IFUs arranged at $\sim 1/3\,\mathrm{R_{eff}}$, $\sim 2/3\,\mathrm{R_{eff}}$, and $\sim\mathrm{R_{eff}}$.

Stacks	R1	R2	R3	R4	R5
Ca I 1.98 μm	0.44±0.22	0.40±0.12	0.48±0.12	0.53±0.21	0.37±0.30
Na I 2.21 μm	1.82±0.14	1.98±0.05	1.63±0.16	0.96±0.24	0.94±0.30
Ca I 2.26 μm	2.94±0.11	2.87±0.07	2.74±0.16	3.12±0.33	2.73±0.45
CO 2.30 μm a	7.14±0.15	7.45±0.06	7.27±0.21	7.13±0.33	5.99±0.64
CO 2.30 μm b	5.45±0.21	5.98±0.05	6.34±0.24	5.56±0.48	6.42±0.61
σ_{stack} /kms^{-1}	199±2	211±1	192±3	166±10	151±14
S/N (68% range)	70—600	170—1210	60—490	30—250	20—160

0.2–0.3Å (and some galaxies in the FIRE sample exhibit stronger FeH than this range). However, it is notable that e.g. Zieleniewski quantifies possible systematics affecting FeH and concludes that true values of the strength as low as 0.2–0.3Å (at 200 kms^{-1} velocity dispersion) are not implausible. It is clear that this feature, so crucial to well-constrained inference of the IMF, can be difficult to measure robustly. The differences between these measurements are significant in terms of the underlying IMF that would be inferred, a point we will explore in Section 6.4.

In the case of redder indices (i.e. the strong Na I 1.14μm feature and the CO bandhead) the telluric correction applied to the FIRE data, which is less sophisticated than that which is used for the KMOS data, is likely at fault; this interpretation is supported by the fact that the stacked data (in which rest-frame systematics are suppressed) agree much better for these features than the individual data do. In Fig. 5.5 we make clear which features are most affected by telluric absorption.

These issues unfortunately suggest that robust inference of stellar population properties may be difficult with the individual FIRE data, despite the nominally very high S/N. The stacked data offer somewhat better prospects, but care must still be taken that any conclusions do not rest principally on the most affected spectral features.

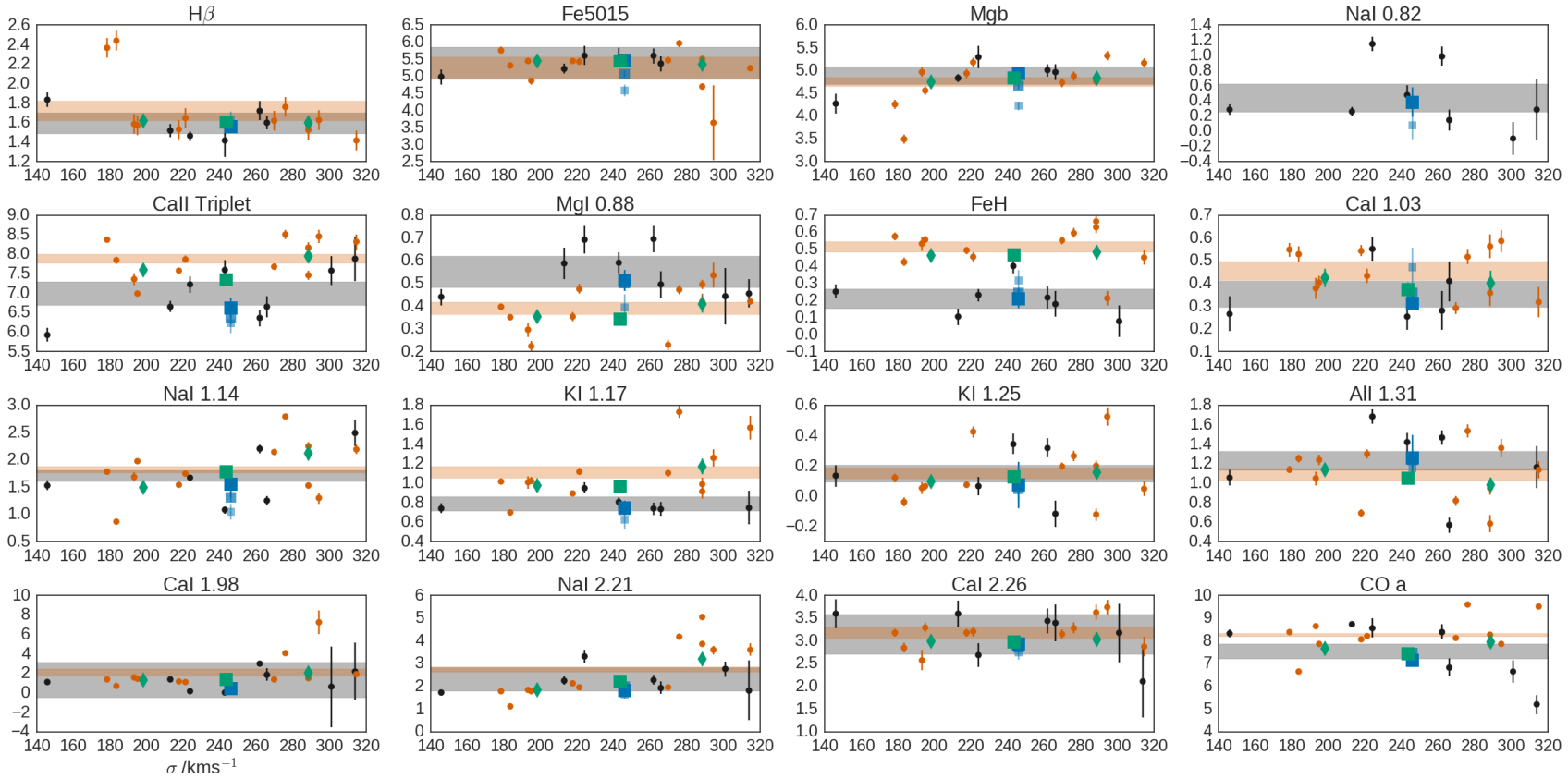

Figure 5.4: We compare the datasets. Orange points: measurements from FIRE spectra. Black points: measurements from KMOS central spectra. Stacked spectra are depicted using larger symbols (green for FIRE, blue for KMOS). We show the low and high velocity dispersion stacks for the FIRE data as diamonds and the whole sample as a square, while the radial variation of the KMOS stacks is also shown (smaller blue squares are extracted at larger radii). Finally, the sample means with errors are shown as transparent bands.

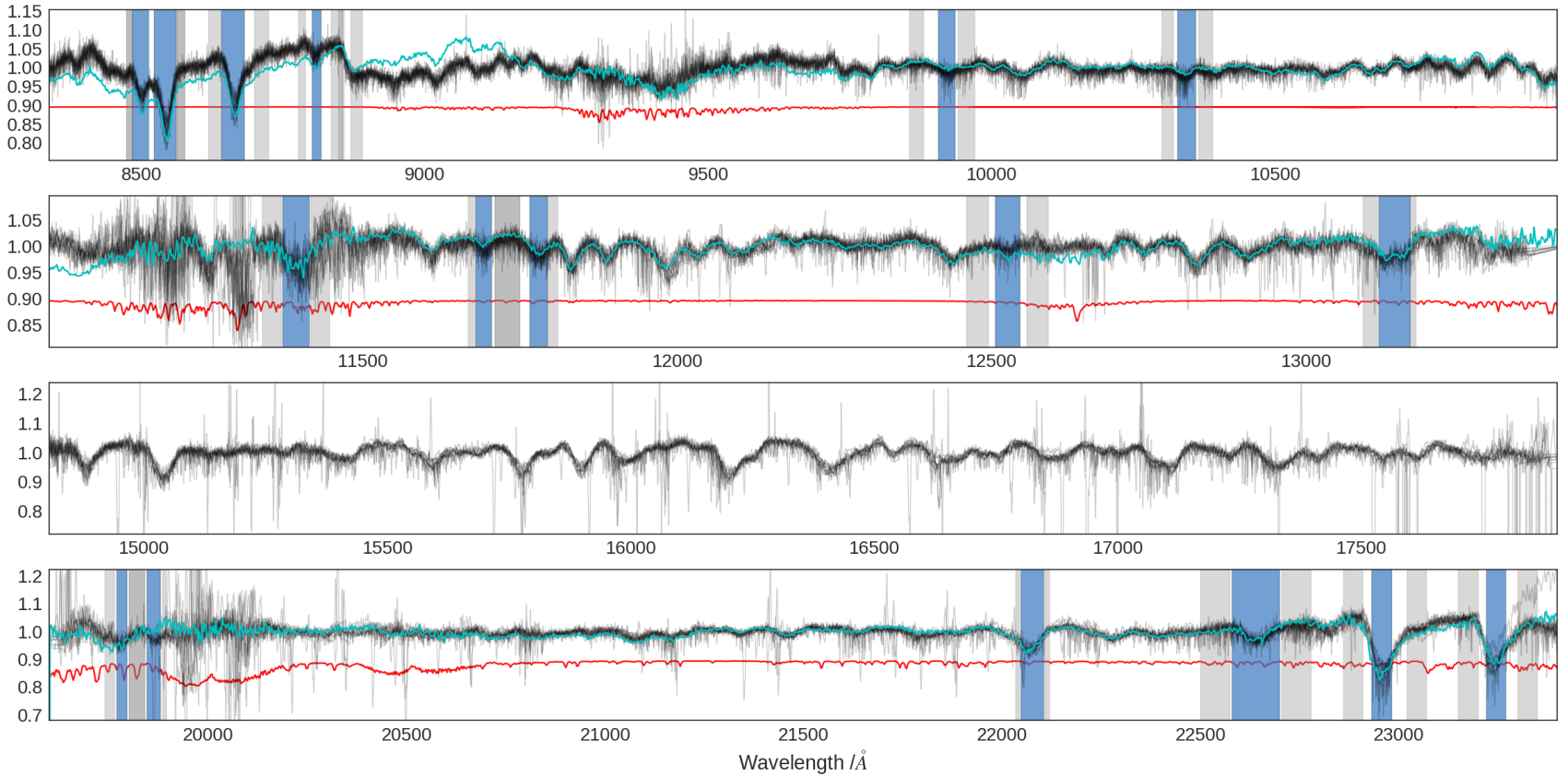

Figure 5.5: This figure shows the individual FIRE data (black) and the KMOS stacked spectrum from the innermost extraction region (cyan) with long-range variations removed. An example atmospheric transmission spectrum, rescaled by a factor of ten and offset (red) has been shifted by the mean redshift of the FIRE sample so that the reader can judge the effect of telluric absorption on the spectra. The locations of the feature and pseudo-continuum bands for each index are also shown.

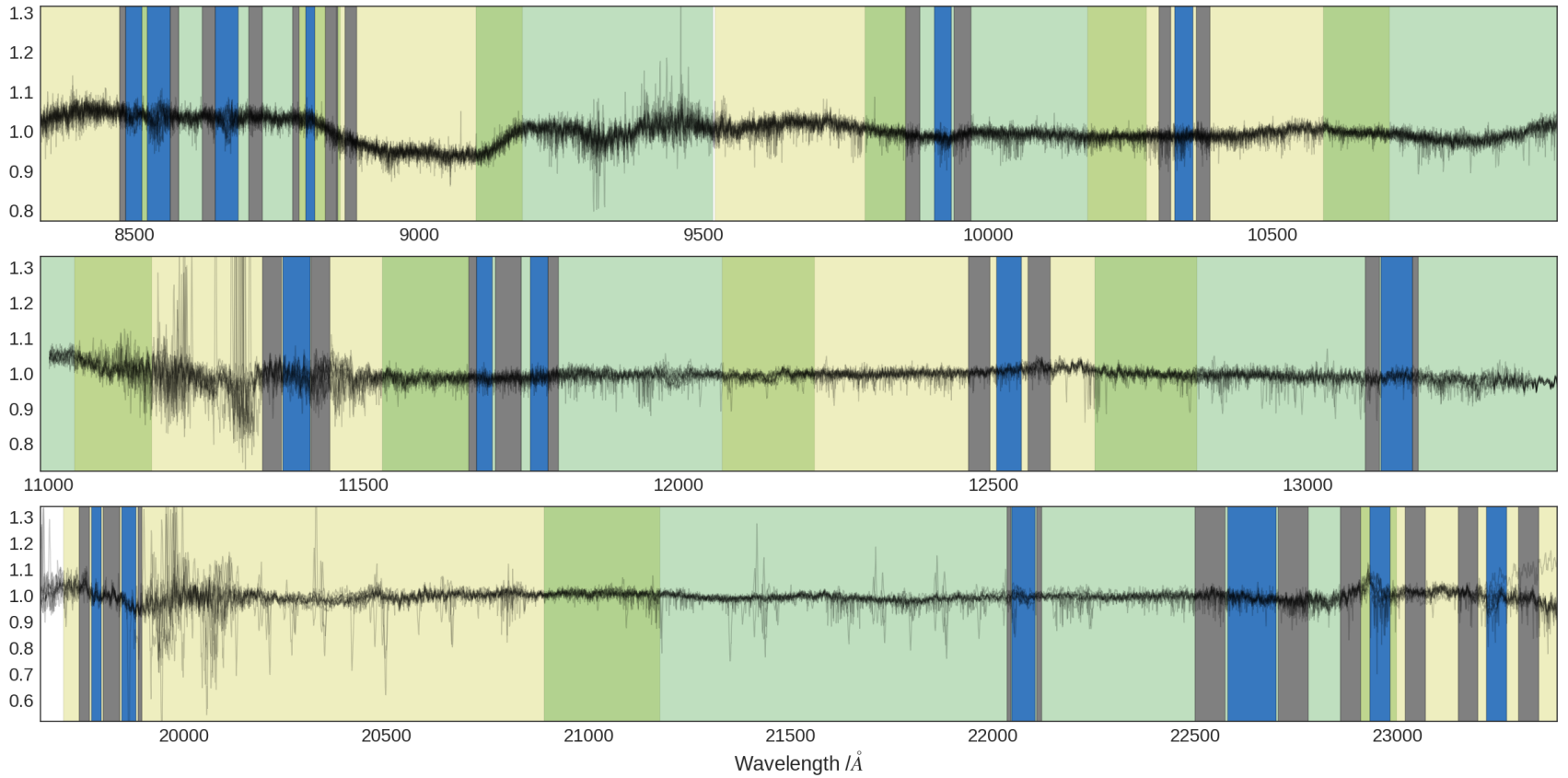

Figure 5.6: This figure shows the ratio of the individual FIRE data and KMOS stacked spectrum presented in Fig. 5.5. The locations of the measured spectral indices are also shown. Alternate echelle orders from FIRE are marked alternately by green and yellow bands; in the IZ band these orders are rather short and this may account for some of the differences between the two datasets.

5.4 Analysis

5.4.1 Interpretation of absorption line strengths

As outlined in Chapter 1, absorption features in stellar population spectra encode information about the properties of the stars as well as kinematic information (recession velocities, velocity broadening). This is because the strength of those features in the light of individual stars depends on chemical composition, the age of the star, and its surface gravity. Because of these dependencies it is in principle possible to constrain the chemical abundance pattern, population age, and relative contribution of dwarf and giant stars to the total light (and thus the IMF).

In the first instance we present radial variations in the strength of four K-band features, for which definitions are given in Table 5.3. These features are as follows:

Ca I 1.98 μm

The comparatively weak Ca I doublet is principally sensitive to Ca abundance and the IMF (it gets stronger as Ca abundance increases and as the IMF becomes more bottom-heavy). This feature was first highlighted in CvD12a as an IMF-sensitive index. In Section 2.4 we showed that (given other constraints on $f_{\rm dwarf}$) it can provide information about the IMF shape. This feature lies next to a band of strong telluric absorption and so in some cases is difficult to measure with precision.

Na I 2.21 μm

The strong Na I feature is, in principle, extremely useful for constraining [Na/Fe], since its sensitivity to the IMF is comparatively limited, in contrast to the Na I lines at 0.82μm and 1.14μm. Previous work (Smith et al., 2015a and see also Chapter 4) has indicated that in the CvD models, the strengths of these lines are in tension with each other, given other constraints. The measurement of other strong Na features is important for resolving this tension.

This K-band feature has been studied previously at an empirical level by Silva et al. (2008) and Mármol-Queraltó et al. (2009). Although at the time accurate SSP models

were not available in the K-band, it was noted to be very strong in comparison to measurements of Milky Way stars and also to correlate strongly and positively with galaxy velocity dispersion. A more recent treatment by La Barbera et al. (2017) using cutting-edge SSP models studied this and other Na features in the optical and near infrared, finding that the strength of the feature could only be reproduced by a combination of Na superabundance *and* a bottom-heavy IMF.

Ca I 2.26 μm

This strong Ca I line is not particularly sensitive to the IMF, being principally sensitive to the Ca abundance in the CvD models, with minor contributions from other elements. Silva et al. (2008) found that it did not correlate strongly with galaxy velocity dispersion, but showed significant scatter. It has not been well-studied using SSP modelling.

CO 2.30 μm bandhead

The extremely strong CO molecular absorption bands at the red end of the K-band are most prominent in giant stars – and so decline in strength if the IMF is bottom-heavy. A competing effect comes from [C/Fe], an increase in which will, of course, strengthen these features. The CO bandhead has in the past been used to measure stellar kinematics (e.g. Lyubenova et al., 2008, Vanderbeke et al., 2011) as well finding use in discussions of stellar populations at an empirical level, e.g. Silva et al., 2008, Cesetti et al., 2009. Both these studies found significant correlation between CO and measurements of optical features). Mármol-Queraltó et al. (2009) discussed this index in the context of stellar population models, arguing that it could be used to test for extended star-formation histories in ETGs by probing the contribution to the light of intermediate-age stars.

5.4.2 Absorption line gradients

In Chapters 3 and 4 we were able to constrain the stellar population gradients in our sample, finding evidence for strong chemical abundance gradients that seemed to be fairly consistent across our sample. We now present radial gradients in the strengths of the K-band absorption lines we have measured (the first time these gradients have been mea-

Table 5.15: Best-fit radial gradients (change in equivalent width per decade in radius) derived from the KMOS stacks.

Feature	best-fit gradient (Å)
Ca I 1.98 μm	0.05±0.02
Na I 2.21 μm	–0.53±0.08
Ca I 2.26 μm	–0.08±0.09
CO 2.30 μm a	–0.11±0.13

sured, in some cases) and compare these with the predictions of the best-fit model from the previous chapter.

In Fig. 5.7 we show the predictions of the models used in Chapter 4 (i.e. not the updated CvD models) against the new measurements, given the best-fit parameters we found. These predictions suggest that the strength of the Ca features should be approximately constant with radius, which the data bear out. However, the 'canonical' model of Chapter 4 severely overpredicts the strengths of the Ca I features. That model also underpredicts the CO bandhead a line, but the model does not account for variations in the abundance of carbon, which the CO bandhead's strength crucially depends on. In the previous chapter we explored a model with a [C/H] parameter included, finding this necessary to account for the low strength of the Hβ line. While the value of this parameter was not very well constrained, this model is much less discrepant with the CO bandhead's strength, suggesting good prospects for constraining the carbon abundance in the updated model framework. We also explored a model that incorporated two additional nuisance parameters, $\Delta T_{\rm eff}$ and [O,Ne,S/α]; this model produced much better estimates for the Ca I lines. Finally, the Na I 2.21 μm line exhibits a steeper gradient than is predicted in any of the models used in Chapter 4 (despite the steep [Na/H] gradient we inferred).

The model sensitivities of these features and good S/N of some our measurements indicate that these data will add significant additional constraining power to our stellar population analysis. In Table 5.15 we give the best-fit empirical spectroscopic gradients we derived for these features (via the same procedure as in Chapter 3), with associated statistical uncertainties.

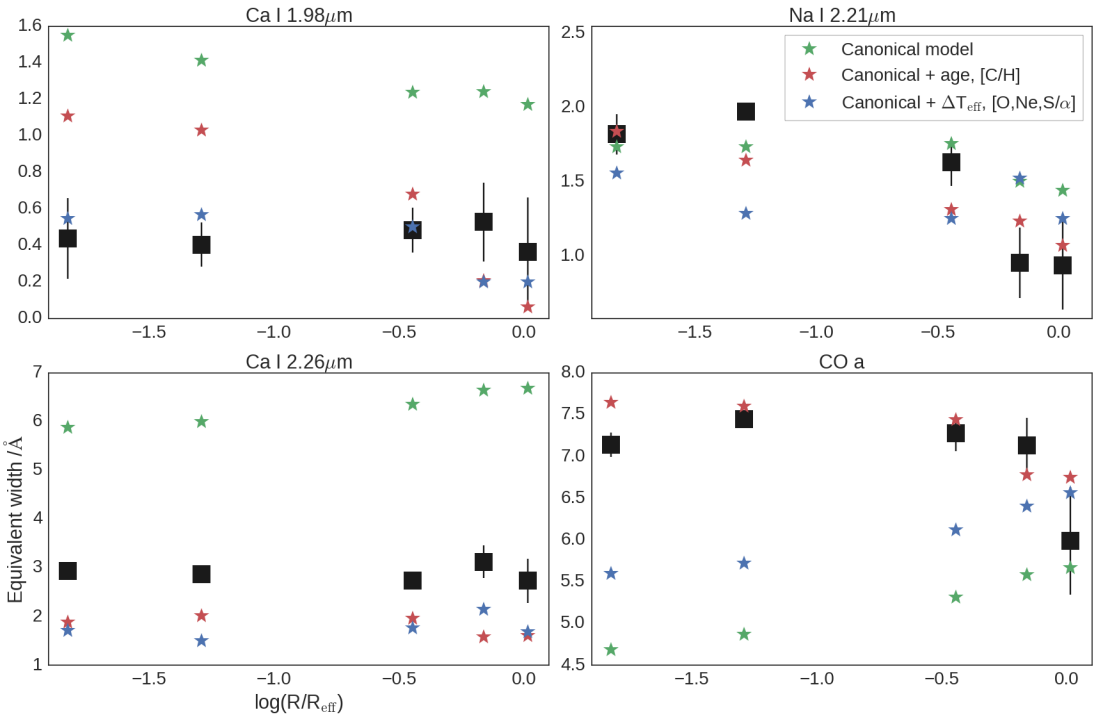

Figure 5.7: Measurements from the stacked KMOS K-band spectra with errors (large black symbols). Also shown are the predictions of the best-fit models from Chapter 4, which were *not* constrained using these data (i.e. these are true predictions).

Green: the 'canonical model' of Chapter 4 (which accounts for [α/H], [Fe/H], [Na/H], [Ca/α], [K/H], as well as the IMF).

Red: an extended model which additionally accounts for stellar population age and [C/H] (the inclusion of both proved necessary to fit the optical Hβ line measurements taken from ATLAS^{3D}).

Blue: an extended version of the canonical model with the fitting process marginalised over the nuisance parameters ΔT_{eff} and [O,Ne,S/α]. This made little difference in the fits to the IZ & YJ band data.

We note that the strengths of the Na I 2.21 μm feature and the CO a line appear to flatten/turn over in the innermost region, where two spectra were extracted from the central IFU for each galaxy. It is important to understand whether this issue results from real variation of the stellar populations or some unaccounted-for observational effect. An instrumental issue seems unlikely, as the two datapoints are extracted from the same IFU. Furthermore, the effect is not seen in the Ca I 2.26 μm feature. The effects of observational seeing can in principle reduce the difference between the two measurements by spreading light from one region into another; we expect this effect to be limited since the seeing for these observations was typically $<1.4''$ (the central extraction region has this diameter). Nor is the seeing for these observations notably worse (on average) than for the IZ and YJ observations we made.

Summary

In this chapter we have introduced four strong K-band spectral features. We have presented measurements of the strengths of these features and of their radial variations in the KINETyS sample, as well as an additional, complementary set of measurements from the innermost regions of a sample of 12 ETGs observed with Magellan-FIRE. We have characterised the systematic differences between these independent sets of measurements and outlined some of the instrumental effects and differences in reduction procedures that might account for these systematic offsets. We have derived average spectroscopic gradients for the KINETyS sample, in particular finding a strong and significant radial gradient in the strength of Na I 2.21 μm and have compared our data with the predictions of the models presented in Chapter 4. This comparison suggests that the new K-band data may add significant constraining power to our analysis.

In the next chapter we will use an updated set of models to fit the full set of measurements for the KINETyS sample (both those presented in Chapter 3 and in this chapter) and will present our conclusions regarding the stellar populations of these galaxies.

Chapter 6

Results from K-band spectral features

Preamble

In the previous chapter we presented measurements and empirical analysis of K-band spectroscopy of the KINETyS sample, as well as an additional sample of 12 ETGs whose cores we observed using the Magellan-FIRE instrument. We examined the systematic differences between these two samples, which may have important implications for attempts to characterise the underlying stellar populations in these galaxies. We measured spectroscopic gradients for four strong K-band features and compared our measurements with the predictions of the models of Chapter 4. We concluded that the new data will add significant constraining power to our inference of the stellar populations in our sample galaxies.

We now present our stellar population analysis of this data using an updated version of our SPINDRIFT code.

In Section 6.1 we present an updated model framework which we use for stellar population inference in this chapter. In Section 6.2 we describe our analysis of the measurements presented in Chapter 5, and our results are given in Section 6.3. We discuss these results in Section 6.4 and present our conclusions in Section 6.5.

6.1 Updated stellar population models

For the work presented in this chapter, we updated the SPINDRIFT code from the version used in Chapter 4. First, the SSP models the code uses were updated, as already mentioned. The updated CvD models are constructed from an expanded library of stellar spectral templates incorporating stars with a variety of metallicities (Villaume et al., 2017), spanning the range [Z/H] = –1.5 to [Z/H] = +0.2.

The updated models allow more freedom in the IMF parametrization. In Chapter 4, IMF variations were parameterised with a single parameter, f_{dwarf}, while the underlying shape of the IMF was assumed to be a single power-law below $1\,M_{\odot}$. We had already shown in Chapter 2 that for the spectral features used in our earlier analysis, index strength variations are approximately linear with respect to the f_{dwarf} parameter, with little dependence on the IMF shape. However, we also showed that the effect of IMF shape is *not* negligible for the K-band indices we have measured here. This is because the strengths of different features trace the contribution to the light from stars in different mass ranges. It is therefore necessary in this work to use models with additional freedom in the IMF parametrization. Therefore, in this chapter the IMF is modelled as a broken power-law, comprising two sections ($0.08\,M_{\odot} - 0.5\,M_{\odot}$ and $0.5\,M_{\odot} - 1.0\,M_{\odot}$) with independent power-law slopes X1 and X2.

The updated models also make use of a different approach to modelling the chemical abundance pattern of the stellar populations. The overall metallicity of the population is now represented using the relative logarithmic abundance [Z/H] (where [Z/H] = 0 corresponds to the solar abundance pattern), while individual variations in element abundances are computed with respect to the overall metallicity (i.e. they are parameterised as [X/Z]). In addition, the response of the index strengths to variations in the abundance of particular elements varies with [Z/H] in the updated models, meaning the responses are now coupled.

The full set of parameters used in the model in this work is given in Table 6.1, along with the cut-offs used in the prior distribution.

For the purpose of presenting our results the model parameters are reorganised. Stellar population age, rather than $\log(t_{age})$ is given. The segmented IMF slopes are converted to

Table 6.1: List of model parameters used in the MCMC inference. X1 and X2 are the IMF power-law slopes over the stellar mass intervals 0.08–0.5 and 0.5–1.0$M_{\odot}$. Z is the total metallicity of the population and the [X/Z] parameters are the relative variations of individual elements with respect to the overall metallicity.

Model parameter	Minimum value	Maximum value
$\log(t_{age}/Gyr)$	log(7.0)	log(14.0)
X1	1.0	3.5
X2	1.0	3.5
$[Z/H]$	–1.0	0.4
$[Fe/Z]$	–0.5	0.3
$[Mg/Z]$	–0.4	0.6
$[Ca/Z]$	–0.4	0.4
$[Ti/Z]$	–0.4	0.6
$[O, Ne, S/Z]$	–0.3	0.3
$[Na/Z]$	–0.6	0.9
$[K/Z]$	–0.3	0.3
$[C/Z]$	–0.3	0.3

f_{dwarf}, and also relative V-band M/L ratio. The latter describes the ratio of M/L for two populations, one formed via the chosen IMF and the other according to a Kroupa IMF (but, to aid comparison, without adjusting for metallicity or age; we assume [Z/H] = 0 and t_{age}=13.5 Gyr). To describe the abundances, we compute [Fe/H] = [Fe/Z] + [Z/H] and, for each of the other elements, [X/Fe] = [X/Z] – [Fe/Z]. These quantities are further adjusted to account for measured deviations in [X/Fe] from the solar ratio in the library stars of different metallicities (Conroy, private communication), since we wish to report [X/Fe] values relative to the solar ratio rather than the library star ratio (see also Thomas et al., 2003b).

6.1.1 Comparison with previous model implementation

To allow a meaningful comparison, we first make use of these models to fit the stacked data presented in Chapter 3, in order to (a) reproduce the results already given and (b) highlight any differences due to the model changes prior to including the information from our new K-band measurements, i.e. isolate the effect of updating the model framework.

To achieve this, we set up the models with the constraint X1 = X2 (i.e. we limited ourselves to the case of a single power-law description of the IMF). We assumed an old age (t = 13.5 Gyr) and included measurements of the optical features Fe 5015 and Mg*b* in the fit. We fit for metallicity, the IMF slope, and abundance variations in Fe, Mg, Na, Ca, and K. The results of a set of MCMC runs with 100 walkers and 900 steps (after 100 burn-in steps) are given in Table 6.2 and may be compared with those given in Table 4.5.

These results are broadly consistent with those presented in Chapter 4. For clarity we reorganise the results presented in Table 4.5 so that they are reported in terms of the same parameters as in Table 6.2 and can thus be directly compared (see Table 6.3). We detect a very similar gradient in [Fe/H] and find [Mg/Fe] strongly enhanced and constant with radius. We also now explicitly calculate the [Z/H] gradient: previously it was implicitly assumed that [Z/H] = 0 at all radii. However, applying the empirical relationship [Z/H] = [Fe/H] + 0.94 [α/Fe] set out in Thomas et al. (2003b) would indicate a gradient of –0.20$\pm$0.03, consistent with the new result. Meanwhile [Ca/Fe] is constant with radius and it's clear that Ca is much less over-abundant than Mg; the new model does however prefer a modest enhancement in the core, which was not the case previously. For [Na/Fe]

Table 6.2: Estimated parameter values for the stacked spectra first presented in Chapter 3, acquired using the updated models. We set X1 = X2 = X and fit for [Z/H] as well as the abundances of various elements of interest (for previous results see Table 4.5). R1 and R2 correspond to the two extraction regions in the central IFU ($< 0.7''$, $> 0.7''$) while R3, R4, and R5 correspond to the rings of IFUs arranged at $\sim 1/3\,R_{eff}$, $\sim 2/3\,R_{eff}$, and $\sim R_{eff}$.

	R1	R2	R3	R4	R5	gradient
X	$1.07^{+0.50}_{-0.05}$	$1.07^{+0.51}_{-0.05}$	$2.16^{+0.55}_{-0.74}$	$1.22^{+1.07}_{-0.14}$	$2.71^{+0.53}_{-1.10}$	0.49±0.36
[Z/H]	$0.24^{+0.04}_{-0.05}$	$0.14^{+0.03}_{-0.04}$	$-0.03^{+0.06}_{-0.11}$	$-0.07^{+0.09}_{-0.13}$	$-0.15^{+0.13}_{-0.15}$	–0.22±0.05
[Fe/H]	$-0.07^{+0.07}_{-0.06}$	$-0.19^{+0.05}_{-0.07}$	$-0.26^{+0.08}_{-0.12}$	$-0.31^{+0.12}_{-0.13}$	$-0.25^{+0.14}_{-0.18}$	–0.13±0.04
[Mg/Fe]	$0.41^{+0.06}_{-0.05}$	$0.44^{+0.05}_{-0.05}$	$0.40^{+0.09}_{-0.07}$	$0.43^{+0.10}_{-0.12}$	$0.28^{+0.15}_{-0.14}$	–0.03±0.03
[Na/Fe]	$0.84^{+0.09}_{-0.09}$	$0.73^{+0.06}_{-0.07}$	$0.43^{+0.15}_{-0.27}$	$0.35^{+0.27}_{-0.38}$	$-0.12^{+0.47}_{-0.31}$	–0.38±0.13
[Ca/Fe]	$0.17^{+0.08}_{-0.08}$	$0.16^{+0.07}_{-0.06}$	$0.11^{+0.10}_{-0.10}$	$0.04^{+0.14}_{-0.14}$	$-0.01^{+0.15}_{-0.21}$	–0.08±0.04
[K/Fe]	$0.16^{+0.12}_{-0.14}$	$0.11^{+0.11}_{-0.10}$	$0.06^{+0.23}_{-0.18}$	$0.16^{+0.22}_{-0.23}$	$0.19^{+0.27}_{-0.30}$	–0.00±0.08
f_{dwarf}	$2.2^{+1.5}_{-0.2}\%$	$2.2^{+1.6}_{-0.1}\%$	$2.9^{+7.0}_{-0.6}\%$	$2.8^{+6.0}_{-0.5}\%$	$3.2^{+13.0}_{-0.9}\%$	0.3±2.7%
M/L	$0.70^{+0.18}_{-0.02}$	$0.69^{+0.18}_{-0.02}$	$0.79^{+0.96}_{-0.08}$	$0.78^{+0.82}_{-0.08}$	$0.86^{+2.04}_{-0.13}$	0.04±0.35

Table 6.3: The results presented in Table 4.5, with the parameters reorganised to match those presented in Table 6.2.

	R1	R2	R3	R4	R5	gradient
[Fe/H]	$0.06^{+0.03}_{-0.03}$	$-0.06^{+0.03}_{-0.03}$	$-0.21^{+0.05}_{-0.05}$	$-0.21^{+0.08}_{-0.08}$	$-0.21^{+0.10}_{-0.10}$	–0.17±0.02
[α/Fe]	$0.34^{+0.04}_{-0.04}$	$0.34^{+0.04}_{-0.04}$	$0.33^{+0.06}_{-0.06}$	$0.31^{+0.09}_{-0.09}$	$0.21^{+0.12}_{-0.12}$	–0.03±0.02
[Na/Fe]	$0.62^{+0.12}_{-0.12}$	$0.53^{+0.08}_{-0.08}$	$0.21^{+0.16}_{-0.19}$	$0.21^{+0.25}_{-0.35}$	$-0.15^{+0.45}_{-0.50}$	–0.31±0.07
[Ca/Fe]	$-0.02^{+0.06}_{-0.06}$	$0.00^{+0.06}_{-0.06}$	$0.02^{+0.08}_{-0.08}$	$-0.10^{+0.13}_{-0.13}$	$-0.22^{+0.18}_{-0.08}$	–0.03±0.02
f_{dwarf}	$9.4^{+2.1}_{-2.1}\%$	$11.1^{+1.5}_{-1.5}\%$	$10.5^{+2.1}_{-2.2}\%$	$6.7^{+3.9}_{-1.6}\%$	$8.0^{+5.6}_{-2.5}\%$	–0.6±0.8%

we infer a stronger enhancement than in the previous chapter, although the two results are not strongly in tension and we find a consistent gradient. Finally, the IMF we infer is more Milky Way-like, rather than modestly bottom-heavy as found previously. In summary, using the updated models we find qualitatively similar results to those which were presented in Chapter 4.

These results are more readily compared with the literature than in the form presented in Chapter 4. It is instructive to make a comparison with the results of McDermid et al. (2015), which were calculated via the models of Schiavon (2007) using the same optical data we used for our analysis (and assuming no IMF variations). In the central $0.125\,R_{eff}$ of the galaxies from our sample (excluding NGC 1407, which they did not observe) the median age they find is 13.7 ± 2.1 Gyr, the median [Z/H] = 0.06 ± 0.05, and the median [α/Fe] is 0.28 ± 0.05. The latter is a little lower than our value, which may be due to the different models used, the extra indices we fit, the use of additional parameters we include, or a combination of all of these.

In the next section we present the results of our full analysis, making use of the K-band data, additional stellar population parameters, and the data from individual galaxies.

6.2 Results from KMOS data

We now run the updated SPINDRIFT code (first described in Chapter 2) with the KMOS measurements of the K-band indices included in the fit. In addition, we include Hβ in the fit: in Chapter 4 we showed that Hβ's sensitivity in the CvD models to various poorly constrained parameters, such a [C/H] and stellar age, reduced its constraining power substantially. However, with the additional sensitivity to these parameters provided by the CO bandhead our ability to constrain these parameters improves somewhat, which makes Hβ a more useful constraint in the context of the model framework used (note that in other models Hβ does not show sensitivity to [C/H], e.g. Thomas et al., 2011b).

While we do not expect to be able to constrain the abundance of α elements other than Mg and Ca, we nevertheless include the parameters [Ti/Fe] and [O,Ne,S/Fe] in order to marginalise over them.

To obtain these results we made use of all available feature measurements, with two

Table 6.4: Headline results for this chapter: estimated parameter values for the stacked spectra, acquired using the updated models and the full set of index measurements. For the IMF we fit a two-part power law with slopes X1 and X2, and we fit for stellar population age and total metallicity, as well as the abundances of various elements of interest. R1 and R2 correspond to the two extraction regions in the central IFU ($< 0.7''$, $> 0.7''$) while R3, R4, and R5 correspond to the rings of IFUs arranged at $\sim 1/3\,\mathrm{R_{eff}}$, $\sim 2/3\,\mathrm{R_{eff}}$, and $\sim \mathrm{R_{eff}}$.

	R1	R2	R3	R4	R5	gradient
age /Gyr	$11.3^{+1.4}_{-1.3}$	$9.1^{+1.0}_{-0.7}$	$7.8^{+2.2}_{-0.5}$	$7.3^{+3.3}_{-0.2}$	$8.9^{+2.5}_{-1.2}$	–1.8±0.8
X1	$2.01^{+0.51}_{-0.67}$	$1.10^{+0.67}_{-0.07}$	$1.12^{+0.86}_{-0.08}$	$1.98^{+0.66}_{-0.65}$	$2.86^{+0.41}_{-1.09}$	0.26±0.39
X2	$1.24^{+0.90}_{-0.16}$	$1.06^{+0.43}_{-0.05}$	$1.49^{+0.87}_{-0.32}$	$1.52^{+0.96}_{-0.35}$	$1.82^{+1.02}_{-0.53}$	0.31±0.40
[Z/H]	$0.17^{+0.03}_{-0.04}$	$0.23^{+0.02}_{-0.02}$	$0.14^{+0.04}_{-0.05}$	$0.02^{+0.07}_{-0.11}$	$-0.14^{+0.13}_{-0.11}$	–0.11±0.03
[Fe/H]	$-0.12^{+0.07}_{-0.11}$	$-0.08^{+0.05}_{-0.06}$	$-0.26^{+0.14}_{-0.07}$	$-0.33^{+0.15}_{-0.13}$	$-0.30^{+0.20}_{-0.18}$	–0.16±0.05
[Mg/Fe]	$0.48^{+0.10}_{-0.05}$	$0.44^{+0.05}_{-0.05}$	$0.42^{+0.08}_{-0.10}$	$0.51^{+0.12}_{-0.14}$	$0.38^{+0.17}_{-0.17}$	–0.01±0.04
[Na/Fe]	$0.77^{+0.12}_{-0.10}$	$0.70^{+0.06}_{-0.05}$	$0.43^{+0.13}_{-0.16}$	$0.34^{+0.21}_{-0.35}$	$-0.11^{+0.40}_{-0.31}$	–0.35±0.09
[Ca/Fe]	$0.20^{+0.11}_{-0.07}$	$0.09^{+0.06}_{-0.05}$	$0.09^{+0.11}_{-0.09}$	$0.11^{+0.17}_{-0.14}$	$0.08^{+0.16}_{-0.25}$	–0.04±0.05
[O, Ne, S/Fe]	$0.78^{+0.13}_{-0.19}$	$0.64^{+0.09}_{-0.10}$	$0.73^{+0.14}_{-0.15}$	$0.70^{+0.19}_{-0.23}$	$0.73^{+0.19}_{-0.40}$	0.02±0.06
[Ti/Fe]	$0.53^{+0.18}_{-0.16}$	$0.22^{+0.12}_{-0.10}$	$0.18^{+0.19}_{-0.25}$	$0.57^{+0.23}_{-0.33}$	$0.39^{+0.31}_{-0.46}$	–0.05±0.11
[C/Fe]	$0.11^{+0.10}_{-0.14}$	$0.07^{+0.05}_{-0.08}$	$0.15^{+0.12}_{-0.13}$	$0.22^{+0.16}_{-0.18}$	$0.09^{+0.24}_{-0.20}$	0.06±0.04
[K/Fe]	$0.19^{+0.17}_{-0.13}$	$0.07^{+0.11}_{-0.06}$	$0.19^{+0.15}_{-0.16}$	$0.25^{+0.21}_{-0.20}$	$0.17^{+0.29}_{-0.29}$	0.06±0.05
$\mathrm{f_{dwarf}}$	$3.9^{+2.8}_{-0.9}\%$	$2.7^{+1.3}_{-0.4}\%$	$4.9^{+2.0}_{-1.5}\%$	$5.7^{+3.0}_{-2.0}\%$	$6.5^{+5.7}_{-2.2}\%$	2.0±1.7%
M/L	$0.91^{+0.37}_{-0.12}$	$0.75^{+0.16}_{-0.05}$	$0.95^{+0.28}_{-0.14}$	$1.04^{+0.45}_{-0.21}$	$1.32^{+0.85}_{-0.35}$	0.19±0.13

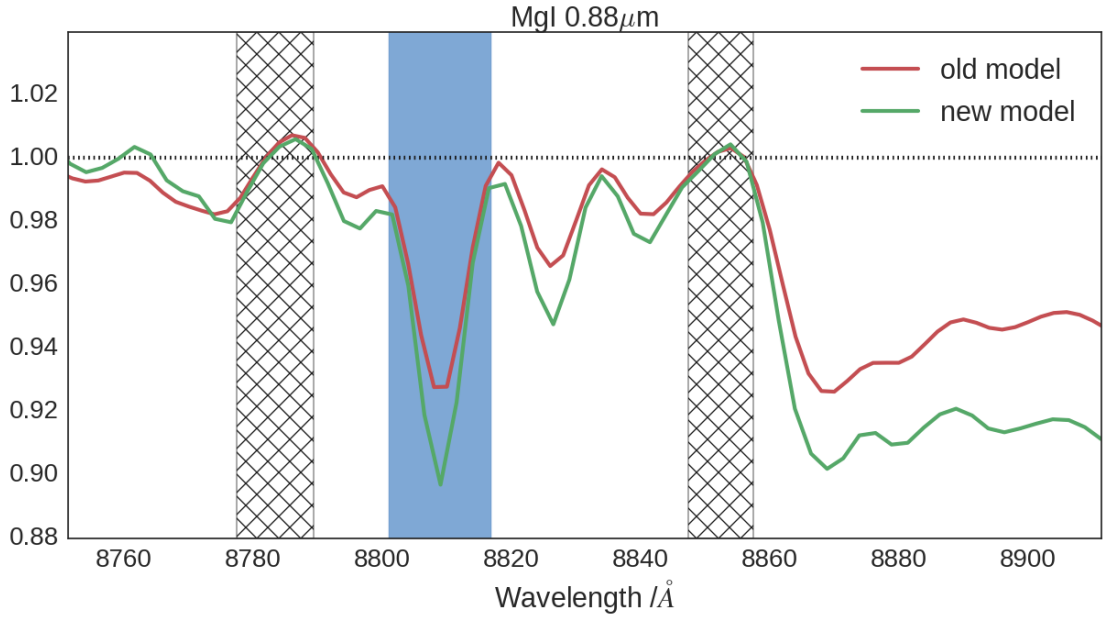

Figure 6.1: We show a fiducial case for the old and new SSP model grids, with a Kroupa IMF, solar abundance pattern, and a stellar population age of 13.5 Gyr. In the updated model grids (which we remind the reader are constructed from an expanded empirical spectral library) the Mg I 0.88 µm feature (the region around which we show here alongside feature and pseudcontinuum definitions) is much stronger.

exceptions. First, we found that in the updated model framework the MgI 0.88 µm line is much stronger, given the same stellar population parameter values, and that this places it in tension with the data (we show the change to the models in Fig. 6.1). Secondly, we were concerned that the CO 2.30 µm b line might be subject to much greater contamination (from a combination of increasing thermal background, stronger telluric absorption, and sky emission lines) than the CO 2.30 µm a line, although in the models the strengths of the two are strongly coupled. We therefore used only the a line in the fit. For this strong feature the formal statistical uncertainty of the equivalent width is small, so we lose very little constraining power by doing this.

In Table 6.4 we give the best-fit stellar population parameters inferred from the stacked spectra and provide best-fit parameter gradients with associated statistical uncertainty. All MCMC runs used 100 walkers and 900 steps after a 100 step burn-in.

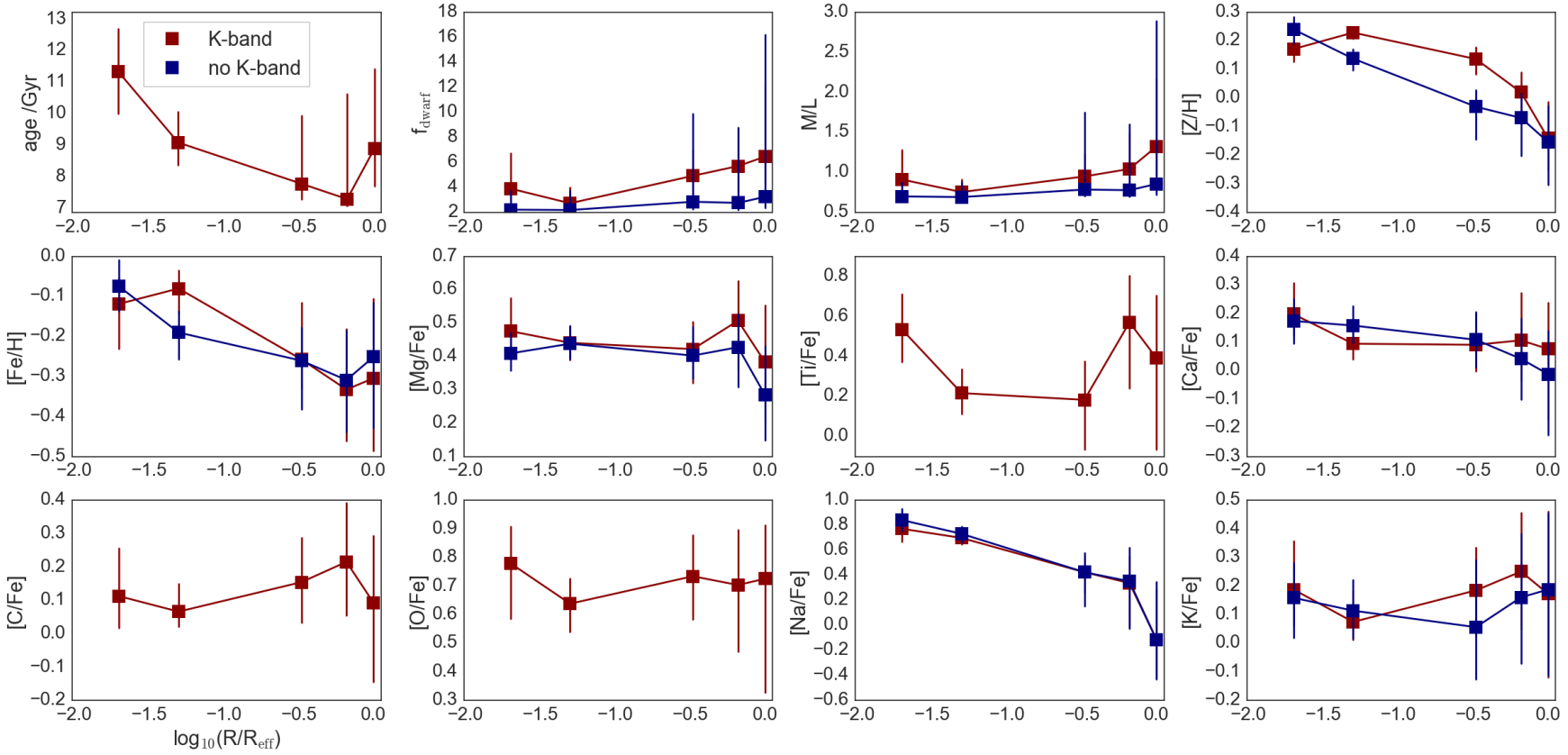

Figure 6.2: Parameter radial variations via two model fits. The parameters inferred from the stacked spectra using only a limited set of indices and a restricted parameter set are shown in blue, while those inferred when data from the K-band and Hβ and additional model parameters are included are shown in red. Generally, as expected, our results are not radically altered with respect to those obtained previously, although the best-fit [Z/H] is an exception. N.B. a Milky Way-like IMF corresponds to $f_{dwarf} = 4.3$, M/L = 1.

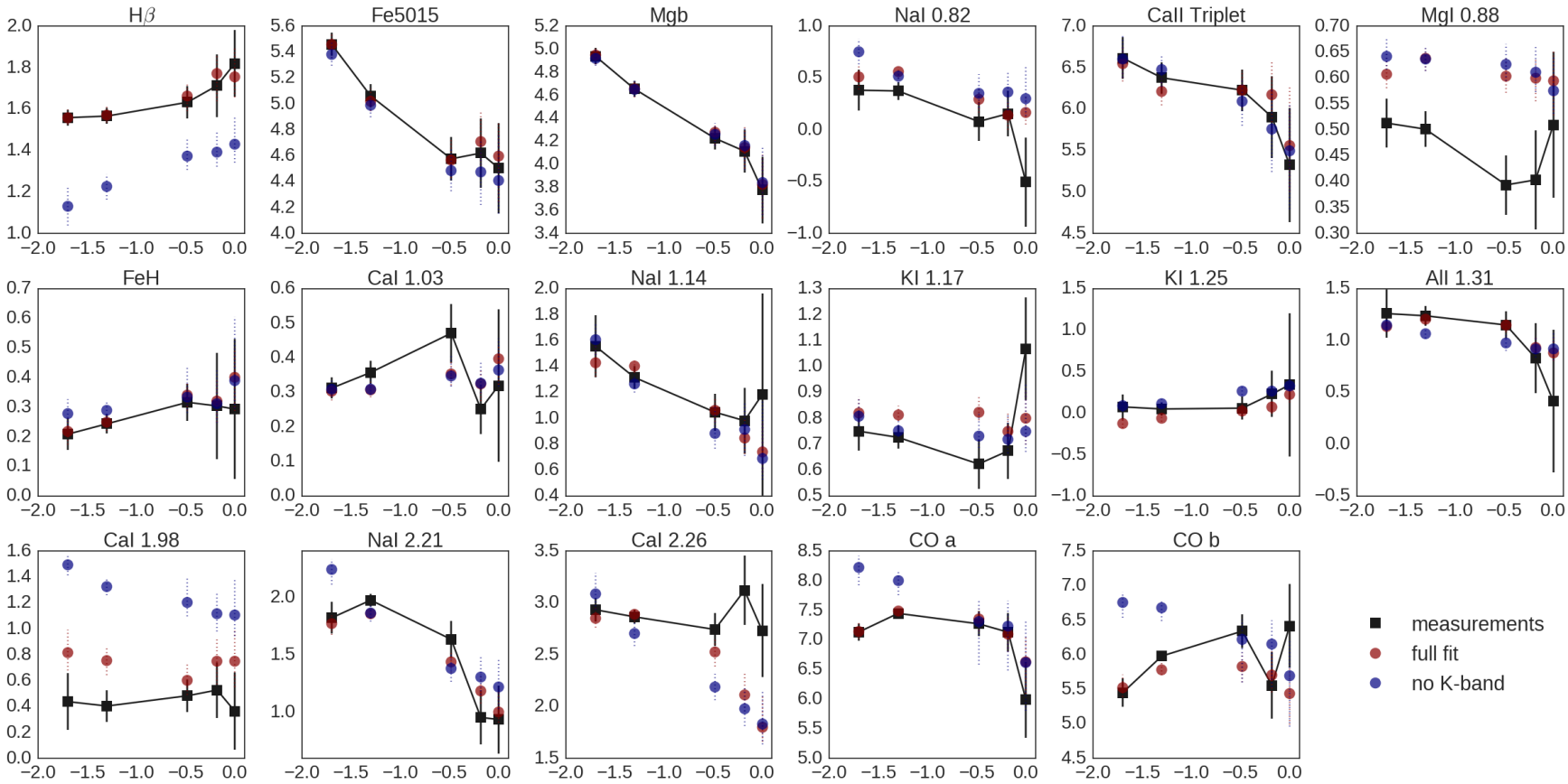

Figure 6.3: Two sets of model predictions generated from the parameters shown in Fig. 6.2. The simpler model (blue) was not fit to Hβ, Mg I 0.88µm, Al I 1.31µm, or any of the K-band indices. The more complex model uses more parameters and is fit to Hβ and the K-band features (except CO *b*).

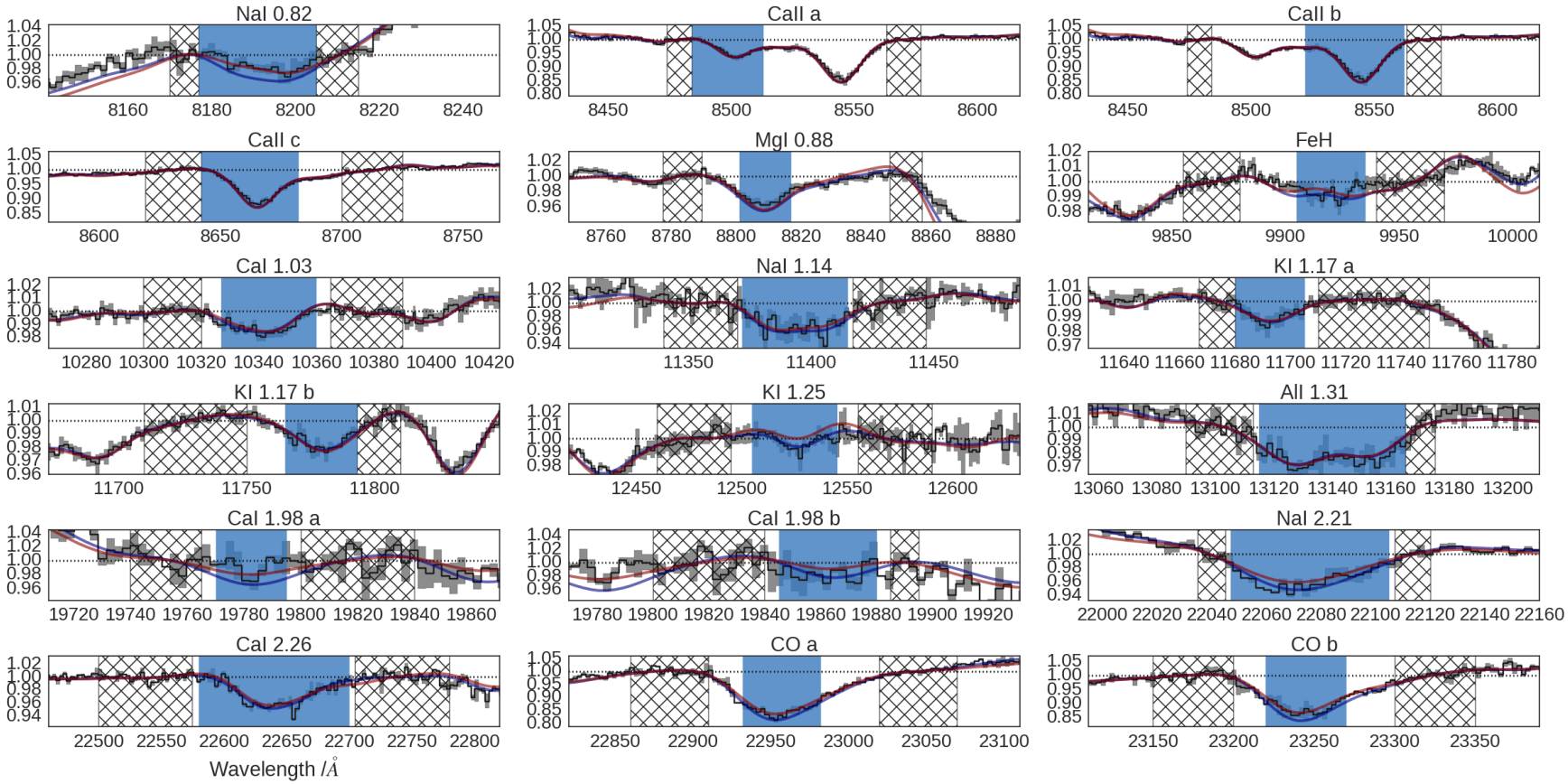

Figure 6.4: The centrally extracted stacked spectrum in the region of each index definition with shaded uncertainties, alongside models generated from the parameters shown in Fig. 6.2 (same colour scheme). The feature band for each index is shaded blue, while the pseudo-continuum regions are hatched. Although the model parameters are inferred from the measured equivalent widths, in most cases the models match the data within the uncertainties fairly well, especially for the strongest features.

6.2.1 Comparison with results from Chapter 4

Including the K-band measurements and additional model parameters modifies our results to some extent. In Fig. 6.2 we show the parameters inferred from the stacks using only a limited set of indices and parameters (blue) and those inferred when data from the K-band and Hβ are included (red). Generally, as expected, our results are not radically altered with respect to those obtained previously, although the best-fit [Z/H] is an exception. The inferred IMF is consistent with Milky Way-like throughout. The inferred age is consistent being constant with radius (approx. 11 Gyr) or else gradually declining with radius. While we initially assumed an extremely old stellar population (13.7 Gyr old) this slight difference does not in practice affect the inferred values of the other model parameters.

In Fig. 6.3 we compare the two sets of model predictions to the actual measured line indices. This demonstrates several key points. For the most part, the simpler model reproduces the optical, IZ band, and YJ band indices adequately. However, as in Chapter 4 it is challenging to simultaneously fit Na I 0.82 μm and Na I 1.14 μm. By contrast, the updated model now underpredicts Hβ, whereas before it tended towards overprediction. As noted in Chapter 4, increased abundance of carbon can weaken Hβ. The inclusion of a metallicity parameter in the model means we now implicitly assume [C/H] rises in the core along with the α-elements and Fe, explaining this change. Likewise, while the CvD model grids do not include variations in [Al/Fe], the Al I 1.31 μm feature's strength is no longer in strong tension with the model, suggesting that the assumption that aluminium tracks overall metallicity is reasonable. This is a significant advantage of the new model formalism.

However, the simpler model does a poor job of predicting the K-band indices (we remind the reader that the simpler model was not fit to these indices). This shows that the K-band indices are adding useful information, which we take advantage of by using the more sophisticated model with additional parameters (a two-part power law IMF, stellar population age, [C/Fe], [Ti/Fe], and [O,Ne,S/Fe]). This model does a much better, though still imperfect job of fitting the K-band data, without compromising the fit to the bluer spectral features.

In Fig. 6.4 we show how the spectral models corresponding to these parameters appear

when directly compared to the data. Specifically, we show the spectral region around each index for the centrally extracted stack, normalised by the pseudo-continuum bands on either side of each feature. This allows us to view the stacked spectrum precisely as it appears when the index measurements are made. We remind the reader that the shaded regions of uncertainty correspond to the scatter amongst the spectra used to construct the stack, rather than the formal statistical error. We constructed the overplotted spectral models by linear interpolation of the CvD models, broadening this model to the velocity dispersion found using pPXF. This allows us to closely examine those features where the measured index strength is less well-fit by the model and perhaps determine the cause.

6.2.2 Full results for individual galaxies

In this section we examine the results for individual galaxies, comparing these with the average radial trends obtained from the stacked data. We fit these galaxies with the same set of model parameters and features as the stack where possible, although for some galaxies a full set of features is not available (note that we do not provide fits for NGC 4486 since, as noted in Chapter 4, the optical data suffer from contamination by AGN emission). Results are provided for the three innermost extraction regions (the subdivided central IFU field and the innermost ring of IFUs at $\sim \frac{1}{3}\,\mathrm{R_{eff}}$) where the S/N is sufficient. For each extraction region we present a table of results spanning the full sample (see Tables 6.5, 6.6, and 6.7). These results are presented in graphical form for key parameters in Fig. 6.5.

Table 6.5: Estimated parameter values for the spectra extracted at $\sim 0.02\,R_{\rm eff}$, acquired using the updated models and the full set of index measurements. We fit for population age, a two-part power law IMF, and [Z/H], as well as the abundances of various elements of interest. Note that we did not obtain additional K-band data for NGC 0524 but have nonetheless fit the data via the updated model formalism.

	NGC 0524	NGC 1407	NGC 3377	NGC 3379	NGC 4552	NGC 4621	NGC 5813
age /Gyr	$10.2^{+2.40}_{-1.96}$	$7.36^{+2.85}_{-0.25}$	$7.08^{+0.58}_{-0.06}$	$7.11^{+0.89}_{-0.07}$	$7.09^{+0.62}_{-0.06}$	$12.69^{+0.87}_{-2.33}$	$8.04^{+2.24}_{-0.73}$
X1	$2.06^{+0.73}_{-0.70}$	$1.83^{+0.59}_{-0.54}$	$2.68^{+0.38}_{-1.02}$	$1.10^{+0.89}_{-0.07}$	$2.47^{+0.55}_{-0.92}$	$1.24^{+0.66}_{-0.16}$	$1.56^{+0.71}_{-0.38}$
X2	$1.46^{+1.10}_{-0.29}$	$1.16^{+1.31}_{-0.11}$	$1.10^{+0.74}_{-0.07}$	$1.22^{+0.44}_{-0.15}$	$1.16^{+1.14}_{-0.11}$	$1.08^{+0.53}_{-0.05}$	$2.04^{+0.87}_{-0.66}$
[Z/H]	$0.09^{+0.06}_{-0.08}$	$0.17^{+0.10}_{-0.17}$	$0.15^{+0.04}_{-0.04}$	$0.24^{+0.06}_{-0.05}$	$0.28^{+0.04}_{-0.05}$	$0.22^{+0.05}_{-0.05}$	$0.13^{+0.06}_{-0.05}$
[Fe/H]	$0.04^{+0.09}_{-0.17}$	$-0.21^{+0.17}_{-0.13}$	$-0.07^{+0.08}_{-0.11}$	$-0.17^{+0.06}_{-0.06}$	$0.24^{+0.05}_{-0.10}$	$0.13^{+0.06}_{-0.06}$	$-0.18^{+0.11}_{-0.10}$
[Mg/Fe]	$0.38^{+0.12}_{-0.08}$	$0.79^{+0.14}_{-0.34}$	$0.34^{+0.10}_{-0.05}$	$0.55^{+0.06}_{-0.05}$	$0.40^{+0.06}_{-0.07}$	$0.25^{+0.06}_{-0.06}$	$0.60^{+0.09}_{-0.09}$
[Na/Fe]	$0.35^{+0.09}_{-0.09}$	$0.71^{+0.15}_{-0.30}$	$0.62^{+0.08}_{-0.08}$	$0.73^{+0.07}_{-0.09}$	$0.90^{+0.06}_{-0.06}$	$0.82^{+0.05}_{-0.05}$	$0.59^{+0.11}_{-0.10}$
[Ca/Fe]	$0.13^{+0.14}_{-0.07}$	$0.36^{+0.15}_{-0.12}$	$0.01^{+0.09}_{-0.06}$	$0.26^{+0.05}_{-0.06}$	$0.04^{+0.08}_{-0.05}$	$0.12^{+0.04}_{-0.06}$	$0.29^{+0.08}_{-0.10}$
[O, Ne, S/Fe]	$-0.24^{+0.22}_{-0.19}$	$-0.05^{+0.63}_{-0.19}$	$0.55^{+0.16}_{-0.12}$	$0.89^{+0.10}_{-0.17}$	$-0.13^{+0.16}_{-0.22}$	$0.61^{+0.07}_{-0.09}$	$0.53^{+0.22}_{-0.20}$
[Ti/Fe]	$0.39^{+0.24}_{-0.18}$	$0.84^{+0.13}_{-0.43}$	$0.40^{+0.19}_{-0.14}$	$0.64^{+0.12}_{-0.11}$	$0.23^{+0.15}_{-0.14}$	$-0.23^{+0.13}_{-0.09}$	$0.71^{+0.16}_{-0.20}$
[C/Fe]	$0.16^{+0.15}_{-0.22}$	$0.20^{+0.18}_{-0.15}$	$0.36^{+0.12}_{-0.08}$	$0.61^{+0.06}_{-0.06}$	$0.16^{+0.08}_{-0.10}$	$0.12^{+0.08}_{-0.09}$	$0.14^{+0.15}_{-0.12}$
[K/Fe]	$0.17^{+0.17}_{-0.19}$	$0.55^{+0.11}_{-0.35}$	$0.15^{+0.16}_{-0.15}$	$0.36^{+0.22}_{-0.15}$	$-0.05^{+0.18}_{-0.13}$	$0.09^{+0.13}_{-0.16}$	$0.13^{+0.23}_{-0.12}$
$f_{\rm dwarf}$ (%)	$4.83^{+4.97}_{-1.60}$	$4.41^{+3.60}_{-1.06}$	$4.92^{+2.87}_{-1.57}$	$3.12^{+1.53}_{-0.56}$	$6.61^{+3.11}_{-2.32}$	$3.06^{+1.29}_{-0.55}$	$5.71^{+2.81}_{-1.74}$
M/L	$1.04^{+0.71}_{-0.22}$	$1.00^{+0.45}_{-0.15}$	$1.00^{+0.48}_{-0.18}$	$0.80^{+0.21}_{-0.07}$	$1.08^{+0.58}_{-0.21}$	$0.79^{+0.17}_{-0.06}$	$1.11^{+0.34}_{-0.21}$

Table 6.6: Estimated parameter values for the spectra extracted at $\sim 0.05\,R_{\rm eff}$, acquired using the updated models and the full set of index measurements. We fit for population age, a two-part power law IMF, and [Z/H], as well as the abundances of various elements of interest. Note that we did not obtain additional K-band data for NGC 0524 but have nonetheless fit the data via the updated model formalism.

	NGC 0524	NGC 1407	NGC 3377	NGC 3379	NGC 4552	NGC 4621	NGC 5813
age /Gyr	$13.54^{+0.32}_{-3.72}$	$8.92^{+2.84}_{-1.32}$	$7.16^{+1.12}_{-0.11}$	$7.26^{+1.90}_{-0.19}$	$7.09^{+0.54}_{-0.06}$	$10.61^{+1.74}_{-2.04}$	$7.48^{+3.70}_{-0.33}$
X1	$2.27^{+0.53}_{-0.77}$	$1.50^{+1.06}_{-0.33}$	$2.45^{+0.58}_{-0.64}$	$1.10^{+1.01}_{-0.07}$	$3.36^{+0.10}_{-1.09}$	$1.20^{+0.84}_{-0.14}$	$1.88^{+0.67}_{-0.57}$
X2	$1.14^{+1.43}_{-0.09}$	$2.08^{+0.79}_{-0.69}$	$1.09^{+0.49}_{-0.06}$	$1.10^{+0.63}_{-0.07}$	$2.14^{+0.62}_{-0.60}$	$1.11^{+0.97}_{-0.08}$	$3.29^{+0.14}_{-1.63}$
[Z/H]	$-0.01^{+0.06}_{-0.12}$	$-0.21^{+0.26}_{-0.16}$	$0.01^{+0.04}_{-0.05}$	$0.11^{+0.07}_{-0.06}$	$0.23^{+0.05}_{-0.05}$	$0.17^{+0.06}_{-0.05}$	$0.08^{+0.08}_{-0.08}$
[Fe/H]	$-0.13^{+0.09}_{-0.13}$	$-0.32^{+0.18}_{-0.24}$	$-0.43^{+0.10}_{-0.07}$	$-0.26^{+0.07}_{-0.08}$	$-0.05^{+0.09}_{-0.10}$	$0.02^{+0.06}_{-0.09}$	$-0.12^{+0.10}_{-0.16}$
[Mg/Fe]	$0.42^{+0.12}_{-0.08}$	$0.49^{+0.28}_{-0.36}$	$0.51^{+0.08}_{-0.09}$	$0.63^{+0.05}_{-0.08}$	$0.53^{+0.10}_{-0.07}$	$0.35^{+0.07}_{-0.06}$	$0.47^{+0.13}_{-0.08}$
[Na/Fe]	$0.22^{+0.12}_{-0.11}$	$0.77^{+0.15}_{-0.26}$	$0.79^{+0.07}_{-0.12}$	$0.71^{+0.07}_{-0.13}$	$0.89^{+0.08}_{-0.06}$	$0.72^{+0.08}_{-0.05}$	$0.53^{+0.11}_{-0.09}$
[Ca/Fe]	$0.15^{+0.12}_{-0.06}$	$0.45^{+0.15}_{-0.17}$	$0.38^{+0.06}_{-0.09}$	$0.27^{+0.05}_{-0.08}$	$0.18^{+0.10}_{-0.07}$	$0.18^{+0.06}_{-0.05}$	$0.21^{+0.14}_{-0.06}$
[O, Ne, S/Fe]	$0.31^{+0.22}_{-0.25}$	$0.43^{+0.30}_{-0.43}$	$0.69^{+0.19}_{-0.15}$	$0.80^{+0.14}_{-0.31}$	$0.10^{+0.14}_{-0.23}$	$0.68^{+0.09}_{-0.11}$	$0.41^{+0.25}_{-0.19}$
[Ti/Fe]	$0.33^{+0.24}_{-0.25}$	$0.35^{+0.39}_{-0.33}$	$0.79^{+0.18}_{-0.20}$	$0.71^{+0.14}_{-0.15}$	$0.64^{+0.16}_{-0.15}$	$-0.11^{+0.17}_{-0.10}$	$0.31^{+0.31}_{-0.18}$
[C/Fe]	$0.20^{+0.14}_{-0.23}$	$0.16^{+0.28}_{-0.16}$	$0.50^{+0.11}_{-0.11}$	$0.58^{+0.08}_{-0.10}$	$0.36^{+0.09}_{-0.14}$	$0.24^{+0.09}_{-0.11}$	$0.14^{+0.16}_{-0.15}$
[K/Fe]	$0.15^{+0.16}_{-0.17}$	$0.25^{+0.25}_{-0.26}$	$0.67^{+0.06}_{-0.17}$	$0.44^{+0.16}_{-0.22}$	$0.26^{+0.14}_{-0.15}$	$0.09^{+0.12}_{-0.13}$	$-0.05^{+0.16}_{-0.08}$
$f_{\rm dwarf}$ (%)	$6.58^{+3.72}_{-2.34}$	$5.23^{+4.32}_{-1.63}$	$4.89^{+2.59}_{-1.36}$	$3.96^{+1.62}_{-1.09}$	$10.66^{+3.04}_{-3.16}$	$4.14^{+1.93}_{-1.06}$	$4.35^{+5.04}_{-1.13}$
M/L	$1.31^{+0.50}_{-0.35}$	$1.07^{+0.60}_{-0.21}$	$1.04^{+0.44}_{-0.19}$	$0.89^{+0.24}_{-0.13}$	$1.93^{+0.55}_{-0.55}$	$0.94^{+0.24}_{-0.14}$	$0.93^{+0.66}_{-0.13}$

Table 6.7: Estimated parameter values for the spectra extracted at $\sim \frac{1}{3}R_{\rm eff}$, acquired using the updated models and the full set of index measurements. We fit for population age, a two-part power law IMF, and [Z/H], as well as the abundances of various elements of interest. Note that we did not obtain additional K-band data for NGC 0524 but have nonetheless fit the data via the updated model formalism.

	NGC 0524	NGC 1407	NGC 3377	NGC 3379	NGC 4552	NGC 4621	NGC 5813
age /Gyr	$11.18^{+1.80}_{-2.54}$	$7.45^{+3.34}_{-0.29}$	$9.14^{+2.86}_{-1.44}$	$8.89^{+1.98}_{-1.22}$	$8.56^{+3.23}_{-0.99}$	$10.04^{+2.29}_{-1.84}$	$9.69^{+2.93}_{-1.74}$
X1	$2.37^{+0.67}_{-0.88}$	$1.66^{+0.80}_{-0.45}$	$1.73^{+0.88}_{-0.48}$	$2.12^{+0.63}_{-0.76}$	$2.50^{+0.59}_{-0.89}$	$1.86^{+0.81}_{-0.57}$	$3.05^{+0.28}_{-1.23}$
X2	$2.61^{+0.55}_{-1.07}$	$1.12^{+1.10}_{-0.08}$	$1.26^{+1.19}_{-0.17}$	$2.10^{+0.81}_{-0.68}$	$3.30^{+0.13}_{-1.40}$	$1.31^{+0.96}_{-0.21}$	$1.22^{+1.36}_{-0.15}$
[Z/H]	$-0.08^{+0.11}_{-0.14}$	$0.36^{+0.03}_{-0.25}$	$-0.43^{+0.14}_{-0.27}$	$0.03^{+0.10}_{-0.09}$	$0.02^{+0.09}_{-0.12}$	$0.07^{+0.09}_{-0.10}$	$-0.15^{+0.16}_{-0.18}$
[Fe/H]	$0.05^{+0.10}_{-0.17}$	$-0.06^{+0.17}_{-0.16}$	$-0.53^{+0.16}_{-0.30}$	$-0.25^{+0.14}_{-0.12}$	$-0.33^{+0.21}_{-0.13}$	$-0.25^{+0.15}_{-0.13}$	$-0.18^{+0.15}_{-0.30}$
[Mg/Fe]	$0.18^{+0.17}_{-0.09}$	$0.59^{+0.26}_{-0.31}$	$0.48^{+0.29}_{-0.20}$	$0.49^{+0.12}_{-0.11}$	$0.59^{+0.16}_{-0.15}$	$0.33^{+0.15}_{-0.10}$	$0.43^{+0.24}_{-0.17}$
[Na/Fe]	$-0.16^{+0.25}_{-0.27}$	$-0.07^{+0.17}_{-0.24}$	$-0.11^{+0.74}_{-0.27}$	$0.87^{+0.19}_{-0.16}$	$0.92^{+0.18}_{-0.21}$	$0.31^{+0.22}_{-0.20}$	$0.03^{+0.59}_{-0.40}$
[Ca/Fe]	$-0.12^{+0.17}_{-0.10}$	$0.08^{+0.20}_{-0.15}$	$0.18^{+0.28}_{-0.17}$	$0.35^{+0.09}_{-0.15}$	$0.36^{+0.13}_{-0.18}$	$0.07^{+0.11}_{-0.15}$	$0.17^{+0.20}_{-0.27}$
[O, Ne, S/Fe]	$-0.24^{+0.32}_{-0.28}$	$0.61^{+0.25}_{-0.47}$	$0.25^{+0.47}_{-0.34}$	$0.56^{+0.28}_{-0.52}$	$0.29^{+0.33}_{-0.26}$	$0.81^{+0.15}_{-0.18}$	$0.15^{+0.51}_{-0.43}$
[Ti/Fe]	$-0.09^{+0.36}_{-0.24}$	$0.67^{+0.18}_{-0.39}$	$0.51^{+0.37}_{-0.32}$	$0.23^{+0.33}_{-0.26}$	$0.64^{+0.22}_{-0.33}$	$0.02^{+0.31}_{-0.16}$	$0.22^{+0.46}_{-0.37}$
[C/Fe]	$-0.16^{+0.24}_{-0.18}$	$0.17^{+0.20}_{-0.19}$	$0.14^{+0.28}_{-0.31}$	$0.26^{+0.18}_{-0.15}$	$0.24^{+0.18}_{-0.19}$	$0.22^{+0.16}_{-0.16}$	$0.03^{+0.33}_{-0.22}$
[K/Fe]	$-0.35^{+0.32}_{-0.10}$	$0.15^{+0.31}_{-0.21}$	$0.05^{+0.31}_{-0.26}$	$0.24^{+0.25}_{-0.21}$	$0.16^{+0.26}_{-0.20}$	$0.19^{+0.28}_{-0.17}$	$0.21^{+0.21}_{-0.31}$
$f_{\rm dwarf}$ (%)	$7.00^{+5.31}_{-2.63}$	$4.47^{+3.52}_{-1.43}$	$3.96^{+4.84}_{-1.04}$	$7.18^{+3.10}_{-2.86}$	$8.56^{+4.43}_{-3.00}$	$4.53^{+3.75}_{-1.29}$	$8.59^{+5.40}_{-4.16}$
M/L	$1.27^{+0.84}_{-0.33}$	$0.93^{+0.49}_{-0.15}$	$0.89^{+0.65}_{-0.12}$	$1.35^{+0.47}_{-0.40}$	$1.34^{+0.77}_{-0.31}$	$0.99^{+0.53}_{-0.17}$	$0.97^{+1.03}_{-0.17}$

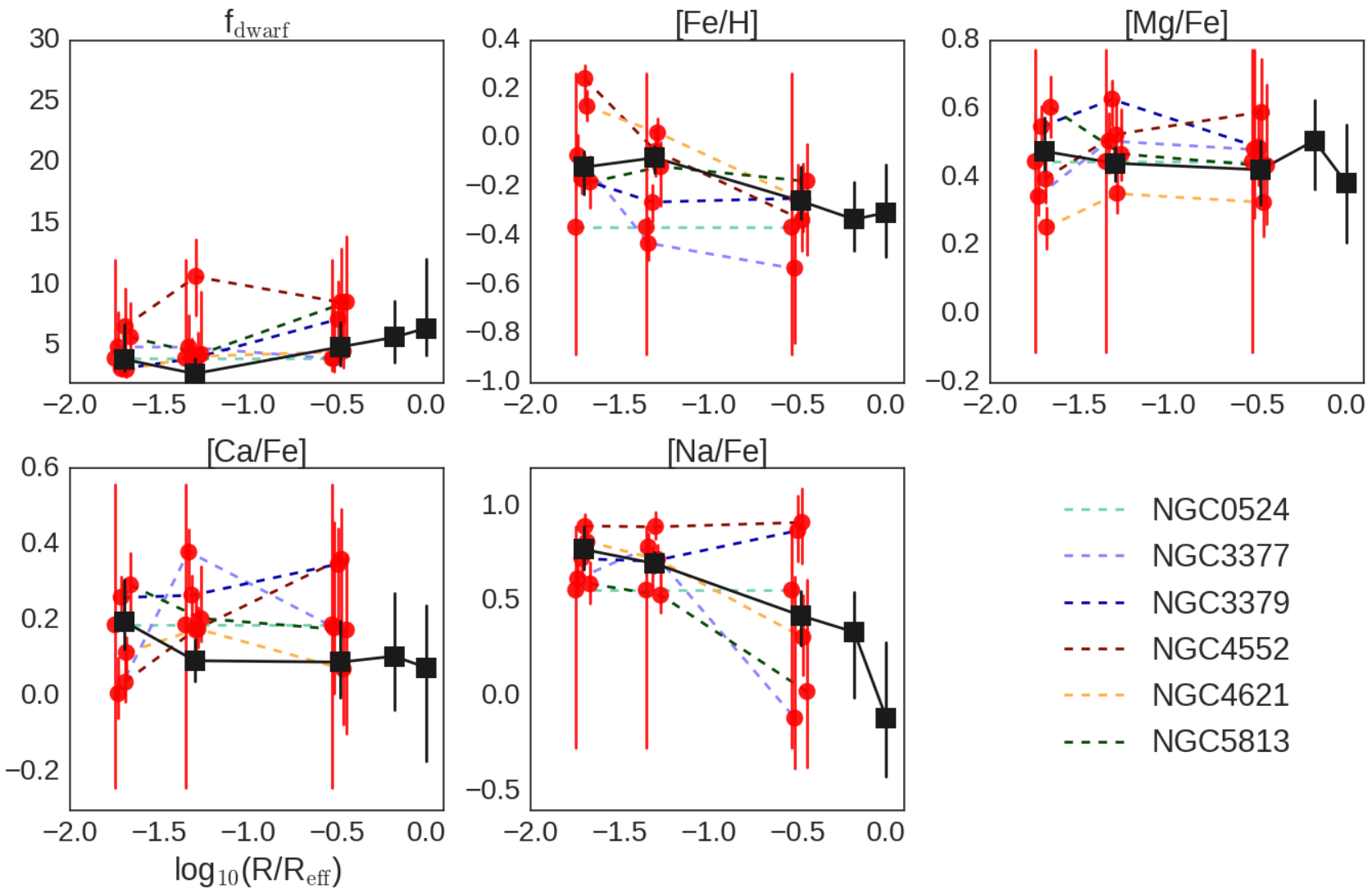

Figure 6.5: Stellar population fitting results for individual galaxies (red circles) as well as the stack (black squares). The fit incorporates the K-band data where available and shows the behaviour of key (well-constrained) parameters.

6.2.3 Analysis of results

[O,Ne,S/Fe]

In the full fit, we marginalise over the nuisance parameter [O,Ne,S/Z] which captures the (small) model variations due to variations in poorly-constrained α-elements. As with other abundance parameters, we convert this to the more informative form [O,Ne,S/Fe]. As is clear from Fig. 6.2, the inferred values of [O,Ne,S/Fe] are extremely high, albeit poorly constrained. While the expected enhancement should be similar to that of [Mg/Fe], the most probable values appear to be systematically offset by approximately 1σ. This appears to be driven by the Na I 0.82 μm feature, which can be weakened somewhat by large values of this parameter, reducing the tension with the redder Na I feature strengths. In Table 6.8 we present the results of fitting the stacks without this parameter (assuming [O,Ne,S/Fe] = 0 instead). This allows us to show that the principal knock-on effect of including the [O,Ne,S/Fe] parameter is to increase the inferred [Na/Fe] value, since larger values can be reconciled with the Na I 0.82 μm feature's strength. The effect on the IMF is negligible.

Mg I 0.88 μm

As mentioned above, in the updated model framework it is challenging to fit our measurements of the Mg I 0.88 μm feature, and so we did not include this feature in the fits so as to avoid biasing them. In Fig. 6.6 we show an index-index plot for the stack measurements; we also show the model grids under variation of metallicity and [Mg/Fe] for a bottom-light and a bottom-heavy IMF. The data appear offset from the model grid.

An examination of the Mg I 0.88 μm line in Fig. 6.4 suggests that the issue could be related to the pseudo-continuum definition in conjunction with differences between the model and the data in terms of long range spectral variations. On the red side of the feature the pseudo-continuum band could be affected by the Ti I 0.89 μm break.

[Na/Fe]

As in Chapter 4, the recovered sodium abundance is often very high. Once again, there is tension in the best-fit model between the various Na I features. Examination of Fig. 6.3

Table 6.8: Estimated parameter values for the stacked spectra, acquired using the updated models and the full set of index measurements. In this table the nuisance parameter [O,Ne,S/Fe] has been excluded from the fit. R1 and R2 correspond to the two extraction regions in the central IFU ($< 0.7''$, $> 0.7''$) while R3, R4, and R5 correspond to the rings of IFUs arranged at $\sim 1/3\,\mathrm{R_{eff}}$, $\sim 2/3\,\mathrm{R_{eff}}$, and $\sim \mathrm{R_{eff}}$.

	R1	R2	R3	R4	R5	gradient
age /Gyr	$8.73^{+1.01}_{-0.88}$	$7.34^{+0.89}_{-0.23}$	$7.17^{+1.32}_{-0.12}$	$7.38^{+2.33}_{-0.25}$	$7.88^{+2.35}_{-0.59}$	–0.71±0.55
X1	$1.79^{+0.70}_{-0.51}$	$1.81^{+0.49}_{-0.56}$	$1.60^{+0.70}_{-0.38}$	$1.13^{+1.14}_{-0.09}$	$1.32^{+1.40}_{-0.22}$	–0.32±0.23
X2	$1.19^{+0.87}_{-0.13}$	$1.08^{+0.51}_{-0.05}$	$1.16^{+0.61}_{-0.11}$	$1.17^{+0.98}_{-0.11}$	$1.58^{+1.07}_{-0.37}$	0.14±0.14
[Z/H]	$0.17^{+0.03}_{-0.03}$	$0.24^{+0.02}_{-0.03}$	$0.15^{+0.03}_{-0.04}$	$0.03^{+0.06}_{-0.09}$	$-0.14^{+0.11}_{-0.10}$	–0.09±0.03
[Fe/H]	$-0.04^{+0.05}_{-0.07}$	$-0.07^{+0.04}_{-0.06}$	$-0.26^{+0.11}_{-0.08}$	$-0.3^{+0.15}_{-0.11}$	$-0.19^{+0.17}_{-0.21}$	–0.16±0.05
[Mg/Fe]	$0.49^{+0.08}_{-0.04}$	$0.48^{+0.05}_{-0.04}$	$0.48^{+0.08}_{-0.08}$	$0.50^{+0.11}_{-0.13}$	$0.30^{+0.21}_{-0.16}$	–0.02±0.04
[Na/Fe]	$0.63^{+0.09}_{-0.11}$	$0.64^{+0.05}_{-0.05}$	$0.32^{+0.13}_{-0.15}$	$0.06^{+0.26}_{-0.23}$	$-0.24^{+0.40}_{-0.27}$	–0.37±0.09
[Ca/Fe]	$0.13^{+0.08}_{-0.06}$	$0.06^{+0.06}_{-0.05}$	$0.10^{+0.08}_{-0.10}$	$0.10^{+0.11}_{-0.17}$	$-0.12^{+0.20}_{-0.18}$	–0.05±0.05
[C/Fe]	$0.06^{+0.09}_{-0.09}$	$0.11^{+0.06}_{-0.06}$	$0.21^{+0.08}_{-0.12}$	$0.17^{+0.14}_{-0.15}$	$-0.01^{+0.21}_{-0.24}$	0.06±0.05
[Ti/Fe]	$0.52^{+0.13}_{-0.13}$	$0.36^{+0.09}_{-0.1}$	$0.37^{+0.17}_{-0.21}$	$0.62^{+0.19}_{-0.34}$	$0.48^{+0.30}_{-0.55}$	–0.02±0.11
[K/Fe]	$0.06^{+0.21}_{-0.10}$	$0.06^{+0.10}_{-0.05}$	$0.2^{+0.21}_{-0.14}$	$0.20^{+0.26}_{-0.20}$	$0.13^{+0.27}_{-0.26}$	0.09±0.07
$\mathrm{f_{dwarf}}$	$4.2^{+2.7}_{-1.1}\%$	$3.0^{+1.7}_{-0.6}\%$	$4.0^{+1.8}_{-1.1}\%$	$4.3^{+3.1}_{-1.3}\%$	$6.3^{+4.7}_{-2.5}\%$	0.7±1.3%
M/L	$0.89^{+0.39}_{-0.11}$	$0.79^{+0.23}_{-0.07}$	$0.83^{+0.28}_{-0.08}$	$0.91^{+0.45}_{-0.14}$	$0.96^{+0.84}_{-0.17}$	0.04±0.08

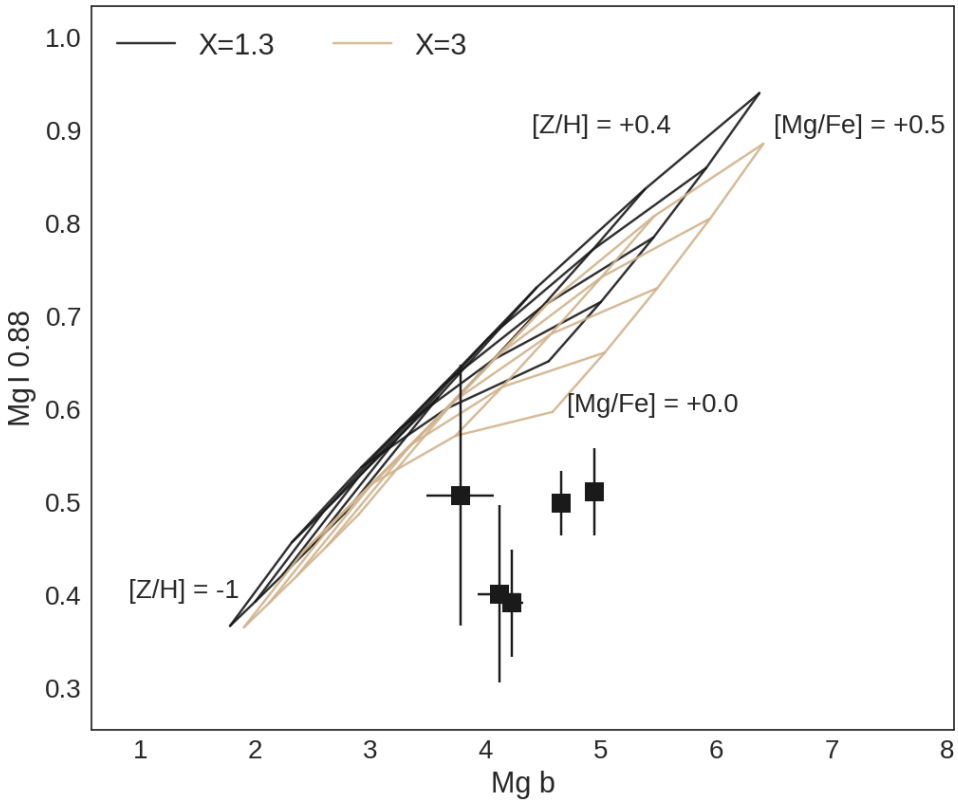

Figure 6.6: Equivalent widths of the Mg features, measured on the stacked spectra, along with model grids where the vertices indicate variation of metallicity and [Mg/Fe]. IMF variation makes relatively little difference to these features. The data and grids appear to be offset from each other.

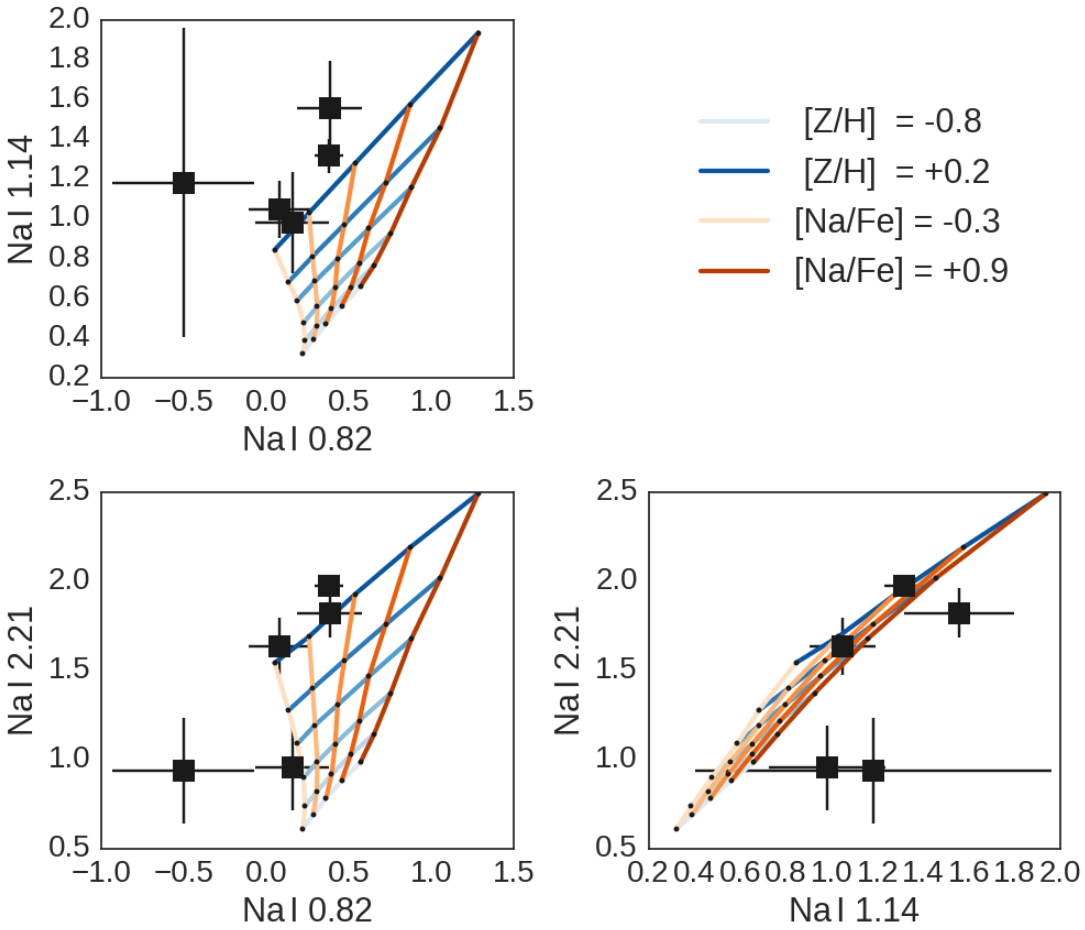

Figure 6.7: Equivalent widths of the Na features, measured on the stacked spectra, along with model grids where the vertices indicate variation of metallicity and [Na/Fe], assuming a Milky Way-like IMF. Blue lines are lines of constant [Z/H], orange lines are lines of constant [Na/Fe]. Darker colours indicate higher values.

suggests that the model tends to overestimate the strength of Na I 0.82 μm and underestimate the strength of Na I 2.21 μm.

As was discussed in Smith et al. (2015a) the Na I 1.14 μm line has been found to be unusually strong in massive ETGs, which is difficult to reconcile with the SSP models without violating other constraints. Our finding of a discrepancy between the Na I 0.82 μm and Na I 2.21 μm lines indicates that the Na I 2.21 μm line is similarly (or perhaps even *more*) discrepant. This contrasts with the findings of La Barbera et al. (2017), in which a different set of stellar population models that include *coupled* spectral responses to changes in the IMF and Na abundance are able to simultaneously match the strength of

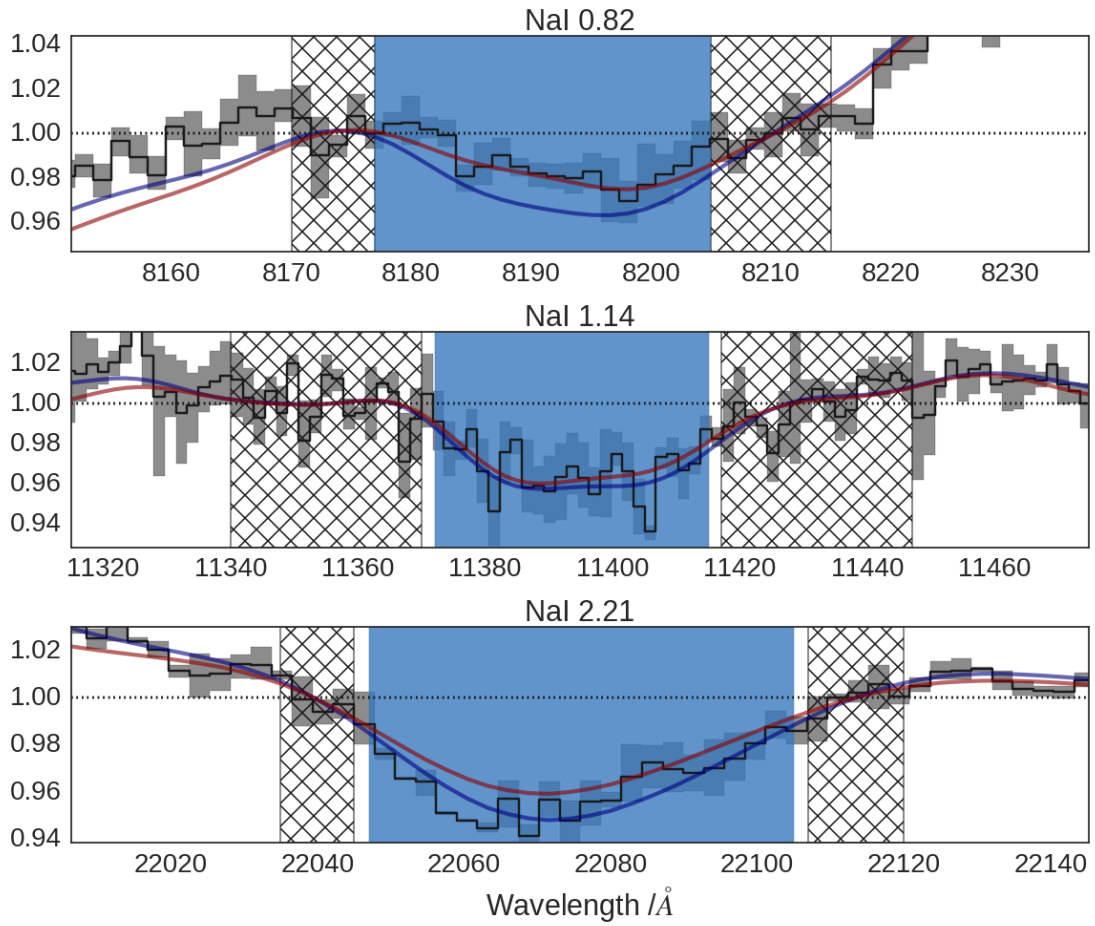

Figure 6.8: Close-up of the stacked spectrum from the innermost extraction region, alongside the models (close up from Fig. 6.4).

these lines in two massive ETGs.

The discrepancy is shown particularly clearly in Fig. 6.7, which shows three index-index plots for the stacked spectra. Na I 0.82 μm is comparatively insensitive to [Z/H] (as [Z/H] increases, the line is expected to get stronger, but changes in the local pseudocontinuum combat this by weakening the line) and is best-fit with a fairly low [Na/Fe] in all cases. By contrast, the other two lines require *either* extremely high [Z/H] or [Na/Fe] (in the case of Na I 1.14 μm, the required [Z/H] would be prohibitively high). In Fig. 6.8 we examine the features from the centrally-extracted stacked spectrum alongside the models. Na I 0.82 μm can be reproduced by the more complex model, but as just discussed is weaker than can be accounted for with the simpler model. Na I 1.14 μm is reproduced by both models, but Na 2.21 μm appears discrepant in shape on the blue side of the feature.

The IMF

The updated model formalism allows the IMF additional flexibility. In practice, this means that the relative contributions of the least massive stars and the $\sim 0.5\,M_{\odot}$ stars can be varied separately – in reality of course varying the upper slope X2 will increase/decrease the contribution of both, so the two parameters have some degeneracy (see Chapter 2).

For the stacked spectra, the IMF we recover is entirely consistent with the Milky Way IMF in all cases (in contrast to Chapter 4, where a modestly bottom-heavy IMF was preferred). Once again, the individual galaxies show scatter, and moreover appear offset from the stack in one case: this may be indicative of unaccounted-for systematics (the [Ca/Fe] abundance shows an offset at a similar level in the same bin).

Compared to the results presented in Chapter 4, however, the distribution of IMFs is considerably tighter than before and the new data prefers lower contributions to the light from dwarf stars (e.g. for the centrally extracted stack, 90% of draws from the posterior probability distribution correspond to $f_{\rm dwarf} < 8.4\%$, corresponding to the Salpeter IMF, whereas in Chapter 4 (see Table 4.5) we found $f_{\rm dwarf} = 9.4 \pm 2.1\%$). Note that this change appears to be primarily driven by the switch from the CvD12 to the CvD16 models (see the direct comparison made in Section 6.1.1).

As was remarked in Chapter 2, the relationship between the IMF slope/slopes and the index strengths is highly non-linear. It is worth exploring the consequences of this for the inferred parameters. In Fig. 6.9 we give as an example the joint and marginal posterior probability distributions over X1 and X2 inferred for the innermost spectrum of NGC 5813. The marginalised distributions of these two parameters are broad and somewhat skewed. While some covariance between the two parameters remains, it has been somewhat mitigated by the use of multi-band data. To aid comparison, we plot three lines of constant $f_{\rm dwarf}$ corresponding to Milky Way-like, Salpeter, and $X = 3$ power law IMFs respectively: most of the joint probability is enclosed between the first two of these.

In Fig. 6.10 we transform this distribution into the posterior probability for $f_{\rm dwarf}$ and relative M/L. These parameters are quite strongly correlated, as is clear from the figure. Note that the posterior probability distributions are less skewed than for X1, X2 (as might be anticipated from the roughly linear dependence of $f_{\rm dwarf}$ on the index strengths, which have symmetric statistical uncertainties). Crucially, these distributions are more

strongly peaked because of the non-linear response of the index strengths to the IMF slope. Expressed another way, the plateau in the X1 posterior distribution is due to the fact that the indices change little for variations in that range (and neither does $f_{\rm dwarf}$). As a result it's not immediately clear from the individual most probable values of X1 and X2 whether or not we find a bottom-heavy IMF, whereas examination of the joint distribution, or the $f_{\rm dwarf}$ distribution does indicate a modestly bottom-heavy IMF (though nevertheless consistent with Milky Way-like within the uncertainties). For this reason we ensure that all results presented in this work include $f_{\rm dwarf}$ and relative M/L values as well as the constraints on the power-law slopes (while cautioning the reader that the most probable values quoted may not appear to agree in an intuitive way).

Shape of the IMF

As we showed in Chapter 2, spectroscopic techniques for constraining the IMF are fairly insensitive to the functional form of the IMF, principally measuring the fractional contribution to the total light from dwarf stars. Nonetheless, given wide wavelength coverage (as in this work), some information about the IMF shape can in principle be recovered. In practice, some covariance between the IMF broken power law slopes X1 and X2 remains, meaning the signal is weak. In Fig. 6.11 we show the posterior probability distribution of the quantity X2–X1, a quantity which we use here as a proxy for IMF shape. The larger this quantity, the more sharply the IMF turns over at low stellar masses. Lines of constant X2–X1 lie approximately orthogonal to lines of constant $f_{\rm dwarf}$ in the (X1,X2) plane (e.g. Fig. 6.9). For a Milky Way IMF X2–X1 = 1, while for a single power law such as the Salpeter IMF it is zero. While some studies have focussed on single power laws, others, for example La Barbera et al. (2016), explore bottom-heavy IMFs with X1 = 1.3 (as in the Milky Way) and X2 $>$ 2.3, i.e. X2–X1 $>$ 1. For the stacked spectra, this proxy for IMF shape is not well-constrained, but does appear to prefer (at a marginal level) IMFs that break less sharply at low mass: this is likely because with poor constraints on the IMF shape the marginalised distribution reflects the imposed prior. MCMC walkers exploring low $f_{\rm dwarf}$ regions are constrained more tightly in X2–X1 around zero, so if $f_{\rm dwarf}$ is now well-constrained in the middle of the prior box then when we marginalise over the full posterior distribution more walkers will be found in the vicinity of X2–X1 = 0 than if we

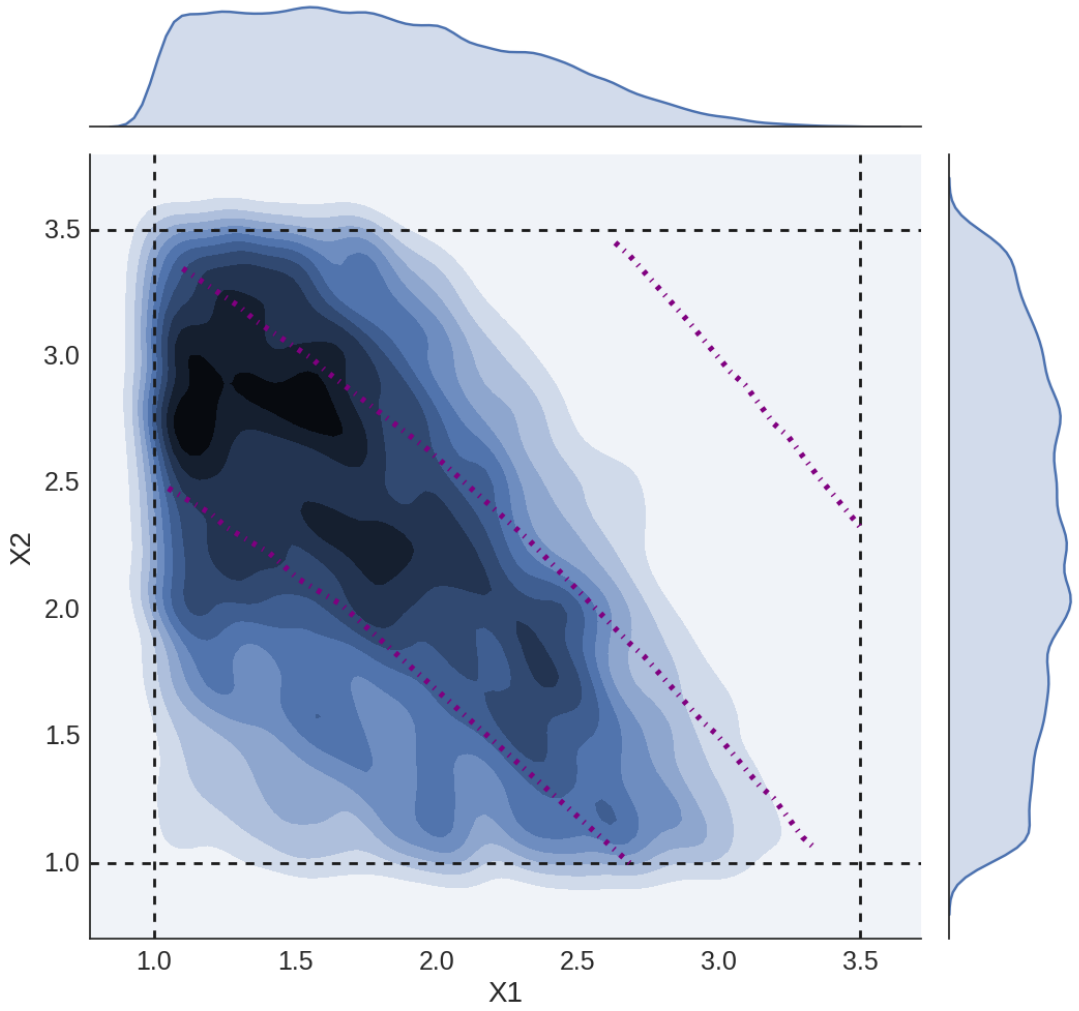

Figure 6.9: The results of fitting feature strengths from the centrally extracted spectrum from NGC 5813 with X1 and X2 varying freely. The joint and marginal distributions are shown via kernel-density estimation. Prior boundaries are indicated by the thick dashed lines, while dot-dashed contours indicate three lines of constant f_{dwarf}, equivalent to Kroupa, Salpeter, and X=3 IMFs (f_{dwarf} = 5.0%, 8.4%, and 19.0%) respectively.

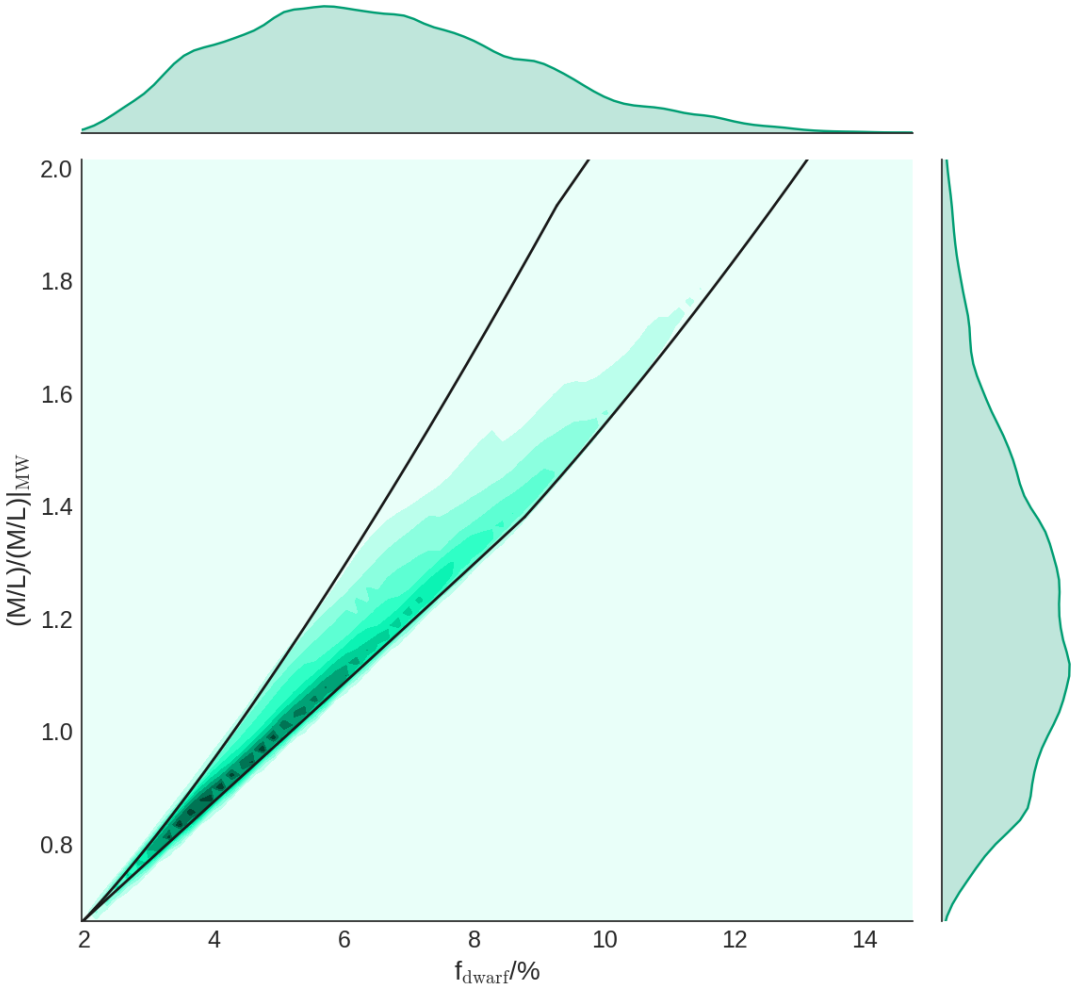

Figure 6.10: This plot corresponds to Fig. 6.9, recast into values of f_{dwarf} and V-band mass-to-light ratio (normalised so that M/L = 1 for a Milky Way-like population). The thick black line corresponds to the region enclosed by the priors on X1 and X2.

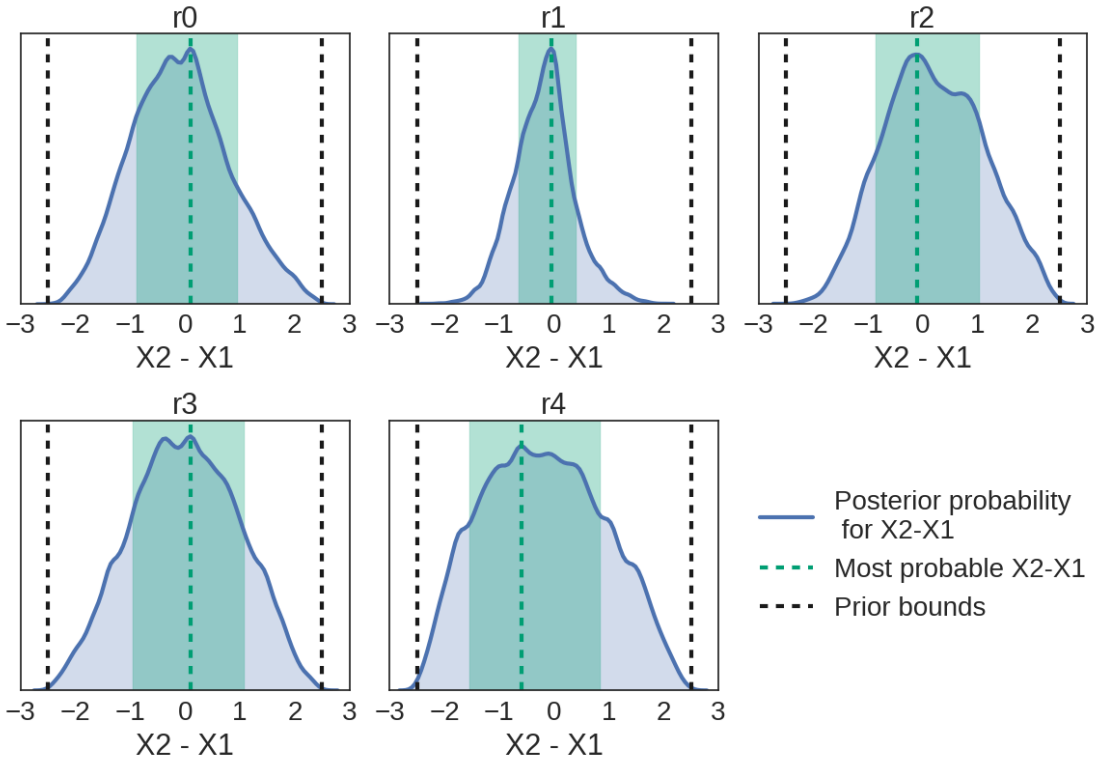

Figure 6.11: This plot indicates our constraints on the shape of the IMF via the difference in the power law slopes X1 and X2. The kernel density estimates show the posterior probability distributions of this quantity for the five stacked spectra. For the Milky Way IMF, X2–X1 = 1, whereas for a single power law (e.g. the Salpeter IMF) it is zero. The signal is weak since the IMF-dependent changes to spectral features principally track f_{dwarf}. Because of this the posterior distributions reflect the imposed prior on X1 and X2, a point we explore in more detail in Section 6.2.4

had drawn uniformly from [f_{dwarf}, X2–X1] instead.

6.2.4 Effect of the prior on inference of the IMF

Evaluation of the posterior probability distribution for the IMF requires that a prior probability distribution be specified. In the work we have presented so far in this Chapter we have assumed an equal prior probability for any value of X1 and X2 within set limits. This is not the only possible choice; an alternative would be to assume equal prior probability for any value of f_{dwarf} within certain limits and likewise for our proxy for IMF shape, X2–X1.

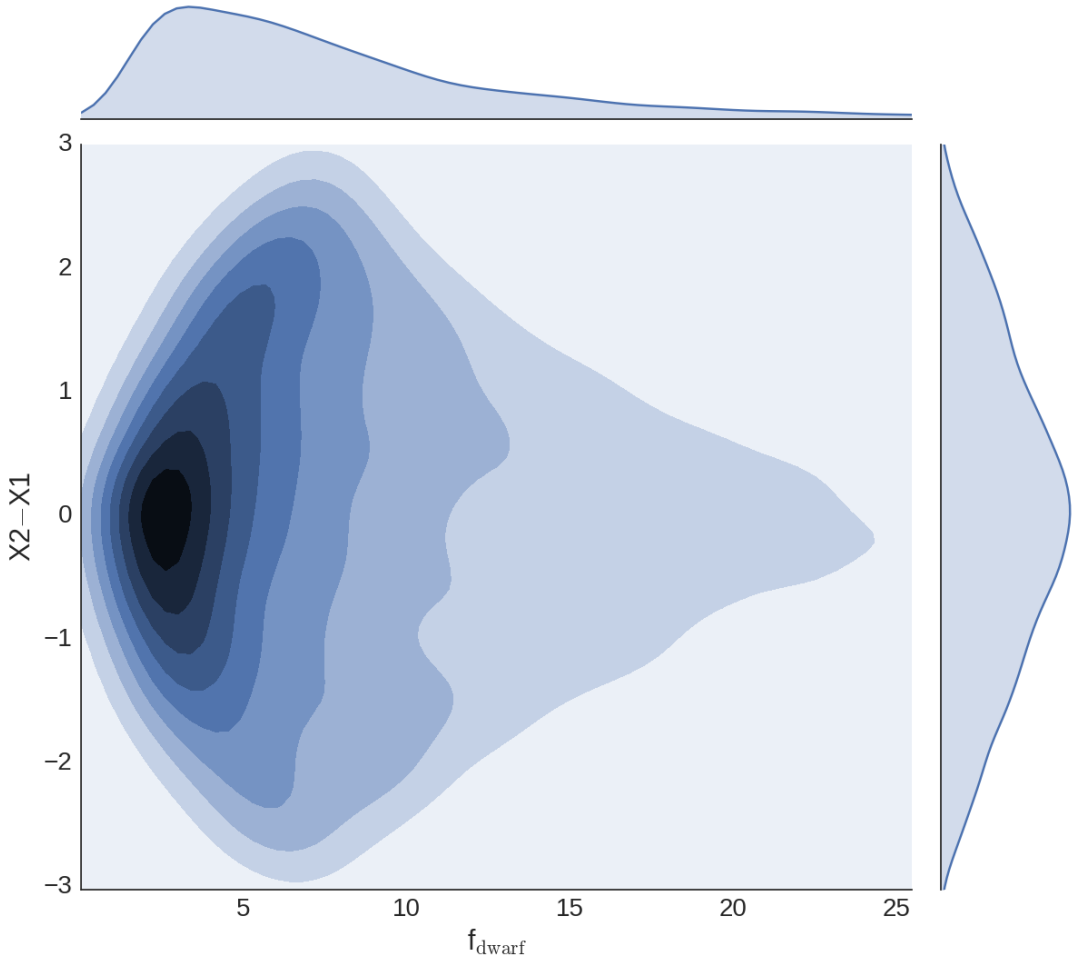

Figure 6.12: Density distribution in f_{dwarf} vs. X2–X1 space for points drawn uniformly from $0.5 < X1, X2 < 3.5$. This demonstrates that a prior probability distribution on X1 and X2 which is uniform between some limits (in this case, $0.5 < X1, X2 < 3.5$) corresponds to a peaked distribution in both f_{dwarf} and X2–X1.

In Fig. 6.12 we demonstrate the difference between these two scenarios. The plot shows the density of points randomly and uniformly drawn from X1 and X2 within the bounds of the prior in f_{dwarf} , X2–X1 space as well as estimates of the marginalised distributions of these points, which we can identify with the corresponding prior on f_{dwarf} and X2–X1. It is clear that this prior picks out preferred values for these quantities. Likewise, a uniform prior on these quantities would pick out preferred values of X1, X2. Note that in the work presented in Chapter 4 we explicitly made use of a uniform prior in f_{dwarf} .

It is crucial to quantify the effect that our choice of prior may have on our results,

so to this end we re-ran MCMC using a uniform prior on both f_{dwarf} and X2–X1. It is important to note that this requires us to explore a more restricted parameter space ($4\% < f_{dwarf} < 15\%$, $-1.5 <$ X2–X1 < 1.5) in order to remain within the CvD model grids. The results for most parameters are unchanged, but the prior unsurprisingly has an effect on the most probable values of the IMF parameters. In Fig. 6.13 we show the marginalised posterior distributions for X2–X1 computed for each of the stacked spectra. This makes clear that in some cases the evidence provided by our data (as averaged in the stacked spectra) generally favours IMFs that steepen at low stellar masses, but not decisively so. For Kroupa, X2–X1 = 1, which in the innermost stacked spectrum is somewhat in tension with the data (about 5% of draws from the posterior distribution have X2–X1 > 1). On the other hand, whereas in Fig. 6.11 the stack from the next extraction region out appeared to decisively exclude the Kroupa shape, Fig. 6.13 shows that the data are completely unable to constrain the shape under our alternative prior. It is clear that any attempt to extract information about the IMF shape from spectroscopic data must pay close attention to the chosen prior probability distribution.

In Table 6.9 we show how our results are modified using the alternative prior. This approach yields somewhat more bottom-heavy IMFs, which are nonetheless consistent with Kroupa (for which $f_{dwarf} \simeq 5\%$). In the central extraction region the inferred f_{dwarf} and X2–X1 would also be consistent with a Salpeter single power-law, similar to the result obtained in Chapter 4 (in which a prior that was uniform in f_{dwarf} was used).

Finally, in Fig. 6.14 we show an equivalent plot to Fig. 6.9 but with the inference carried out under a prior that is uniform in f_{dwarf} and X2–X1. The results for this spectrum are comparable: a bottom-heavy IMF that steepens at lower stellar mass is preferred.

6.3 Results from FIRE data

While the FIRE data is affected by certain systematic effects (described in Section 5.3.3), we here present a brief analysis of the stacked data. We remind the reader that the FIRE observations are extracted in the innermost regions of the target galaxies, so are to some extent comparable with the KMOS data taken from the innermost extraction region. Moreover, the two FIRE stacks bracket the KMOS sample in average velocity dispersion.

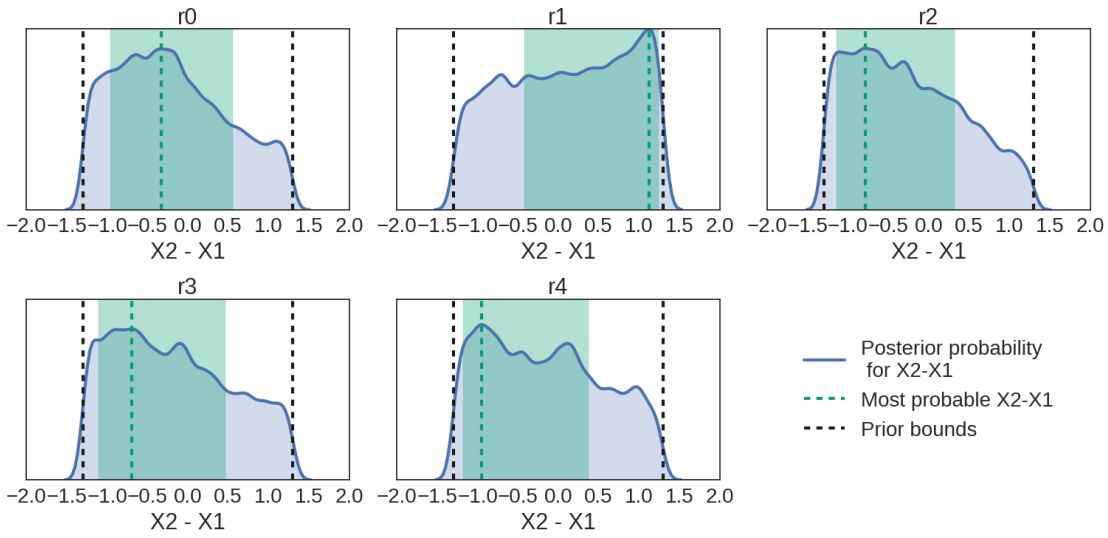

Figure 6.13: This plot indicates our constraints on the shape of the IMF via the difference in the power law slopes X1 and X2. The kernel density estimates show the posterior probability distributions of this quantity for the five stacked spectra. For the Milky Way IMF, X2–X1 = 1, whereas for a single power law (e.g. the Salpeter IMF) it is zero. The signal is weak since the IMF-dependent changes to spectral features principally track $f_{\rm dwarf}$. Because of this the posterior distributions reflect the imposed prior on X1 and X2; by contrast to Fig. 6.11 a uniform prior on X2–X1 has been used here.

Table 6.9: Estimated parameter values for the stacked spectra, acquired using the updated models and the full set of index measurements. For the IMF we fit a two-part power law with slopes X1 and X2, but used a prior distribution that was uniform in f_{dwarf} and X2–X1 (instead of in X1 and X2). We also fit for stellar population age and total metallicity, as well as the abundances of various elements of interest (we note that the IMF prior has negligible impact on these).

	R1	R2	R3	R4	R5	gradient
age /Gyr	$10.75^{+1.39}_{-1.43}$	$8.82^{+0.92}_{-0.68}$	$8.47^{+1.70}_{-0.90}$	$7.50^{+3.33}_{-0.32}$	$8.86^{+2.25}_{-1.22}$	–1.09±0.64
f_{dwarf} /%	$6.8^{+3.4}_{-1.9}$	$4.2^{+0.9}_{-0.1}$	$4.9^{+2.9}_{-0.6}$	$6.8^{+4.0}_{-1.9}$	$10.0^{+3.1}_{-3.8}$	1.7±1.9
X2–X1	$-0.33^{+0.89}_{-0.63}$	$1.13^{+0.12}_{-1.55}$	$-0.79^{+1.11}_{-0.35}$	$-0.70^{+1.16}_{-0.41}$	$-0.95^{+1.32}_{-0.23}$	–0.06±0.50
[Z/H]	$0.15^{+0.04}_{-0.04}$	$0.23^{+0.02}_{-0.02}$	$0.13^{+0.04}_{-0.06}$	$0.05^{+0.06}_{-0.13}$	$-0.04^{+0.08}_{-0.16}$	–0.06±0.04
[Fe/H]	$-0.18^{+0.08}_{-0.10}$	$-0.11^{+0.04}_{-0.06}$	$-0.19^{+0.09}_{-0.13}$	$-0.34^{+0.16}_{-0.11}$	$-0.21^{+0.16}_{-0.20}$	–0.08±0.05
[Mg/Fe]	$0.57^{+0.07}_{-0.08}$	$0.45^{+0.05}_{-0.04}$	$0.46^{+0.07}_{-0.11}$	$0.50^{+0.09}_{-0.14}$	$0.35^{+0.18}_{-0.17}$	–0.05±0.04
[Na/Fe]	$0.84^{+0.09}_{-0.13}$	$0.71^{+0.06}_{-0.05}$	$0.41^{+0.14}_{-0.14}$	$0.25^{+0.23}_{-0.31}$	$-0.17^{+0.42}_{-0.26}$	–0.41±0.08
[Ca/Fe]	$0.24^{+0.11}_{-0.07}$	$0.11^{+0.06}_{-0.05}$	$0.15^{+0.09}_{-0.11}$	$0.15^{+0.11}_{-0.16}$	$-0.08^{+0.25}_{-0.17}$	–0.06±0.04
[O, Ne, S/Fe]	$0.83^{+0.12}_{-0.22}$	$0.67^{+0.08}_{-0.09}$	$0.80^{+0.12}_{-0.16}$	$0.76^{+0.14}_{-0.26}$	$0.65^{+0.23}_{-0.31}$	0.03±0.06
[C/Fe]	$0.22^{+0.15}_{-0.11}$	$0.13^{+0.08}_{-0.05}$	$0.20^{+0.13}_{-0.12}$	$0.27^{+0.14}_{-0.17}$	$0.10^{+0.19}_{-0.25}$	0.03±0.04
[Ti/Fe]	$0.61^{+0.20}_{-0.15}$	$0.32^{+0.10}_{-0.11}$	$0.23^{+0.20}_{-0.23}$	$0.53^{+0.22}_{-0.27}$	$0.38^{+0.35}_{-0.45}$	–0.07±0.09
[K/Fe]	$0.19^{+0.19}_{-0.11}$	$0.10^{+0.09}_{-0.06}$	$0.20^{+0.17}_{-0.15}$	$0.14^{+0.25}_{-0.17}$	$0.28^{+0.23}_{-0.38}$	0.05±0.08

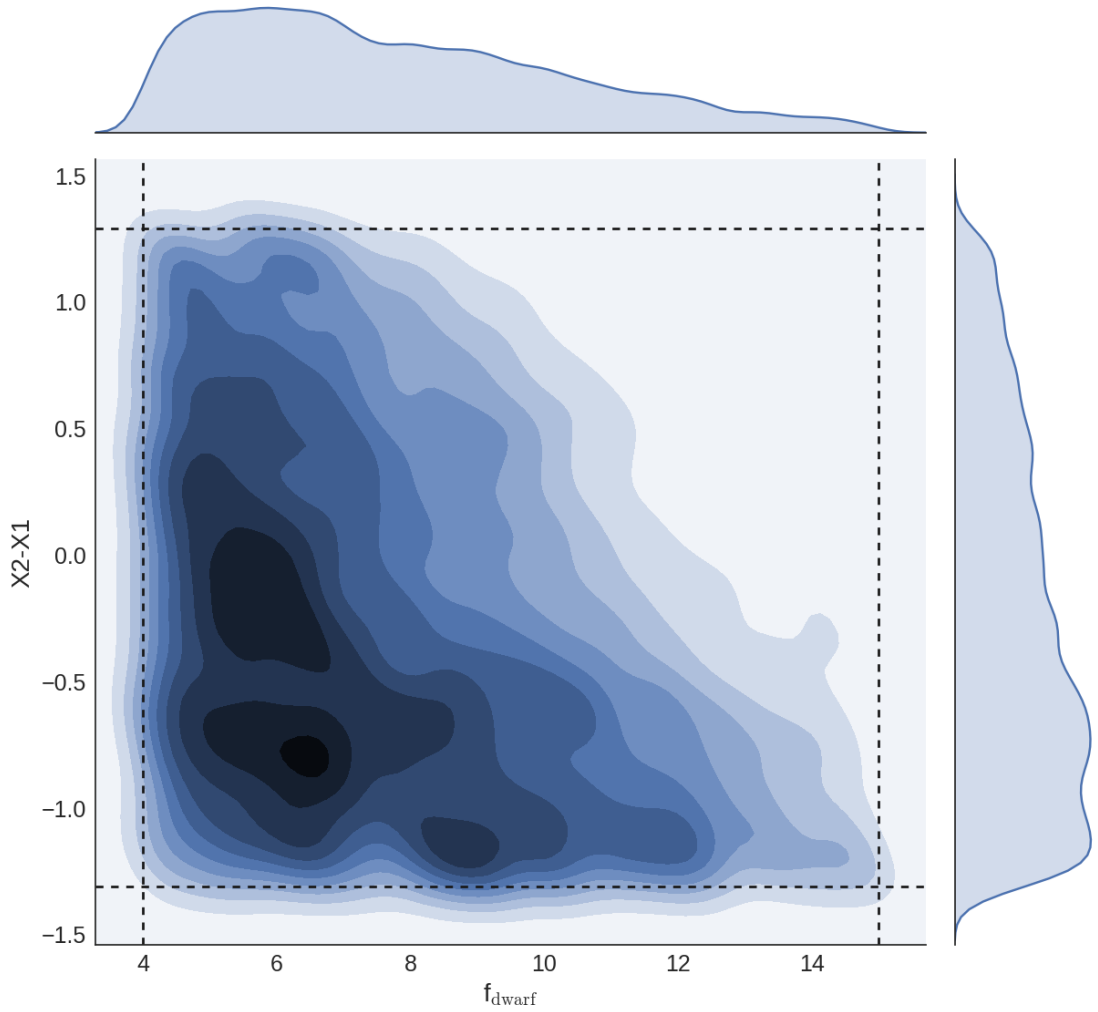

Figure 6.14: The results of fitting feature strengths from the centrally extracted spectrum from NGC 5813 with a uniform prior on f_{dwarf} and X2–X1 (corresponds to Fig. 6.9, other than the change to the prior). The joint and marginal distributions are shown via kernel-density estimation. Prior boundaries are indicated by the thick dashed lines. The results are consistent; a somewhat bottom-heavy IMF that steepens at low stellar masses is recovered.

We analysed the FIRE data in the same way as the KMOS data in order to aid comparison, i.e. we fit for all available indices except the Mg I 0.88 μm line and the CO b line. Due to the FIRE wavelength coverage Na I 0.82μm was not available.

The results are summarised in Fig. 6.15. The results are somewhat discrepant from those obtained from the KMOS innermost stack; we find $f_{\rm dwarf} = 8.5 \pm 2.3\%$ (relative M/L$= 1.7 \pm 0.4$) for the high σ stack and $f_{\rm dwarf} = 8.2 \pm 2.2\%$ (relative M/L$= 1.6 \pm 0.4$) for the low σ stack. The distribution of X2–X1 (the quantity we are using as a proxy for IMF shape) is skewed; for the high σ stack we find a most probable value of $-1.6^{+1.0}_{-0.4}$ for the low σ stack $-1.6^{+1.3}_{-0.4}$. This indicates an IMF that steepens at low mass, although the uncertainties are such that the data are not strongly in tension with the single-slope power law case (i.e. the Salpeter IMF) and, as explained in the previous section, this result is sensitive to the prior we use on X2–X1.

The biggest discrepancy with the equivalent KMOS results (summarised in Table 6.4) is the abundance of the α-elements (apart from Ca), which for the KMOS data appear to be much more abundant than the FIRE stacks suggest. Other abundances (e.g. [Na/Fe]) and the overall [Z/H] are consistent with the two posterior probability distributions from the FIRE stacks, as expected.

Marginalised over each parameter, the two FIRE stacks are generally not readily distinguishable. However, the data do indicate a strong trend of central [Na/Fe] with σ.

Given the systematic discrepancies between the FIRE measurements and the KMOS measurements for certain features, it is particularly important to make a comparison between the model fits and the stacked spectra. In Figs. 6.16 and 6.17 we show the FIRE stacked spectra normalised in the region of each measured feature, along with a model generated from the best-fit velocity dispersion (from pPXF) and stellar population parameters (from SPINDRIFT). As with the KMOS data, there is a clear issue with the model fit to the Mg I 0.88μm line – most obvious for the low velocity dispersion stack. Unlike the KMOS data, there is a clear discrepancy between the spectral shape of the stack and the model around the CO bandhead. There was a large systematic discrepancy between the FIRE and KMOS measurements for this feature. However, no clear issue affects the Wing-Ford band, where a large systematic discrepancy was also apparent.

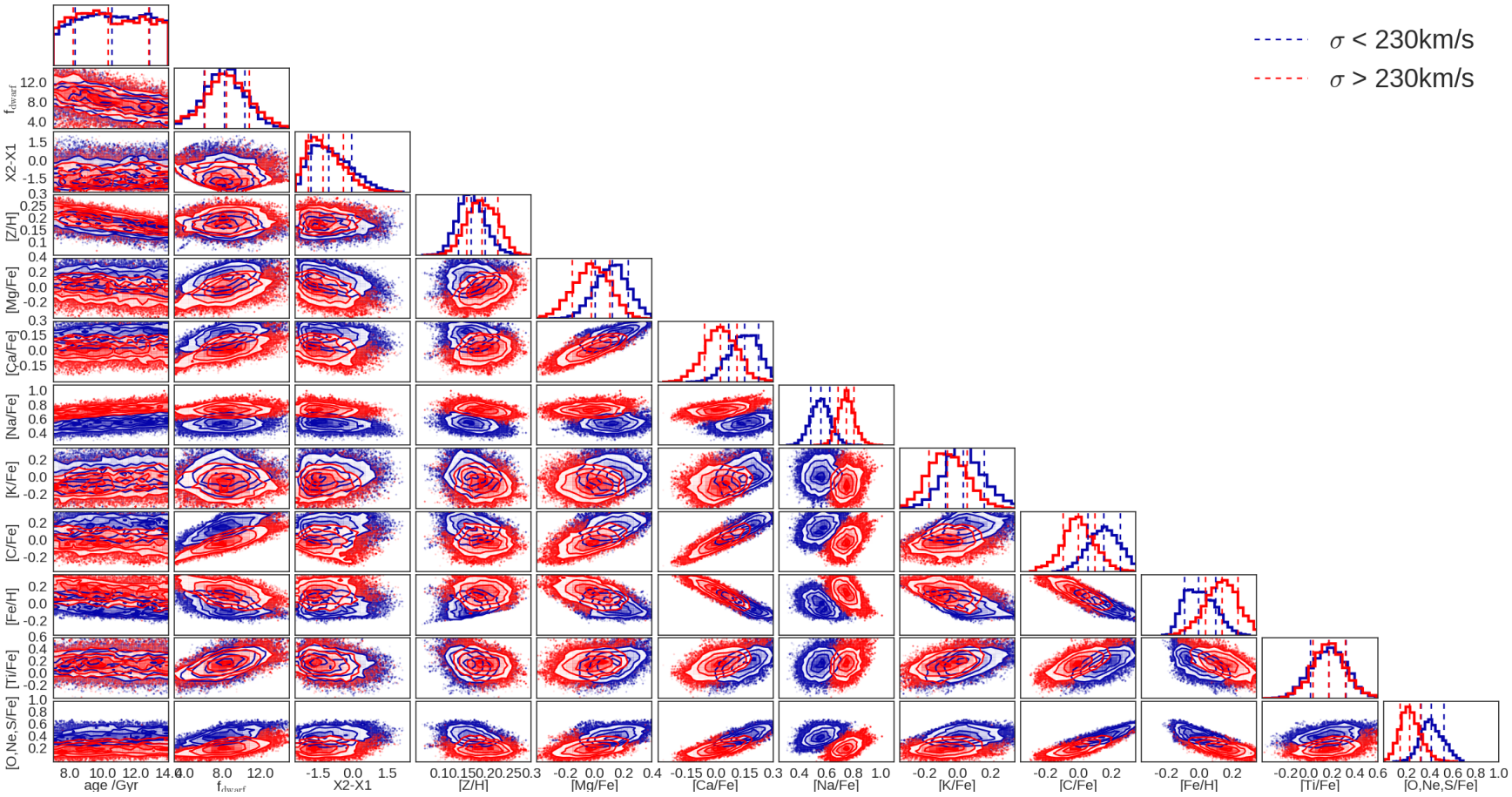

Figure 6.15: This plot shows the results of the MCMC runs for the high- and low-σ FIRE stacked spectra. The results have been rescaled for presentation in a similar way as the KMOS results, i.e. f_{dwarf} is calculated from X1, X2 and abundance parameters are recast into [X/Fe] and [Fe/H].

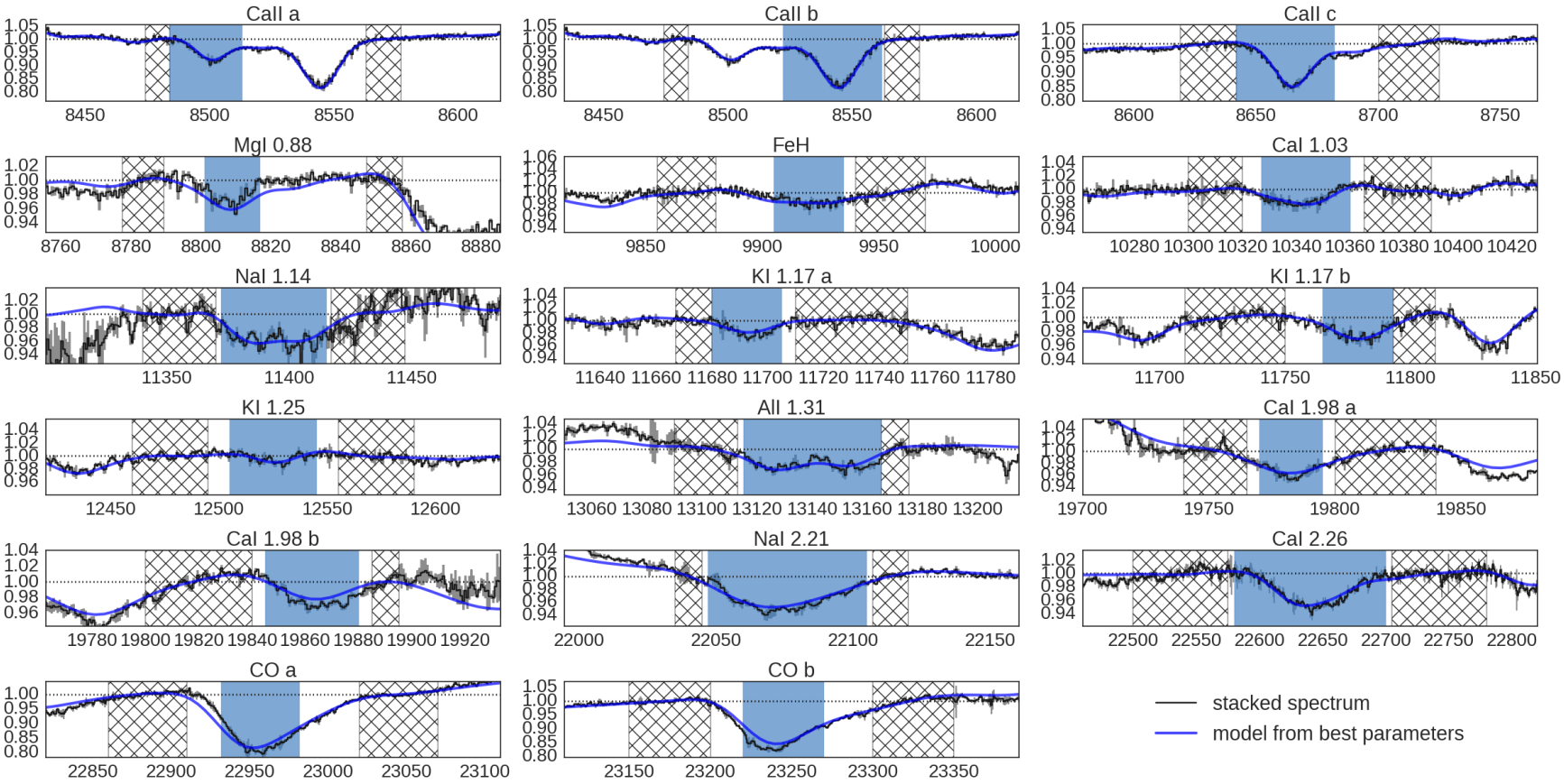

Figure 6.16: The stacked spectrum for lower velocity dispersion galaxies ($\sigma < 230\,\mathrm{kms}^{-1}$) in the FIRE sample, along with a spectral model generated from the best fit parameters from Fig. 6.15.

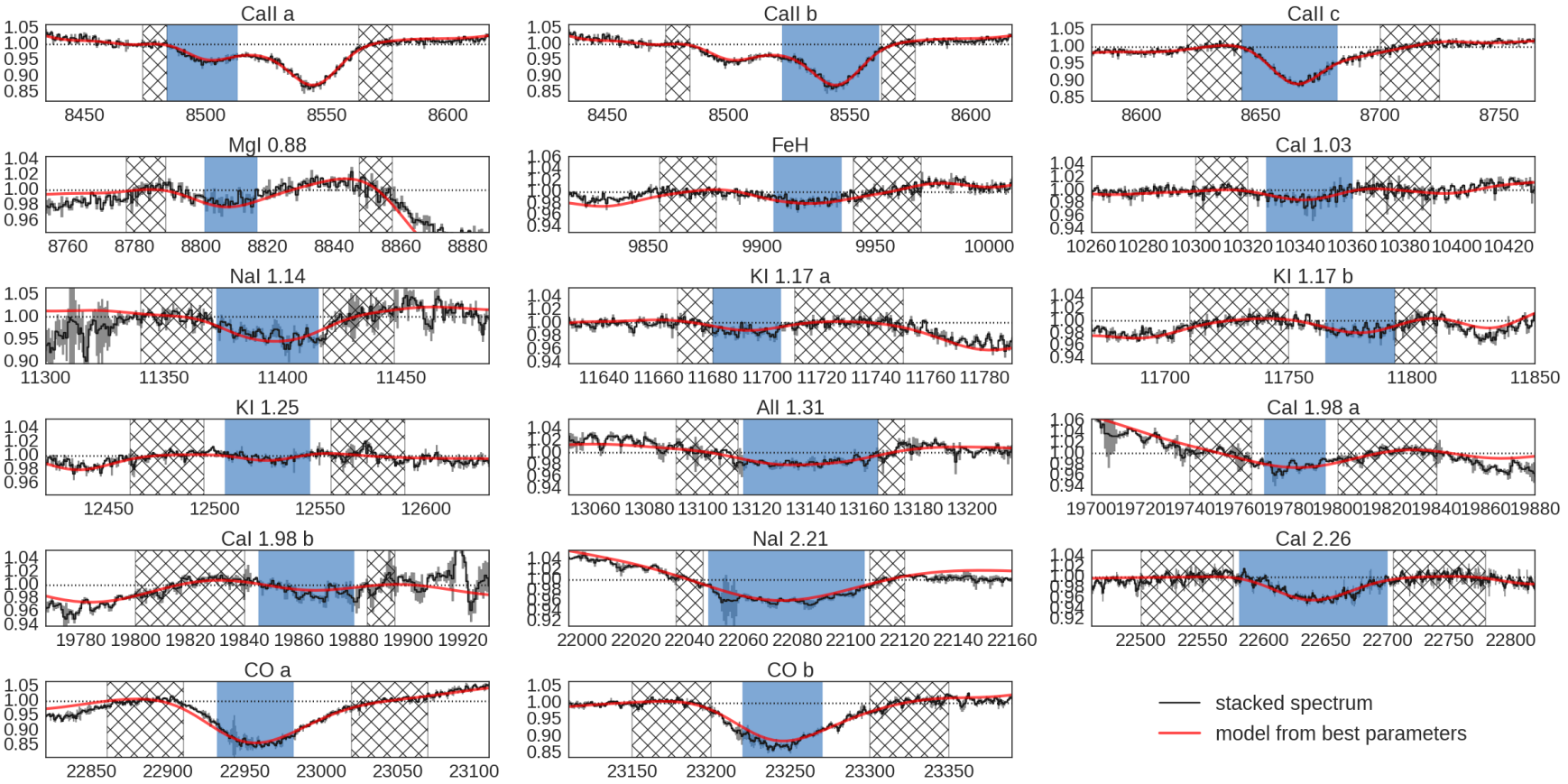

Figure 6.17: The stacked spectrum for lower velocity dispersion galaxies ($\sigma > 230\,\mathrm{kms}^{-1}$) in the FIRE sample, along with a spectral model generated from the best fit parameters from Fig. 6.15.

6.4 Discussion

We have measured the radially-varying strengths of several K-band absorption lines for seven of the eight ETGs in the KINETyS sample, finding a significant gradient in the strength of the Na I 2.21 μm line and rather flat radial profiles for the Ca I features at 1.98 μm and 2.26 μm and also the CO bandhead at 2.30μm.

Using an updated version of the CvD SSP models and our own SPINDRIFT code for stellar population parameter fitting, we extended the work presented in Chapters 3 and 4. Our results are broadly consistent with those previously presented, but the more extensive parameter coverage of the new models – combined with the additional data – allow us to place better constraints on the IMF and chemical abundance properties of our sample than was previously possible.

As before, we do not find strong evidence for IMF variations in our sample of galaxies, either on average (via the stacked data) nor in individual galaxies. Indeed, the new parameter fits generally favour Milky Way-like IMFs and provide no evidence for an IMF gradient. Moreover, we now model the IMF as a two-part power law, mitigating any issues that might have arisen from our previous single parameter treatment, though at the expense of some additional ambiguity in the interpretation of the results.

Concerning the recovered abundance gradients, in the new formalism we fit explicitly for total metallicity and then consider the variations of particular elements on top of this trend. On average, we find strong [Na/Fe] radial gradients in our sample, i.e. [Na/H] ramps up in the core faster than the overall metallicity trend would predict (by contrast, while Mg and perhaps Ca are enhanced, they are superabundant by a constant factor with respect to Fe throughout). This reinforces our conclusion, first given in Chapter 4, that the metallicity-dependent yield of Na is playing a role in these galaxies. In addition to this, the stacked FIRE data suggest a strong correlation between central [Na/Fe] and σ. The extreme [Na/H] values we infer (typically 0.5–0.6 in the central extraction regions of the KINETyS sample, consistent with the result from the stacked spectrum for this region) potentially pose a challenge; SSP models must rely on theoretical predictions rather than empirical spectra since metal-rich stars so superabundant in Na are very rare in the Milky Way.

Our results indicate some tension between the measurements of different Na lines, which might be accounted for by a modelling issue of this kind. In Fig. 6.7 we showed how for the stacked spectra the Na I 0.82 μm line strength at face value appears to prefer lower values of [Na/Fe]. Index vs. index grids should be treated with caution due to the cumulative minor effects of various unaccounted-for parameters. For example, in this case the inclusion of a [Ti/Fe] parameter (as in the more complex model presented above) can reduce the tension significantly, though not entirely. This is because Na I 0.82 μm lies within a broad Ti absorption band. The effect of this enhanced Ti is to weaken the measured equivalent-width somewhat. This and other parameters can therefore help to reconcile the measurements by allowing weaker Na I 0.82 μm at higher [Na/Fe]. Nevertheless, some systematic tension remains between the three infrared Na I features, which may be partially due to the modelling of these features in highly Na-enhanced populations.

Proper constraints on [Na/Fe] are crucial, as Na abundance has important effects on the strength of other indices, in particular the Wing-Ford band. In Fig. 6.18 we show how this effect can explain the radial behaviour of the Wing-Ford band in the stacked KMOS spectra. The same figure shows that it would be challenging to reconcile this measurement with a systematically bottom-heavy IMF in the cores of our sample galaxies. By contrast, as was demonstrated in Fig. 5.4 the measurements of the Wing-Ford band for the stacked FIRE spectra are significantly higher. This is clearly a crucial systematic since these measurements are then more consistent with a bottom-heavy IMF, which is reflected in the best-fit parameters. The difference in strength is visible in Fig. 5.5; as shown in Fig. 5.6, the feature's blue pseudo-continuum band falls into the overlap region between adjacent echelle orders, which may account for this offset.

The infrared is a challenging regime in which to make accurate, percent-level measurements of spectroscopic features. It may be the case that systematic errors in the measurements of the strengths of several crucial spectral features can explain the apparent discrepancy between IMF measurements inferred principally from optical spectroscopy and those that we (and others) have presented inferred from infrared spectroscopy. Our independent measurements of infrared spectra from the core regions of a second sample of ETGs have allowed us to address this possibility. Stacked measurements from this

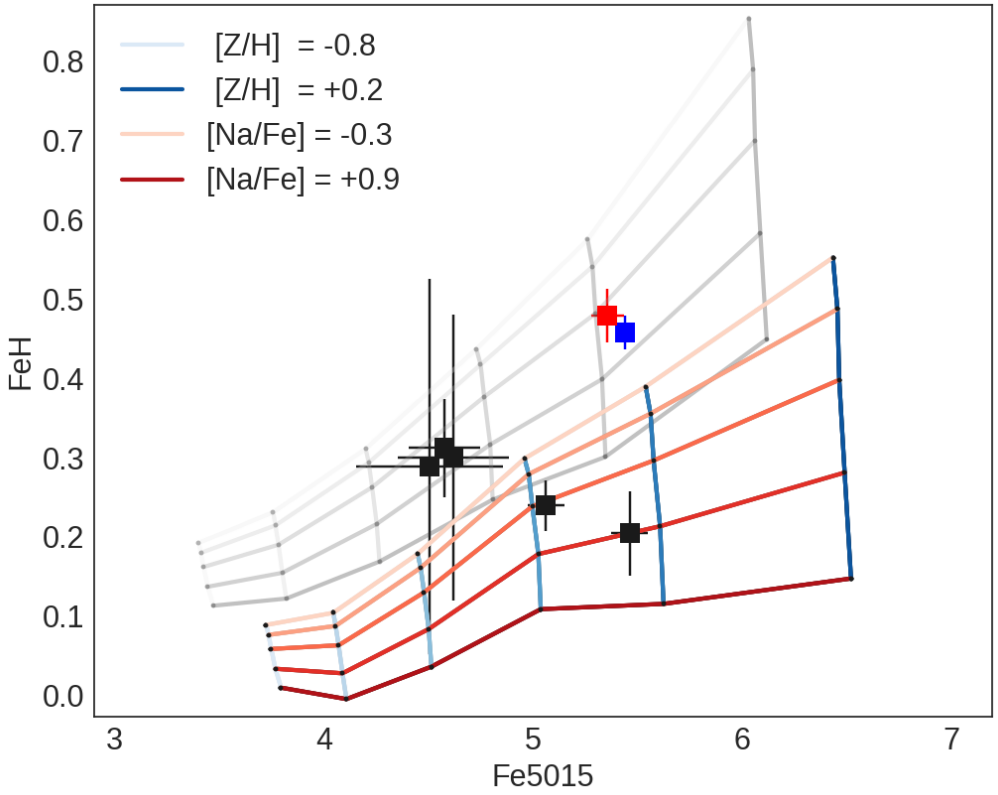

Figure 6.18: Index-index grid for the optical Fe 5015 index and the Wing-Ford (FeH) band, computed at $[\alpha/\mathrm{Fe}] = +0.5$ for a Kroupa IMF. The KMOS data are superimposed in black, while the FIRE stacks of low and high velocity dispersion galaxies are shown in blue and red respectively. The stacked measurements of the Wing-Ford band are weakest for the innermost extraction region (e.g. see Fig. 6.3), consistent with the strongly increasing Na abundance, which barely affects Fe 5015 but has a significant effect on the Wing-Ford band. Note that a more bottom-heavy IMF would tend to make FeH stronger while leaving Fe 5015 largely unchanged – the shift for a Salpeter single power law is indicated by the offset light grey grid – so would require e.g. even more extreme Na abundance to match the KMOS measurements. By contrast, the FIRE measurements are clearly offset and are consistent with a bottom-heavy IMF.

sample do indeed indicate a bottom-heavy IMF on average for galaxies of both lower and higher velocity dispersion than the average of the KMOS sample.

Summary

We have built upon the work presented in Chapters 3 and 4 in several important ways. First, we have deployed a significantly more advanced implementation of the SPINDRIFT stellar population parameter inference code. The updated code uses a much-improved stellar spectral library, capitalising on recent advances in the field, and a more comprehensive set of stellar population parameters, including the ability to model IMFs with different shapes and to vary the overall metallicity. Secondly, we have obtained K-band spectroscopy of almost all of the KINETyS sample, allowing us to make measurements of previously underutilised spectral features as stellar population diagnostics. This adds significant discriminatory power to our method, allowing us to further break degeneracies between model parameters. Finally, we have also investigated the same set of features in the innermost regions of an additional sample of twelve nearby ETGs using the FIRE instrument. This has allowed us to investigate the potential effect of systematic errors on our method and also to probe the variation of stellar populations in the cores of ETGs with velocity dispersion. Our conclusions are as follows:

1. In the previous chapter, we used stacked spectra extracted from different radii within the KINETyS sample to investigate the radial behaviour of four K-band spectral features. We found a strong decline in the strength of the Na I 2.21μm line with radius (-0.53 ± 0.08 per decade in $R/R_{\rm eff}$), and fairly constant strength for two Ca I features. The CO 2.30 μm a line likewise appears roughly constant in strength (-0.11 ± 0.13).

2. We use our updated stellar population spectral index fitting code, SPINDRIFT, in conjunction with these measurements, to place additional constraints on the stellar populations of our sample. From the stacked spectra we recover an average metallicity gradient Δ[Z/H] of -0.11 ± 0.03 per decade in $R/R_{\rm eff}$ and measure the abundances of several α-capture elements, finding flat trends in the relative abundances

[Mg/Fe], [Ca/Fe], [Ti/Fe], and [O,Ne,S/Fe]. The latter two parameters are not well constrained, but we find [Ca/Fe] much less enhanced than [Mg/Fe], consistent with our previous findings.

3. We find a very strong radial gradient in [Na/Fe] of -0.35 ± 0.09, a better constraint than that presented in the previous chapter, aided by our measurements of the Na I 2.21μm line. However, there is mild tension between the absolute strengths of the three Na I features we measure, which may be a consequence of the theoretical modelling of Na line strengths in stellar populations where Na is superabundant. The extreme abundance of Na implied by our measurements in the cores of massive ETGs may be explained by the metallicity-dependent nucleosynthetic yield of Na. We also find evidence in the FIRE sample for a velocity-dispersion dependence of the Na abundance.

4. For the IMF, we infer a Milky Way-like, non-radially varying IMF for the KINETyS sample, both for the stacked spectra and the individual galaxies in the sample. We do however note that our results may be affected by systematic effects; in the FIRE sample, which is affected by different systematics and in which we probe only the core regions of the galaxies, a more bottom-heavy IMF is inferred. The two results are in tension at the $\sim 2\sigma$ level.

Chapter 7

NGC 1407: results from additional data

Preamble

In the preceding chapters we have presented our inferences about the stellar populations of massive ETGs, finding results that are in tension, to some extent, with the literature. We neither find strong evidence for IMF variations in the most of the systems we have analysed and nor do we find evidence, on average, for radial variations in the IMF functional form. Most previous analyses have been confined to analysis of features at $\lambda < 1.0\,\mu$m, whilst ours has explored redder wavelengths out to 2.4 μm.

We have made clear that the infrared can be a challenging wavelength regime to work in for studies requiring measurements of spectral features with percent-level accuracy. In this chapter we present additional spatially-resolved optical spectroscopy of the nearby, nearly-isolated elliptical NGC 1407. We analyse this data via the same methodology outlined in earlier chapters.

Until now we have been unable to include reliable results for the galaxy NGC 1407, since it was not included in the ATLAS^{3D} sample, from which our optical data was drawn. Without this crucial information it is not possible to place adequate constraints on [Fe/H], stellar age etc. and this has consequences for our ability to robustly infer the form of the IMF. NGC 1407 is one of the highest velocity dispersion galaxies in our sample and is notable for being a slow rotator (see, for example, Arnold et al., 2014). While not in the original sample of CvD12b, in van Dokkum et al. (2017) observations of NGC 1407 covering the wavelength range 0.4–1.015 μm were used to characterise the stellar pop-

ulations from the innermost regions out to the effective radius. The stellar population synthesis models they used for their fitting procedure are the same as those which we made use of in the previous chapter. A very bottom-heavy IMF was found for R $< 7.6''$, with relative r-band M/L > 2.6, while a Milky Way-like IMF (i.e. relative M/L ~ 1) was found for R $>30''$.

In this chapter we utilise combined optical and infrared data in order to explore the stellar populations of NGC 1407 and test for a discrepancy between our results and those found in the recent literature. In Section 7.1 we present the data and our analysis thereof follows in Section 7.2. In Section 7.3 we discuss our findings and we summarise our conclusions in Section 7.4.

7.1 Data

For this work we have made use of pre-existing observations of NGC 1407 made using the Wide-Field Spectograph (WiFeS) on the ANU 2.3m telescope (courtesy of C. Usher and N. Pastorello). WiFeS is an integral-field spectrograph with a $25'' \times 38''$ field of view comprising $1''$ squared spaxels, covering the wavelength range 3200–9800Å with R = 2900. The field of view is sufficiently well-matched to the J-band effective radius of NGC 1407 ($36.2''$) for our purpose and the wavelength coverage allows us to access numerous additional features. The galaxy was observed for a total of 3000s with seeing of $1.9''$ (somewhat larger than the KMOS observations for this galaxy, which must be borne in mind for any analysis of gradients).

The WiFeS data were pre-reduced via the standard PyWiFeS pipeline. Although the data cover certain near-infrared features, for the purposes of stellar population inference we preferred to use the KMOS IZ-band spectra for these features, for which we utilised more sophisticated corrections for the atmospheric absorption and emission that become problematic at these wavelengths (see Chapter 3), and were not adequately dealt with by the WiFeS reduction.

To match the WiFeS data to the KMOS data as closely as possible, we summed spectra in three apertures: the central $1''$ squared spaxel, $0.7''<$R$<2.8''$, and $5''<$R$<15''$, giving S/N of 30–40 per Å in the central spaxel and 100–150 and 200–300 in the subsequent

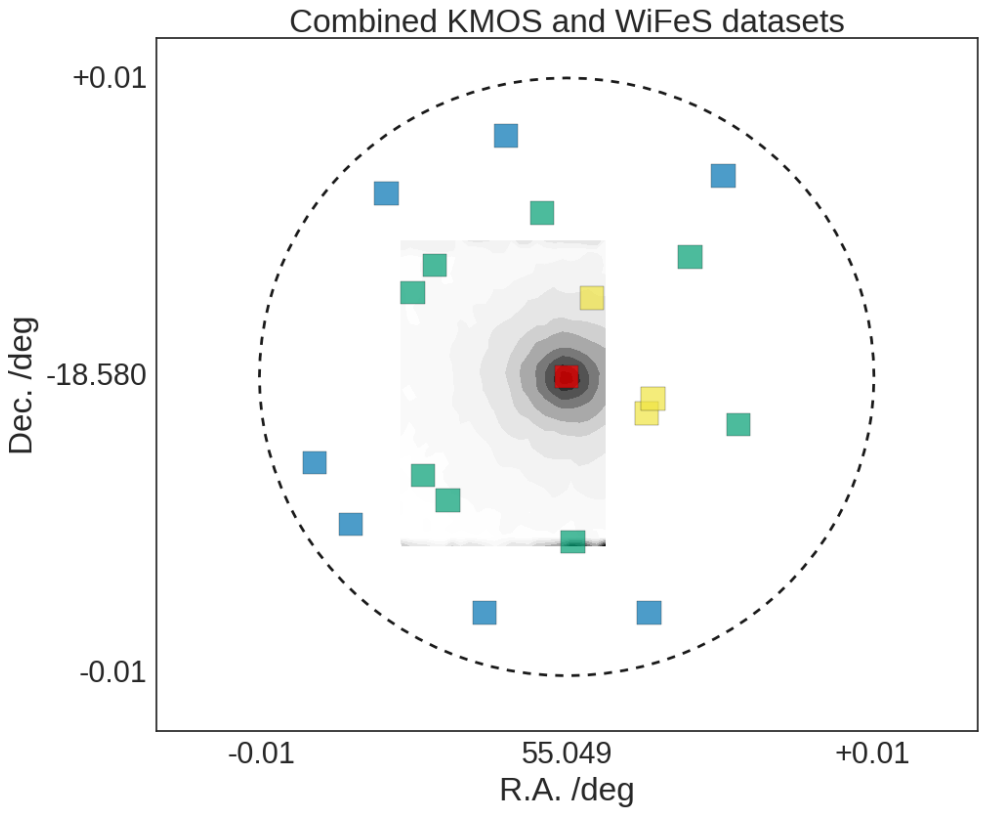

Figure 7.1: This map shows how the WiFeS observations (grey contours) correspond to the existing KMOS observations of NGC 1407. IFU fields deployed in our sparse mosaic observing strategy are shown to scale. The central IFU field (red) is decomposed into inner and outer regions. The WiFeS field allows high S/N sampling of the stellar populations along the isophote to which the first ring of IFUs (yellow) are deployed. The J-band effective radius is shown by the dashed circle.

apertures. For comparison, we show how the KMOS and WiFeS data complement each other in Fig. 7.1.

To supplement the KMOS data we measured the equivalent widths of a series of features between 4500–6000Å (see Table 2.1 for feature definitions). We also used pPXF over the spectral range 4600–5400Å in order to obtain velocity dispersions for these spectra and used these to correct the measurements to a common velocity dispersion of 230 kms^{-1}, just as we did for the KMOS measurements. The full set of measurements from the WiFeS spectra are given Table 7.1 (infrared measurements for this galaxy reused in this chapter can be found in Tables 3.4 and 5.7).

Table 7.1: Measurements of various optical features from optical spectra of NGC 1407 in three radial regimes. Feature equivalent widths given in Å, corrected for velocity dispersion to a reference value of 230 kms^{-1}.

Index	R1	R2	R3
C_2 0.47 μm	9.11±0.70	8.94±0.19	8.16±0.13
Hβ	1.56±0.31	1.61±0.08	1.53±0.05
Fe 5015	5.64±0.63	5.42±0.21	4.85±0.13
Mg*b*	4.83±0.31	4.94±0.09	4.80±0.06
Fe I 0.52 μm	3.14±0.30	3.00±0.09	2.84±0.06
Fe I 0.53 μm	2.49±0.39	2.91±0.11	2.59±0.07
Na I 0.59 μm	5.90±0.22	5.61±0.06	5.00±0.03

7.2 Inference of stellar population parameters

To infer the underlying stellar population in NGC 1407 we used the SPINDRIFT code (specifically, the same version as was used in the preceding chapter) to fit the optical, IZ-, and K-band feature measurements with the same set of parameters and priors as we used before. The MCMC runs used 100 walkers over 1000 steps (following an ample burn-in of 250 steps).

The results of this procedure are summarised in Table 7.2, while the full marginalised and two-parameter joint distributions for the three datasets are displayed in Fig. 7.2.

Next we show the extent to which these parameter fits reproduce the data. In Figs. 7.3, 7.4, and 7.5, we show the WiFeS data from the three different extraction regions, normalised by the pseudo-continuum around each measured index. Overplotted is a spectroscopic model generated from the pPXF-derived velocity dispersion and the best-fit stellar population parameters found by SPINDRIFT. Note that the measured equivalent widths of the near-infrared indices presented here (Na I 0.82 μm, Ca II Triplet, and Mg I 0.88 μm) were not used in the overall fit; these were instead taken from the higher-fidelity KMOS data.

Table 7.2: Inferred parameters for the stellar populations of NGC 1407 in three different radial extraction regions. R1: R $< 1''$, R2: $0.7'' <$ R $< 2.8''$, R3: R $\sim 10''$.

parameter list	R1	R2	R3
age /Gyr	$7.4^{+3.0}_{-0.3}$	$8.2^{+2.0}_{-1.2}$	$7.6^{+2.2}_{-0.4}$
$f_{\rm dwarf}$	$4.3^{+3.1}_{-1.1}\%$	$4.3^{+2.1}_{-1.2}\%$	$3.0^{+2.5}_{-0.6}\%$
X2–X1	$0.29^{+0.98}_{-1.04}$	$-0.02^{+1.04}_{-0.75}$	$-0.01^{+0.77}_{-0.87}$
[Z/H]	$0.16^{+0.09}_{-0.09}$	$-0.03^{+0.07}_{-0.07}$	$0.19^{+0.05}_{-0.10}$
[Mg/Fe]	$0.40^{+0.11}_{-0.08}$	$0.38^{+0.03}_{-0.05}$	$0.39^{+0.04}_{-0.03}$
[Ca/Fe]	$0.26^{+0.08}_{-0.08}$	$0.14^{+0.05}_{-0.04}$	$0.01^{+0.06}_{-0.06}$
[Na/Fe]	$0.68^{+0.09}_{-0.08}$	$0.53^{+0.06}_{-0.04}$	$0.46^{+0.05}_{-0.03}$
[K/Fe]	$0.20^{+0.22}_{-0.21}$	$-0.22^{+0.25}_{-0.18}$	$0.08^{+0.24}_{-0.17}$
[C/Fe]	$0.26^{+0.09}_{-0.12}$	$0.05^{+0.06}_{-0.04}$	$0.28^{+0.03}_{-0.07}$
[Fe/H]	$0.00^{+0.08}_{-0.09}$	$0.16^{+0.05}_{-0.06}$	$0.00^{+0.04}_{-0.04}$
[Ti/Fe]	$0.57^{+0.18}_{-0.19}$	$0.21^{+0.11}_{-0.15}$	$0.16^{+0.08}_{-0.12}$
[O, Ne, S/Fe]	$0.30^{+0.26}_{-0.44}$	$0.10^{+0.21}_{-0.45}$	$0.50^{+0.16}_{-0.27}$
red. χ^2	10.7	3.6	17.7

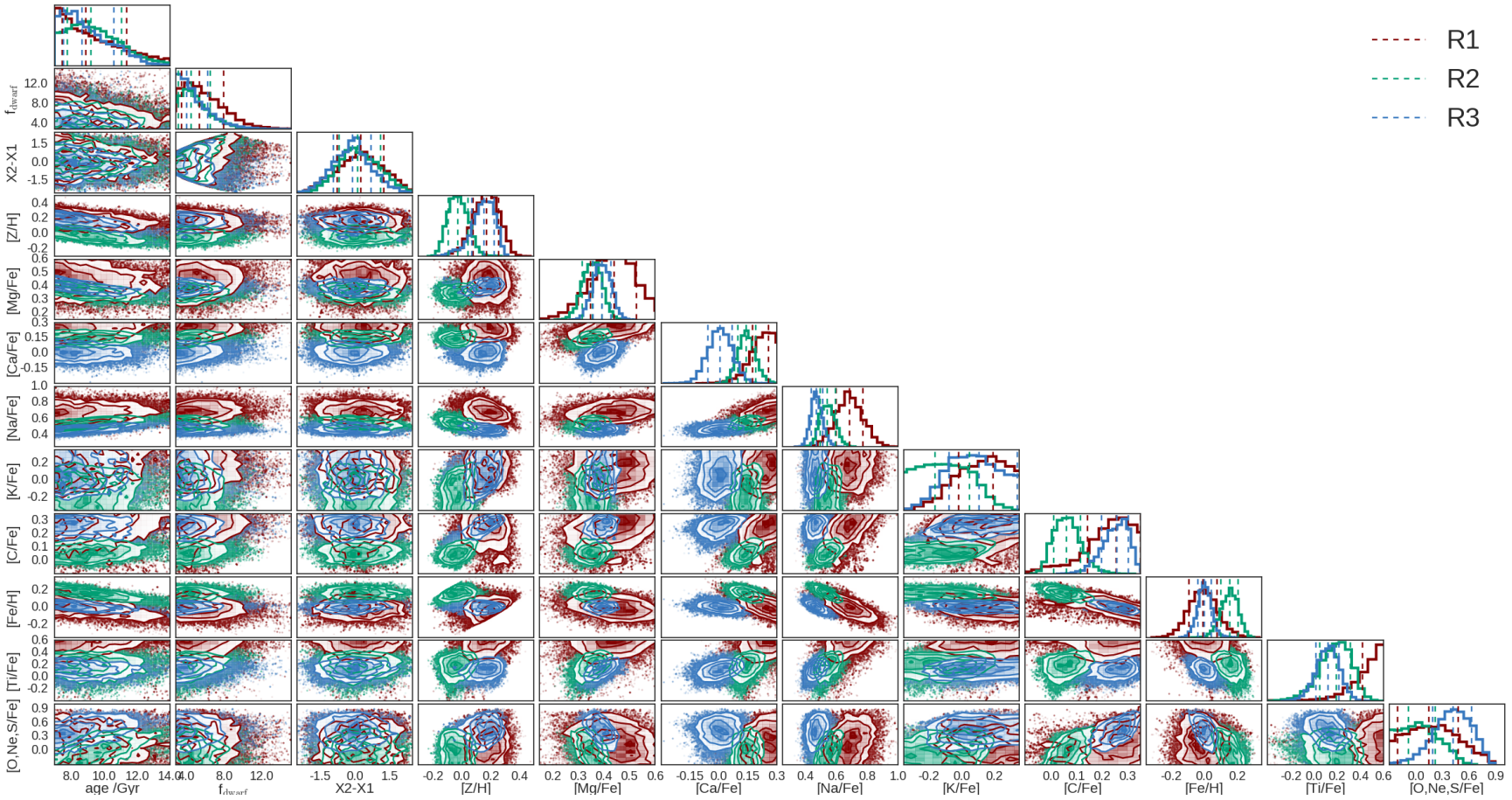

Figure 7.2: This plot shows the results of the MCMC runs for the combined optical and infrared data, for three extraction regions. The results have been rescaled for presentation as in Table 7.2, i.e. f_{dwarf} is calculated from X1, X2 and abundance parameters are recast into [X/Fe] and [Fe/H].

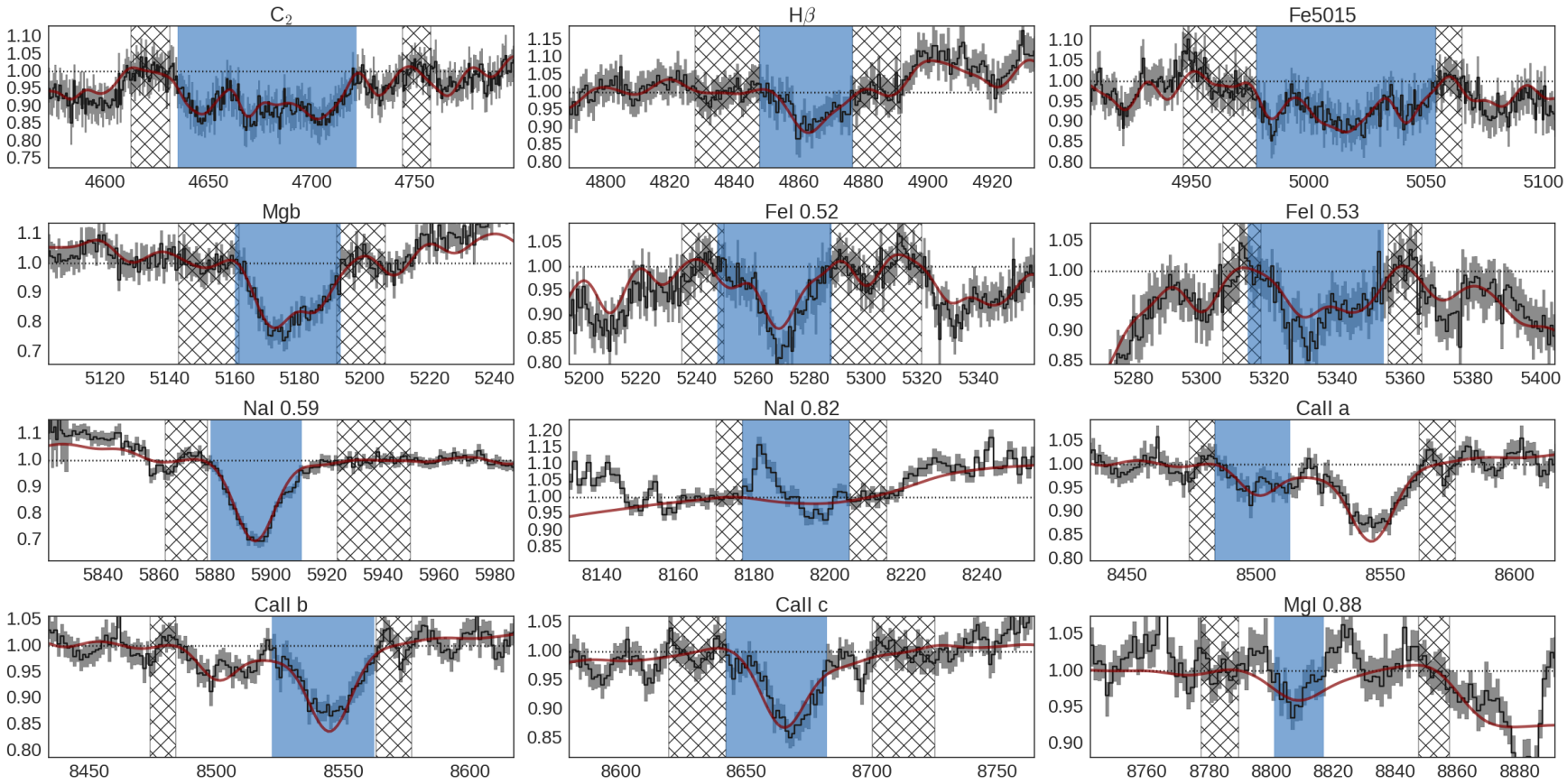

Figure 7.3: Spectrum from the central WiFeS spaxel (1″ by 1″) with shaded uncertainties, displayed in each measured index region (blue vertical band) and normalised by a linear fit to the flux averaged in the pseudo-continuum bands on either side (hatched regions). Overplotted in red: model spectrum generated from the best-fit stellar population parameters (i.e. not a direct fit to the spectrum). Note that the strengths of the near-infrared features (Na I 0.82 μm, Ca II Triplet, and Mg I 0.88 μm) were measured from the corresponding KMOS spectrum, which has undergone a more sophisticated treatment for correcting atmospheric absorption and emission.

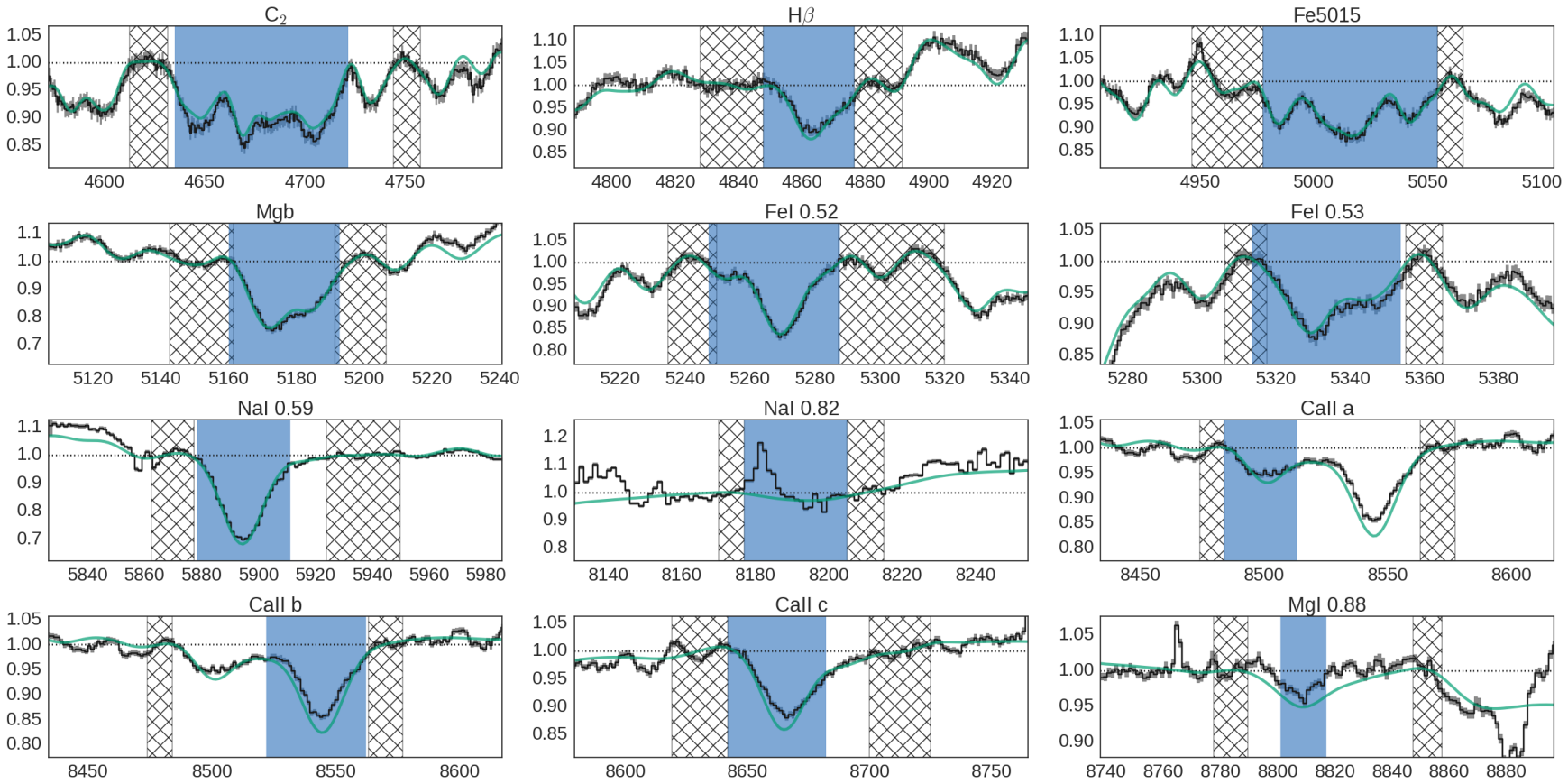

Figure 7.4: Spectrum from the inner WiFeS annulus ($1'' < R < 2.8''$) with shaded uncertainties, displayed in each measured index region (blue vertical band) and normalised by a linear fit to the flux averaged in the pseudo-continuum bands on either side (hatched regions). Overplotted in green: model spectrum generated from the best-fit stellar population parameters (i.e. not a direct fit to the spectrum). Note that the strengths of the near-infrared features (Na I 0.82 μm, Ca II Triplet, and Mg I 0.88 μm) were measured from the corresponding KMOS spectrum, which has undergone a more sophisticated treatment for correcting atmospheric absorption and emission.

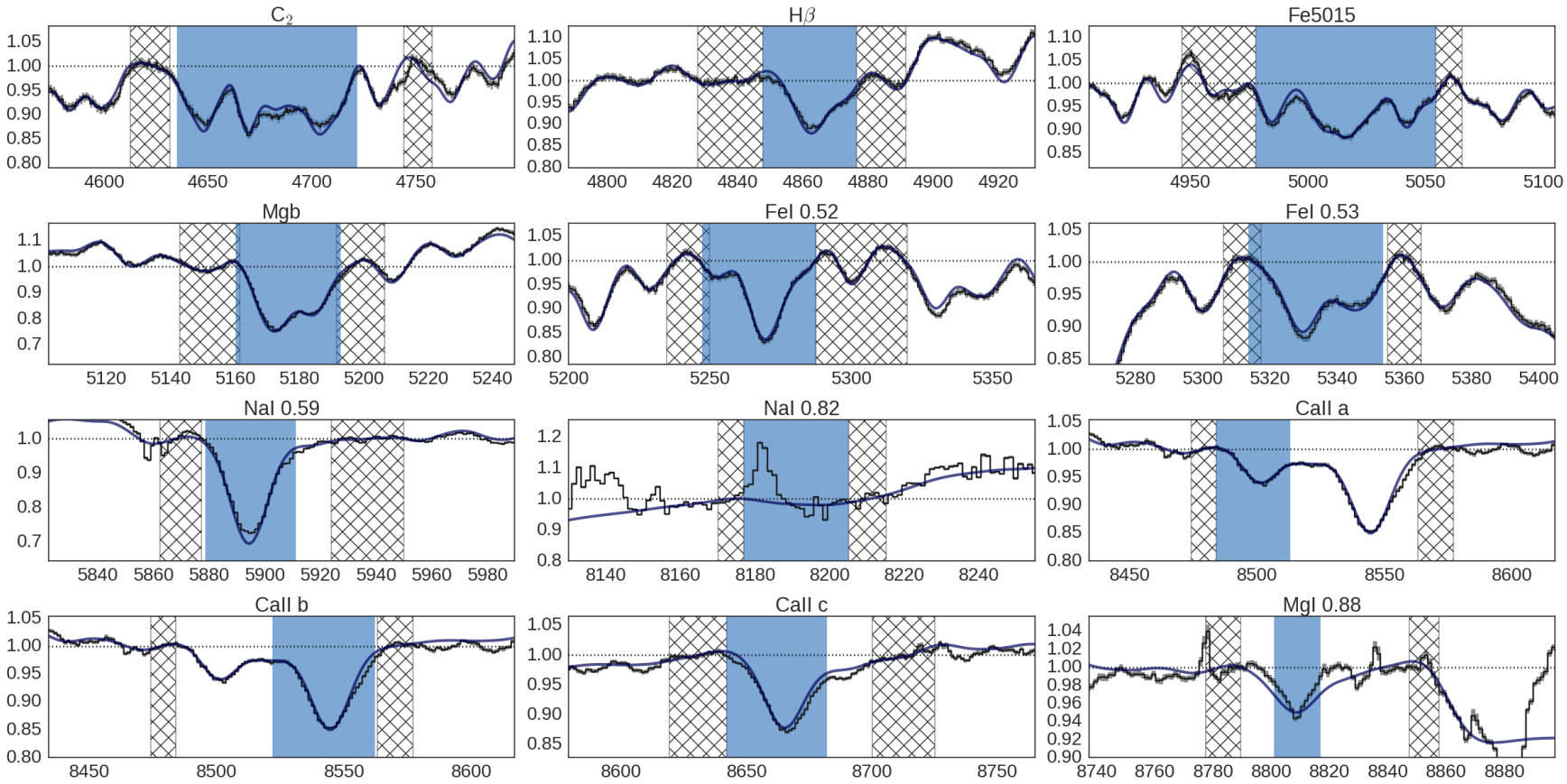

Figure 7.5: Spectrum from the outer WiFeS annulus ($5'' < R < 15''$) with shaded uncertainties, displayed in each measured index region (blue vertical band) and normalised by a linear fit to the flux averaged in the pseudo-continuum bands on either side (hatched regions). Overplotted in dark blue: model spectrum generated from the best-fit stellar population parameters (i.e. not a direct fit to the spectrum). Note that the strengths of the near-infrared features (Na I 0.82 µm, Ca II Triplet, and Mg I 0.88 µm) were measured from the corresponding KMOS spectrum, which has undergone a more sophisticated treatment for correcting atmospheric absorption and emission.

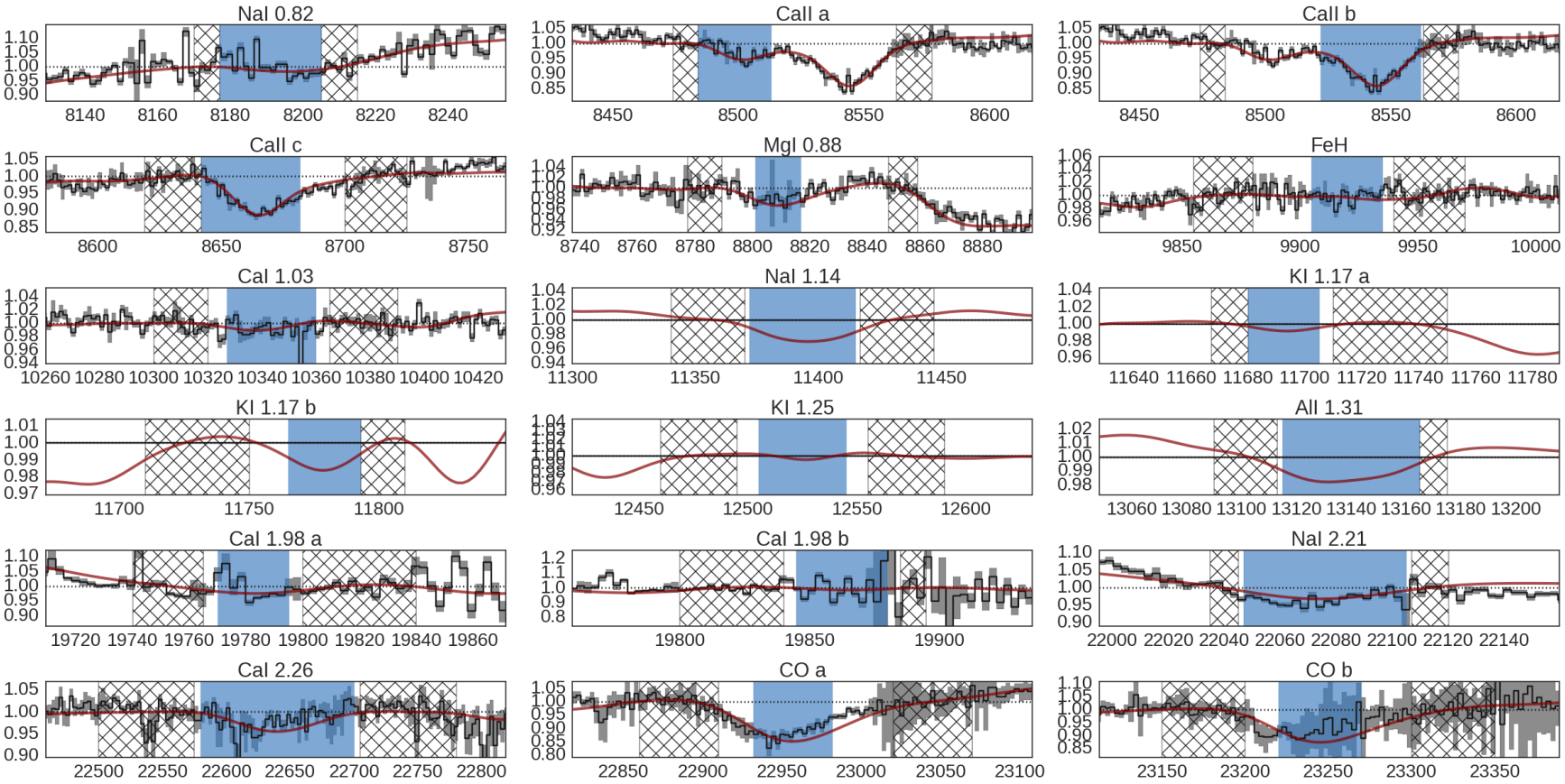

Figure 7.6: Spectrum from the central KMOS extraction region (R<0.7″) with shaded uncertainties, displayed in each measured index region (blue vertical band) and normalised by a linear fit to the flux averaged in the pseudo-continuum bands on either side (hatched regions). Overplotted in red: model spectrum generated from the best-fit stellar population parameters (i.e. not a direct fit to the spectrum). Note that YJ band data was not taken so for these indices a predicted spectrum is shown.

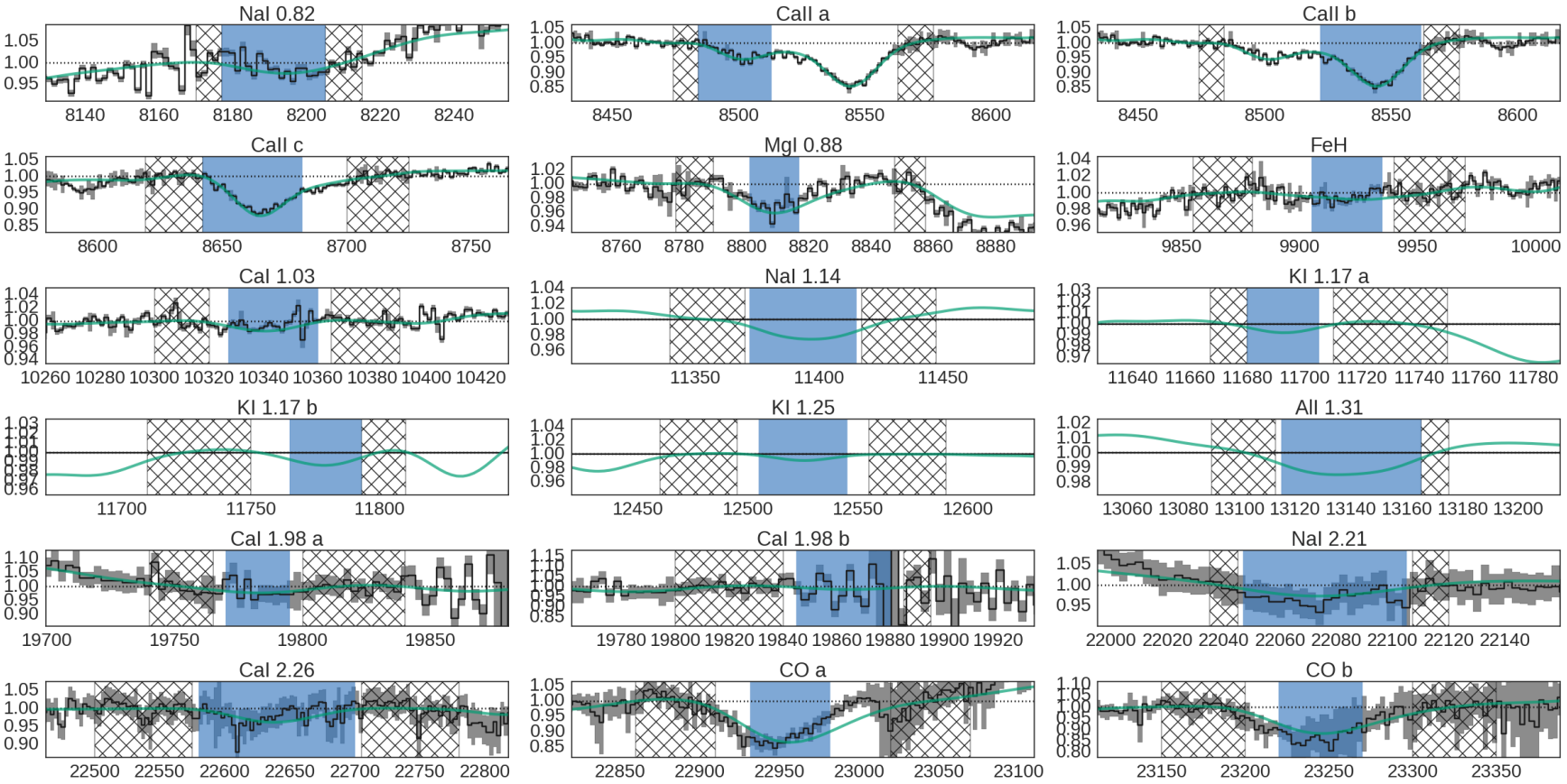

Figure 7.7: Spectrum from the outer part (R>0.7″) of the KMOS central IFU with shaded uncertainties, displayed in each measured index region (blue vertical band) and normalised by a linear fit to the flux averaged in the pseudo-continuum bands on either side (hatched regions). Overplotted in green: model spectrum generated from the best-fit stellar population parameters (i.e. not a direct fit to the spectrum). Note that YJ band data was not taken so for these indices a predicted spectrum is shown.

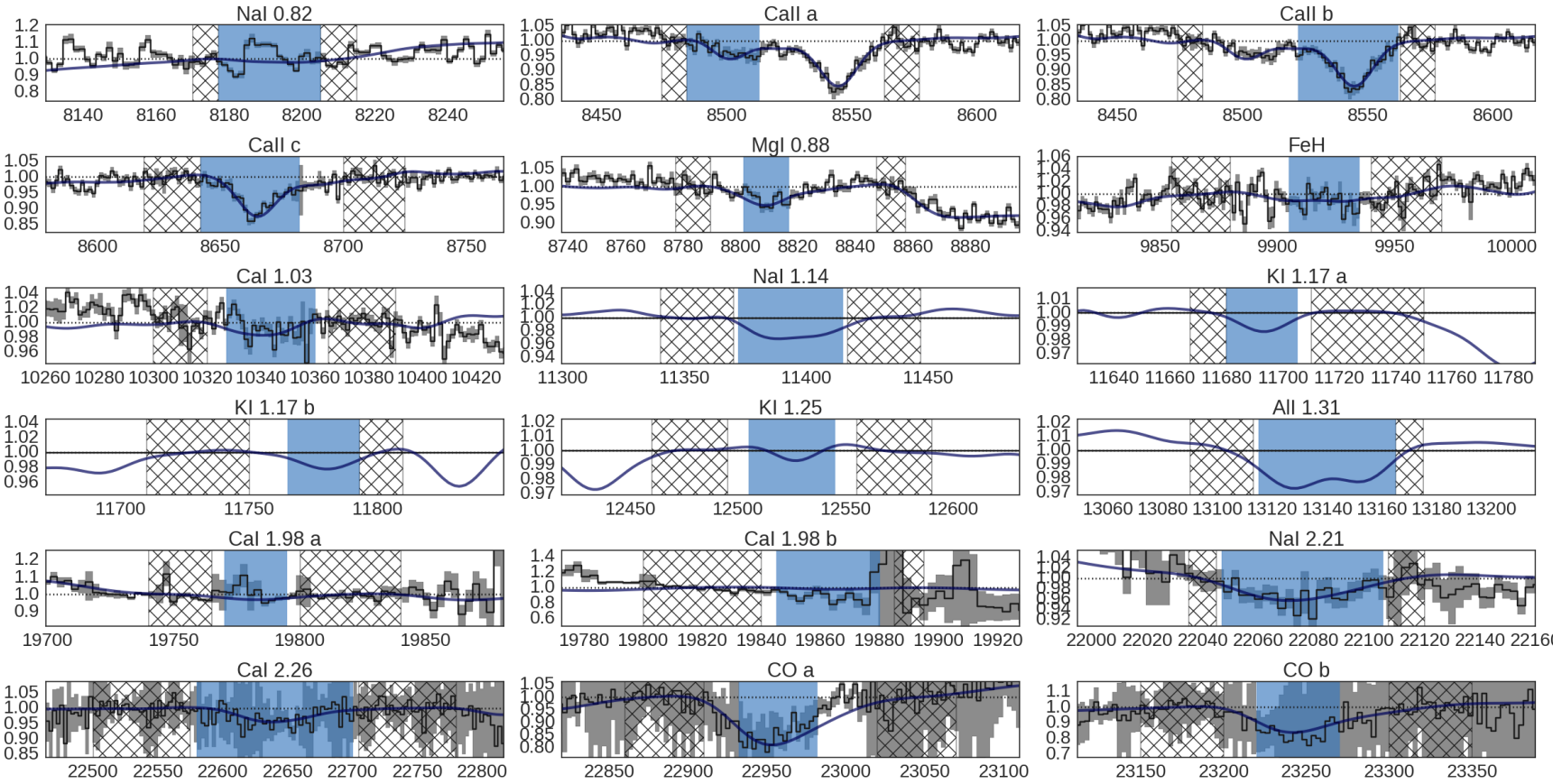

Figure 7.8: Spectrum from the first ring of KMOS IFUs (R = 10″) with shaded uncertainties, displayed in each measured index region (blue vertical band) and normalised by a linear fit to the flux averaged in the pseudo-continuum bands on either side (hatched regions). Overplotted in dark blue: model spectrum generated from the best-fit stellar population parameters (i.e. not a direct fit to the spectrum). Note that YJ band data was not taken so for these indices a predicted spectrum is shown.

The KMOS data is shown in Figs. 7.6, 7.7, and 7.8. This clearly shows the better removal of systematics from e.g. Na I 0.82 μm, justifying the choice just mentioned. Note that for the K-band indices we propagated the variance of the best-fit atmospheric profile (which in reality is *expected* to change over observation timescales) to later stages of the reduction, so the uncertainties are actually conservative estimates. In general, the IZ band data are reproduced well by the model, although some K-band indices appear to be affected by systematics, most likely due to the difficulty of making accurate telluric corrections to some low-transmission wavelength ranges.

7.3 Discussion

Our best-fit models are characterised by IMFs with Milky Way-like $f_{\rm dwarf}$, with only weak constraints on the IMF shape (as in Chapter 6, this is dominated by the specified prior probability distribution). For NGC 1407 the K-band observations consisted of 1440s on-source, half as much as most of our other targets. The data quality for the K-band features is therefore less good than for some other targeted galaxies. We also lack YJ-band observations. However, Figs. 7.6, 7.7, and 7.8 show clearly the quality of the IZ band data. This allows us to place reasonably strong constraints on $f_{\rm dwarf}$, finding $4.3^{+3.1}_{-1.1}\%$, $4.3^{+2.1}_{-1.2}$, and $3.0^{+2.5}_{-0.6}\%$ for the three extraction regions (see Table 7.2).

There is a hint in the data that the integrated light from the innermost extraction region would be consistent with a slightly bottom-heavy IMF that steepens for low stellar masses. This is qualitatively similar to, but much less extreme than, a result published in Conroy et al., 2017, where a highly flexible IMF model was used in a spectral fit to this galaxy's core. In that work, a comparison was made to a fit with a two-part power law IMF with the same definition as used here; with that model the recovered $f_{\rm dwarf}$ was $16.2^{+4.1}_{-3.5}\%$, strongly in tension with our result.

For this innermost aperture a combination of relatively low signal-to-noise for the WiFeS data, the effect of atmospheric seeing, and aperture effects might conspire to suppress the signal from IMF variations. However, our best fit to the data comes from the annulus at $R < 2.8''$ that surrounds this central region. There, our constraints are in tension with a Salpeter IMF, whereas in van Dokkum et al. (2017) an IMF much more

bottom-heavy than a Salpeter power law was recovered out to 7.6″. That study covered a wavelength range from ~ 0.4–$1.0\,\mu$m and made use of a full-spectrum fitting method. Their method uses a sophisticated stellar population model with many more parameters than our own. In contrast, our study uses a simpler model to fit the integrated strengths (i.e. equivalent widths) of absorption features throughout the same wavelength range, as well as the strengths of a number of K-band features.

In order to provide a comprehensive treatment of the data, we also fit the data under the alternative prior probability distribution first described in Section 2.6.4, i.e. a prior that is uniform in $f_{\rm dwarf}$ and in X2–X1. The joint posterior probability distributions for the three fits are given in Fig. 7.9. We obtain qualitatively similar results; in the central extraction region a modestly bottom heavy Salpeter power law IMF is not excluded, but even this case is excluded quite strongly in the annulus at $R < 2.8''$. A Kroupa IMF is clearly favoured at $\frac{1}{3}R_{\rm eff}$.

We find strong abundance enhancements in NGC 1407, with [Mg/Fe] ~ 0.4 and a strong [Na/Fe] enhancement throughout the inner regions, rising somewhat in the core (> 0.6). We note that there is some mild tension between Na D (Na I 0.59 μm) and the Na I 2.21 μm feature. NGC 1407's redshift ($z = 0.0059$) is such that a band of strong atmospheric absorption contaminates the Na I 0.82 μm feature. This is fairly well-corrected for in the high S/N central KMOS observations (less so in the observations from $\sim \frac{1}{3}R_{\rm eff}$), but the additional K-band information nonetheless provides a valuable additional constraint on the Na abundance.

Stellar ages are not well-constrained. However, our model reproduces the strength of the age-sensitive Hβ line and none of the other parameters are strongly covariant with stellar age, so this does not affect our results.

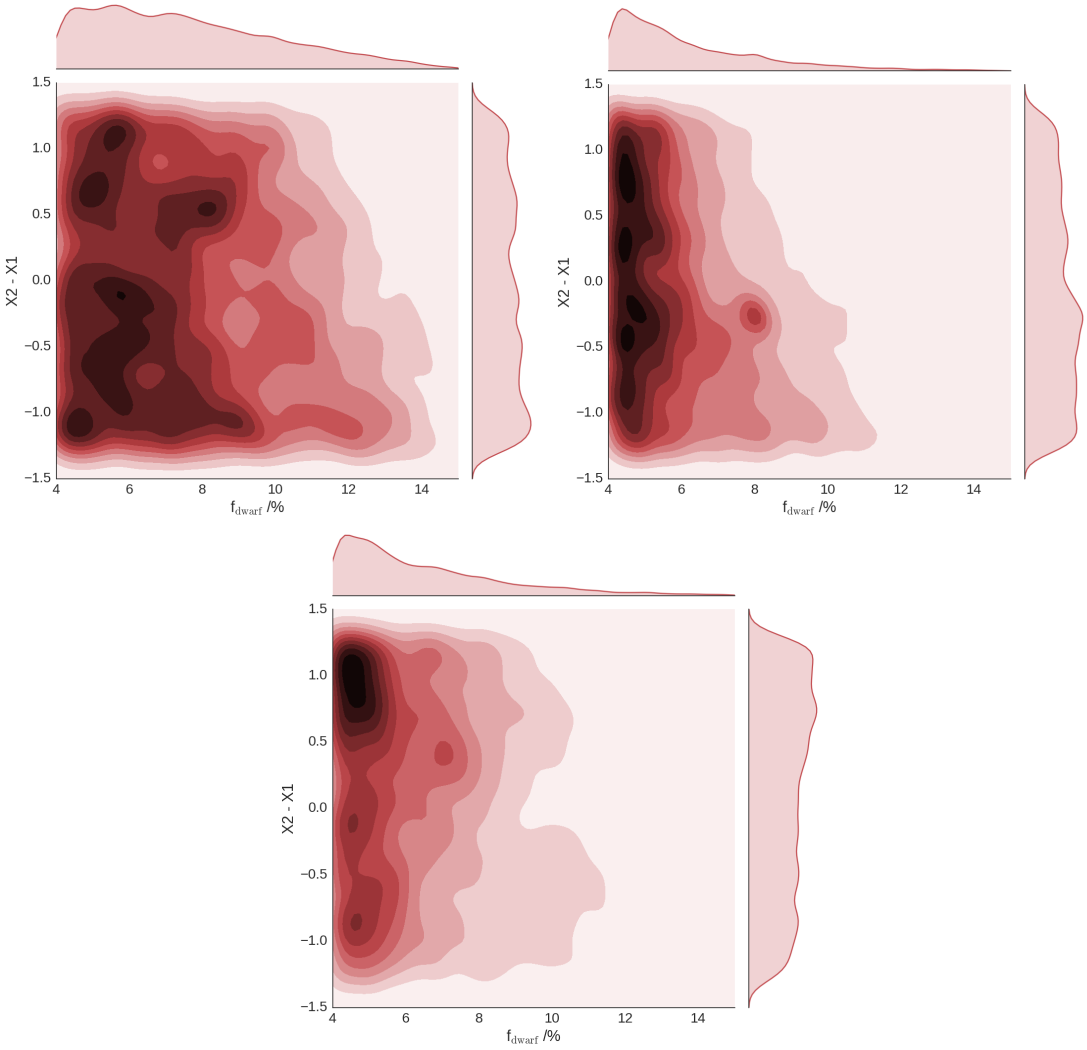

Figure 7.9: Joint posterior probability distributions for the data from extraction regions R1 (top left), R2, and R3 (bottom), subject to an alternative prior probability distribution that is uniform in f_{dwarf} and X2–X1. Extremely bottom-heavy IMFs are excluded by our data.

Summary

In conclusion, using our methods from the previous chapter we find an IMF in NGC 1407 that is consistent with being Milky Way-like; this result is found both in the central regions ($f_{dwarf} = 4.3^{+2.1}_{-1.2}\%$) and also at $R = 10''$ ($f_{dwarf} = 3.0^{+2.5}_{-0.6}\%$). Our result is strongly in tension with published literature – in which this galaxy is found to have a very bottom-heavy IMF with estimated $f_{dwarf} = 16.2^{+4.1}_{-3.5}\%$ – but very much in accordance with the results we presented in the previous chapter for the wider sample (for which our optical data were limited). The chemical abundance pattern we infer is also similar to the average behaviour found in Chapter 6, with a strong, radially constant [Mg/Fe] enhancement of ~ 0.4 and a strongly peaked [Na/Fe] abundance, ranging from $0.46^{+0.05}_{-0.03}$ at $R = 10''$ to $0.68^{+0.09}_{-0.08}$ at $R = 1''$.

In the next chapter we discuss this issue, our overall findings, and the implications for the wider picture of galaxy formation/star formation physics. We discuss the next steps that might be taken in this field.

Chapter 8

Summary and final thoughts

8.1 Overview of principal results

In this work we have used spatially-resolved infrared and optical spectroscopy to investigate the stellar populations of nearby, massive early-type galaxies (ETGs). In particular, we have focused on radial variations of the stellar populations with the aim of linking our findings to models for galaxy mass assembly. We have measured the strengths of a variety of infrared spectroscopic features, including some which are not hitherto well-explored, in eight ETGs (the KINETyS sample). Further, we have reported empirical radial gradients in the strengths of some of these features (Chapters 3 and 5), which correspond to radial variations in the underlying stellar populations of our target galaxies. Combining the outputs of state-of-the-art stellar population synthesis models with a new code that uses a Markov-Chain Monte-Carlo method for Bayesian model parameter estimation (SPINDRIFT, described in Chapter 2), we have been able to place constraints on the age, chemical abundance pattern, and initial mass function (IMF) of the stellar populations in these galaxies (Chapters 4, 6, and 7).

Our principal findings are that the IMF appears to be consistent, on average, with either a Milky Way-like form or an at-most modestly bottom-heavy form (e.g Salpeter power law) in our sample. Furthermore, we do not detect significant radial variations in the contribution of dwarf stars to the total light. While we measure some significant empirical spectroscopic gradients in the strengths of stellar population indices spanning the near-infrared (e.g. in the three Na I features at 0.82, 1.14, and 2.21 μm; and the Ca II

triplet), these variations can be explained solely in terms of radial variations in chemical abundances (and perhaps stellar population ages). In particular, we find strong gradients in [Na/Fe] with superabundant [Na/Fe] throughout our sample of ETGs. In addition, this Na excess appears to correlate with galaxy velocity dispersion. This may be linked to the metallicity dependent yield of Na, since the galaxies in our sample are found to have strong metallicity gradients. We also find evidence for an enhancement in [Mg/Fe] but not its fellow α-capture element, Ca. Neither quantity exhibits a significant radial trend. Our constraints on stellar population age are not strong, with uncertainties of $\pm$ several Gyr, but on average the populations are consistent with being uniformly old ($>$10 Gyr), and marginalising over age does not strongly affect our inference of other stellar population parameters.

8.2 Discussion of our findings

Taken at face value, our IMF measurements for the KINETyS sample appear to stand in contrast to other observational data, in which the balance of evidence favours systematic variation of the IMF at a significant level in (the cores of) massive ETGs, e.g. Cappellari et al. (2012), Conroy & van Dokkum (2012b), van Dokkum et al. (2017). It is conceivable that line strengths in the cores of ETGs can be accounted for solely through abundance effects, despite painstaking efforts to decouple chemical and IMF variations. However, in this case the independent measurement of enhanced M/L ratios in massive ETGs must also be explained. This would likely require variations in the density profile of the dark matter halos hosting ETGs (e.g. as proposed, alongside IMF variations, in Auger et al., 2010). Smith et al. (2015b) reported that in the cores of three massive ETGs (where dark matter is subdominant and therefore the dark matter profile is not a factor) the M/L ratio does not deviate significantly from that of the Milky-Way stellar populations, potentially offering support for this scenario. Additionally, Oldham & Auger (2016) recently reported that dynamical measurements of M87 (NGC 4486, which is included in our sample and which was originally reported in CvD12b as having an M/L of 1.9) are consistent with a heavyweight IMF only under the assumption of orbital isotropy. Their more flexible treatment of orbital anisotropy yields an M/L measurement consistent with a Milky Way-

like IMF. This indicates that M/L constraints from dynamics can sometimes be sensitive at a significant level to the mass-anisotropy degeneracy in slow-rotator galaxies. However, as noted by Cappellari et al. (2012), this alone cannot account for the σ vs. M/L trend they find for ETGs, and variations in the dark matter profile would have to be substantial to remove the trend entirely.

As stellar population synthesis models have become more sophisticated, especially with regard to their treatment of the IMF functional form, it has become apparent that IMF variations may be quite subtle in many cases. For example, Newman et al. (2016) showed that a stacked spectrum derived from observations of high-mass ETGs ($\sigma \simeq 280\,\mathrm{kms}^{-1}$) can, when modelled with a flexible IMF model consisting of a two-part power law and a variable low-mass cut-off, be reproduced with only a modest enhancement in stellar M/L. The same observations require a power law with a steeper-than-Salpeter slope if a single-slope IMF with fixed low-mass cut-off is assumed. Moreover, the authors show that a model with such a flexible IMF can significantly reduce the tension between results from spectroscopy and from lensing measurements for the three lensed ETGs with Milky Way-like M/L presented in Smith et al. (2015b). If these fairly modest enhancements to the dwarf star content of ETGs are typical, the contribution of dwarf stars to the integrated light may be increased by only one or two percent in the majority of galaxies similar to those in the sample first presented in Chapter 3. Nevertheless, in the case of individual galaxies (such as the one investigated in Chapter 7) the tension between our work and some published results that make use of flexible IMF models remains significant.

We have shown that the inference of the IMF is quite sensitive to systematic effects, which may be much larger than the formal statistical uncertainties. Characterising and correcting for these effects is crucial to obtaining robust results in the stellar population analysis. Moreover, for our data it is clear that the choice of prior probability distribution can affect results, potentially reducing the tension between our analysis and some others. Nevertheless, we do not find evidence for strong changes in the IMF within the effective radius either in individual galaxies or on average, in contrast to some other studies (including some which observed the same galaxies).

As outlined in Chapter 1, if IMF variations are characteristic of stellar populations formed in high star formation rate systems with high gas densities and pressures, this

could naturally lead to radial gradients in the IMF. If the IMF is in fact Milky Way-like in ETGs, or else is bottom-heavy but does *not* vary radially within the effective radius, then we must seek a different paradigm. In the first case, the lack of IMF variation even under extremely divergent star forming conditions would be noteworthy in its own right. In the second, a more global driving mechanism for IMF variations would need to be sought, since in the current paradigm they are thought to be driven locally by the star forming conditions (which become more extreme in the cores of ETGs). Moreover, stars accreted via minor mergers would have to be deposited principally beyond the effective radius, or else the IMF would need to also vary (to a similar extent!) in the low mass, low metallicity systems from which such stars originate.

The chemical abundance gradients we measure in our sample can also inform us about the physical processes by which massive ETGs are assembled. In particular, the very large enhancements in sodium abundance at the cores of massive ETGs and the strong radial gradients that go with this are yet to be adequately explained. In this work we have suggested that if the yield of sodium is metallicity dependent then the large enhancements could be a natural consequence of the metallicity gradients common in ETGs. The large sodium abundances also create a practical problem, since stars with such large [Na/Fe] are simply not found in the Milky Way and therefore empirical library spectra for such stars are not available. This in principal could lead to systematic issues with the models in the highly chemically enriched systems we are exploring.

8.3 Future directions

Our analysis has made clear that there are still substantial uncertainties in the results of spectroscopic IMF analyses due to a variety of observational and methodological challenges. These include (but are not limited to) model degeneracies, uncertain model extrapolations, corrections for atmospheric emission and absorption, and model selection/assumptions. Comparisons between constraints on the M/L ratios of massive ETGs via stellar kinematics and lensing, and the direct constraints on the IMF obtained e.g. via spectroscopy will be of crucial importance in the future. Such comparisons are beginning to bear fruit and will be vital for better understanding where and how the IMF varies.

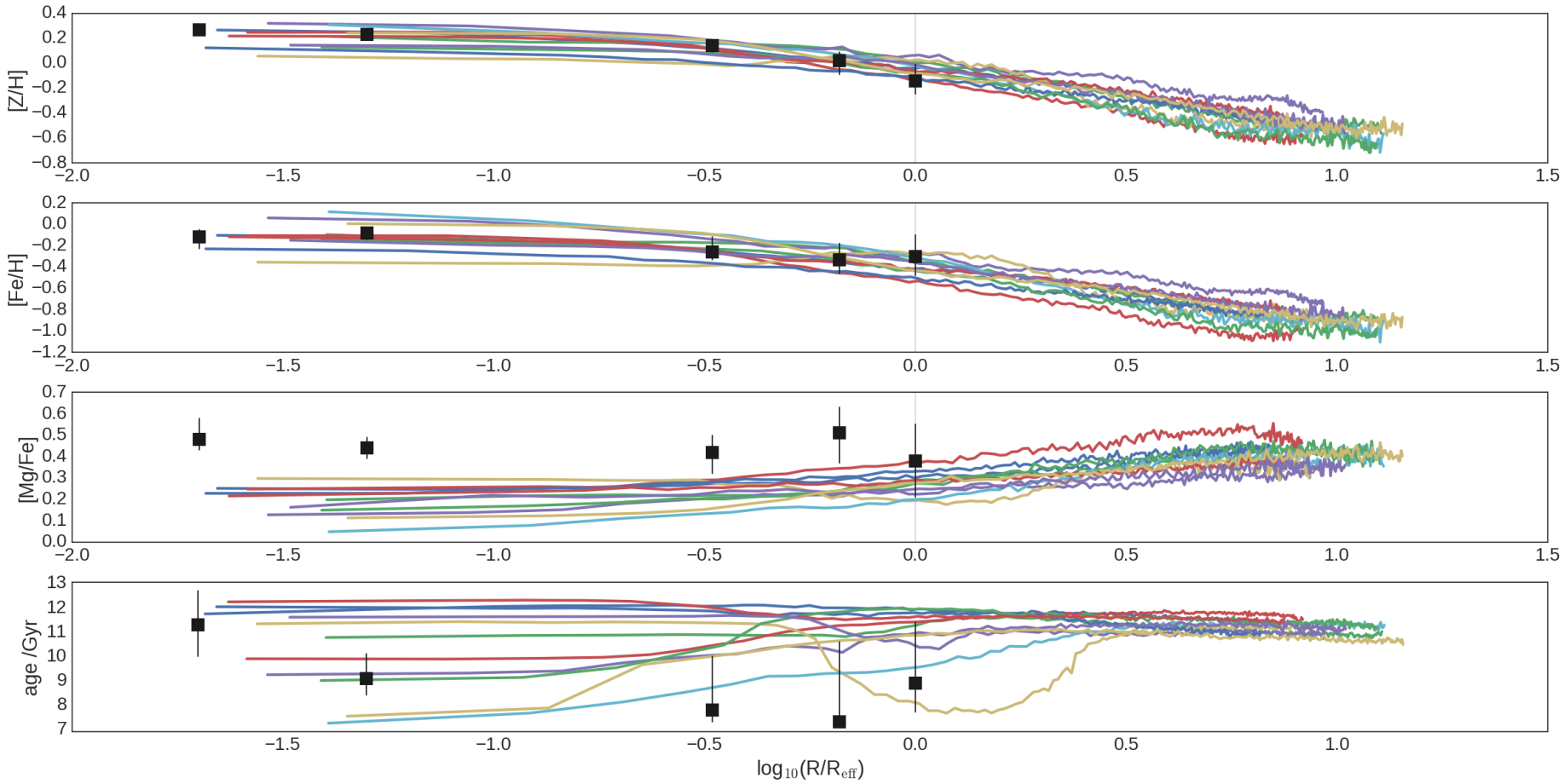

Figure 8.1: A comparison between our inferred (average) stellar population parameters as a function of radius and those predicted for the most massive red-sequence galaxies in the EAGLE hydrodynamic simulation (intended to be a comparable population to the sample we investigated – stellar masses enclosed within 30 kpc range from 2.5–4.5$\times10^{11}$ M$_\odot$).

The advent of high fidelity integral-field spectroscopic surveys (e.g. MaNGA, Bundy et al., 2015; and SAMI, Croom et al., 2012) promises to deliver a much wider sample of galaxies in the future. This step-change in scale for studies of the kind we have pursued will allow us to draw much more general conclusions with regard to the IMF, allowing variations to be linked much more surely to particular conditions prevailing in massive galaxies. Nevertheless, careful treatment of systematic effects and robust statistical inference will still be required. Further in the future, spatially-resolved infrared spectroscopic observations made in space (e.g. via the James Webb Space Telescope's NIRSpec instrument) promise to overcome the most serious of these limitations.

The results of stellar population analyses such as those we have presented can be compared with the outputs of state-of-the-art cosmological simulations. In Fig. 8.1 we show some chemical abundance gradients found in the EAGLE simulation for the most massive ETGs simulated (comparable to those in the KINETyS sample), along with the results of our analysis. Abundance yields in this simulation were calculated assuming a universal, Milky Way-like IMF. The average metallicity gradient we derived appear to be comparable, but the level of Mg enhancement inferred from our data appears greater than in the simulations. Stellar population ages are loosely constrained by our data within the range 7–14 Gyr, but the simulation predicts a spread in ages for massive galaxies.

While in this case we intend only to illustrate the worth of such a comparison, in future this approach may help validate the results of analyses like our own, or even provide new tests of simulations, which must aim to create galaxies with realistic abundance patterns. Similar methods could be used to constrain the high-mass IMF, since chemical abundance yields depend on the supernova rate, and therefore on the IMF. Tests of this kind will become easier as stellar population analyses and simulations become more sophisticated.

In this work we aimed to link the small scale physics that governs star formation with the large scale processes which determine galaxy formation. Our results present an ambiguous picture, with radial IMF variations somewhat constrained, if not ruled out. We have seen that instrumental systematics, modelling assumptions, and choice of prior probability distributions and features to examine can have important impacts on results – but also that these issues can be overcome both in principle and in practice, with sufficient care.

Bibliography

Alton, P. D., Smith, R. J., & Lucey, J. R. 2017, MNRAS, 468, 1594

Arnold, J. A., Romanowsky, A. J., Brodie, J. P., et al. 2014, ApJ, 791, 80

Auger, M. W., Treu, T., Gavazzi, R., et al. 2010, ApJ, 721, L163

Baldry, I. K. 2008, Astronomy and Geophysics, 49, 5.25

Baldry, I. K., Glazebrook, K., Brinkmann, J., et al. 2004, ApJ, 600, 681

Bastian, N., Covey, K. R., & Meyer, M. R. 2010, ARA&A, 48, 339

Bezanson, R., van Dokkum, P. G., Tal, T., et al. 2009, ApJ, 697, 1290

Bois, M., Bournaud, F., Emsellem, E., et al. 2010, MNRAS, 406, 2405

Bromm, V., & Larson, R. B. 2004, ARA&A, 42, 79

Bruzual, G., & Charlot, S. 2003, MNRAS, 344, 1000

Bundy, K., Bershady, M. A., Law, D. R., et al. 2015, ApJ, 798, 7

Cappellari, M., & Emsellem, E. 2004, PASP, 116, 138

Cappellari, M., Emsellem, E., Krajnović, D., et al. 2011, MNRAS, 413, 813

Cappellari, M., McDermid, R. M., Alatalo, K., et al. 2012, Nature, 484, 485

Cappellari, M., Scott, N., Alatalo, K., et al. 2013a, MNRAS, 432, 1709

Cappellari, M., McDermid, R. M., Alatalo, K., et al. 2013b, MNRAS, 432, 1862

Carter, D., Visvanathan, N., & Pickles, A. J. 1986, ApJ, 311, 637

Cenarro, A. J., Gorgas, J., Vazdekis, A., Cardiel, N., & Peletier, R. F. 2003, MNRAS, 339, L12

Cesetti, M., Ivanov, V. D., Morelli, L., et al. 2009, A&A, 497, 41

Chabrier, G. 2003, PASP, 115, 763

Chabrier, G., Hennebelle, P., & Charlot, S. 2014, ApJ, 796, 75

Coccato, L., Gerhard, O., & Arnaboldi, M. 2010, MNRAS, 407, L26

Cohen, J. G. 1979, ApJ, 228, 405

Conroy, C., Graves, G. J., & van Dokkum, P. G. 2014, ApJ, 780, 33

Conroy, C., & van Dokkum, P. 2012a, ApJ, 747, 69

Conroy, C., & van Dokkum, P. G. 2012b, ApJ, 760, 71

Conroy, C., van Dokkum, P. G., & Villaume, A. 2017, ApJ, 837, 166

Coulter, D. A., Lehmer, B. D., Eufrasio, R. T., et al. 2017, ApJ, 835, 183

Crampin, J., & Hoyle, F. 1961, MNRAS, 122, 27

Croom, S. M., Lawrence, J. S., Bland-Hawthorn, J., et al. 2012, MNRAS, 421, 872

Davies, R. I. 2007, MNRAS, 375, 1099

Eggen, O. J., Lynden-Bell, D., & Sandage, A. R. 1962, ApJ, 136, 748

Emsellem, E., Cappellari, M., Peletier, R. F., et al. 2004, MNRAS, 352, 721

Emsellem, E., Cappellari, M., Krajnović, D., et al. 2007, MNRAS, 379, 401

Faber, S. M. 1973, ApJ, 179, 731

Ferreras, I., Weidner, C., Vazdekis, A., & La Barbera, F. 2015, MNRAS, 448, L82

Foreman-Mackey, D. 2016, The Journal of Open Source Software, 24, doi:10.21105/joss.00024

Foreman-Mackey, D., Hogg, D. W., Lang, D., & Goodman, J. 2013, PASP, 125, 306

Goddard, D., Thomas, D., Maraston, C., et al. 2017, MNRAS, 466, 4731

Goodman, J., & Weare, J. 2010, CAMCoS, 5, 65

Greene, J. E., Janish, R., Ma, C.-P., et al. 2015, ApJ, 807, 11

Gunawardhana, M. L. P., Hopkins, A. M., Sharp, R. G., et al. 2011, MNRAS, 415, 1647

Hilz, M., Naab, T., & Ostriker, J. P. 2013, MNRAS, 429, 2924

Ho, L. C., Filippenko, A. V., & Sargent, W. L. W. 1997, ApJS, 112, 315

Hopkins, P. F. 2013, MNRAS, 433, 170

Hopkins, P. F., Bundy, K., Hernquist, L., Wuyts, S., & Cox, T. J. 2010, MNRAS, 401, 1099

Hopkins, P. F., Bundy, K., Murray, N., et al. 2009, MNRAS, 398, 898

Hoyle, F. 1953, ApJ, 118, 513

Hunter, D. A., Elmegreen, B. G., & Ludka, B. C. 2010, AJ, 139, 447

Jarrett, T. H., Chester, T., Cutri, R., Schneider, S. E., & Huchra, J. P. 2003, AJ, 125, 525

Johansson, J., Thomas, D., & Maraston, C. 2012, MNRAS, 421, 1908

Kausch, W., Noll, S., Smette, A., et al. 2015, A&A, 576, A78

Khochfar, S., Emsellem, E., Serra, P., et al. 2011, MNRAS, 417, 845

Kobayashi, C. 2004, MNRAS, 347, 740

Kobayashi, C., Umeda, H., Nomoto, K., Tominaga, N., & Ohkubo, T. 2006, ApJ, 653, 1145

Kroupa, P. 2001, MNRAS, 322, 231

Krumholz, M. R., Cunningham, A. J., Klein, R. I., & McKee, C. F. 2010, ApJ, 713, 1120

Kuntschner, H., Emsellem, E., Bacon, R., et al. 2010, MNRAS, 408, 97

La Barbera, F., Ferreras, I., Vazdekis, A., et al. 2013, MNRAS, 433, 3017

La Barbera, F., Vazdekis, A., Ferreras, I., et al. 2017, MNRAS, 464, 3597

La Barbera, F., Vazdekis, A., Ferreras, I., et al. 2016, MNRAS, 457, 1468

Lacey, C. G., Baugh, C. M., Frenk, C. S., et al. 2016, MNRAS, 462, 3854

Landt, H., Bentz, M. C., Ward, M. J., et al. 2008, ApJS, 174, 282

Larson, R. B. 2005, MNRAS, 359, 211

Lecureur, A., Hill, V., Zoccali, M., et al. 2007, A&A, 465, 799

Lee, J. C., Gil de Paz, A., Tremonti, C., et al. 2009, ApJ, 706, 599

Luhman, K. L., Briceño, C., Stauffer, J. R., et al. 2003, ApJ, 590, 348

Lyubenova, M., Kuntschner, H., & Silva, D. R. 2008, A&A, 485, 425

Maoz, D., Mannucci, F., & Brandt, T. D. 2012, MNRAS, 426, 3282

Maraston, C. 1998, MNRAS, 300, 872

Marks, M., Kroupa, P., Dabringhausen, J., & Pawlowski, M. S. 2012, MNRAS, 422, 2246

Mármol-Queraltó, E., Cardiel, N., Sánchez-Blázquez, P., et al. 2009, ApJ, 705, L199

Martín-Navarro, I., Barbera, F. L., Vazdekis, A., Falcón-Barroso, J., & Ferreras, I. 2015, MNRAS, 447, 1033

McConnell, N. J., Lu, J. R., & Mann, A. W. 2016, ApJ, 821, 39

McDermid, R. M., Alatalo, K., Blitz, L., et al. 2015, MNRAS, 448, 3484

McKee, C. F., & Ostriker, E. C. 2007, ARA&A, 45, 565

Mehlert, D., Thomas, D., Saglia, R. P., Bender, R., & Wegner, G. 2003, A&A, 407, 423

Meurer, G. R., Wong, O. I., Kim, J. H., et al. 2009, ApJ, 695, 765

Miller, G. E., & Scalo, J. M. 1979, ApJS, 41, 513

Milone, A. D. C., Sansom, A. E., & Sánchez-Blázquez, P. 2011, MNRAS, 414, 1227

Naab, T., Oser, L., Emsellem, E., et al. 2014, MNRAS, 444, 3357

Newman, A. B., Smith, R. J., Conroy, C., Villaume, A., & van Dokkum, P. 2016, ArXiv e-prints, arXiv:1612.00065

Noll, S., Kausch, W., Kimeswenger, S., et al. 2014, A&A, 567, A25

Nordh, H. L., Lindgren, B., & Wing, R. F. 1977, A&A, 56, 1

Oldham, L. J., & Auger, M. W. 2016, MNRAS, 457, 421

Oser, L., Naab, T., Ostriker, J. P., & Johansson, P. H. 2012, ApJ, 744, 63

Oser, L., Ostriker, J. P., Naab, T., Johansson, P. H., & Burkert, A. 2010, ApJ, 725, 2312

Peacock, M. B., Zepf, S. E., Maccarone, T. J., et al. 2014, ApJ, 784, 162

Pietrinferni, A., Cassisi, S., Salaris, M., & Castelli, F. 2004, ApJ, 612, 168

Prieto, M. A., Fernández-Ontiveros, J. A., Markoff, S., Espada, D., & González-Martín, O. 2016, MNRAS, 457, 3801

Rayner, J. T., Cushing, M. C., & Vacca, W. D. 2009, ApJS, 185, 289

Rees, M. J. 1976, MNRAS, 176, 483

Rodriguez-Gomez, V., Pillepich, A., Sales, L. V., et al. 2016, MNRAS, 458, 2371

Saglia, R. P., Maraston, C., Thomas, D., Bender, R., & Colless, M. 2002, ApJ, 579, L13

Salpeter, E. E. 1955, ApJ, 121, 161

Schiavon, R. P. 2007, ApJS, 171, 146

Sharples, R., Bender, R., Agudo Berbel, A., et al. 2013, The Messenger, 151, 21

Silva, D. R., Kuntschner, H., & Lyubenova, M. 2008, ApJ, 674, 194

Smette, A., Sana, H., Noll, S., et al. 2015, A&A, 576, A77

Smith, R. J. 2014, MNRAS, 443, L69

Smith, R. J., Alton, P., Lucey, J. R., Conroy, C., & Carter, D. 2015a, MNRAS, 454, L71

Smith, R. J., Lucey, J. R., & Carter, D. 2012, MNRAS, 426, 2994

Smith, R. J., Lucey, J. R., & Conroy, C. 2015b, MNRAS, 449, 3441

Spiniello, C., Barnabè, M., Koopmans, L. V. E., & Trager, S. C. 2015a, MNRAS, 452, L21

Spiniello, C., Trager, S. C., & Koopmans, L. V. E. 2015b, ApJ, 803, 87

Spiniello, C., Trager, S. C., Koopmans, L. V. E., & Chen, Y. P. 2012, ApJ, 753, L32

Spinrad, H., & Taylor, B. J. 1971, ApJS, 22, 445

Thomas, D. 1999, MNRAS, 306, 655

Thomas, D., Johansson, J., & Maraston, C. 2011a, MNRAS, 412, 2199

Thomas, D., Maraston, C., & Bender, R. 2003a, MNRAS, 343, 279

Thomas, D., Maraston, C., & Bender, R. 2003b, MNRAS, 339, 897

Thomas, D., Maraston, C., Bender, R., & Mendes de Oliveira, C. 2005, ApJ, 621, 673

Thomas, D., Maraston, C., & Johansson, J. 2011b, MNRAS, 412, 2183

Thomas, J., Saglia, R. P., Bender, R., et al. 2011c, MNRAS, 415, 545

Tinsley, B. M. 1968, ApJ, 151, 547

Tinsley, B. M. 1972, ApJ, 178, 319

Trager, S. C., Faber, S. M., Worthey, G., & González, J. J. 2000, AJ, 119, 1645

Vacca, W. D., Cushing, M. C., & Rayner, J. T. 2003, PASP, 115, 389

van Dokkum, P., Conroy, C., Villaume, A., Brodie, J., & Romanowsky, A. 2016, ArXiv e-prints, arXiv:1611.09859

van Dokkum, P., Conroy, C., Villaume, A., Brodie, J., & Romanowsky, A. J. 2017, ApJ, 841, 68

van Dokkum, P. G., & Conroy, C. 2010, Nature, 468, 940

van Dokkum, P. G., Franx, M., Kriek, M., et al. 2008, ApJ, 677, L5

Vanderbeke, J., Baes, M., Romanowsky, A. J., & Schmidtobreick, L. 2011, MNRAS, 412, 2017

Vaughan, S. P., Houghton, R. C. W., Davies, R. L., & Zieleniewski, S. 2016, ArXiv e-prints, arXiv:1612.00364

Vazdekis, A., Casuso, E., Peletier, R. F., & Beckman, J. E. 1996, ApJS, 106, 307

Villaume, A., Conroy, C., Johnson, B., et al. 2017, ArXiv e-prints, arXiv:1705.08906

Weidner, C., Ferreras, I., Vazdekis, A., & La Barbera, F. 2013, MNRAS, 435, 2274

White, S. D. M., & Rees, M. J. 1978, MNRAS, 183, 341

Wing, R. F., & Ford, Jr., W. K. 1969, PASP, 81, 527

Worthey, G. 1994, ApJS, 95, 107

Worthey, G., Faber, S. M., & Gonzalez, J. J. 1992, ApJ, 398, 69

Worthey, G., Faber, S. M., Gonzalez, J. J., & Burstein, D. 1994, ApJS, 94, 687

Zieleniewski, S., Houghton, R. C. W., Thatte, N., & Davies, R. L. 2015, MNRAS, 452, 597

Zieleniewski, S., Houghton, R. C. W., Thatte, N., Davies, R. L., & Vaughan, S. P. 2017, MNRAS, 465, 192